NASA Technical Memorandum 83222

# Pressure Distributions and Shock Shapes for 12.84°/7° On-Axis and Bent-Nose Biconics in Air at Mach 6

Charles G. Miller III and Peter A. Gnoffo
*Langley Research Center*
*Hampton, Virginia*

| 1. Report No.<br>NASA TM-83222 | 2. Government Accession No. | 3. Recipient's Catalog No. |
|---|---|---|
| 4. Title and Subtitle<br><br>PRESSURE DISTRIBUTIONS AND SHOCK SHAPES FOR 12.84°/7° ON-AXIS AND BENT-NOSE BICONICS IN AIR AT MACH 6 | | 5. Report Date<br>December 1981 |
| | | 6. Performing Organization Code<br>506-51-13-01 |
| 7. Author(s)<br><br>Charles G. Miller III and Peter A. Gnoffo | | 8. Performing Organization Report No.<br>L-14896 |
| 9. Performing Organization Name and Address<br><br>NASA Langley Research Center<br>Hampton, VA 23665 | | 10. Work Unit No. |
| | | 11. Contract or Grant No. |
| 12. Sponsoring Agency Name and Address<br>National Aeronautics and Space Administration<br>Washington, DC 20546 | | 13. Type of Report and Period Covered<br>Technical Memorandum |
| | | 14. Sponsoring Agency Code |

15. Supplementary Notes

16. Abstract

Pressure distributions and shock shapes were measured on a spherically blunted, 12.84°/7° on-axis biconic and a spherically blunted, 12.84°/7° bent-nose biconic (fore-cone bent 7° upwards relative to aft-cone) at Mach 6 in air. The angle of attack, referenced to the axis of the aft-cone, was varied from 0° to 25° in nominal 5° increments. Two values of free-stream Reynolds number based on model length were tested, $0.7 \times 10^6$ and $5.3 \times 10^6$. Predictions from simple theories and from a Supersonic, Three-dimensional, External INviscid code, referred to as STEIN, were compared with measured values. Predicted (STEIN) shock shapes and windward pressures were in good agreement with measured values for both biconics over the present range of angle of attack; somewhat poorer agreement was observed for the leeward surface pressure.

| 17. Key Words (Suggested by Author(s))<br><br>Biconic<br>Hypersonic<br>Pressure distribution<br>Shock shape | 18. Distribution Statement<br>Unclassified - Unlimited<br><br><br>Subject Category 02 | | |
|---|---|---|---|
| 19. Security Classif. (of this report)<br>Unclassified | 20. Security Classif. (of this page)<br>Unclassified | 21. No. of Pages<br>125 | 22. Price<br>A06 |

# SUMMARY

Pressure distributions and shock shapes were measured on a spherically blunted, 12.84°/7°, on-axis biconic, a spherically blunted, 12.84°/7°, bent-nose biconic (fore-cone bent 7° upwards relative to aft-cone), and a spherically blunted 12.84° cone at Mach 6 in air. The angle of attack, referenced to the axis of the aft-cone, was varied from 0° to 25° in nominal 5° increments. Two values of free-stream Reynolds number based on model length were tested, $0.7 \times 10^6$ and $5.3 \times 10^6$. Predictions from simple theories and from a Supersonic, Three-dimensional, External INviscid code, referred to as STEIN, were compared with measured values.

Predicted (STEIN) shock shapes and windward pressures were in good agreement with measured values for both biconics over the present range of angle of attack; somewhat poorer agreement was observed for the leeward pressure. For values of the fore-cone angle of attack exceeding the fore-cone half-angle, schlieren photograhs illustrate the existence of an imbedded shock within the shock layer on the leeward side, and a minimum was observed in the circumferential pressure distribution (the surface pressure on the most leeward ray (0°) exceeded that on the 45° ray). This minimum has been observed in previous cone studies and is attributed to flow separation and the formation of two symmetrical, supersonic, counter-rotating vortices. No significant effect of Reynolds number on surface pressure was observed; however, there was an appreciable effect on base pressure. For the present range of angle of attack, the leeward base pressure was less than the leeward model-surface pressure just upstream of the base, implying a lack of communication between the two flow regions.

# INTRODUCTION

To maximize the scientific return of a planetary-exploration program, the entry vehicle must be designed to have high volumetric efficiency and low weight. One means of achieving these design objectives is to minimize the rocket propulsion system by using aerodynamic forces to capture the vehicle into a closed orbit in the atmosphere of the planet (ref. 1). The use of lift and drag to capture a vehicle or modify an orbit has been under consideration since the beginning of space exploration with probes; however, this principle has not been applied, primarily because of inadequate navigation or inadequate knowledge of the atmosphere of the planet (ref. 1). As more information is obtained on the atmospheres, and navigational shortcomings are overcome, the aerocapture and aerobraking techniques become more promising. (The aerobraking technique uses the drag during successive passes through the upper atmosphere of a planet to circularize a highly elliptical orbit. Aerocapture represents a transfer of the vehicle into a closed stable orbit from a fly-by trajectory. The one-pass aerocapture technique calls for precise control and requires a higher level of technolgy than does aerobraking.)

The external design of the aerocapture vehicle is usually evolved from the initial trade-off studies, in which the aerodynamicist must identify the combination of basic body and control systems with attendant stability and control characteristics. Several basic factors determine the vehicle aerodynamic shape and corresponding performance characteristics, such as volumetric efficiency, vehicle design mass, and accuracy. For proposed flights to Mars, Venus, Saturn, and Titan, the feasibility studies of references 1 to 3 conclude that biconic shapes offer the most attractive

compromise of high lift-drag ratio for inserting accuracy, low hypersonic ballistic coefficient, and high volumetric efficiency. Also, biconic shapes would fit nicely into the Shuttle orbiter bay. The leading candidate selected in reference 3 for planetary missions involving the aerocapture technique is a 12.84°/7° bent-nose biconic with a bend angle of 7°. The geometric asymmetry of this configuration generates a lift-drag ratio of approximately 1.5. The bend angle is usually held to a relatively small value to reduce heating of the fore-cone section and therefore reduce heat-shield mass loss via ablation.

To avoid a conservative design involving larger and heavier control characteristics, thus reducing scientific return, an accurate data base on vehicle performance during entry is needed. Because wind tunnels are not capable of duplicating the full flight trajectory of a planetary-entry vehicle, numerical techniques must be relied upon heavily to furnish this data base, that is, to furnish the flow environment surrounding the vehicle during entry. However, experimental results are needed in order to validate the results from the numerical flow-field codes.

To assist in providing such a data base at hypersonic conditions, a study has been initiated at the Langley Research Center. The purpose of this report is to present preliminary results from this study. Pressure distributions and shock shapes measured on an on-axis biconic, a bent-nose biconic, and a sphere-cone in the Langley 20-Inch Mach 6 Tunnel are presented for angles of attack from 0° to 25° and Reynolds numbers of $0.7 \times 10^6$ and $5.3 \times 10^6$ based on model length. These data are compared with predicted results obtained with modified Newtonian theory, the semiempirical theory of Amick (ref. 4), the method of High and Blick (ref. 5), and the inviscid flow-field code of reference 6, referred to as STEIN (Supersonic Three-dimensional, External INviscid code). Also presented herein are results from a calibration of the Langley 20-Inch Mach 6 Tunnel. (See appendix.)

<div align="center">SYMBOLS</div>

| | | |
|---|---|---|
| $C_p$ | pressure coefficient, | $\dfrac{p_s - p_\infty}{q_\infty}$ |
| i.d. | inside diameter | |
| L | model length, m | |
| M | Mach number | |
| o.d. | outside diameter | |
| p | pressure, Pa | |
| q | dynamic pressure, Pa | |
| R | unit Reynolds number, $m^{-1}$ | |
| r | radial coordinate measured from axis of aft-cone section, normal to axis | |
| $r_b$ | base radius, m | |
| $r_n$ | nose radius, m | |
| T | temperature, K | |

2

| | |
|---|---|
| t | time, sec |
| U | velocity, m/sec |
| w | test-section width, m |
| x,y,z | model coordinates (see fig. 2), or test-section coordinates (see fig. 18) |
| $\alpha$ | angle of attack, deg |
| $\alpha_{p,max}$ | angle of attack for maximum pressure on the most windward ray, deg |
| $\beta$ | see equation (10) |
| $\gamma$ | ratio of specific heats |
| $\delta$ | angle that front elliptical plane of aft-cone section of bent-nose biconic model makes with a line perpendicular to the axis of revolution, deg (See fig. 2(b).) |
| $\eta$ | angle between axis of revolution of fore-cone section and aft-cone section of biconic, deg ($\eta = 0$ for on-axis biconic, see fig. 2) |
| $\theta$ | cone half-angle, deg |
| $\phi$ | circumferential angle measured from the most leeward meridian, deg |

Subscripts:

| | |
|---|---|
| a | aft section |
| b | base |
| c | cone surface |
| core | across the core |
| cp | center probe of survey rake |
| e | equivalent |
| f | fore section |
| $\ell$ | immediately upstream of base |
| m | measured |
| max | maximum |
| s | surface |
| stag | stagnation |
| t,1 | reservoir stagnation conditions |

t,2        stagnation conditions behind normal shock

∞          free-stream conditions

A bar over a symbol denotes a mean value.


## FACILITY

The Langley 20-Inch Mach 6 Tunnel (refs. 7 and 8) is a blowdown wind tunnel that uses dry air as the test gas. Air is supplied from a 4.14-MPa tank field and is heated to a maximum temperature of 560 K by an electrical resistance heater; maximum reservoir pressure is 3.5 MPa. The general arrangement of this facility is shown schematically in figure 1. A fixed-geometry, two-dimensional, contoured nozzle is used. The sidewalls are parallel, forming a 0.86-cm by 50.8-cm throat section and a 52.1-cm by 50.8-cm test section. The length from the nozzle throat to the centerline of the most upstream schlieren window is 2.27 m. This tunnel is equipped with a variable second minimum and exhausts either into a vacuum sphere, or when the annular ejector is used, into the atmosphere. Maximum run time is 2 minutes with the vacuum sphere and 20 minutes with the ejector. Models are mounted on an injector system located beneath the test section. This system includes a remote-controlled sting support capable of moving the model through an angle-of-attack range from -5° to 55°, and a yaw range of -10° to 4°.


## MODELS

A planform view and dimensions of the biconic models and the sphere-cone model are shown in figure 2. Model 1 (fig. 2(a)) is an on-axis biconic having a fore-cone-section half-angle of 12.84°, aft-cone-section half angle of 7°, spherical nose radius of 5.79 mm, and base diameter of 7.62 cm. Model 2 (fig. 2(b)) has the same basic dimensions as model 1, but the fore-cone section is bent upwards ($\eta = 7°$) relative to the aft-cone section. This bend requires that the base of the fore-cone section be cut at a slant, thereby providing an elliptical cross section that must be matched to that of the aft-cone section. The angle $\delta$ (fig. 2(b)) describing this cutting and matching of the fore-cone and aft-cone sections, in terms of the bend angle $\eta$, is given by the expression

$$\tan \delta = \sin \eta \bigg/ \left( \cos \eta + \frac{\cos \theta_f}{\cos \theta_a} \right) \tag{1}$$

Models 1 and 2 are referred to as the on-axis biconic and bent-nose biconic models, respectively. The models were sting mounted; the sting diameter was 2.54 cm and the ratio of sting length to sting diameter exceeded seven.

Also tested was a spherically blunted cone (model 3, fig. 2(c)) having the same half-angle (12.84°) and nose radius (5.79 mm) as the fore-cone section of the biconic models and a base diameter of 7.62 cm. This sphere-cone model provided more detailed pressure distributions than obtained on the biconic fore-cone sections. The detail of the pressure distributions for all models was dictated in part by the number of pressure tubes that could be passed through the sting.

The models were fabricated from stainless steel and had a wall thickness of approximately 2.5 mm. The biconic models had 62 surface pressure orifices, and the

4

sphere cone had 61 orifices. Each model also had two pressure orifices on the flat base. The surface orifices were distributed along five rays (the most windward, the most leeward, and three rays at 45° increments between the windward and leeward rays). Pressure tubing was stainless steel with an inside diameter of 1.02 mm and was mounted normal to and machined flush with the surface. These tubes were stepped up to a 1.52-mm inside-diameter stainless-steel tube within the model shell. The measured locations of the pressure orifices monitored in this study (see section "Instrumentation") are presented in table I for the three models.

## INSTRUMENTATION

Model surface pressures were measured using variable-capacitance diaphragm transducers having 7 ranges of pressure, the maximum being 133 kPa. Twenty such transducers were available for use. The signals from the transducers were recorded on a magnetic tape by an analog-to-digital recording system. Output signals from 8 of the 20 pressure transducers were displayed on an oscillograph, and data were taken at selected times. This interaction with the system allowed the taking of data for a steady-flow condition (reservoir pressure, reservoir temperature, and test-section pitot pressure constant with time); also, pressure-lag effects due to the long length of tubing (approximately 3 m) could be observed and data could be taken after allowing sufficient time for the model surface pressure to become nearly constant. To decrease the response time of the pressure-measuring system, the transducers and reference manifold were subjected to a pressure prior to the run that was expected to be close to that on the leeward side of the model surface during the run. A switching device referred to as a pinch bar allowed the 20 pressure transducers to be used to measure 56 surface pressures and the leeside base pressure during a run. (The pitot pressure at the test section was monitored during the run with a fixed position, single-pitot pressure probe. This pitot pressure was measured on all 3 pinch bars, leaving 19 transducers available on each pinch bar for measuring model pressure.)

Shock shapes were recorded using a single-pass schlieren system. A point light source was operated in a continuous mode during tunnel start-up. Once steady flow was obtained over the model, a mirror was inserted into the schlieren system to reflect a short-duration light pulse from the lamp into a camera equipped with a fast opening shutter; hence, a single frame was obtained during a run. Representative schlieren photographs for the bent-nose biconic at various angles of attack are shown in figure 3.

## TEST CONDITIONS

Tests were performed for two values of reservoir pressure, 0.34 and 3.46 MPa. The lower value of reservoir pressure results in a value of the unit free-stream Reynolds number close to that obtained in the Langley Hypersonic $CF_4$ Tunnel (ref. 9) (see appendix); the higher reservoir pressure represents the maximum value of Reynolds number possible in the Langley 20-Inch Mach 6 Tunnel without flow-condensation effects. Nominal flow conditions for the present study are as follows:

| $P_{t,1}$, MPa | $T_{t,1}$, K | $p_\infty$, Pa | $T_\infty$, K | $M_\infty$ | $R_\infty$, m$^{-1}$ | $P_{t,2}$, kPa |
|---|---|---|---|---|---|---|
| 0.34 | 452 | 252 | 57.5 | 5.855 | $3.6 \times 10^6$ | 11.2 |
| 3.46 | 503 | 2200 | 61.4 | 5.996 | $28.7 \times 10^6$ | 102.9 |

5

The high-reservoir-pressure tests offer several advantages over the low-reservoir-pressure tests, such as reducing pressure-lag effects, allowing the pressure transducers to operate in a more accurate range, diminishing possible orifice effects (ref. 10), and enhancing schlieren quality.

Calibrations of the Langley 20-Inch Mach 6 Tunnel performed prior to the present study covered reservoir pressures from 0.52 to 3.03 MPa (refs. 7 and 8). In order to extend the facility calibration to include the reservoir pressures of the present study, a calibration was performed for reservoir pressures from 0.3 to 3.6 MPa. The results of this calibration are presented in the appendix.

The biconic models were tested over a range of angle of attack from 0° to 25° in nominal 5° increments. The angle of attack $\alpha$ is referenced to the axis of the aft-cone section, which corresponds to the sting axis. The spherically blunted cone was tested at the same angles of attack and also at $\alpha = 32°$, corresponding to the angle of attack of the fore-cone section $\alpha_f$ of the bent-nose biconic at $\alpha = 25°$.

## DATA REDUCTION AND UNCERTAINTY

Free-stream and post-normal-shock flow conditions were determined for each run by assuming an isentropic expansion of the air test gas between the reservoir and nozzle test section. For the range of reservoir conditions and flow conditions of the Langley 20-Inch Mach 6 Tunnel, the test air behaves ideally. The free-stream Mach number $M_\infty$ was determined from the measured reservoir pressure $p_{t,1}$ and pitot pressure $p_{t,2}$ by using a second-order least-squares fit applied to the tabulated results of reference 11 for $5.8 < M_\infty < 6.1$. This curve-fit expression is

$$M_\infty = 8.300676 - 106.163818\left(\frac{p_{t,2}}{p_{t,1}}\right) + 963.509616\left(\frac{p_{t,2}}{p_{t,1}}\right)^2 \tag{2}$$

Corresponding free-stream conditions and post-normal-shock conditions were obtained by using the ideal-air relations of reference 11.

Pitot pressure $p_{t,2}$ was measured at various times during the run with a fixed-position, single-pitot pressure probe. This probe was inserted into the tunnel from the top of the test section and positioned 6.35 mm downstream of the center of the schlieren window and 10.8 cm above and 9.70 cm to the right of the nozzle centerline looking upstream. The pitot probe remained in the test section during each run to provide information on the steadiness of the flow. Schlieren photographs revealed the presence of a family of oblique shocks at the bottom of the test section for model angles of attack exceeding 10°. The present pitot pressure time histories did not reveal any significant blockage effects for the present range of angle of attack. The model stagnation point at zero incidence was 5.9 cm to 6.5 cm upstream of the pitot pressure probe. As noted in the appendix, the axial variation in pitot pressure for a distance of 5.9 cm to 6.5 cm is quite small and no correction for nozzle axial gradients is applied to the present results.

Comparison of the pitot pressure measured with the fixed probe to the pressure measured at the model stagnation point at zero incidence revealed the stagnation-point pressure was approximately 3 percent higher than the pitot pressure. Measured surface-pressure distributions presented herein are nondimensionalized by the calculated free-stream static pressure $p_\infty$. At Mach 6, a 3-percent discrepancy in pitot pressure $p_{t,2}$ corresponds to a 4.5-percent discrepancy in $p_\infty$. Because of

6

the observed difference in pitot pressure and model stagnation pressure, a 10.16-cm-diameter sphere pressure model was tested, and the results are presented in the appendix. Based on these tests with the sphere, the pitot pressure measured with the single probe was multiplied by 1.032 to obtain the corresponding value of $p_{t,2}$ on the nozzle centerline. This corrected value of $p_{t,2}$ was used to compute flow conditions. (This correction factor of 1.032 was obtained at reservoir pressures between 0.19 and 0.82 MPa; thus, this factor is applicable to the tests made at a reservoir pressure of 0.34 MPa. Since the difference between the pitot pressure and model stagnation-point pressure was essentially the same for both values of reservoir pressure tested (0.34 and 3.46 MPa), this value of the correction factor is believed to be applicable at the highest reservoir pressure as well.)

Due to the long pressure-tube lengths and relatively low level of surface pressure for the present models, significant pressure-lag effects were experienced, particularly at the lowest reservoir pressure. For the most part, the tunnel run time was sufficient to obtain nearly constant values of surface pressure from all three pinch bars. Based on previous experience with the present instrumentation and the data scatter in the surface pressures measured on the on-axis biconic and sphere-cone models at zero angle of attack, the measured values of windward pressure are believed accurate to within 4 to 5 percent. Leeward pressures are believed accurate to within 6 percent at the higher value of $p_{t,1}$ and 7 to 8 percent at the lower value of $p_{t,1}$. Pitot pressure measured with the single probe is accurate to within 1.5 percent.

The detachment distance of the shock from the model surface was read manually from enlargements of the schlieren photographs to approximately 1.4 times actual model size. These readings were made using a digitizing system having a sensitivity of 100 counts per 2.54 mm. The maximum uncertainty in measured shock detachment distance is believed to be less than 5 percent.

For the present tests, the model angle of attack was set with an inclinometer prior to the run and the model was injected into the flow at this angle after steady flow was established in the nozzle; that is, only one angle of attack was examined for each run. As a check on this setting, the angle of attack was read from the schlieren photographs using the vertical plumb line as a reference. (See fig. 3.) At the higher reservoir pressure, the angle of attack inferred from the schlieren photographs differed somewhat from the angle of attack set prior to the run. Although this difference is typical of sting bending, the cause was traced to the fact that the magnetic clutch on the angle-of-attack mechanism was out of adjustment. Values of $\alpha$ set prior to the test and the corresponding values read from the schlieren photographs $\alpha_m$ for the two biconic models and the sphere-cone model at the higher unit Reynolds number (reservoir pressure) are as follows:

| $\alpha$, deg | $\alpha_m$, deg | | |
|---|---|---|---|
| | On-axis (model 1) | Bent-nose (model 2) | Sphere-cone (model 3) |
| 5 | 5.0 | 5.0 | 5.0 |
| 10 | 10.25 | 10.6 | 10.55 |
| 15 | 15.5 | 15.8 | 15.8 |
| 20 | 20.7 | 21.0 | 21.0 |
| 25 | 25.85 | 26.25 | 26.0 |
| 32 | | | 33.0 |

Measured values of angle of attack for the sphere-cone model at the lower unit Reynolds number agreed to within 0.1° of the inclinometer setting prior to the run for all angles of attack. (Schlieren photographs were not obtained for the biconic models at the lower unit Reynolds number.)

The angle of attack for the bent-nose biconic (model 2) is referenced to the axis of revolution of the aft-cone section, which is coincident with the axis of the sting. In the comparison of measured and predicted pressure distributions and shock shapes, the data are plotted as a function of $z$, where the z-axis is coincident with the axis of revolution of the fore-cone section and $z = 0$ at the tip of the spherical nose. (See fig. 2.)

## PREDICTION METHODS

Surface-pressure distributions on the most windward ray ($\phi = 180°$), and the most leeward ray ($\phi = 0°$) of the models for $\alpha_f < \theta_f$, were predicted by using the modified Newtonian expression for a cone at incidence (ref. 4)

$$C_{p,\phi=180°,0°} = C_{p,stag} \sin^2 (\theta \pm \alpha) \tag{3}$$

where $C_{p,stag}$ is the pressure coefficient at the stagnation point behind a normal shock and the sign for $\alpha$ is positive for the windward side and negative for the leeward side. For a flat-faced cylinder ($\theta = 90°$, $\alpha = 0$), the pressure coefficient at the stagnation point for Mach 5.85 to Mach 6 airflow is 1.8165; thus, equation (3) may be expressed as

$$\frac{P_s}{P_\infty} = 1.27155 M_\infty^2 \sin^2 (\theta \pm \alpha) + 1 \tag{4}$$

Surface pressures were also predicted using the semiempirical expression of Amick (ref. 4)

$$C_{p,\phi=180°,0°} = C_{p,stag} \left(\frac{C_{p,max}}{C_{p,stag}}\right) \sin^2 \left[\frac{\frac{\pi}{2} (\theta \pm \alpha)}{\alpha_{p,max} + \theta}\right] \tag{5}$$

where $C_{p,max}$ is the maximum pressure coefficient for a given cone angle and Mach number and $\alpha_{p,max}$ is the angle of attack for maximum pressure on the most windward ray. (The maximum pressure on a cone at $\alpha_{p,max}$ will be somewhat greater than the stagnation pressure behind a normal shock because the shock is not quite normal (ref. 4).) For the present cone half-angles of 7° and 12.84° and for the present Mach number, $C_{p,max}/C_{p,stag}$ is less than 1.01 (ref. 4) and is taken herein to be unity. The angle of attack for maximum pressure on the most windward ray was obtained from a linear fit applied to the results of figure 6 in reference 4, and yields the expression

$$\alpha_{p,max} = \frac{\pi}{2} - 1.4\theta \tag{6}$$

In terms of surface pressure, equation (5) becomes

$$\frac{P_s}{P_\infty} = 1.27155M_\infty^2 \sin^2 \left( \frac{\theta \pm \alpha}{1 - \frac{0.8\theta}{\pi}} \right) + 1 \tag{7}$$

The Newtonian expression for the circumferential pressure distribution about a cone is

$$C_p = C_{p,\phi=180°} \cos^2 \beta \qquad (\beta < \pi/2)$$

and

$$C_p = 0 \qquad (\beta > \pi/2) \tag{8}$$

or, in terms of surface pressure

$$\frac{P_s}{P_\infty} = 1.27155M_\infty^2 \sin^2 (\alpha + \theta) \cos^2 \beta + 1 \qquad (\beta < \pi/2)$$

and

$$\frac{P_s}{P_\infty} = 1 \qquad (\beta > \pi/2) \tag{9}$$

where

$$\beta = \cos^{-1} \left[ \frac{\cos \theta \cos (180° - \phi) \sin \alpha + \sin \theta \cos \alpha}{\sin (\alpha + \theta)} \right] \tag{10}$$

The semiempirical expression of Amick (ref. 4) for the circumferential pressure is

$$C_p = C_{p,\phi=180°} \left\{ 1.1 \cos^3 (0.75\beta) - 0.1 + \sin^3 \beta [0.00097\beta - 0.15 \cos^3 (\alpha + \theta)] \right\} \tag{11}$$

Circumferential pressure distributions were also predicted using the method of High and Blick (ref. 5). For convenience, this method is outlined as follows:

$$\frac{P_s}{P_\infty} = 1 + \frac{\gamma_\infty M_\infty^2}{2}\left[C_{p,e} - (C_{p,e} - C_{p,e}^*)\ f(M)\right] \tag{12}$$

where

$$C_{p,e} = \frac{4\ \sin^2\theta_e\left(2.5 + 8\ \sqrt{M_\infty^2 - 1}\ \sin\theta_e\right)}{\left(1 + 16\ \sqrt{M_\infty^2 - 1}\ \sin\theta_e\right)} \tag{13}$$

and

$$\theta_e = \sin^{-1}\ [\sin\theta\ \cos\alpha + \cos\theta\ \sin\alpha\ \cos\ (180° - \phi)] \tag{14}$$

For $\alpha < \theta$,

$$C_{p,e}^* = C_{p,e,\phi=90°} \tag{15}$$

and

$$f(M) = M_{c,\phi=90°}^{-1.5} \tag{16}$$

For $\alpha > \theta$,

$$C_{p,e}^* = M_{c,\phi=180°}^{1.5}\ [2\ \sin^2\ (\alpha + \theta)] + (1 - M_{c,\phi=180°}^{1.5})C_{p,e,\phi=180°} \tag{17}$$

and

$$f(M) = M_{c,\phi}^{-1.5} \tag{18}$$

10

For $M_\infty \sin \theta_e < 1$,

$$M_c = \frac{M_\infty \cos \theta_e \sqrt{1 - \dfrac{\sin \theta_e}{M_\infty}}}{\sqrt{[1 + \exp(-1 - 1.52 M_\infty \sin \theta_e)]\left[1 + \left(\dfrac{M_\infty \sin \theta_e}{2}\right)^2\right]}} \tag{19}$$

and for $M_\infty \sin \theta_e > 1$,

$$M_c = \frac{M_\infty \cos \theta_e \sqrt{1 - \dfrac{\sin \theta_e}{M_\infty}}}{\sqrt{1 + 0.35(M_\infty \sin \theta_e)^{1.5}}} \tag{20}$$

One of the primary objectives of the present study was to compare surface pressure distributions and shock shapes obtained with a steady, three-dimensional inviscid flow-field code (ref. 6) to measurement. This code, referred to as STEIN (Supersonic Three-dimensional External INviscid), uses a MacCormack-like scheme to integrate the three-dimensional Euler equations. Shock waves are computed as discontinuities via the Rankine-Hugoniot jump conditions. The Mach number in the marching direction (an axis running from the nose of the vehicle to the base) must be supersonic at every point in the flow field, and the geometry must be such that no imbedded regions of subsonic flow exist. The subsonic-supersonic flow about the spherical nose was computed using the blunt body code of Moretti (ref. 12).

Predictions of the pressure distribution and shock shape for the two biconic models using the STEIN code were made prior to discovery of the difference in the post-run setting of the angle of attack and the actual angle of attack during the run. Because of the computer time and expense necessary to rerun all these cases, the decision was made to rerun only the case for the bent-nose biconic at an angle of attack of 21°. This angle was selected because it is representative of the angle of attack required for aerocapture in the Titan atmosphere.

## RESULTS AND DISCUSSION

### Shock Shapes

Measured shock shapes for the on-axis biconic (model 1) and bent-nose biconic (model 2) are shown in figures 4 and 5, respectively, for angles of attack from 0° to 25°. Although the angle of attack $\alpha$ for the bent-nose biconic is referenced to the axis of the aft-cone section, the measured shock shapes for this model (fig. 5) are plotted relative to the fore-cone section (i.e., as a function of $z/L$). The measured shock shapes of figures 4 and 5 correspond to tests performed at the higher value of free-stream unit Reynolds number. Also shown in figures 4 and 5 are predicted (ref. 6) shock shapes. Attempts to run the STEIN code (ref. 6) at $\alpha = 25°$ for the bent-nose biconic (fig. 5(f)) were unsuccessful.

An inflection in the measured shock downstream of the spherical nose on the windward side occurs for both models, and is most pronounced for $5° < \alpha < 15°$. This inflection is caused by the overexpansion of the flow from the blunt nose and is discussed in reference 13 and illustrated subsequently. Measured and predicted shock shapes on the windward and leeward rays are in good agreement (within about 2 percent) for both biconics at $\alpha = 0°$ and $5°$. For $\alpha > 10°$, the windward shock-detachment distance is predicted quite well by STEIN, whereas the leeward shock-detachment distance is underpredicted by 2.5 to 5 percent. As discussed in the section "Data Reduction and Uncertainty," the load on the model during a run resulted in an increase in the angle of attack over the value set prior to the run. For this reason, the STEIN code was run for a measured angle of attack of 21° for the bent-nose biconic, and these calculations are compared to the measured values in figure 5(e). The calculated shock shape for $\alpha_m = 21°$ is in good agreement with the measured values for both the windward and leeward rays. The comparisons of figures 4 and 5 demonstrate that the STEIN code accurately predicts the shock shape for fore-cone section angles of attack $\alpha_f$ to 25°.

The effect of angle of attack on measured shock shape is shown in figure 6 for both biconic models. The shock-detachment distance on the leeward side is 3 to 4 times more sensitive to angle of attack than on the windward side. For example, the variation of leeward shock-detachment distance at $x/L = 0.6$ or $z/L = 0.6$ with angle of attack is given to within 2 percent for both biconic models by the expression

$$y/L = 0.2337 + 9.148 \times 10^{-3}\alpha_{f,m} + 1.513 \times 10^{-4}\alpha_{f,m}^2 \tag{21}$$

where $\alpha_{f,m}$ is the measured angle of attack of the fore-cone section. This expression shows that the leeward shock-detachment distance increases about 3.5 percent for a 1° change in angle of attack as compared to a near-constant value of $y/L$ (-0.21) on the windward side at the same value of $x/L$ or $y/L$ and $0° < \alpha_{f,m} < 25°$. For values of $x/L$ and $z/L$ in excess of 0.4, the leeward shock angle relative to the axis of the fore-cone section is approximately equal to $\theta_f + \alpha_f$ for both models.

The schlieren photographs of figure 3 illustrate the existence of an imbedded shock on the leeward side of the bent-nose biconic. An imbedded shock was also observed for the on-axis biconic and the sphere-cone, and occurs for values of the fore-cone angle-of-attack $\alpha_f$ exceeding the fore-cone half-angle $\theta_f$. The schlieren photograph for the bent-nose biconic at $\alpha = 20°$ was of sufficient quality to show that this shock originates on the fore-cone surface just downstream of the sphere-cone junction at $z/L \approx 0.036$. For values of $x/L$ or $z/L$ between 0.3 and 0.8, the imbedded shock is inclined approximately $\alpha_f + 11°$ with the fore-cone axis. This shock may be due to flow separation from the spherical nose and reattachment onto the fore-cone section, resulting in an adverse pressure gradient. However, it should be noted that a calculation using the parabolized Navier-Stokes method (refs. 14 and 15) for $\theta_f = 12.84°$, $\alpha_f = 20°$, $\gamma_\infty = 1.4$, and $M_\infty = 32$ revealed the existence of a leeward embedded shock, but no axial-flow separation was observed. Thus, a more plausible explanation may be that the flow expands around the spherical nose to a supersonic condition and recompresses because of the presence of the cone section. The recompression starts as a continuous compression on the surface just downstream of the sphere-cone junction, and the Mach lines in the compression region converge so that an embedded shock wave is formed.

12

The difference between the angle of inclination of the windward shock and the aft-cone surface in the region of the base decreases with increasing angle of attack. For $\alpha > 20°$, the windward shock at $z/L = 0.95$ is essentially parallel (within $0.75°$) to the aft-cone surface for the bent-nose biconic. At these high angles of attack, a longitudinal density gradient appears in the schlieren photographs (figs. 3(e) and 3(f)). This gradient takes on the appearance of a shock and is embedded within the shock layer on the windward side of the aft-cone section. A gradient also appears for the on-axis biconic at the highest angle of attack. At this angle of attack, the windward shock is parallel to the aft-cone surface.

Shock shapes measured on the sphere-cone (model 3) at the higher unit Reynolds number are compared in figure 7 with those measured on the biconic models for several angles of attack. The length $L$ used to nondimensionalize the shock-detachment distance for the sphere-cone model is the value for the on-axis biconic, which is nearly the same as for the bent-nose biconic. This allows a direct comparison of the shock shapes for all three models. For a given angle-of-attack setting, the measured angle of attack for the three models is within $0.3°$. (See section "Data Reduction and Uncertainty.") The shock-detachment distance on the leeward side of the sphere-cone model is in good agreement with the biconic models; that is, the leeward shock for the biconics is independent of the aft-cone section. At $\alpha = 10°$ (fig. 7(a)), the windward shock-detachment distance of the sphere-cone model is in good agreement with that of the on-axis biconic for $x/L < 0.8$. Near $x/L = 0.8$, the shock shape indicates an awareness of the fore-cone--aft-cone junction, which is at $x/L = 0.57$ for the on-axis biconic. The point at which the windward shock turns inward, because of this junction, moves slowly towards the nose with increasing angle of attack. At $\alpha = 25°$, this point occurs at $x/L \approx 0.7$ for the on-axis biconic.

In figure 8, shock shapes measured on the sphere-cone model for two values of Reynolds number are compared for several angles of attack. This comparison shows the shock shapes for the two values of $R_{\infty,L}$ are within the experimental uncertainty for the present range of angle of attack. Figure 8 indicates the absence of a significant effect of the boundary-layer displacement thickness on shock shape for the conditions of this study.

## Pressure Distributions

Effect of angle of attack.- Measured pressure distributions for the on-axis biconic, bent-nose biconic, and sphere-cone are presented in figures 9, 10, and 11, respectively, for a range of angle of attack. In figures 9 to 11, the measured surface pressure $p_s$ is nondimensionalized by the calculated free-stream static pressure $p_\infty$ and plotted as a function of $x/L$ or $z/L$ for the five rays of orifices at $\phi = 0°$ (most leeward), $45°$, $90°$, $135°$, and $180°$ (most windward). The data of figures 9 to 11 correspond to the higher value of unit Reynolds number. Also shown in these figures are pressure distributions predicted using the STEIN code (ref. 6) and modified Newtonian theory, the semiempirical method of Amick (ref. 4), and the method of High and Blick (ref. 5).

The variation of measured windward ($\phi = 180°$) surface-pressure ratio $p_s/p_\infty$ with $x/L$ for the on-axis biconic (fig. 9) illustrates the overexpansion of the flow from the spherical nose to the fore-cone section (ref. 13) and the expansion of the flow from the fore-cone section to the aft-cone section. The region of this overexpansion-recompression of the windward flow from the nose diminishes with increasing angle of attack (effective cone half-angle, which is equal to $\theta_f + \alpha_f$),

such that $p_s/p_\infty$ is nearly constant for $0.2 < x/L < 0.57$ and $\alpha > 10°$. At angles of attack of 0° and 5°, the measured windward surface pressure just downstream of the fore-cone—aft-cone junction decreases monotonically to a constant value. For $\alpha = 10°$, 15°, and 20°, the windward surface pressure is essentially constant on the aft-cone section, whereas for $\alpha = 25°$. The pressure distribution exhibits the trend of overexpansion; which is also predicted by the STEIN code. (That is, the surface pressure decreases with $x/L$ downstream of the junction, then increases in the direction of the base.) The difference between the windward surface pressure just upstream of the junction and that in the region of constant pressure on the aft cone decreases with angle of attack.

At angles of attack of 15° and 20° for the on-axis biconic (figs. 9(d) and 9(e)), the leeward surface-pressure ratio along the most leeward ray ($\phi = 0°$) exceeds that along the $\phi = 45°$ ray. That is, a minimum in the circumferential pressure distribution occurs on the leeward side. This phenomenon has been observed in previous cone studies performed at Mach numbers up to 14 (e.g., refs. 16 to 22) and occurs for $\alpha_f > 0.7\theta_f$. It is attributed to flow separation on the leeward side and the formation of two symmetrical, supersonic, counter-rotating, longitudinal vortices with an attachment line on the most leeward ray. As noted in references 17 and 18, the origin of this leeward separated flow region occurs closer to the nose with increasing angle of attack.

In general, the variation of windward surface-pressure ratio with $x/L$ for the on-axis biconic (fig. 9) is predicted quite well by the STEIN code (ref. 6). For $\alpha = 0°$ and 5°, corresponding to $\alpha = \alpha_m$, the windward surface-pressure ratio is slightly underpredicted by STEIN. (Measured and predicted $p_s/p_\infty$ are within 5 percent on the fore-cone and 8 to 10 percent on the aft-cone.) A previous comparison of measured pressure distributions on a 9.33°/5.00° on-axis biconic ($M_\infty = 10$ and $\alpha = 2°$), with distributions predicted by the STEIN code also showed inviscid values of $p_s/p_\infty$ were consistently below measured values (ref. 23). However, values of $p_s/p_\infty$ predicted using a three-dimensional viscous shock-layer approach (ref. 23) were in good agreement with measurement at Mach 10, implying significant viscous effects at this Mach number. Comparisons of inviscid and viscous predictions of $p_s/p_\infty$ for on-axis biconics at Mach 10 (refs. 19 and 23) show viscous effects to be more significant on the leeward side. This trend is not apparent for the present on-axis biconic at $\alpha = 5°$ (fig. 9(b)). At $\alpha = 0°$ (fig. 9(a)), the STEIN code underpredicts the measured monotonic decrease in $p_s/p_\infty$ just downstream of the fore-cone—aft-cone junction. It is interesting to note that the hypersonic viscous shock-layer approach of reference 23 and the parabolized Navier-Stokes approach of references 14 and 19 provided a more accurate description of the measured data just downstream of the junction than does STEIN.

Predictions using Newtonian theory, Amick's semiempirical method (ref. 4), and the procedure of High and Blick (ref. 5) are also shown in figure 9. These methods do not predict the overexpansion from the nose nor the monotonic decrease in surface pressure downstream of the fore-cone—aft-cone junction at the lower angles of attack. In general, references 4 and 5 represent the data over the present angle-of-attack range better than modified Newtonian theory. The windward surface-pressure ratios just upstream of the junction and near the base are predicted by Amick's method to within 5 to 6 percent for all angles of attack. This method was derived from data on 5° and 15° half-angle sharp and blunt cones at Mach 3.86. The fairly good agreement between this method and the present Mach 6 data supports the finding of reference 24, performed at Mach 8, of the general validity of Amick's method at higher Mach numbers. For $\alpha > 10°$, the methods of references 4 and 5 agreed to within 2 percent on the fore-cone and within 3 to 4 percent on the aft-cone.

14

Measured surface pressures on the windward ray of the bent-nose biconic (fig. 10) illustrate an overexpansion of the flow from the nose for $0° < \alpha < 10°$; the pressure is approximately constant on the fore-cone for $\alpha > 15°$. The more pronounced expansion of the windward flow at the fore-cone—aft-cone junction, relative to the on-axis biconic, is evident. The windward surface pressure is essentially constant on the aft cone for $\alpha > 5°$ and is nearly the same value (within 10 percent) as that measured on the on-axis biconic for a given angle of attack. The trend of increasing $p_s/p_\infty$ in the direction of the base observed for the on-axis biconic at $\alpha = 25°$ is not observed for the bent-nose biconic. The small compression that occurs as the flow approaches the junction on the leeward side is not distinguishable from the leeward pressure distributions. As observed for the on-axis biconic, the leeward surface pressure at $\phi = 0°$ exceeds that at $\phi = 45°$ on the fore-cone and aft-cone sections for values of $\alpha$ corresponding to the values when the leeward side is nearly shielded or fully shielded from the flow.

The windward surface-pressure ratio $p_s/p_\infty$ for the bent-nose biconic is predicted quite well by the STEIN code at the lower angles of attack, where $\alpha = \alpha_m$. To determine the effect of $\alpha_m$ on the predicted pressure distribution, an input value of $\alpha_m = 21°$ was used for the STEIN code. As observed in figure 10(e), the windward data are slightly underpredicted on the fore-cone by STEIN ($\alpha = 21°$) and predicted quite accurately on the aft-cone. At the two lower angles of attack (figs. 10(a) and 10(b)), STEIN underpredicts the leeward surface-pressure ratio on the fore-cone, but accurately predicts the aft-cone pressures. At $\alpha = 21°$ (fig. 10(e)), values of $p_s/p_\infty$ on the leeward side predicted with STEIN are in good agreement with measured values on the fore-cone section, and in fair agreement on the aft-cone section.

Surface-pressure distributions for the sphere-cone are presented in figure 11 for various angles of attack. As in the comparison of shock shapes, the length L used to nondimensionalize x in figure 11 corresponds to the length of the on-axis biconic model. The data of figure 11 provide a more detailed pressure distribution than those measured on the fore-cone section of the biconic models. These data illustrate the overexpansion of the flow from the nose and the nature of the surface pressure distribution as the flow approaches the station corresponding to the junction of the biconic models. At $\alpha = 10°$, the leeward pressures for $\phi = 0°$ and $\phi = 45°$ are essentially the same; for $\alpha > 10°$, the surface pressure along the most leeward ray exceeds that along the $\phi = 45°$ ray.

The variation of the surface-pressure ratio $p_s/p_\infty$ with measured angle of attack is shown in figure 12 for both biconic models. In figure 12, the surface-pressure ratio at several values of x/L or z/L on the most windward ray ($\phi = 180°$) is plotted as a function of measured angle of attack. The two intermediate values of x/L or z/L correspond to the pressure orifices located just upstream and downstream of the fore-cone—aft-cone junction. For comparison purposes, the variation of $p_s/p_\infty$ with $\alpha$ predicted from references 4 and 5 is also shown in figure 12. The relatively large sensitivity of fore-cone-section windward pressure to angle of attack is evident from this figure, particularly for the bent-nose biconic.

Effect of Reynolds number.- Pressure distributions for the two values of unit Reynolds number are shown in figures 13 and 14 for the on-axis biconic and bent-nose biconic, respectively. With the exception of the on-axis biconic at zero angle of attack, the windward ($\phi = 180°$ and $135°$) surface-pressure ratios $p_s/p_\infty$ at the higher Reynolds number exceed those at the lower Reynolds number for both biconics at all angles of attack. As an example of the magnitude of this difference, the

15

windward surface-pressure ratio $p_s/p_\infty$ on the fore-cone of the on-axis biconic at the higher Reynolds number exceeds that at the lower Reynolds number by 5 to 6 percent for $\alpha > 5°$. The trend of the leeward surface pressure along the $\phi = 0°$ ray exceeding that along the $\phi = 45°$ ray at the higher angles of attack is observed for both values of Reynolds number.

One reason for this difference in windward surface-pressure ratio between the two Reynolds numbers is a result of the difference in Mach number. The Mach number corresponding to the lower Reynolds number is 5.85, compared with 6.0 for the higher Reynolds number. The method of Amick (ref. 4) shows that the windward surface-pressure ratio for Mach 6 is approximately 4 percent greater than that for Mach 5.85 over the present angle-of-attack range. (See figs. 13 and 14.) When the values of surface-pressure ratio presented in figures 13 and 14 are used to compute corresponding values of pressure coefficient, the agreement between the two Reynolds numbers is, in general, within 2 percent. That is, when the data are viewed in a manner in which Mach number effects are diminished, the data for the two values of Reynolds number are in better agreement.

A second contributor to this difference in surface-pressure ratio is the angle of attack. The actual angle of attack for the higher Reynolds number is somewhat larger than that for the lower Reynolds number, as the loads on the model are about 9 times greater at the higher pressure. (See section "Data Reduction and Uncertainty.") As an example of a worst case for $\alpha_f = 20°$, an uncertainty in $\alpha_f$ of 0.7° corresponds to a 3.5 percent variation in $p_s/p_\infty$ (ref. 4). From these considerations, it is concluded that no appreciable effect of Reynolds number on windward surface-pressure ratio exists for the present study. (Because of the extremely low levels of pressure existing on the leeward side at the lower Reynolds number, the surface pressure in some runs did not reach a steady state in the available time. For this reason, no conclusion concerning the effect of Reynolds number on leeward surface pressures is made.)

Circumferential distributions.- Circumferential pressure distributions for the on-axis biconic and bent-nose biconic are shown in figures 15 and 16, respectively. These data correspond to the higher value of unit Reynolds number. The surface pressure ratio $p_s/p_\infty$ for several values of $x/L$ or $z/L$ is plotted as a function of $\phi$ for the present range of angle of attack. The circle and square symbols correspond to the fore-cone section and the other symbols denote the aft-cone section. These figures illustrate the previously discussed trend of the fore-cone and aft-cone-section surface pressure on the most leeward ray ($\phi = 0°$) exceeding that on the $\phi = 45°$ ray for both biconics (at $\alpha = 15°$ and 20° for the on-axis and $\alpha = 5°$ to 15° for the bent-nose). They also illustrate that the fore-cone-section pressure ratio $p_s/p_\infty$ at $\phi = 90°$ is equal to 3 to 4 for both biconics at all angles of attack, and that the aft-cone-section pressure ratio is equal to 2 to 2.5. Predictions using Amick's method (ref. 4) and the method of High and Blick (ref. 5) are shown in figures 15 and 16. In general, the semiempirical method of reference 4 provides a more accurate prediction of the circumferential pressure distribution for both biconics than does reference 5.

Base Pressure.- The leeward ($\phi = 0°$) base pressure measured at $r/r_b = 0.77$ is shown in figure 17 as a function of angle of attack for both biconic models. Open symbols denote base pressures corresponding to the lower value of unit Reynolds number, and closed symbols denote base pressures corresponding to the higher Reynolds number. In figure 17(a), the base pressure is nondimensionalized by the free-stream static pressure. Because the base pressure is governed largely by local flow

16

conditions immediately ahead of the base, the base pressure was nondimensionalized by the measured leeward surface pressure immediately upstream of the base $p_b/p_\ell$. (See fig. 17(b).)

The results of figure 17 show a strong influence of Reynolds number on leeward base pressure for both biconics over the present range of angle of attack. The base-pressure ratios $p_b/p_\infty$ and $p_b/p_\ell$ increase with decreasing Reynolds number. At the higher Reynolds number, the base-pressure ratios of the on-axis biconic and bent-nose biconic are nearly the same for a given angle of attack. Also, the base-pressure ratios for the on-axis biconic exceed those of the bent-nose biconic at the lower Reynolds number. The base-pressure ratio $p_b/p_\ell$ (fig. 17(b)) increases with angle of attack and is nearly the same value for both biconics and both values of Reynolds number at $\alpha = 25°$. For the present range of $\alpha$, $p_\ell > p_b$, implying no significant communication between the two separated flow regions (leeward side and base). However, the results of figure 17(b) show that communication between the two regions will likely occur for $\alpha > 25°$.

The trends of figure 17 are characteristic of a Reynolds number effect on base pressure for laminar flow (ref. 25). However, they are also characteristic of transition. For the same value of local Mach number, the base-pressure ratio $p_b/p_\ell$ is greater for laminar flow than for turbulent flow (ref. 26). As discussed in reference 27, the origin of transition on a cone moves forward on the leeward side with increasing angle of attack, and moves rearward on the windward side. Since boundary-layer transition is expected to occur in the present study at the higher Reynolds number, the leeward-side flow approaching the base was probably turbulent for both biconics over the present range of angle of attack. The results of figure 17 suggest that the model boundary layer was laminar at the lower Reynolds number and turbulent at the higher Reynolds number.

## CONCLUSIONS

Pressure distributions and shock shapes were measured on a spherically blunted, 12.84°/7°, on-axis biconic and a spherically blunted, 12.84°/7°, bent-nose biconic (fore-cone bent 7° upwards relative to aft-cone) at Mach 6 in air. The angle of attack, referenced to the axis of the aft-cone, was varied from 0° to 25° in nominal 5° increments. Also tested was a 12.84° sphere-cone with the same nose radius as the biconics. Two values of free-stream Reynolds number based on biconic model length were examined, $0.7 \times 10^6$ and $5.3 \times 10^6$. Predictions from simple theories and from a Supersonic, Three-dimensional, External INviscid code, referred to as STEIN, were compared with measured values. Results of this study led to the following conclusions:

1. Predicted (STEIN) shock shapes were in good agreement with measurements for both biconics over the present range of angle of attack.

2. Schlieren photographs revealed the existence of an imbedded shock within the shock layer on the leeward side at values of the fore-cone angle of attack exceeding the fore-cone half-angle. This shock originates on the fore-cone surface just downstream of the sphere-cone junction.

3. In general, the measured windward surface-pressure distributions for both biconics were predicted reasonably well by the STEIN code. The agreement between predicted and measured surface pressures on the leeward side was somewhat poorer than observed for the windward side.

4. No significant effect of Reynolds number on windward surface pressure was observed.

5. For fore-cone angles of attack exceeding the fore-cone half-angle, a minimum in the circumferential pressure distribution was observed; that is, the surface pressure on the most leeward ray (0°) exceeded that on the 45° ray. This phenomenon has been observed in previous cone studies and is attributed to flow separation and the formation of two symmetrical, supersonic, counter-rotating, longitudinal vortices.

6. The leeward-side base pressure, nondimensionalized by the leeward-side surface pressure immediately upstream of the base, increased with decreasing Reynolds number and increasing angle of attack. The base pressure was approximately the same for both biconics at the higher value of Reynolds number; at the lower Reynolds number, the base pressure ratio for the on-axis biconic exceeds that for the bent-nose biconic at a given angle of attack.

7. For the present range of angle of attack, the leeward-side base pressure was less than the model-surface pressure just ahead of the base. This implies a lack of communication between the two separated flow regions.

8. The present base pressures suggest that the leeward-side flow just upstream of the base may be laminar at the lower Reynolds number and turbulent at the higher Reynolds number.

Langley Research Center
National Aeronautics and Space Administration
Hampton, VA 23665
November 19, 1981

APPENDIX

CALIBRATION OF THE LANGLEY 20-INCH MACH 6 TUNNEL

Real-gas effects are examined at the Langley Research Center by testing a given model in the Langley 20-Inch Mach 6 Tunnel (ideal airflow with a normal shock-density ratio of 5.3) and the Langley Hypersonic $CF_4$ Tunnel (Mach 6 $CF_4$ flow having a density ratio of 12). As shown in reference 9, the $CF_4$ tunnel has a limited range of unit Reynolds number. Therefore, to obtain similar values of free-stream Mach number and unit Reynolds number in the two facilities, the Mach 6 tunnel must be operated at relatively low values of reservoir pressure. In the present study, the biconic models and sphere-cone model were tested at a relatively low reservoir pressure (0.3 MPa) to match Mach number and Reynolds number for the two facilities; these models were also tested at the maximum reservoir pressure of the Mach 6 tunnel (3.6 MPa). Because previous calibrations of this tunnel (refs. 7 and 8) do not include these values of reservoir pressure (previous calibrations covered a range of $p_{t,1}$ of 0.5 to 3 MPa), a calibration was performed to examine flow characteristics at the reservoir conditions of the present study. This calibration consisted of pitot-pressure profiles measured over a range of reservoir pressure (0.3 to 3.6 MPa) at two nozzle axial stations. Horizontal and vertical pitot-pressure profiles were measured simultaneously over 80 percent of the nozzle test-section width and height. The primary purpose of this appendix is to present the results of this calibration.

As part of this calibration, pressures measured at the stagnation region of a 10.16-cm-diameter sphere were compared with the pitot pressure from the single pitot-pressure probe for several reservoir pressures, two ratios of probe outside diameter to probe inside diameter, and different combinations of model and probe injection and retraction sequence. The purpose of these tests with the sphere pressure model was to determine whether the difference observed between the pressure measured at the stagnation point of the on-axis biconic and sphere-cone models at 0° incidence and the pitot pressure also existed for this sphere.

Pitot-Pressure Surveys

The pitot-pressure surveys were measured using a cross-pattern rake with 17 pitot probes (including the center probe) positioned vertically and 18 pitot probes positioned horizontally. The pitot probes were flat-faced tubes with an inside diameter of 1.52 mm, an outside diameter of 2.34 mm, and a length of 1.59 cm. The body of the rake was 9.5-mm-thick steel-bar stock, with a sharp leading edge having a total angle of 20°. The probes were spaced 2.54 cm apart; therefore, this 35-probe rake covered a vertical distance of 40.6 cm and a horizontal distance of 45.7 cm.

Tests were performed with the probes 2.4 cm and 24.2 cm downstream of the centerline of the 42.9-cm-diameter schlieren windows (i.e., $x = -2.4$ cm and $x = -24.2$ cm). For $x = -2.4$ cm, the center probe was located at $y = 0$ and $z = -7.9$ mm; for $x = -24.2$ cm, the center probe was located at $y = 0$ and $z = -5.6$ mm. (See fig. 18 for illustration of $x$, $y$, $z$ coordinate system.) In this region of the two-dimensional contoured nozzle, which ends 44.4 cm downstream of the schlieren window centerline, the side walls containing the flush-mounted schlieren windows are parallel, whereas the top and bottom walls are slightly divergent ($\approx 1°$ to the horizontal).

Pitot pressures were measured using 20 variable-capacitance diaphragm transducers having 7 ranges of pressure. The maximum transducer pressure was 133 kPa. A switching device referred to as a pinch bar allowed the 35 pitot pressures to be measured with the 20 pressure transducers during a run. The sequence used with the rake was to first record the pitot pressures from the vertical ray (pinch bar 1), then from the horizontal ray (pinch bar 2), and finally from the vertical ray a second time. The purpose of this sequence, and the reason that the center pitot probe was connected to both pinch bars, was to provide information on the possible variation of flow conditions with run time (refs. 7 and 8). Outputs from these pressure transducers, the reservoir pressure transducers (three transducers with ranges to 0.69, 1.38, and 3.45 MPa), and a thermocouple installed in the reservoir were recorded by a 99-channel analog-to-digital system at 20 samples per second. Real-time histories of selected probes on the vertical and horizontal rays were displayed on a visicorder. These real-time histories informed the operator of possible pressure-lag effects due to the long pressure tubes from the rake to the pinch bar. Data were recorded on the analog-to-digital system only after it was determined that the pitot pressure was essentially constant with time.

Reservoir pressure was varied from 0.26 MPa to the design maximum of 3.6 MPa. Mean values of the measured reservoir pressure and reservoir temperature are presented in table II along with a corresponding percent variation in reservoir pressure and temperature over the time interval of the flow period for which data were recorded.

Time histories of the reservoir pressure, reservoir temperature, and ratio of the center-probe pitot pressure to reservoir pressure are shown in figures 19 and 20 for nozzle axial stations $x$ of -2.4 cm and -24.2 cm, respectively. These time histories for a given nozzle axial station correspond to the highest and lowest values of reservoir pressure examined. In general, the variation of reservoir pressure and temperature for the present test times was less than 2.5 percent. (See figs. 19 and 20 and table II.) For the lowest value of reservoir pressure, the pitot pressure ratio $p_{t,2}/p_{t,1}$ varied 0.2 percent for the 40-second test time with $x = -2.4$ cm (fig. 19(a)) and 0.35 percent for the 60-second test time with $x = -24.2$ cm (fig. 20(a)). Therefore, for the lowest value of reservoir pressure, the free-stream Mach number was constant to within 0.1 percent for the present test time. At the highest value of reservoir pressure (figs. 19(b) and 20(b)), the pitot-pressure ratio decreased approximately 1 percent for the present test time, corresponding to an increase in the free-stream Mach number of 0.3 percent.

Values of the pitot-pressure ratio $p_{t,2}/p_{t,1}$ of the center-11 probes for the initial reading on pinch bar 1 (vertical profile) were compared with the final reading. The variation of $p_{t,2}/p_{t,1}$ with time was less than 0.3 percent for reservoir pressures less than 0.5 MPa. For reservoir pressures greater than 0.5 MPa, this variation in $p_{t,2}/p_{t,1}$ with time increased with reservoir pressure and exceeded 1 percent at the highest value (3.6 MPa). The measured variation in Mach number with time is attributed primarily to temperature effects on the nozzle wall and the nozzle boundary layer (refs. 7 and 8). (Although the increase in reservoir temperature between $p_{t,1} = 0.5$ MPa and $p_{t,1} = 3.6$ MPa was only about 8 percent, the mass flow was 7 times greater at the higher pressure. This higher mass flow causes a higher heat-transfer rate to the model, model support system, and nozzle wall.) It should be noted that the facility operational procedure for the present calibration was the same as generally used for model testing; that is, the interior walls of the test section were not preheated, and only a single reservoir pressure was examined for a run. Also, the single pitot probe was removed from the test section for the present

calibration so as not to generate a possible disturbance in the flow, particularly when the survey rake is in the most downstream position.

Vertical and horizontal pitot-pressure profiles for a range of reservoir pressure are shown in figure 21 for $x = -2.4$ cm and in figure 22 for $x = -24.2$ cm. The mean value of the pitot-pressure ratio $P_{t,2}/P_{t,1}$ for both the vertical and horizontal profiles was determined from the center-11 pitot-pressure probes. For the range of reservoir pressure tested, the mean value of $P_{t,2}/P_{t,1}$ for the vertical profile was 1.013 to 1.019 times the mean value for the horizontal profile. The contribution of data-acquisition time to this difference between the mean values of $P_{t,2}/P_{t,1}$ for the two profiles is believed to be small. For example, the two readings at different times for the vertical profile (pinch bar 1) for run 12 show the variation in $P_{t,2}/P_{t,1}$ with time is less than 0.3 percent; however, the pressure ratio $P_{t,2}/P_{t,1}$ for the vertical profile (initial reading of pinch bar 1) is 1.019 times that of the horizontal profile. This implies that the flow at $x = -2.4$ cm may be somewhat nonuniform. At this most upstream axial station, the two profiles (fig. 21) tend to form a horizontal figure eight with the intersection in the vicinity of the center of the nozzle. This characterization is illustrated in figure 23 for several runs, where the pitot pressures for the vertical and horizontal rays have been nondimensionalized by the center-probe pitot pressure. In general, the maximum difference between the two profiles forming this figure eight occurs around $y/w = z/w = \pm0.4$. For these values of $y/w$ and $z/w$, the pitot pressure from the vertical profile is 2 to 3.5 percent greater than that of the horizontal profile for the present range of reservoir pressure. A horizontal figure-eight pattern also exists in the pitot-pressure profiles presented in references 7 and 8 for $x = 1.16$ cm and a reservoir-pressure range of 0.52 to 3.03 MPa. As was observed in references 7 and 8, this figure-eight pattern diminishes with distance downstream (figs. 21 and 22).

Because the pitot-pressure profiles at the two axial stations could not be measured simultaneously, some difference in reservoir conditions and temperature effects exists between runs made at the two axial stations for a given reservoir pressure. Therefore, it is not possible to obtain an exact determination of the variation of flow conditions between the two axial stations. However, the variation in reservoir conditions between runs made at a given value of $P_{t,1}$ was relatively small in the present calibration, with reservoir pressure being within 3.6 percent and reservoir temperature within 2.1 percent. From figures 21 and 22, the vertical and horizontal pitot-pressure profiles experience a small variation in the mean pitot-pressure ratio $P_{t,2}/P_{t,1}$ between the two axial stations. The pitot-pressure ratio at the upstream station exceeds that at the downstream station by no more than 1.3 percent for $0.26$ MPa $< P_{t,1} < 3.06$ MPa and 2 percent for the highest reservoir pressure. For the worst case (highest reservoir pressure), the variation in free-stream Mach number for an axial variation of 21.8 cm is 0.03, or three times the gradient reported in references 7 and 8.

The inviscid test core is defined herein as the region for which the pitot pressure for the vertical and the horizontal profiles is within 1.1 percent of the mean value of pitot pressure inferred from the center-11 vertical pitot probes or center-11 horizontal probes. The profiles of figures 21 and 22 show that the test core has a width and height of 28 to 31 cm at the lowest reservoir pressure and a height of 25 to 28 cm and width of 31 to 33 cm at the higher reservoir pressures. The pitot-pressure ratio and free-stream flow conditions within the test core are presented in table III.

APPENDIX

Sphere Pressure Model

The 10.16-cm-diameter sphere pressure model was tested at relatively low reservoir pressures of 0.19, 0.4, and 0.82 MPa. The pressure orifices on this model were arranged in a cross pattern with the crossing point located at the geometric stagnation point of the sphere. The orifice at the stagnation point and the adjacent orifice on each ray were used to obtain an average value of the stagnation-point pressure. All five orifices were located within 4° of the stagnation point. According to predictions (refs. 28 and 29) for ideal airflow, the surface pressure at 4° is within 0.7 percent of the stagnation-point pressure. This averaging of the five center orifices was used to improve the uncertainty in the measured sphere pressure. Although the same pressure transducers were used for the sphere as for the survey rake, an on-site, quick-look data-acquisition system was used in place of the 99-channel analog-to-digital system. This on-site system consisted of a scanner that switches analog input signals to a voltmeter interfaced to a desk computer and is believed to be quite accurate. The pressure transducers and system were calibrated throughout the test series by subjecting the pressure transducers to an accurately known pressure. For this series of runs, the pressure measured at the stagnation point of the sphere was within ±0.5 percent of the average of the five center orifices.

When injected into the flow, the sphere came to rest with the stagnation point 1.51 cm above the nozzle centerline and at the same axial station as the single-pitot probe (x = -0.7 cm). (This probe was 10.8 cm above and 9.70 cm to the right of the nozzle centerline looking upstream.) For several runs, the pitot probe remained in the flow for the entire run. Therefore, data were obtained with and without the model in the flow. One run was made with the model in the flow for the entire run. The pitot probe was initially out of the flow and was then injected and retracted. The purpose of these sequences of model injection-retraction was primarily to determine whether interference effects, between the model and the probe, and blockage effects were present. To determine whether viscous effects (ref. 30) were present for the pitot probe at these relatively low values of reservoir pressure, two values of probe outside-to-inside diameter were examined (1.41 and 1.95). To check the pressure transducer used to monitor the pitot pressure, this transducer was interchanged with the transducer used for the stagnation-point orifice on the sphere for two runs.

The ratio of pitot pressure from the single probe to the sphere stagnation-point pressure is shown in figure 24 as a function of reservoir pressure. The present study showed no significant effect of reservoir pressure, injection-retraction sequence for the probe and sphere, ratio of outside-to-inside diameter of the probe, or interchange of pressure transducers on the ratio of pitot pressure to model stagnation pressure. For the conditions of this study, the ratio of pitot pressure to model stagnation pressure was 0.969 with a ±0.4 percent uncertainty.

Based on the findings of this calibration, it is recommended that, whenever possible, models tested in the region near the center of the upstream schlieren windows (fig. 1) be contained within ±5.1 cm of the centerline in the y- and z-directions. Also, to obtain a nozzle centerline value of the stagnation pressure behind a normal shock, the value measured with the single probe should be corrected by multiplying by 1.032.

# REFERENCES

1. French, James R.; and Cruz, Manuel I.: Aerobraking and Aerocapture for Planetary Missions. Astronaut. & Aeronaut., vol. 18, no. 2, Feb. 1980, pp. 48-55, 71.

2. Florence, Dwight E.: Aerothermodynamic Design Feasibility of a Mars Aerocapture/ Aeromaneuver Vehicle. AIAA-81-0350, Jan. 1981.

3. Florence, Dwight E.: Aerothermodynamic Design Feasibility of a Generic Planetary Aerocapture/Aeromaneuver Vehicle. AIAA-81-1127, June 1981.

4. Amick, James L.: Pressure Measurements on Sharp and Blunt 5°- and 15°-Half-Angle Cones at Mach Number 3.86 and Angles of Attack to 100°. NASA TN D-753, 1961.

5. High, M. D.; and Blick, E. F.: Cone Pressure Distribution at Large and Small Angles of Attack. AIAA J., vol. 2, no. 11, Nov. 1964, pp. 2054-2055.

6. Marconi, Frank; Salas, Manuel; and Yaeger, Larry: Development of a Computer Code for Calculating the Steady Super/Hypersonic Inviscid Flow Around Real Configurations. Volume I - Computational Technique. NASA CR-2675, 1976.

7. Goldberg, Theodore J.; and Hefner, Jerry N. (appendix by James C. Emery): Starting Phenomena for Hypersonic Inlets With Thick Turbulent Boundary Layers at Mach 6. NASA TN D-6280, 1971.

8. Keyes, J. Wayne: Force Testing Manual for the Langley 20-Inch Mach 6 Tunnel. NASA TM-74026, 1977.

9. Midden, R. E.; and Miller, C. G.: Description and Preliminary Calibration Results for the Langley Hypersonic $CF_4$ Tunnel. NASA TM-78800, 1978.

10. Guy, R. W.; and Winebarger, R. M.: Effect of Orifice Size and Heat-Transfer Rate on Measured Static Pressures in a Low-Density Arc-Heated Wind Tunnel. NASA TN D-3829, 1967.

11. Ames Research Staff: Equations, Tables, and Charts for Compressible Flow. NACA Rep. 1135, 1953. (Supersedes NACA TN 1428.)

12. Moretti, Gino; and Bleich, Gary: Three-Dimensional Flow Around Blunt Bodies. AIAA J., vol. 5, no. 9, Sept. 1967, pp. 1557-1562.

13. Cleary, Joseph W.: Effects of Angle of Attack and Nose Bluntness on the Hypersonic Flow Over Cones. AIAA Paper No. 66-414, June 1966.

14. Rizk, Y. M.; Chaussee, D. S.; and McRae, D. S.: Computation of Hypersonic Viscous Flow Around Three-Dimensional Bodies at High Angles of Attack. AIAA-81-1261, June 1981.

15. Chaussee, D. S.; and Steger, J. L.: Three Dimensional Viscous Flow Field Program. Part 3 - Parabolized Navier-Stokes Program (Interim Report). AFWAL-TM-81-65-FIMG, U.S. Air Force, Mar. 1981.

16. Rainbird, W. J.; Crabbe, R. S.; Peake, D. J.; and Meyer, R. F.: Some Examples of Separation in Three-Dimensional Flows. Canadian Aeronaut. Space J., vol. 12, no. 10, Dec. 1966, pp. 409-423.

17. Rainbird, William John: Turbulent Boundary-Layer Growth and Separation on a Yawed Cone. AIAA J., vol. 6, no. 12, Dec. 1968, pp. 2410-2416.

18. Stetson, Kenneth F.: Boundary-Layer Separation on Slender Cones at Angle of Attack. AIAA J., vol. 10, no. 5, May 1972, pp. 642-648.

19. Helliwell, William S.; Dickinson, Richard P.; and Lubard, Stephen C.: Viscous Flow Over Arbitrary Geometries at High Angles of Attack. AIAA J., vol. 19, no. 2, Feb. 1981, pp. 191-197.

20. Lubard, Stephen C.; and Helliwell, William S.: Calculation of the Flow on a Cone at High Angle of Attack. AIAA J., vol. 12, no. 7, July 1974, pp. 965-974.

21. Dearing, J. David: Laminar Heat-Transfer Distributions for a Blunted-Cone, Cone-Frustum Reentry Configuration at Mach 10. NASA TN D-5146, 1969.

22. Krogmann, Paul: An Experimental Investigation of Laminar and Transitional Heat Transfer to a Sharp Slender Cone at $Ma_\infty = 5$, Including Effects of Angle of Attack and Circumferential Heat Transfer. AIAA Paper No. 74-628, July 1974.

23. Mayne, Arloe W., Jr.: Calculation of the Laminar Viscous Shock Layer on a Blunt Biconic Body at Incidence to Supersonic and Hypersonic Flow. AEDC-TR-123, U.S. Air Force, Dec. 1976. (Available from DTIC as AD A033 225.)

24. Bushnell, Dennis M.; Jones, Robert A.; and Huffman, Jarrett K.: Heat-Transfer and Pressure Distributions on Spherically Blunted 25° Half-Angle Cone at Mach 8 and Angles of Attack up to 90°. NASA TN D-4792, 1968.

25. Cassanto, John M.: Radial Base-Pressure Gradients in Laminar Flow. AIAA J. (Tech. Notes), vol. 5, no. 12, Dec. 1967, pp. 2278-2279.

26. Miller, Charles G., III: Experimental Base Pressures on 9° Spherically Blunted Cones at Mach Numbers From 10.5 to 20. NASA TN D-4800, 1968.

27. Stetson, Kenneth F.: M = 6 Wind Tunnel Experiments of Boundary Layer Transition on a Cone at Angle of Attack. AIAA-81-1226, June 1981.

28. Barnwell, Richard W.: A Time-Dependent Method for Calculating Supersonic Blunt-Body Flow Fields With Sharp Corners and Embedded Shock Waves. NASA TN D-6031, 1970.

29. Lomax, Harvard; and Inouye, Mamoru: Numerical Analysis of Flow Properties About Blunt Bodies Moving at Supersonic Speeds in an Equilibrium Gas. NASA TR R-204, 1964.

30. Bailey, A. B.; and Boylan, D. E.: Some Experiments on Impact-Pressure Probes in a Low-Density, Hypervelocity Flow. AEDC-TN-61-161, U.S. Air Force, Dec. 1961.

# TABLE I.- LOCATION OF PRESSURE ORIFICES MONITORED

## (a) On-axis biconic (model 1)

| φ, deg | x/L | φ, deg | x/L | φ, deg | x/L |
|---|---|---|---|---|---|
| 180 | 0 | 135 | 0.640 | 45 | 0.547 |
| | .104 | | .695 | | .584 |
| | .215 | | .751 | | .640 |
| | .326 | | .862 | | .695 |
| | .436 | 90 | .104 | | .751 |
| | .492 | | .215 | | .862 |
| | .547 | | .326 | 0 | .104 |
| | .584 | | .436 | | .215 |
| | .640 | | .492 | | .326 |
| | .695 | | .549 | | .436 |
| | .751 | | .584 | | .547 |
| | .806 | | .640 | | .584 |
| | .862 | | .695 | | .640 |
| | .917 | | .751 | | .695 |
| 135 | .326 | | .806 | | .806 |
| | .436 | | .917 | | .917 |
| | .492 | 45 | .326 | | 1.000 |
| | .547 | | .436 | | |
| | .584 | | .492 | | |

## (b) Bent-nose biconic (model 2)

| φ, deg | z/L | φ, deg | z/L | φ, deg | z/L |
|---|---|---|---|---|---|
| 180 | 0 | 135 | 0.657 | 45 | 0.546 |
| | .104 | | .714 | | .574 |
| | .214 | | .769 | | .630 |
| | .325 | | .826 | | .684 |
| | .435 | | .880 | | .738 |
| | .490 | 90 | .104 | | .882 |
| | .546 | | .325 | 0 | .104 |
| | .608 | | .435 | | .214 |
| | .663 | | .490 | | .325 |
| | .720 | | .546 | | .435 |
| | .776 | | .588 | | .546 |
| | .833 | | .644 | | .569 |
| | .887 | | .699 | | .625 |
| | .942 | | .754 | | .679 |
| 135 | .325 | | .809 | | .787 |
| | .435 | | .918 | | .894 |
| | .490 | 45 | .325 | | 1.000 |
| | .546 | | .435 | | |
| | .601 | | .490 | | |

TABLE I.- Concluded

(c) Sphere-cone (model 3)

| φ, deg | x/L[a] | φ, deg | x/L[a] | φ, deg | x/L[a] |
|--------|--------|--------|--------|--------|--------|
| 180 | 0 | 135 | 0.436 | 45 | 0.270 |
| ↓ | .049 | ↓ | .547 | ↓ | .326 |
|  | .104 |  | .713 |  | .436 |
|  | .159 | 90 | .049 |  | .547 |
|  | .215 |  | .104 | ↓ | .713 |
|  | .270 |  | .159 | 0 | .049 |
|  | .326 |  | .215 |  | .104 |
|  | .381 |  | .270 |  | .159 |
|  | .436 |  | .326 |  | .215 |
|  | .492 |  | .381 |  | .270 |
|  | .547 |  | .436 |  | .326 |
|  | .644 |  | .492 |  | .381 |
|  | .713 |  | .547 |  | .436 |
| 135 | .049 |  | .644 |  | .492 |
| ↓ | .104 | ↓ | .713 |  | .547 |
|  | .159 | 45 | .049 |  | .644 |
|  | .215 | ↓ | .104 | ↓ | .713 |
|  | .270 |  | .159 |  |  |
|  | .326 |  | .215 |  |  |

[a]L  is length of on-axis biconic (model 1).

26

## TABLE II. - RESERVOIR PRESSURE AND TEMPERATURE

| Run | x, cm | $\bar{p}_{t,1}$, MPa | $\Delta p_{t,1}$, percent | $\bar{T}_{t,1}$, K | $\Delta T_{t,1}$, percent | $\Delta t$, sec |
|---|---|---|---|---|---|---|
| 10 | -2.4 | 0.262 | ±0.2 | 442.2 | ±2.0 | 36 |
| 11 | -2.4 | .397 | 1.6 | 432.5 | 2.4 | 39 |
| 12 | -2.4 | .497 | .1 | 478.2 | 1.1 | 28 |
| 13 | -2.4 | 1.130 | 1.4 | 474.7 | 2.4 | 40 |
| 6 | -2.4 | 2.182 | .2 | 486.3 | .4 | 34 |
| 8 | -2.4 | 3.054 | .4 | 495.3 | .4 | 31 |
| 14 | -2.4 | 3.637 | .4 | 505.5 | 2.0 | 31 |
| 17 | -24.2 | .271 | .7 | 433.2 | 2.8 | 50 |
| 18 | -24.2 | .402 | 3.0 | 439.9 | .1 | 39 |
| 19 | -24.2 | .515 | .4 | 471.0 | .5 | 44 |
| 20 | -24.2 | 1.137 | .3 | 479.7 | .9 | 36 |
| 21 | -24.2 | 2.177 | .3 | 491.8 | .5 | 47 |
| 22 | -24.2 | 3.056 | .5 | 502.0 | .1 | 33 |
| 23 | -24.2 | 3.611 | .6 | 507.4 | .5 | 35 |

## TABLE III.- FLOW CONDITIONS FOR LANGLEY 20-INCH MACH 6 TUNNEL

| Run | x, cm | $p_{t,1}$, MPa | $T_{t,1}$, K | $\left(\dfrac{p_{t,2}}{p_{t,1}}\right)_{core}$ | $p_\infty$, kPa | $T_\infty$, K | $M_\infty$ | $R_\infty$, $m^{-1}$ |
|---|---|---|---|---|---|---|---|---|
| 10 | -2.4 | 0.261 | 443.7 | 0.0342 | 0.204 | 57.5 | 5.796 | $2.88 \times 10^6$ |
| 11 | -2.4 | .397 | 433.3 | .0331 | .296 | 55.4 | 5.841 | 4.48 |
| 12 | -2.4 | .497 | 478.8 | .0327 | .363 | 60.8 | 5.862 | 4.72 |
| 13 | -2.4 | 1.130 | 474.6 | .0312 | .772 | 59.2 | 5.926 | 10.62 |
| 6 | -2.4 | 2.182 | 485.6 | .0304 | 1.433 | 59.8 | 5.965 | 19.45 |
| 8 | -2.4 | 3.062 | 496.0 | .0300 | 1.971 | 60.8 | 5.984 | 26.18 |
| 14 | -2.4 | 3.626 | 504.1 | .0299 | 2.326 | 61.7 | 5.988 | 30.14 |
| 17 | -24.2 | .272 | 434.5 | .0339 | .211 | 56.1 | 5.808 | 3.10 |
| 18 | -24.2 | .400 | 439.9 | .0329 | .296 | 56.1 | 5.851 | 4.38 |
| 19 | -24.2 | .514 | 470.7 | .0323 | .369 | 59.5 | 5.877 | 4.98 |
| 20 | -24.2 | 1.137 | 479.3 | .0310 | .768 | 59.5 | 5.938 | 10.46 |
| 21 | -24.2 | 2.176 | 491.7 | .0301 | 1.406 | 60.3 | 5.981 | 18.89 |
| 22 | -24.2 | 3.064 | 502.2 | .0297 | 1.943 | 61.3 | 5.999 | 25.52 |
| 23 | -24.2 | 3.596 | 508.3 | .0294 | 2.249 | 61.8 | 6.012 | 29.21 |
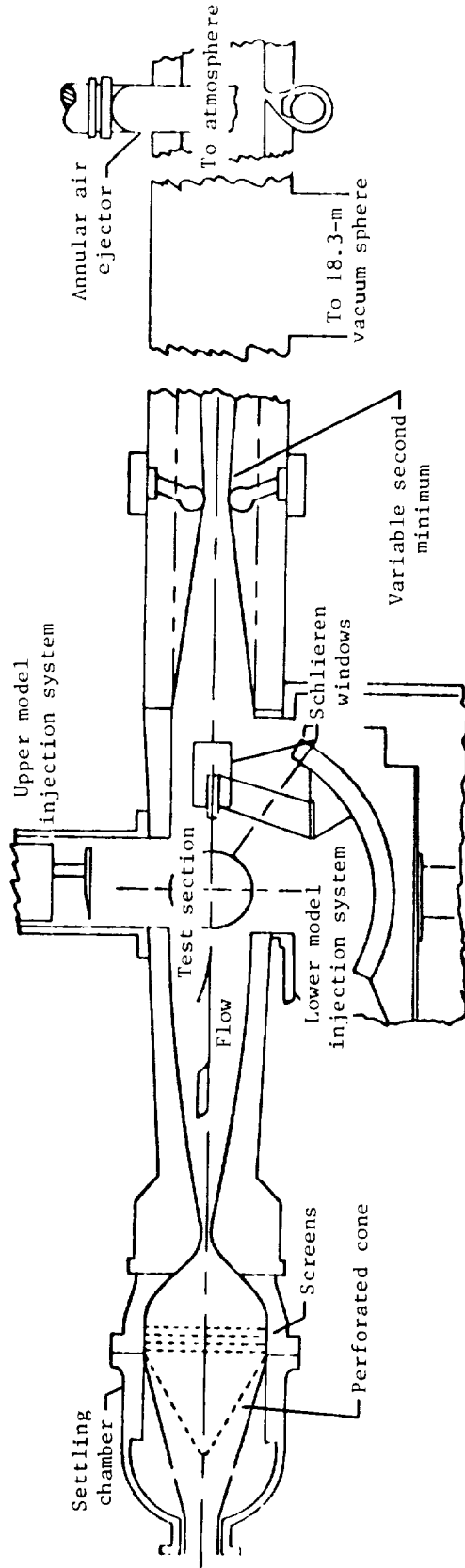
Figure 1.- Schematic of Langley 20-Inch Mach 6 Tunnel.    (From ref. 8.)
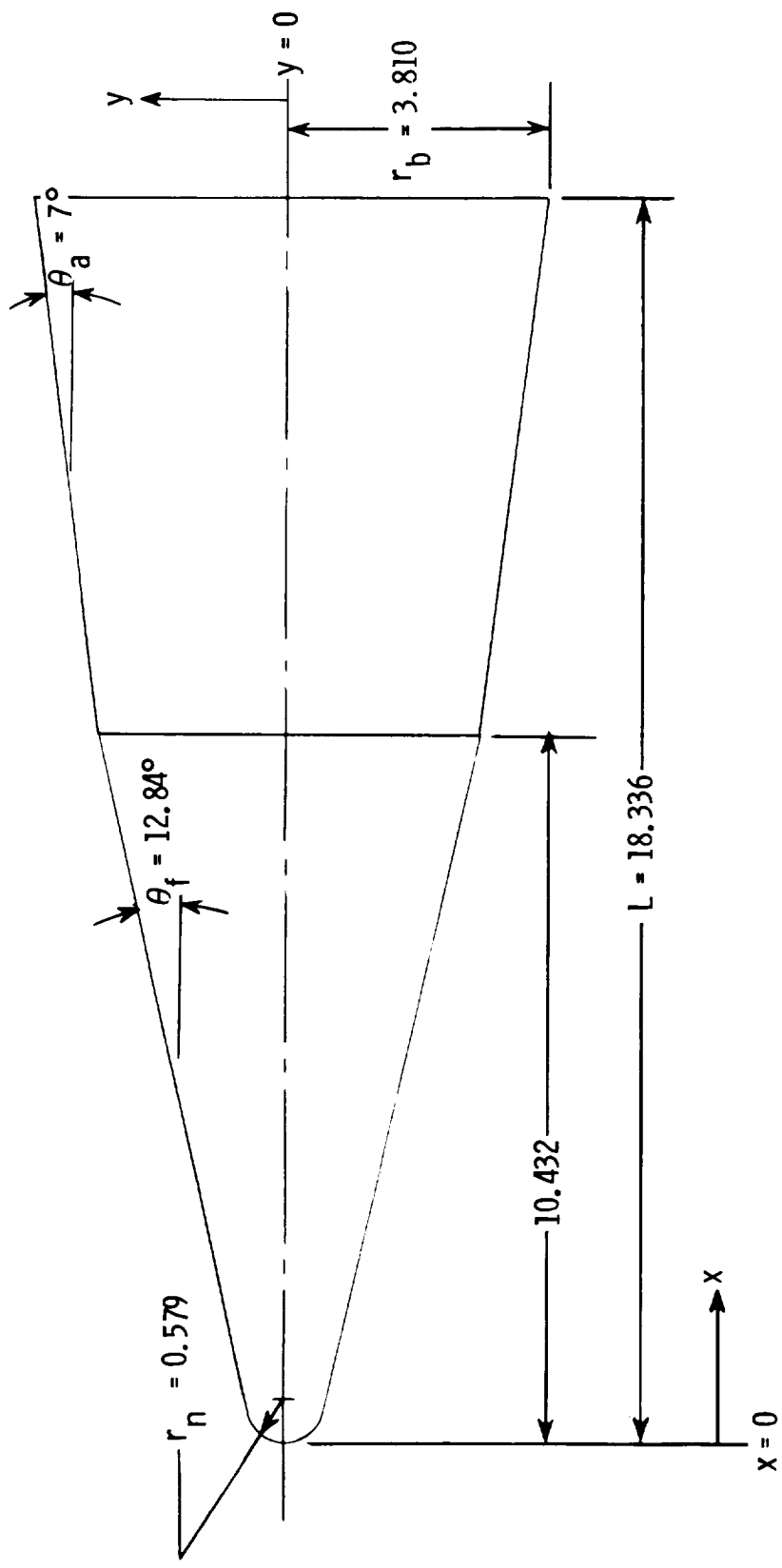
(a) On-axis biconic (model 1).

Figure 2.- Planform view and dimensions of models. All dimensions in cm.
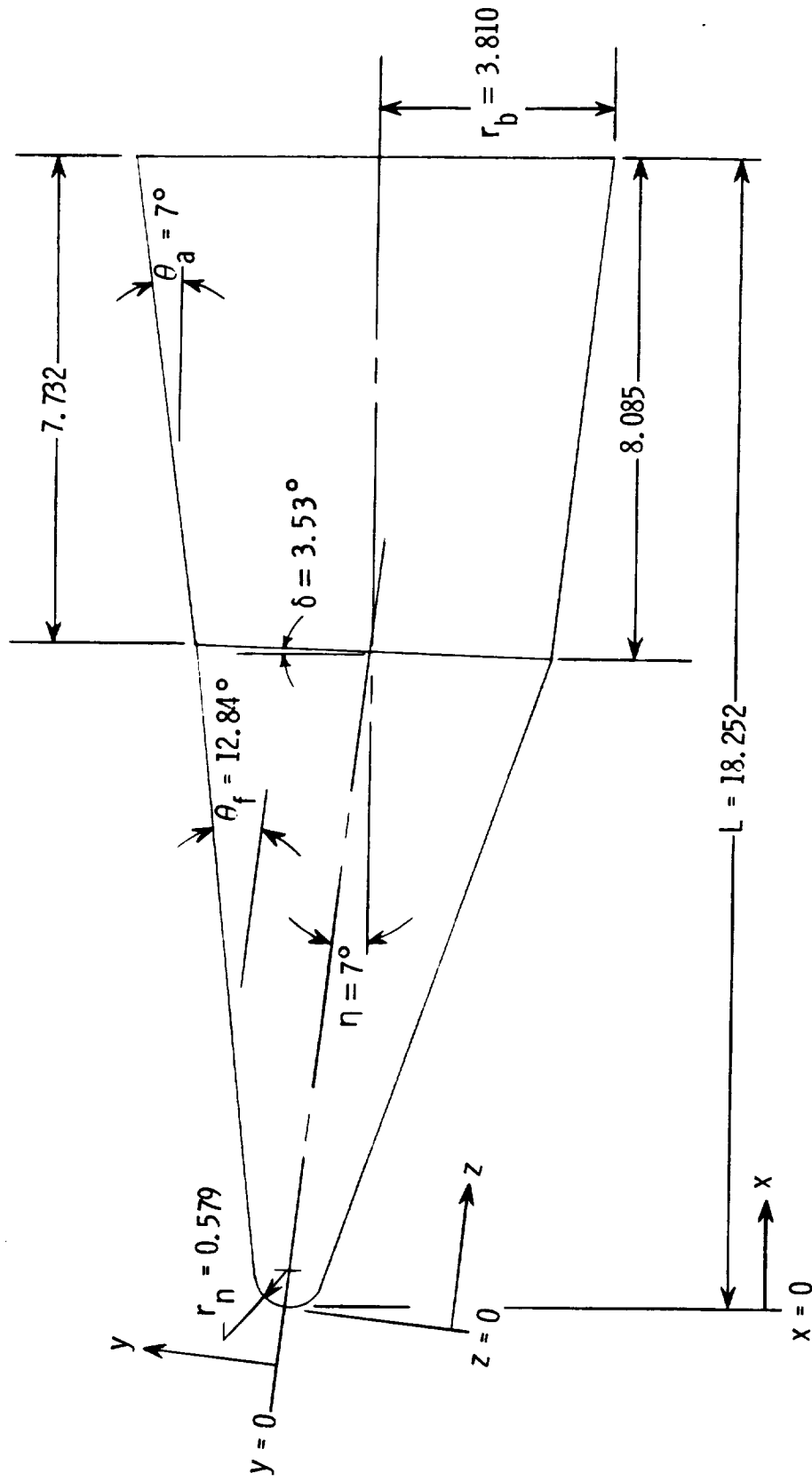
(b) Bent-nose biconic (model 2).

Figure 2.- Continued.
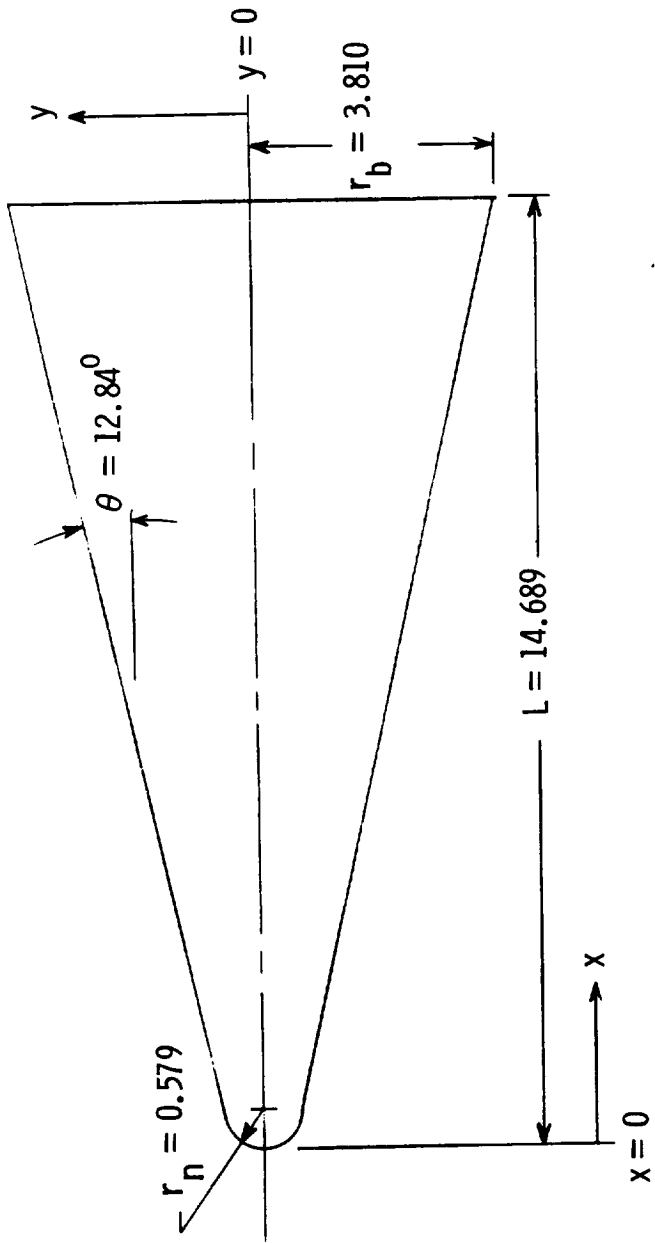
(c) Sphere-cone (model 3).

Figure 2.- Concluded.
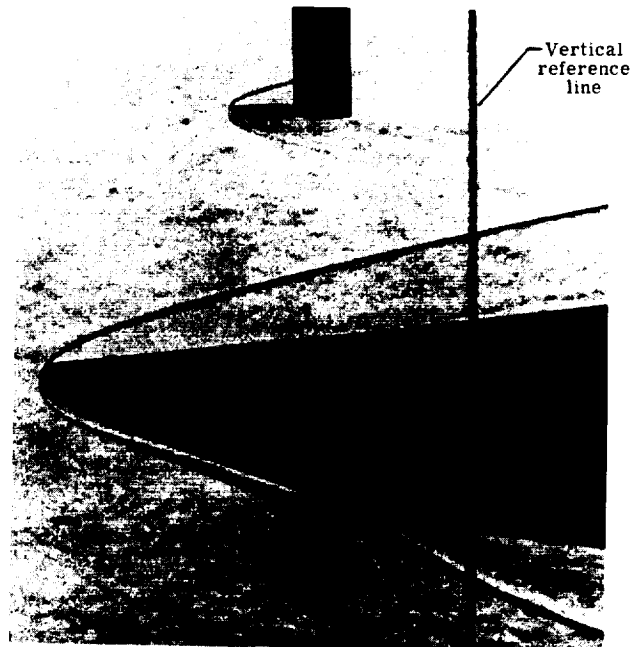
L-81-256

(a)   $\alpha_m = 0°$.
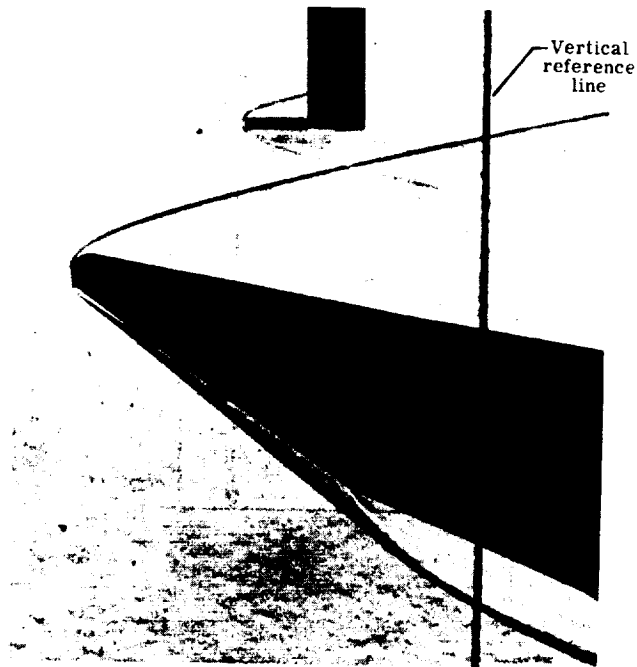


L-81-257

(b)   $\alpha_m = 5°$.

Figure 3.- Representative schlieren photographs
for bent-nose biconic at various angles of
attack.   $M_\infty = 6.0$;   $R_{\infty,L} = 5.3 \times 10^6$.
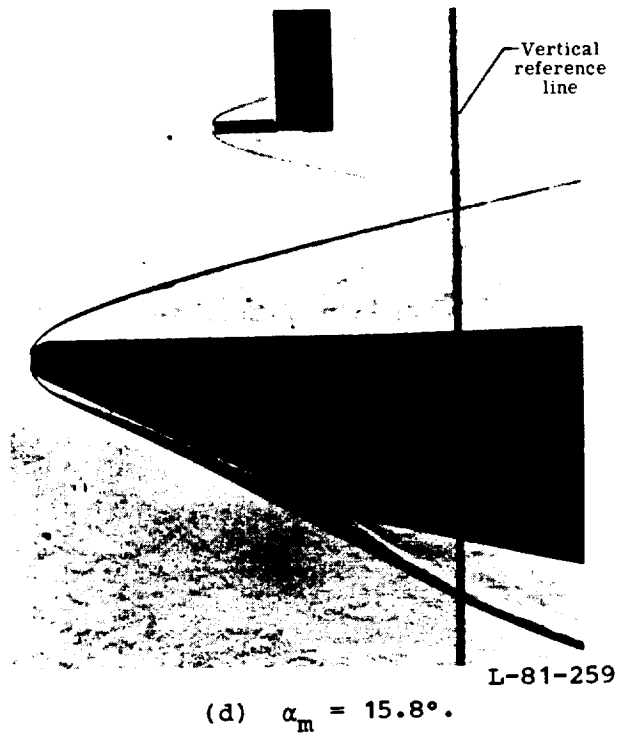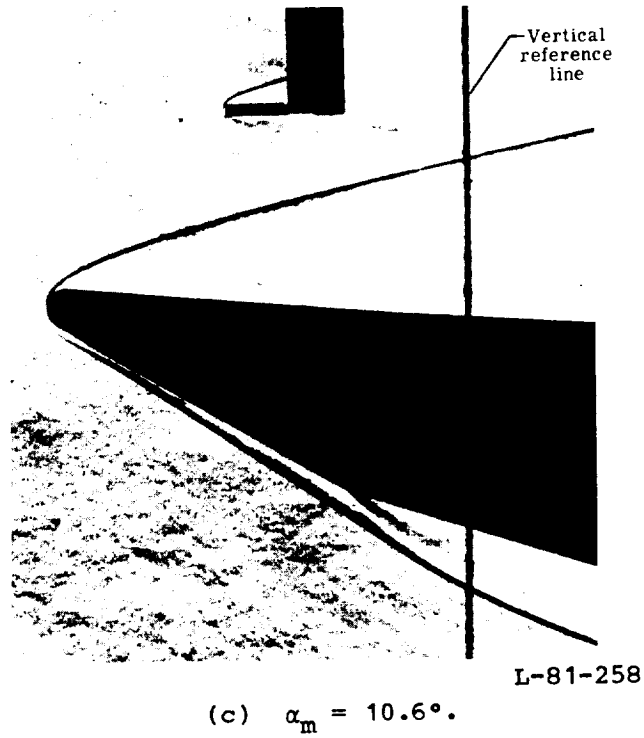
(c)  $\alpha_m = 10.6°$.



(d)  $\alpha_m = 15.8°$.

Figure 3.- Continued.

33
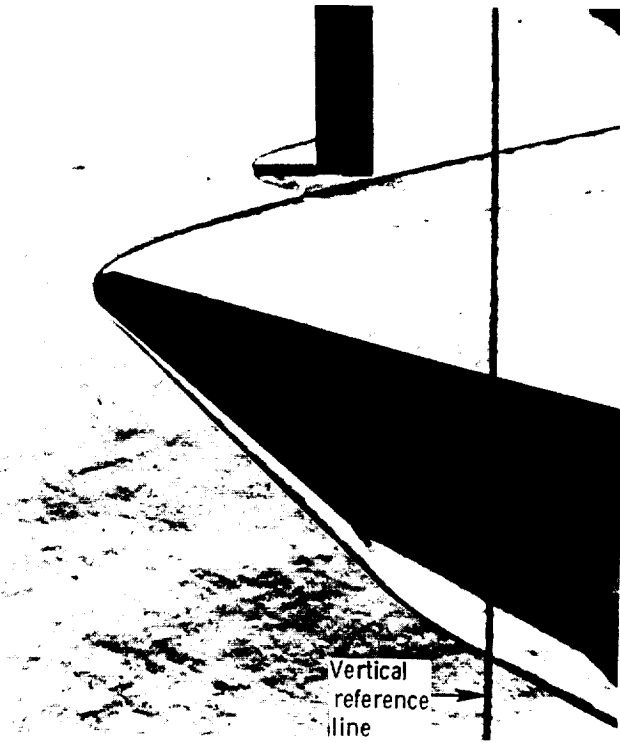
L-81-260

(e) $\alpha_m = 21°$.
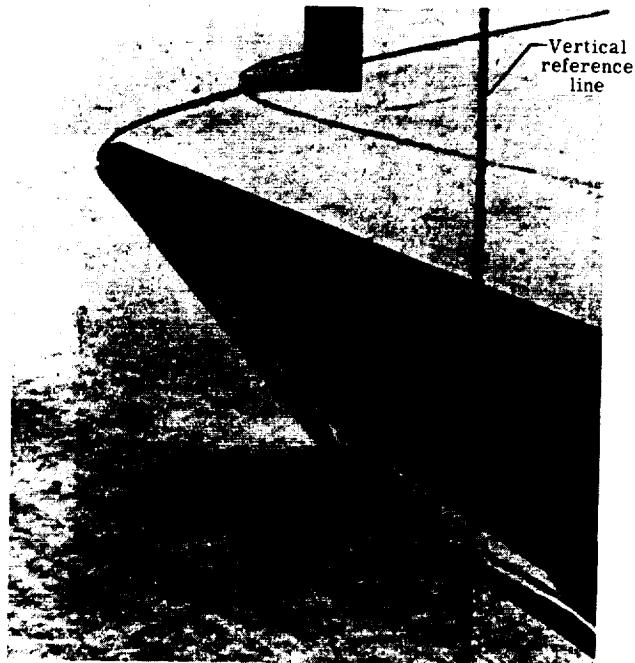
L-81-261

(f) $\alpha_m = 26.25°$.

Figure 3.- Concluded.

34
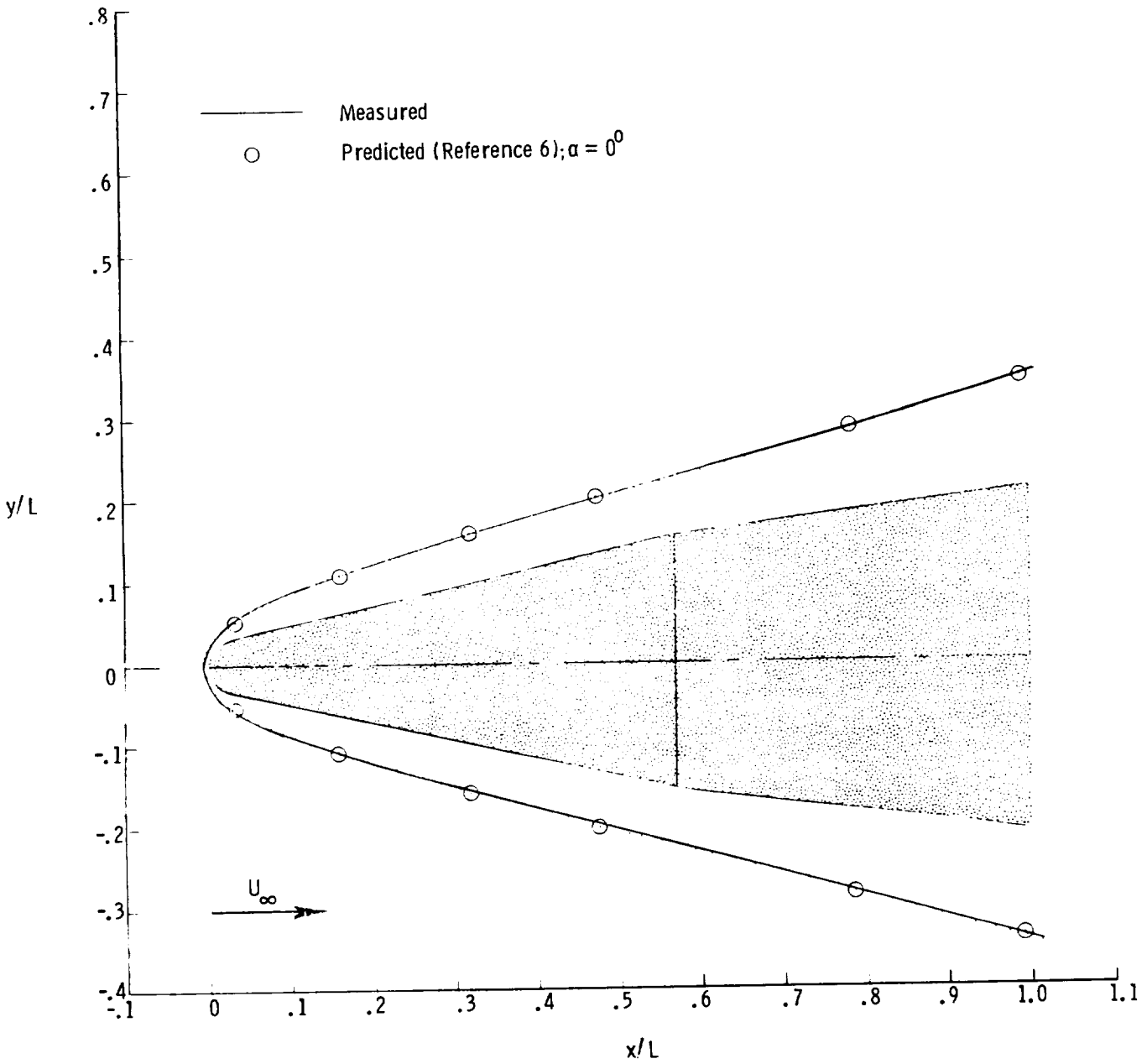
(a) $\alpha_m = 0°$.

Figure 4.- Measured and predicted shock shapes for on-axis biconic at various nominal angles of attack. $M_\infty = 6.0$; $R_{\infty,L} = 5.3 \times 10^6$.

35

(b)  $\alpha_m = 5°$.
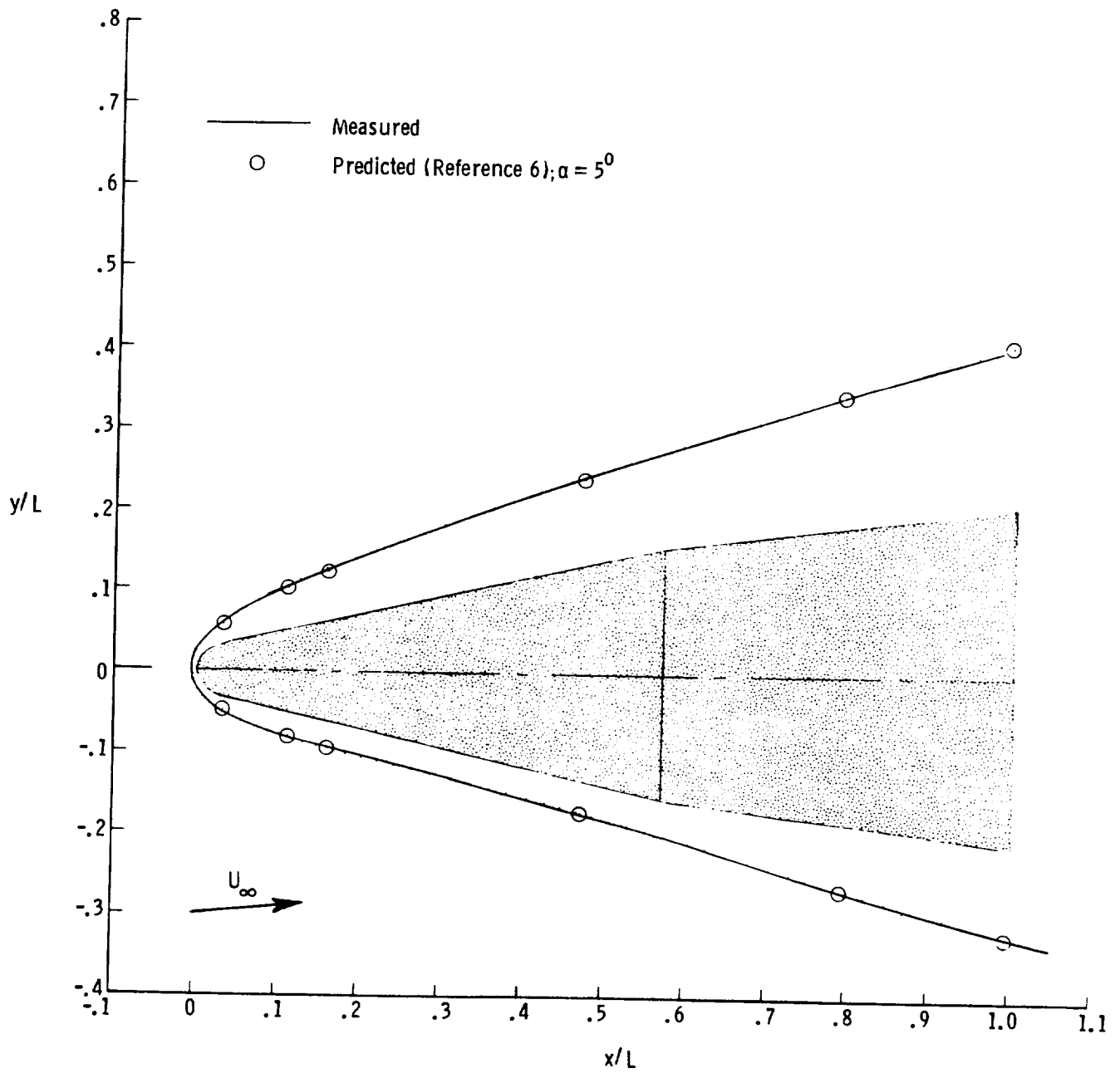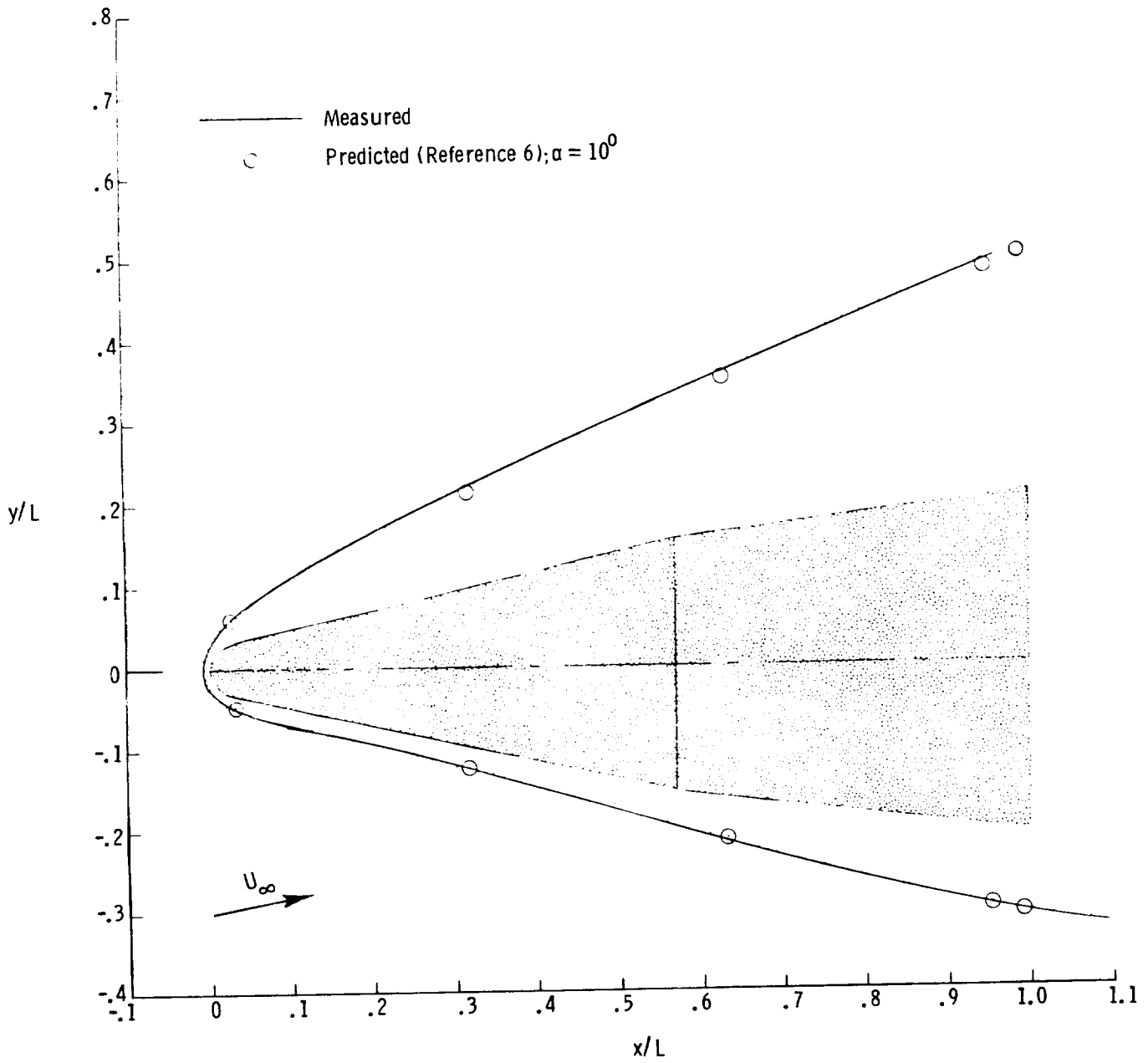
Figure 4.- Continued.

(c) $\alpha_m = 10.25°$.
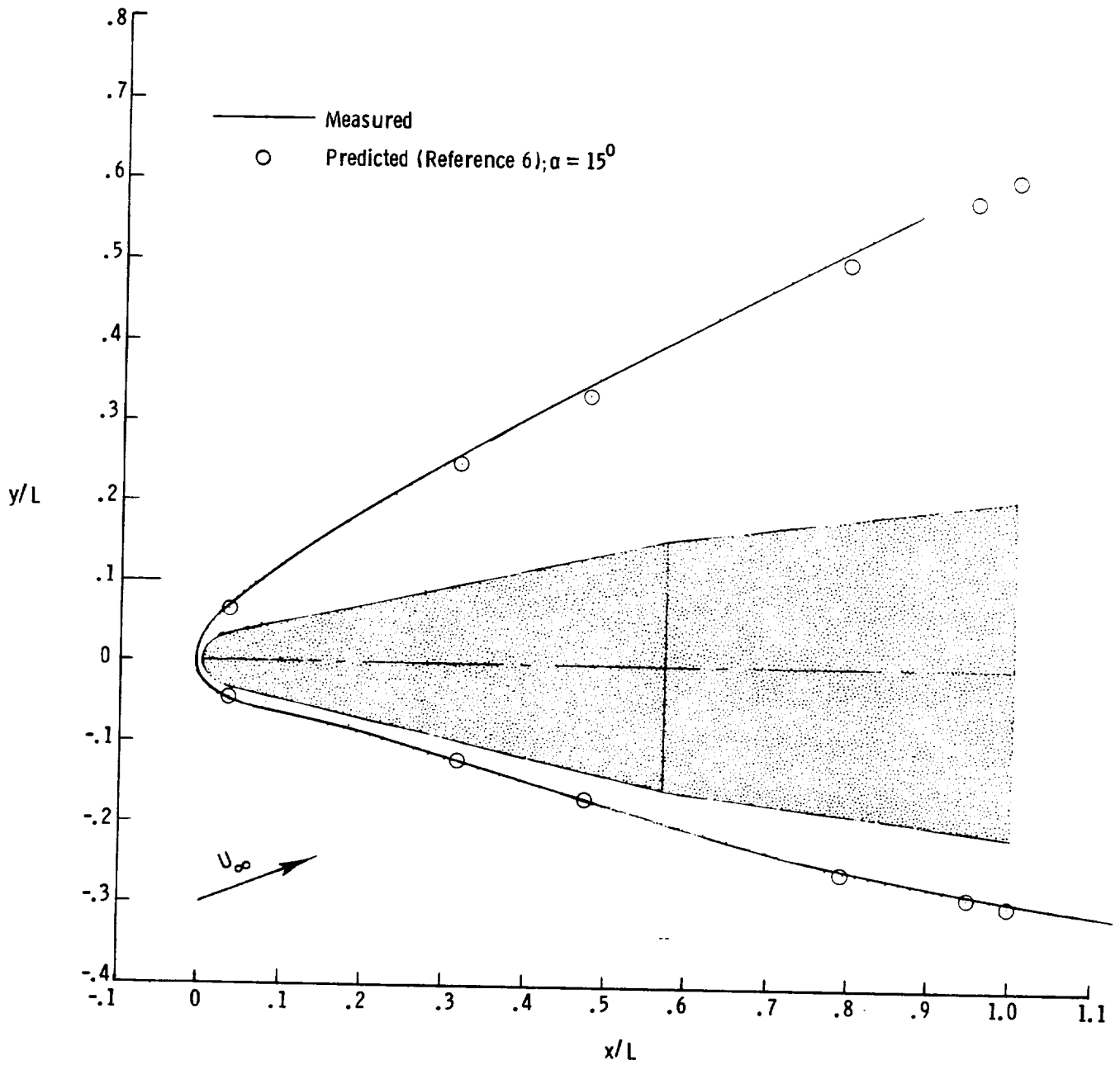
Figure 4.- Continued.

(d)  $\alpha_m = 15.5°$.
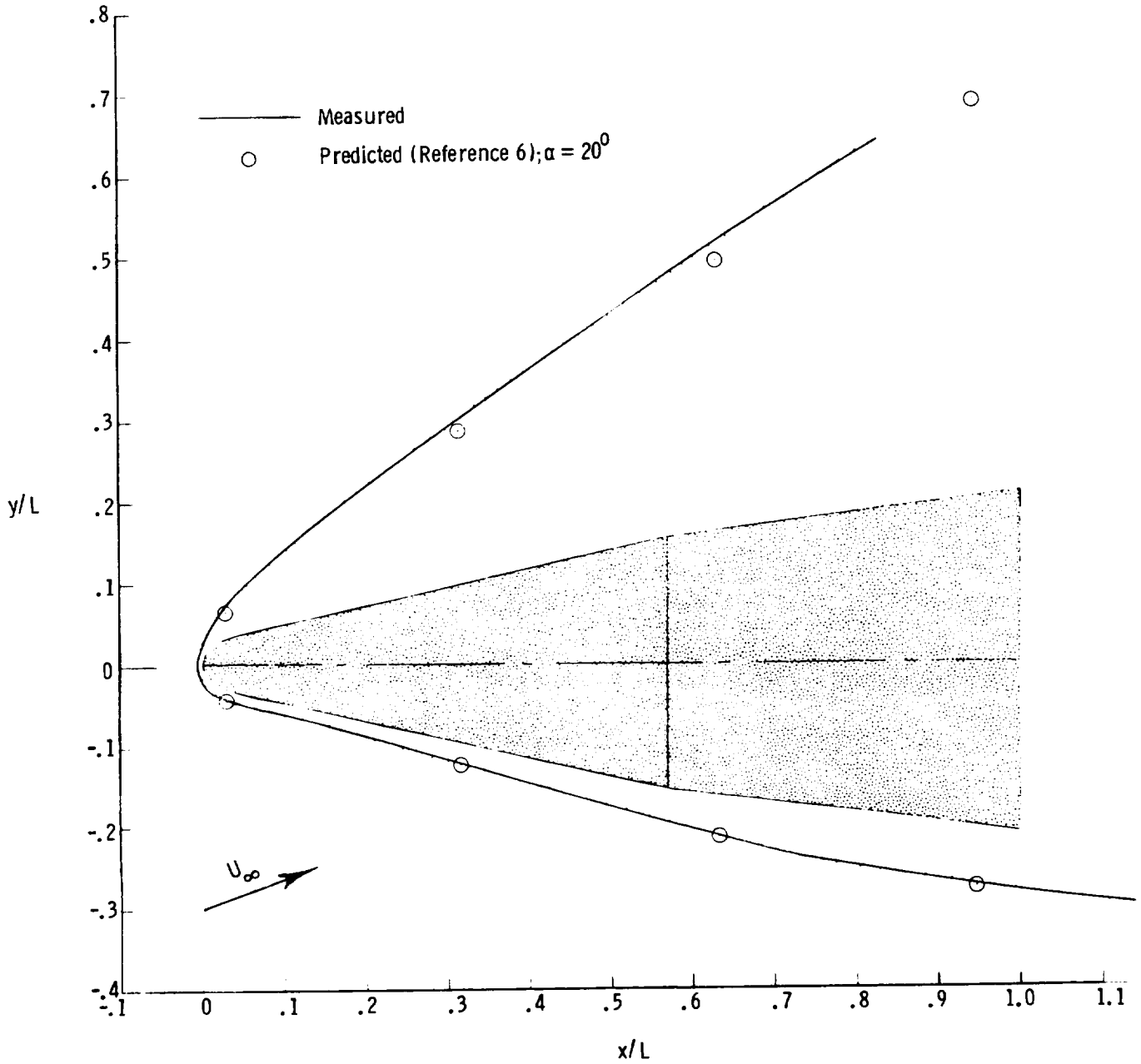
Figure 4.- Continued.

(e)  $\alpha_m = 20.7°$.
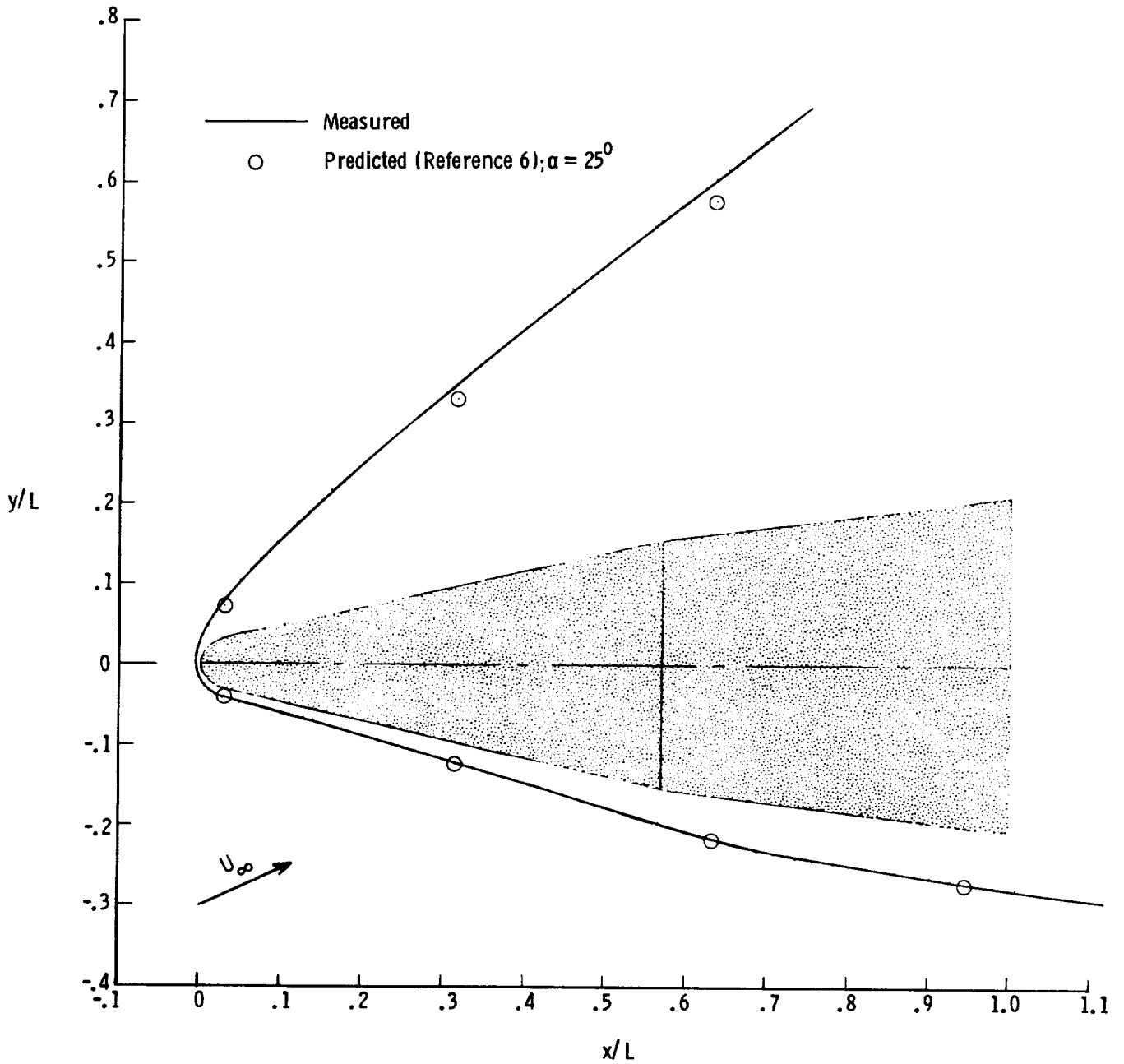
Figure 4.- Continued.

(f)   $\alpha_m$ = 25.85°.

Figure 4.- Concluded.
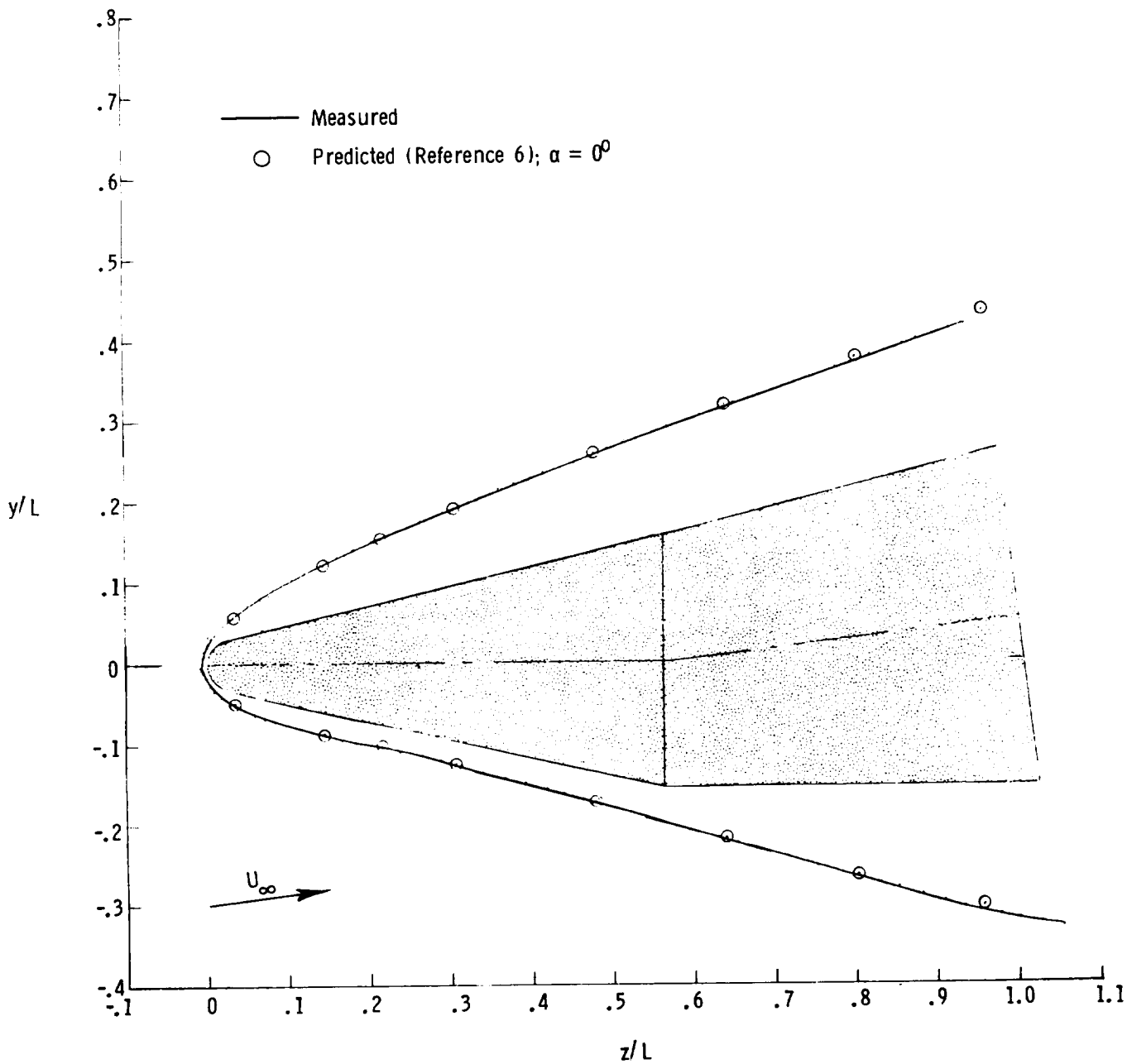
(a)  $\alpha_m = 0°$.

Figure 5.- Measured and predicted shock shapes for bent-nose biconic at various nominal angles of attack.  $M_\infty = 6.0$;  $R_{\infty,L} = 5.3 \times 10^6$.

(b)  $\alpha_m = 5°$.
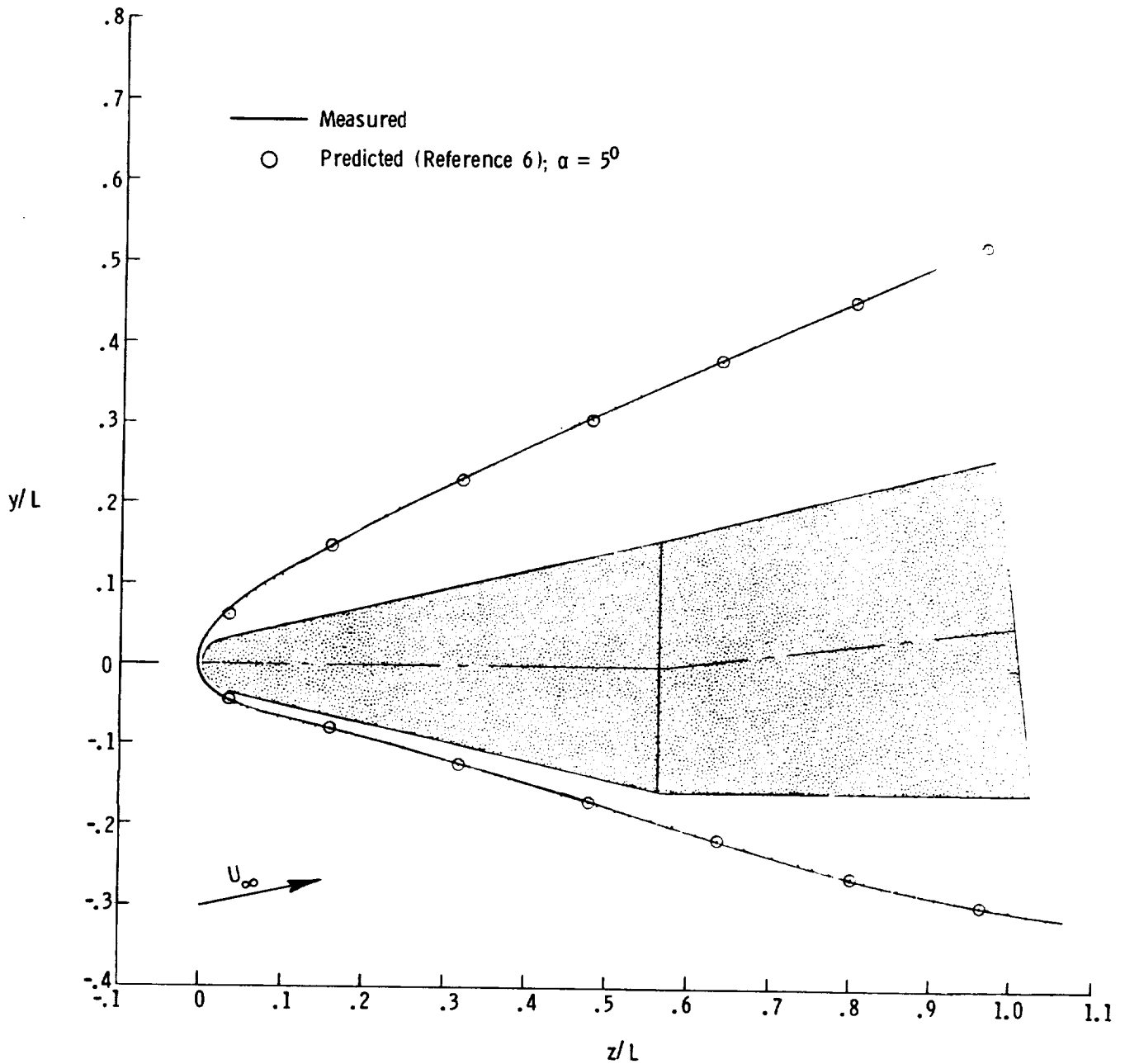
Figure 5.- Continued.
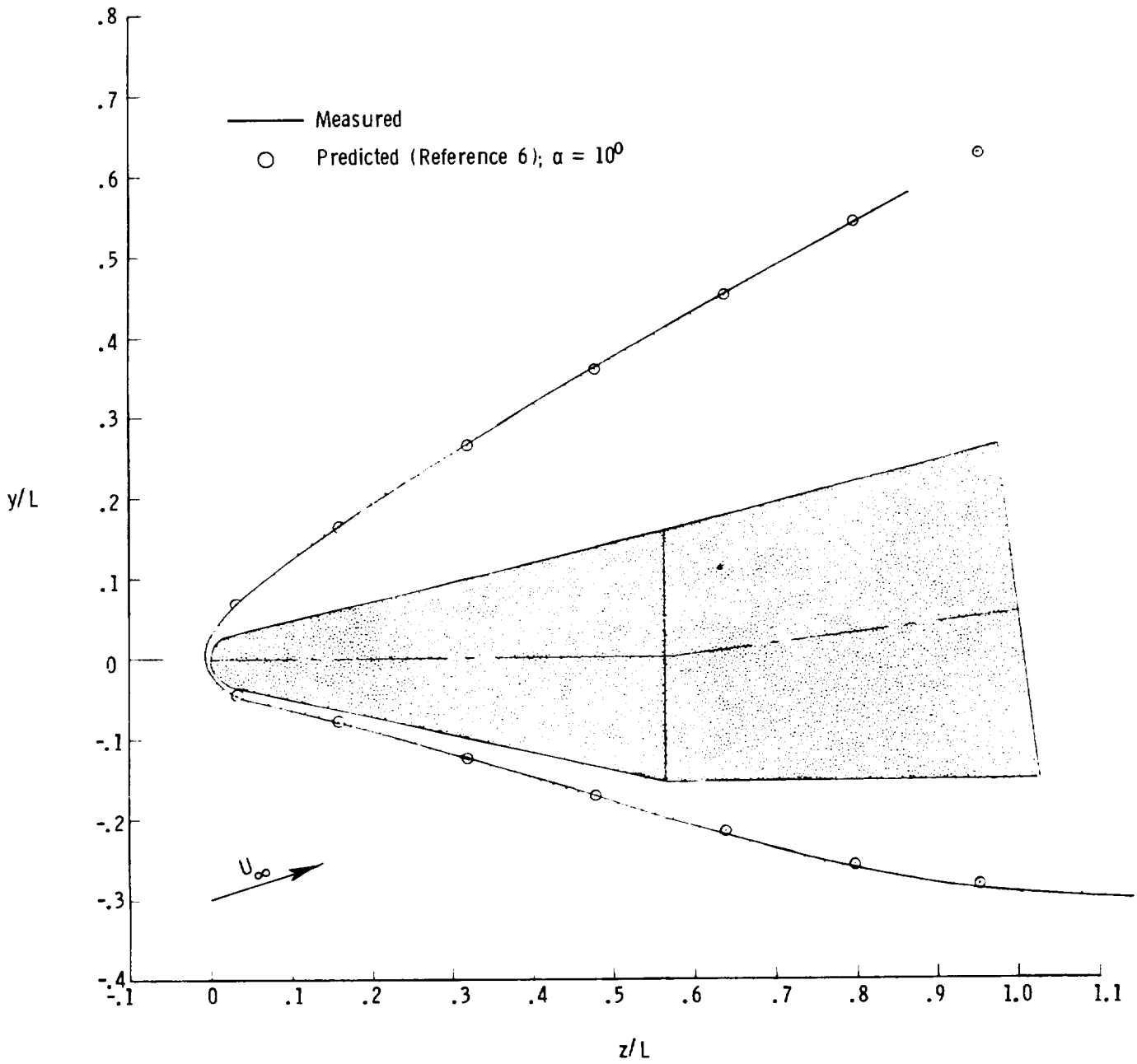
(c)  $\alpha_m = 10.6°$.
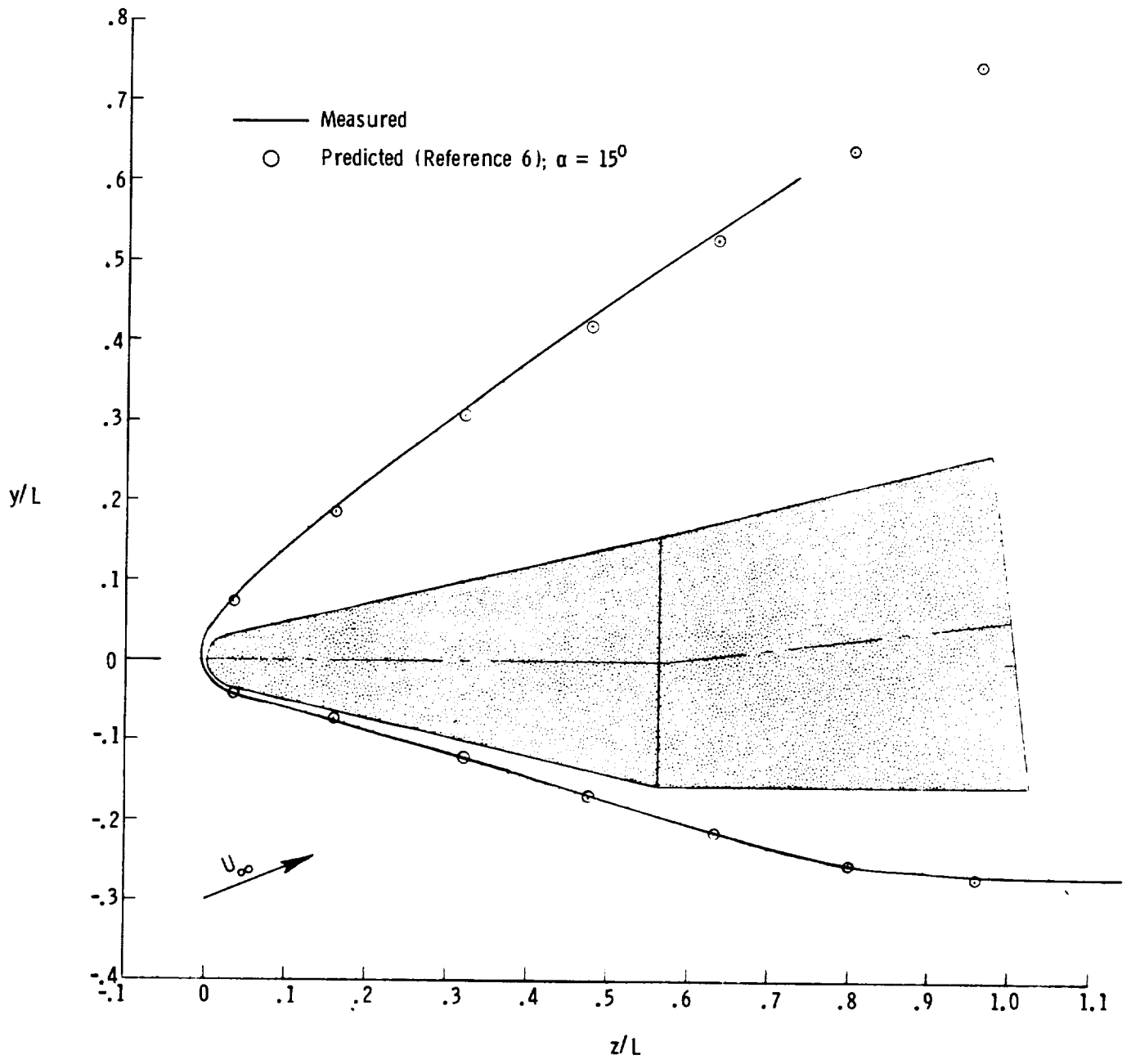
Figure 5.- Continued.

(d)  $\alpha_m = 15.8°$.

Figure 5.- Continued.
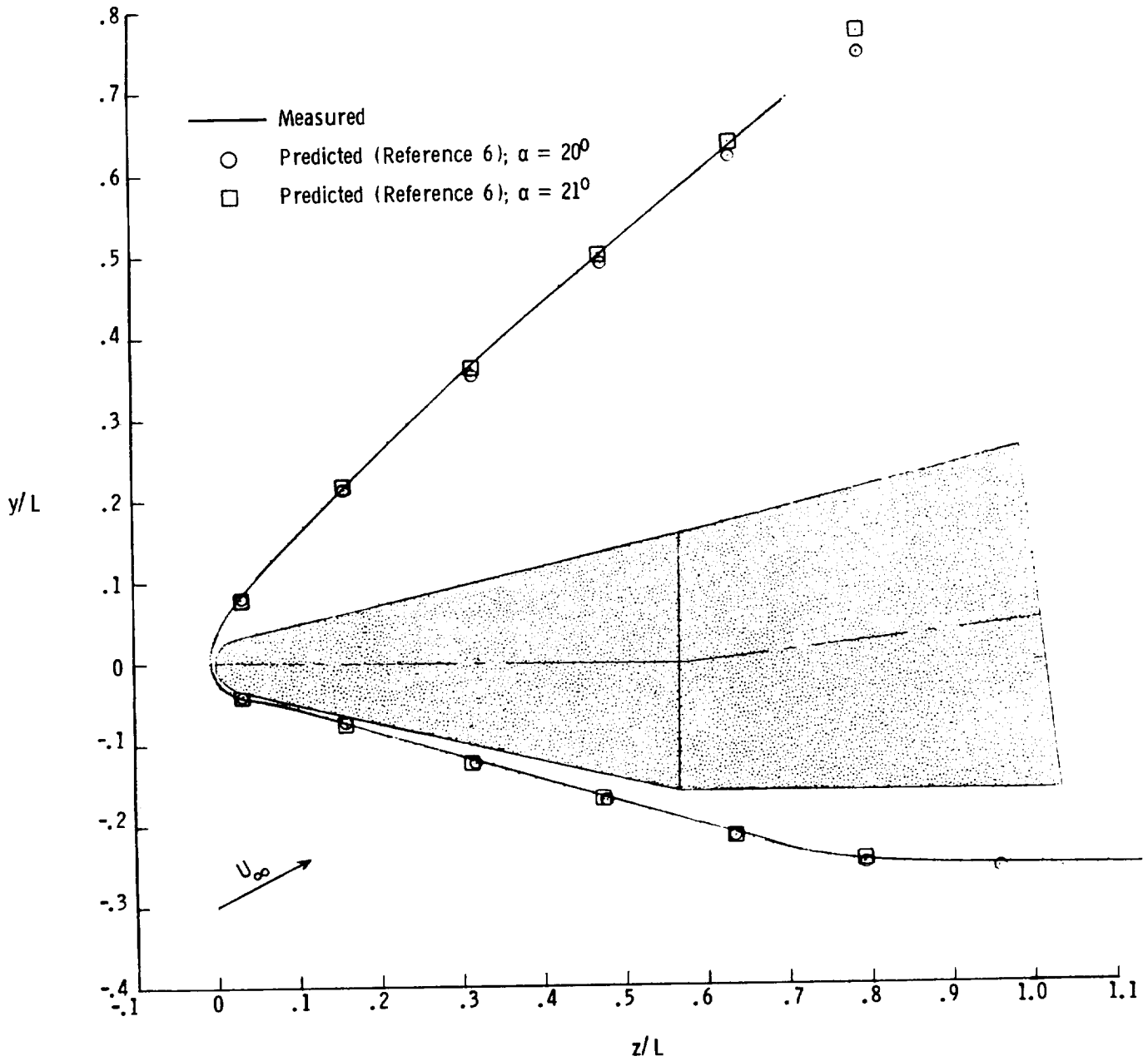
(e) $\alpha_m = 21°$.

Figure 5.- Continued.
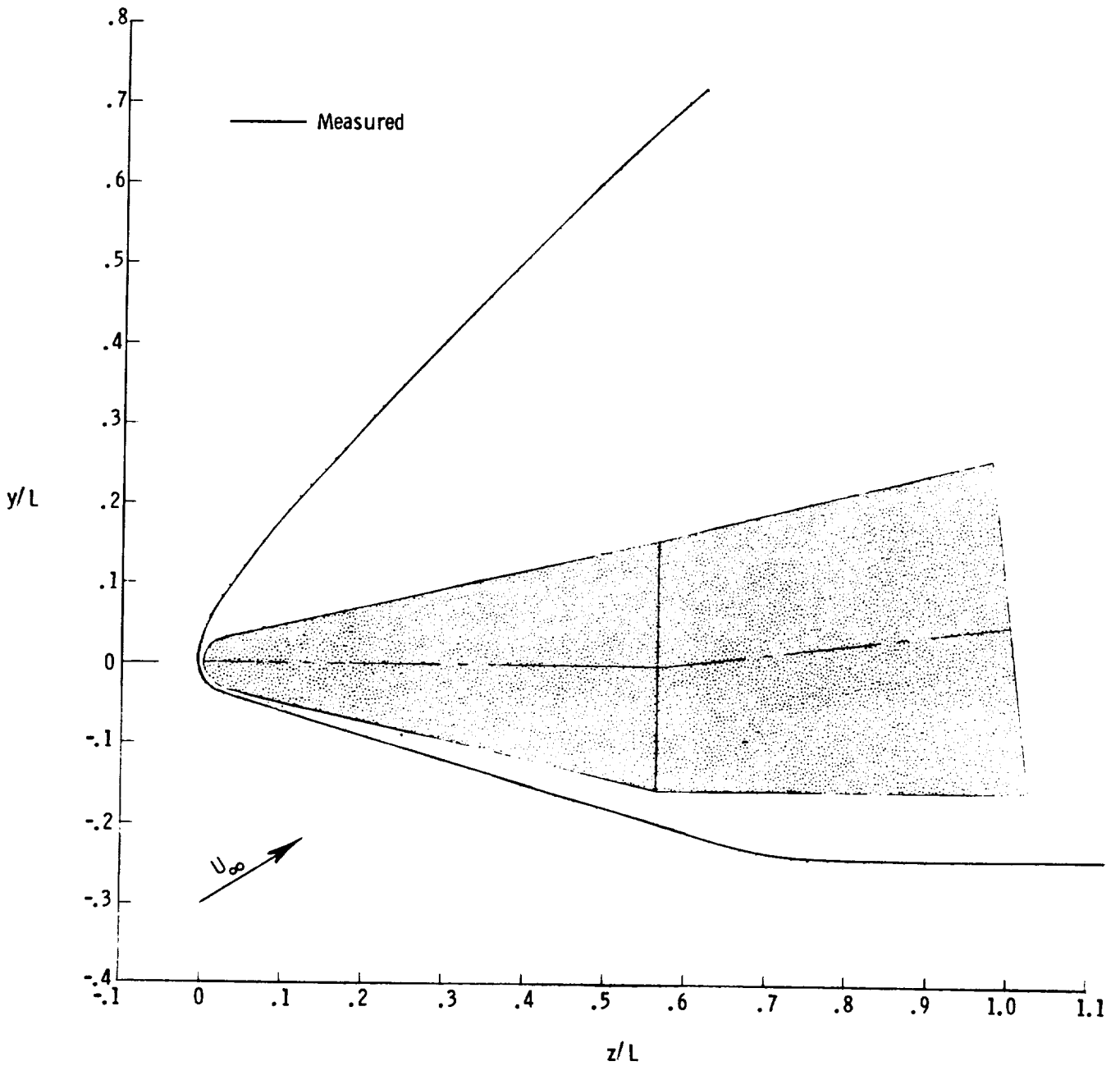
(f)  $\alpha_m = 26.25°$.

Figure 5.- Concluded.
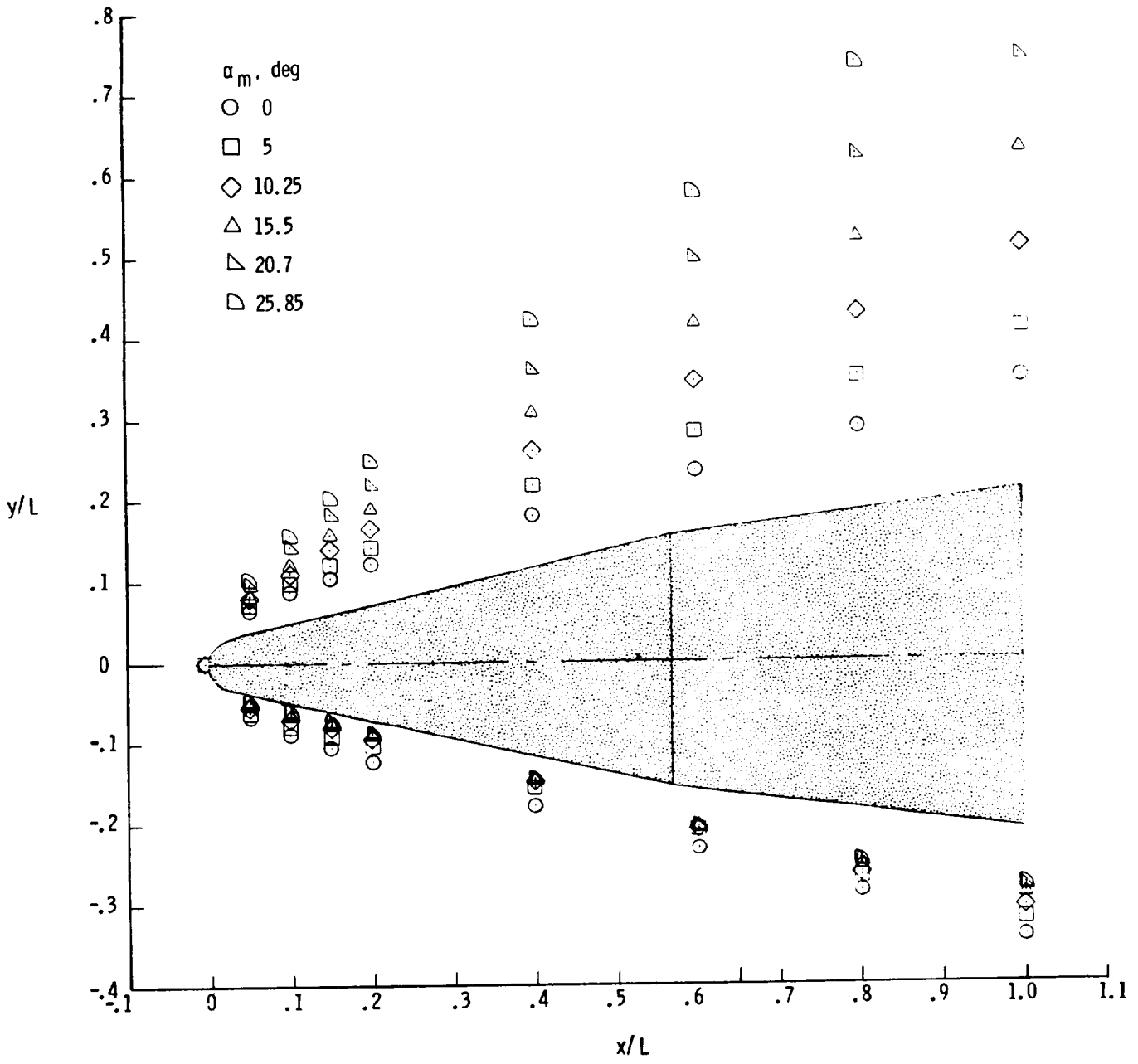
(a) On-axis biconic.

Figure 6.- Effect of angle of attack on measured shock shape for on-axis biconic and bent-nose biconic. $M_\infty = 6.0$; $R_{\infty,L} = 5.3 \times 10^6$.
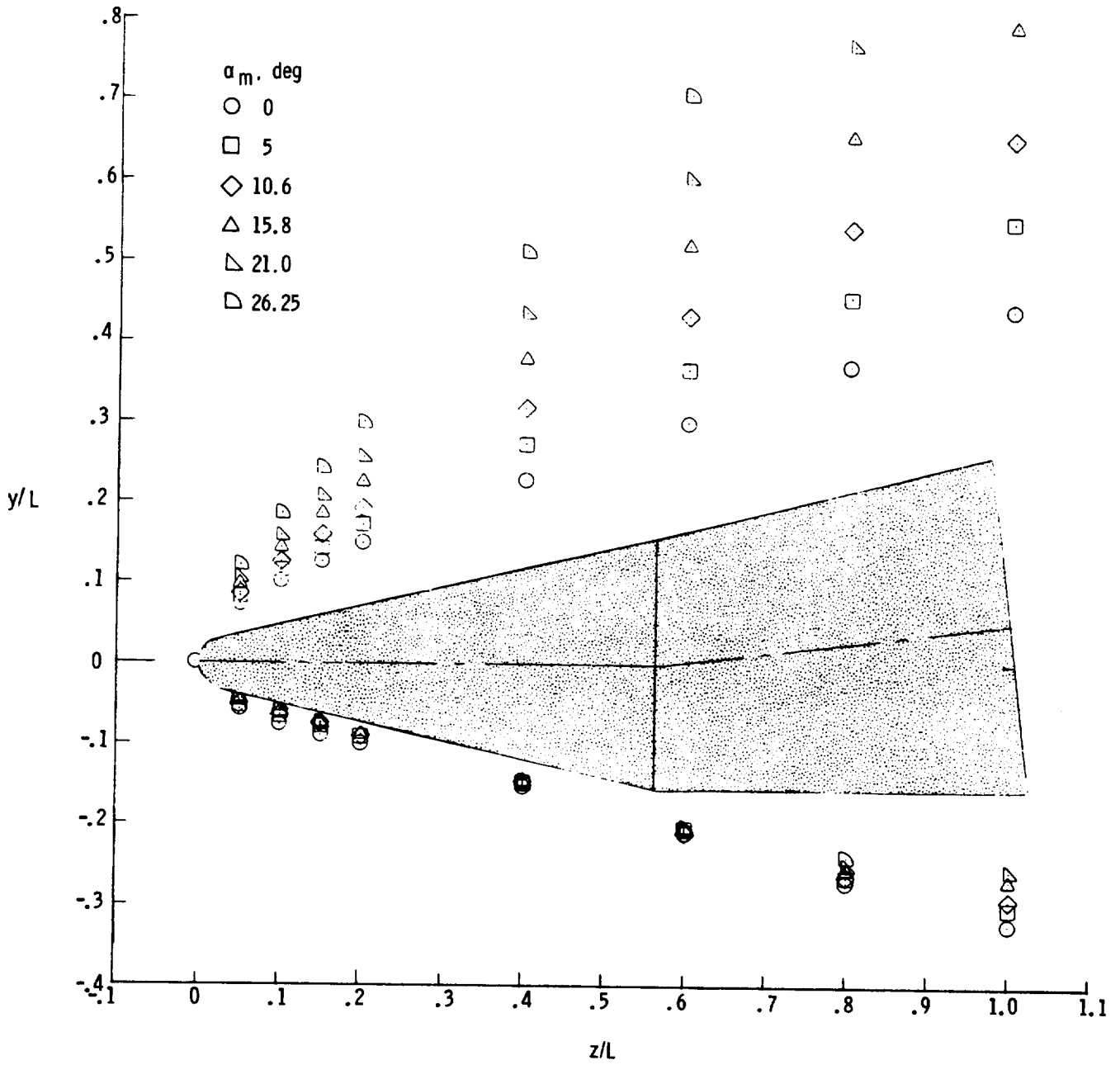
(b) Bent-nose biconic.

Figure 6.- Concluded.
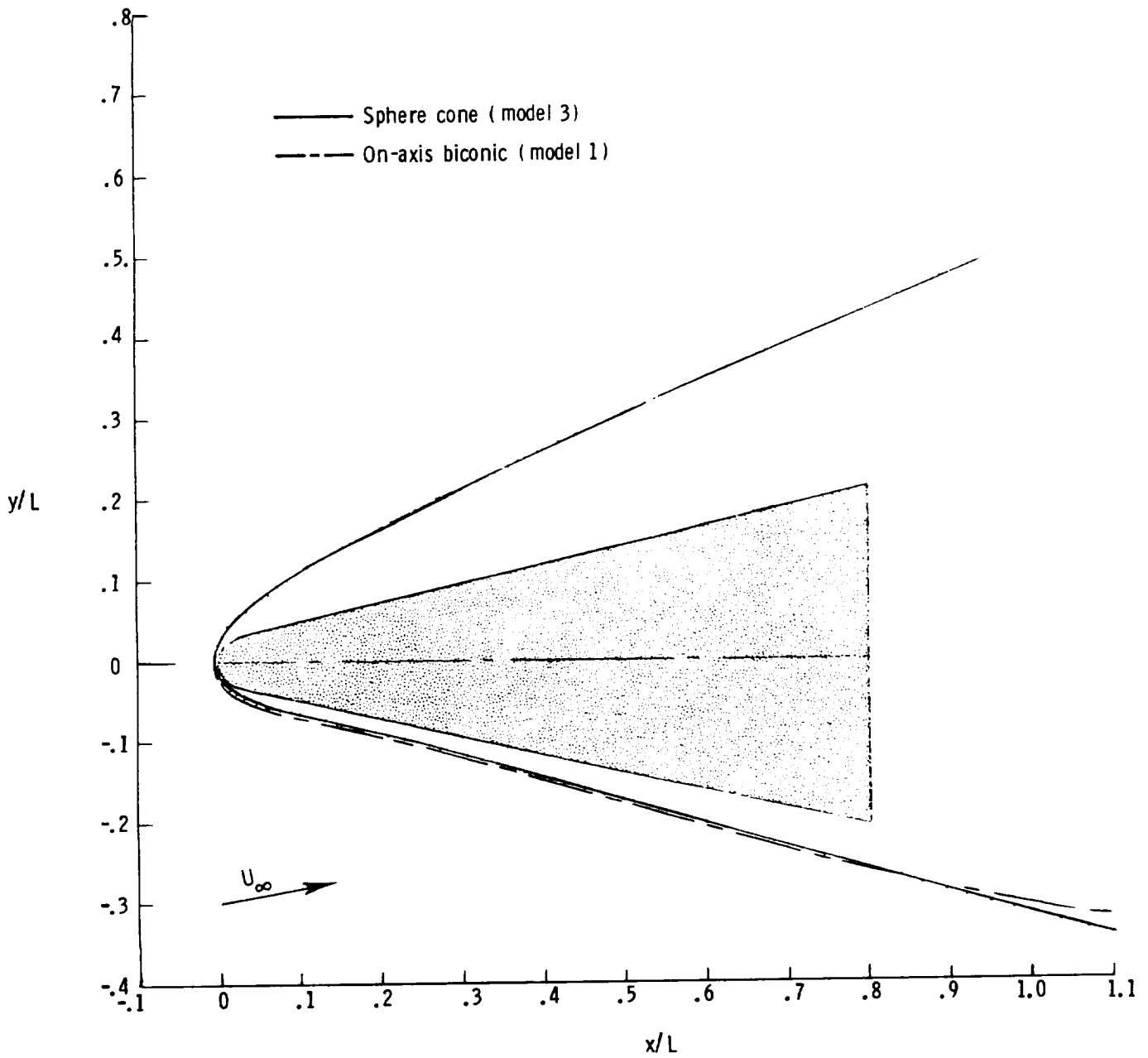
(a)  $\alpha_m \approx 10.4°$.

Figure 7.- Comparison of measured shock shape for sphere-cone to shock shape
for on-axis biconic and bent-nose biconic at various nominal angles of
attack.  $M_\infty = 6.0$;  $R_{\infty,L} = 5.3 \times 10^6$.
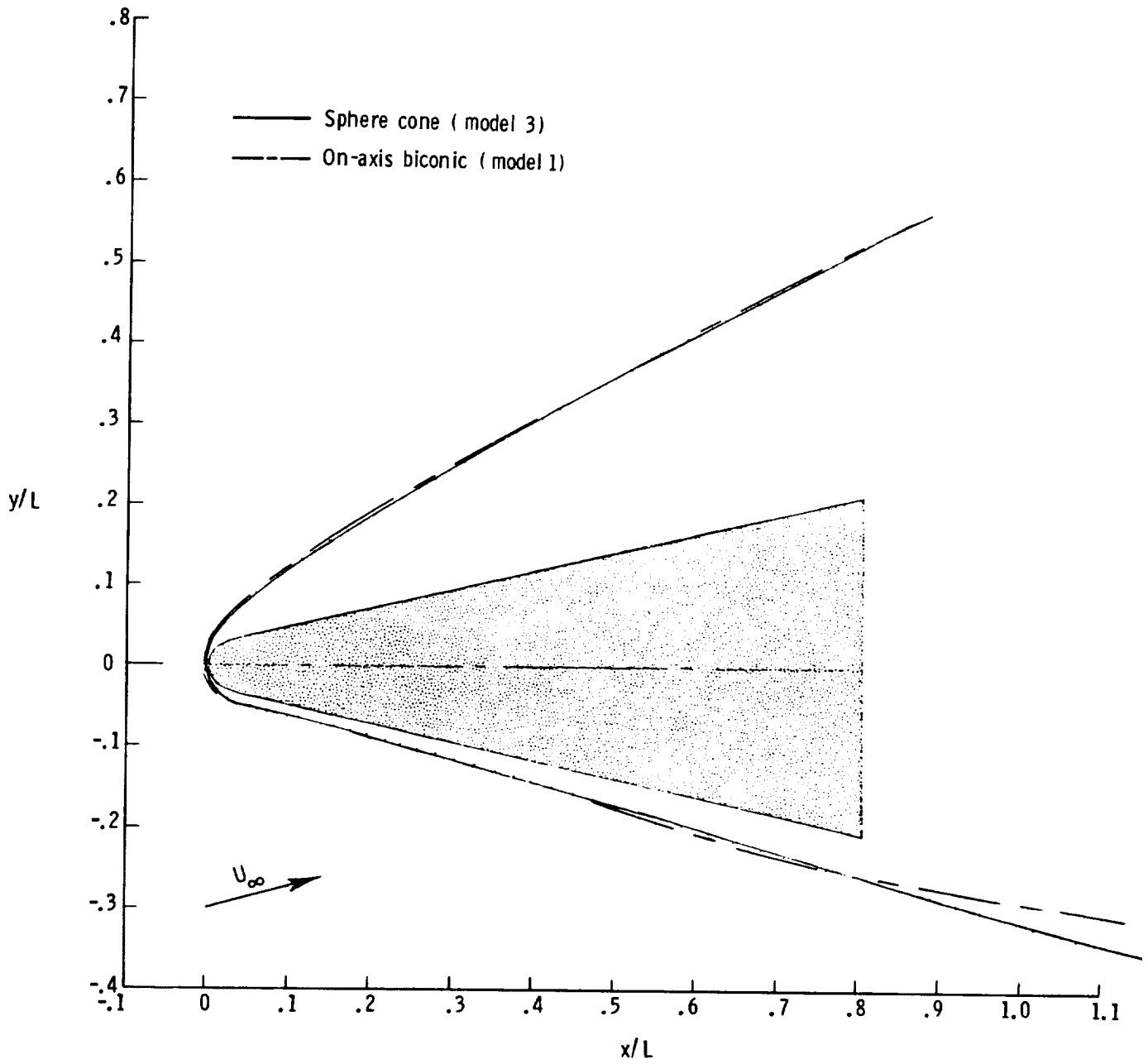
(b) $\alpha_m \approx 15.65°$.
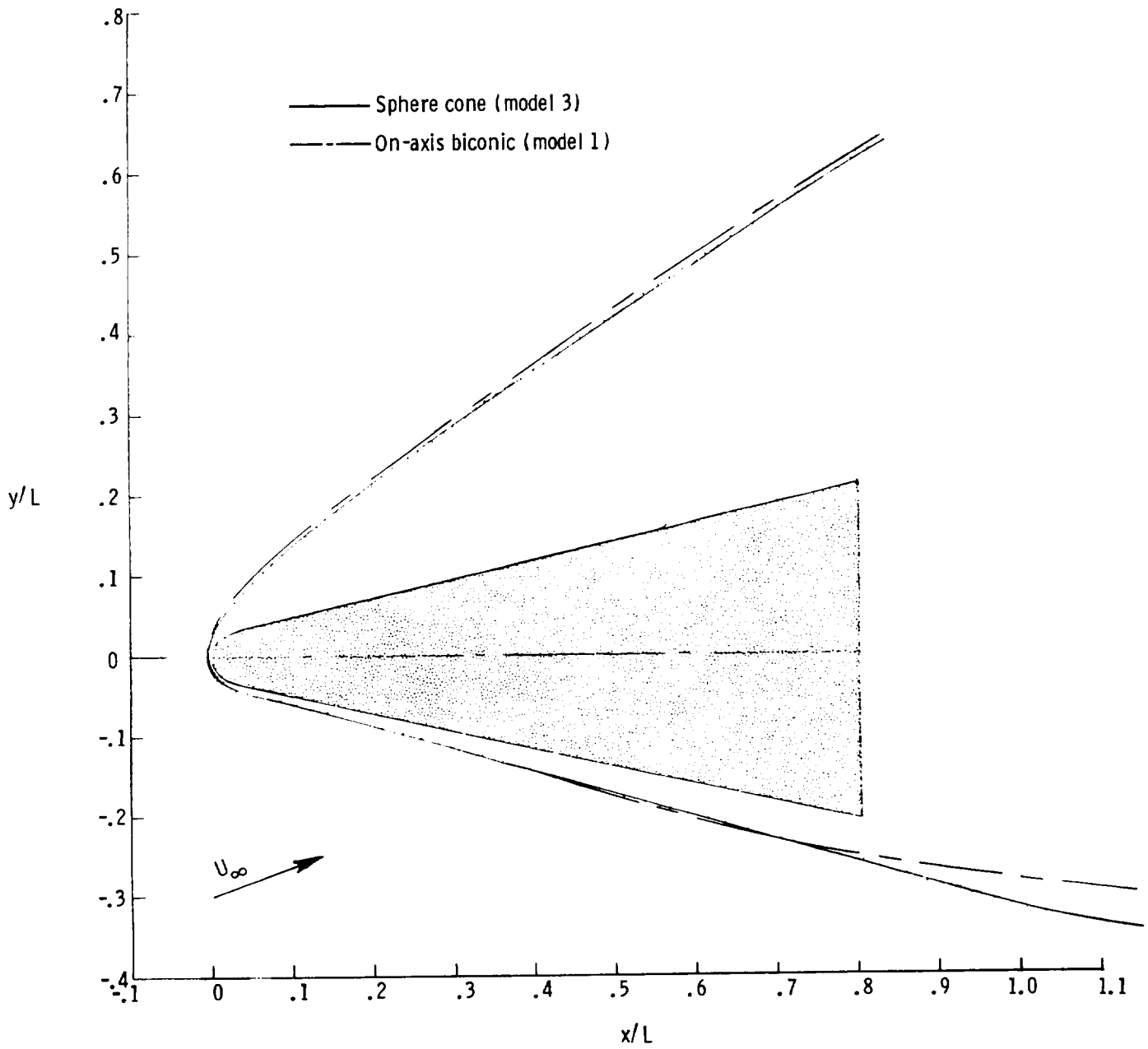
Figure 7.- Continued.

(c) $\alpha_m \approx 20.85°$.
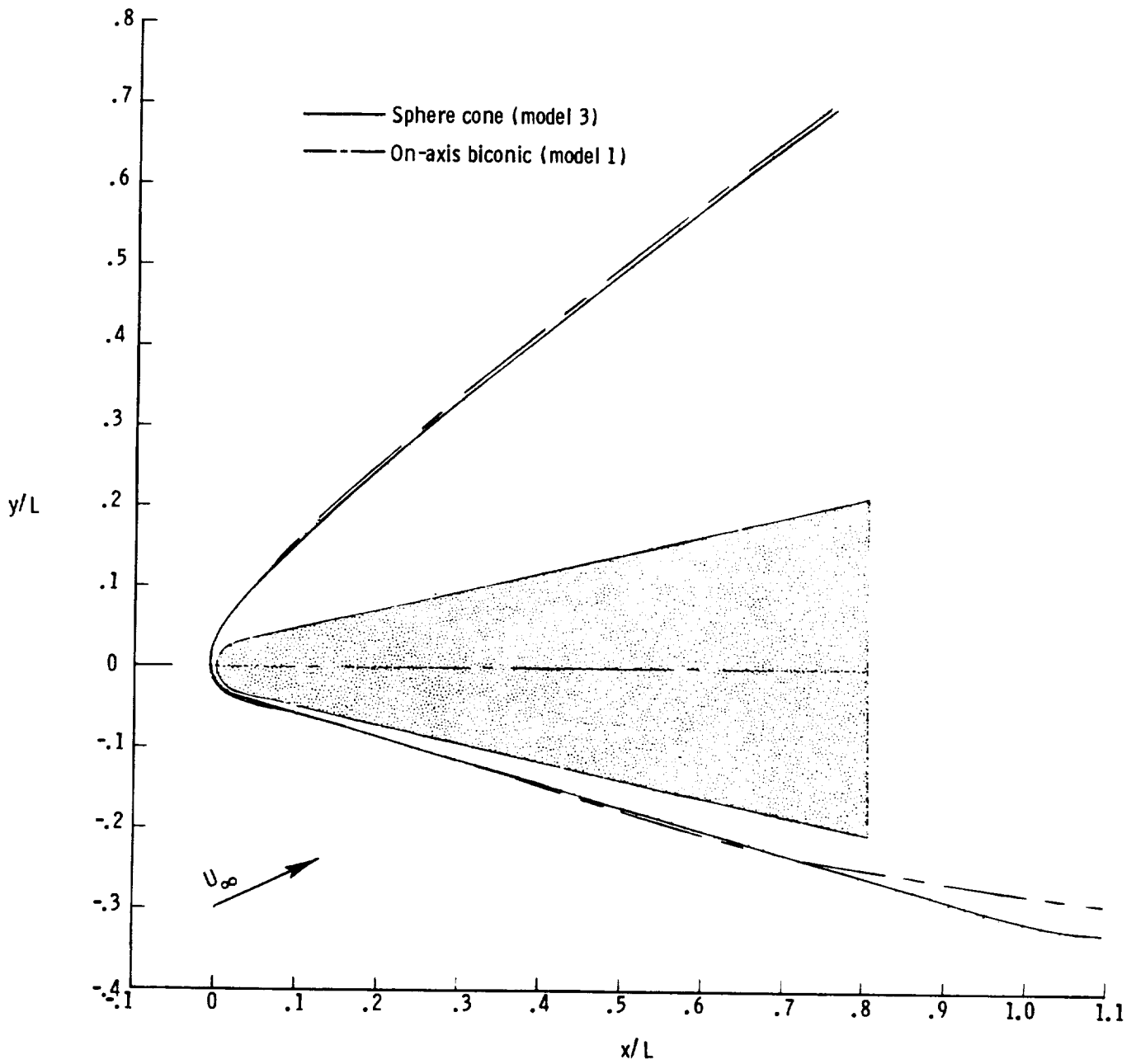
Figure 7.- Continued.

(d)  $\alpha_m \approx 25.9°$.

Figure 7.- Continued.
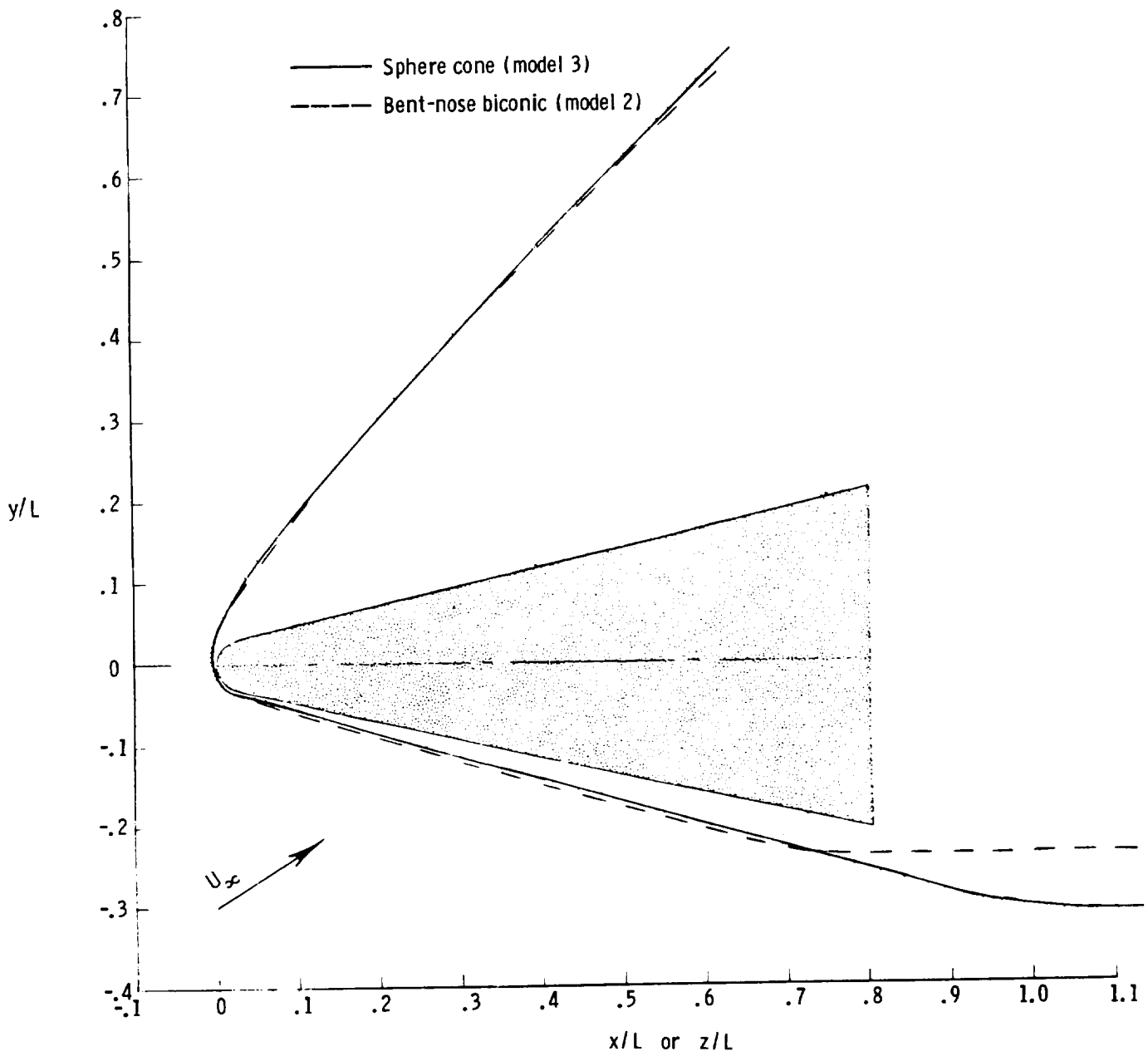
(e) $\alpha_m \approx 33.1°$.

Figure 7.- Concluded.

$M_\infty$    $R_{\infty, L}$

———— 5.85    $0.5 \times 10^6$

-- -- -- 6.00    $4.2 \times 10^6$

.8

.7

.6

.5

.4

.3

y/L  .2

.1

0

-.1

-.2

-.3

-.4

-.1  0   .1   .2   .3   .4   .5   .6   .7   .8   .9   1.0  1.1

x/L
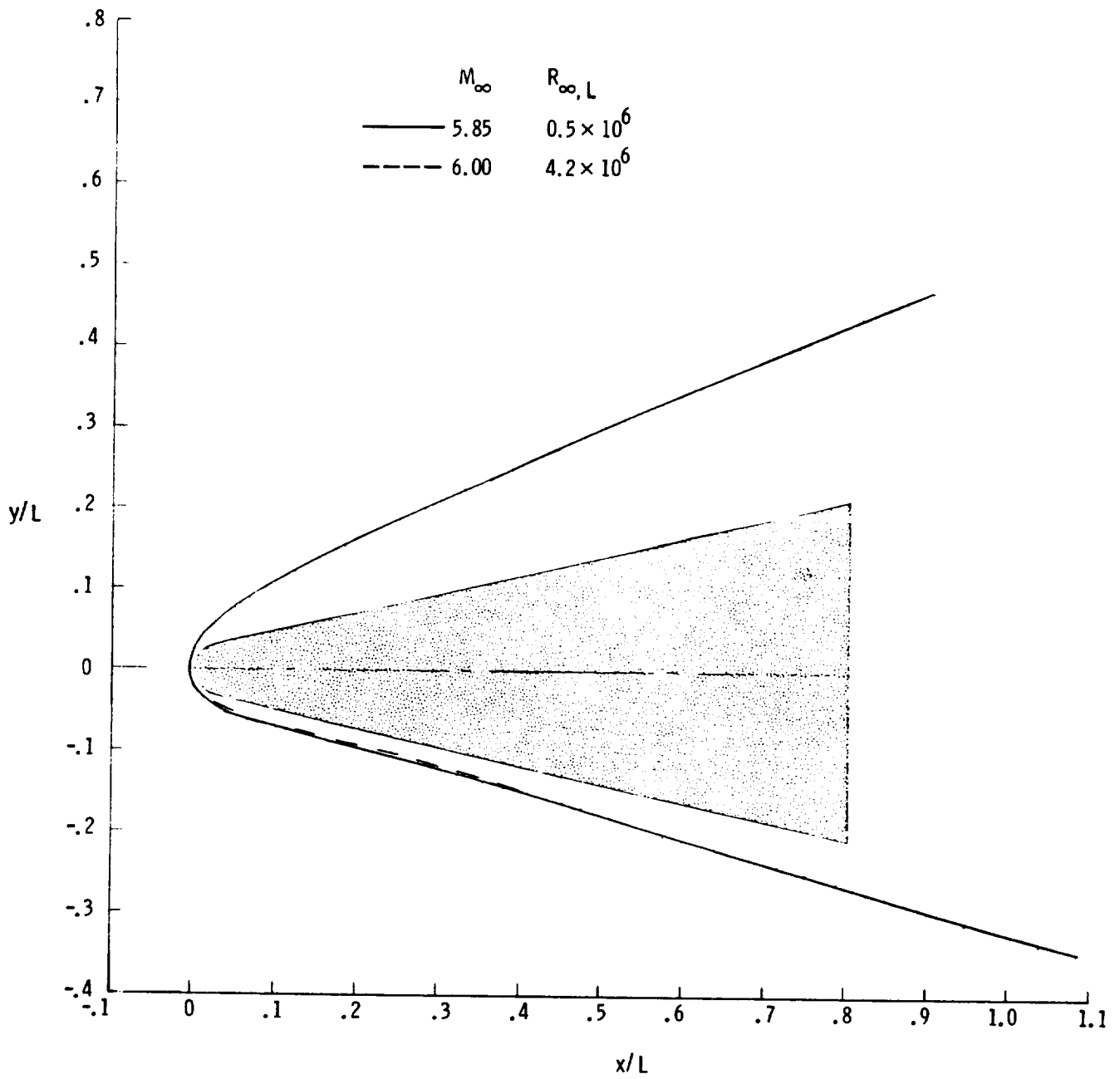
(a)  $\alpha = 10°$.

Figure 8.- Effect of Reynolds number on measured shock shape for sphere-cone at various angles of attack (L used to nondimensionalize x and y is value for on-axis biconic).
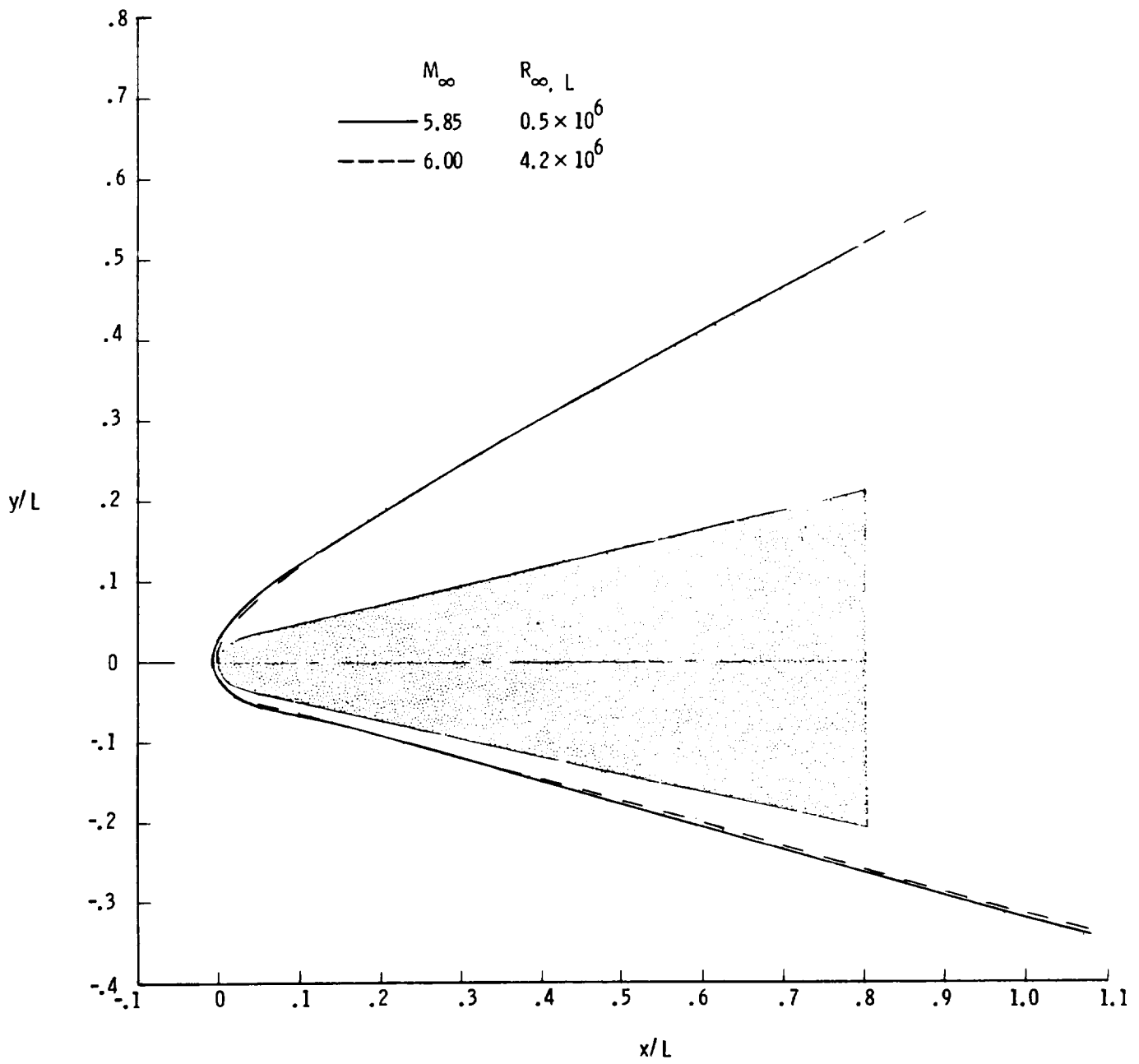
(b) $\alpha = 15°$.

Figure 8.- Continued.
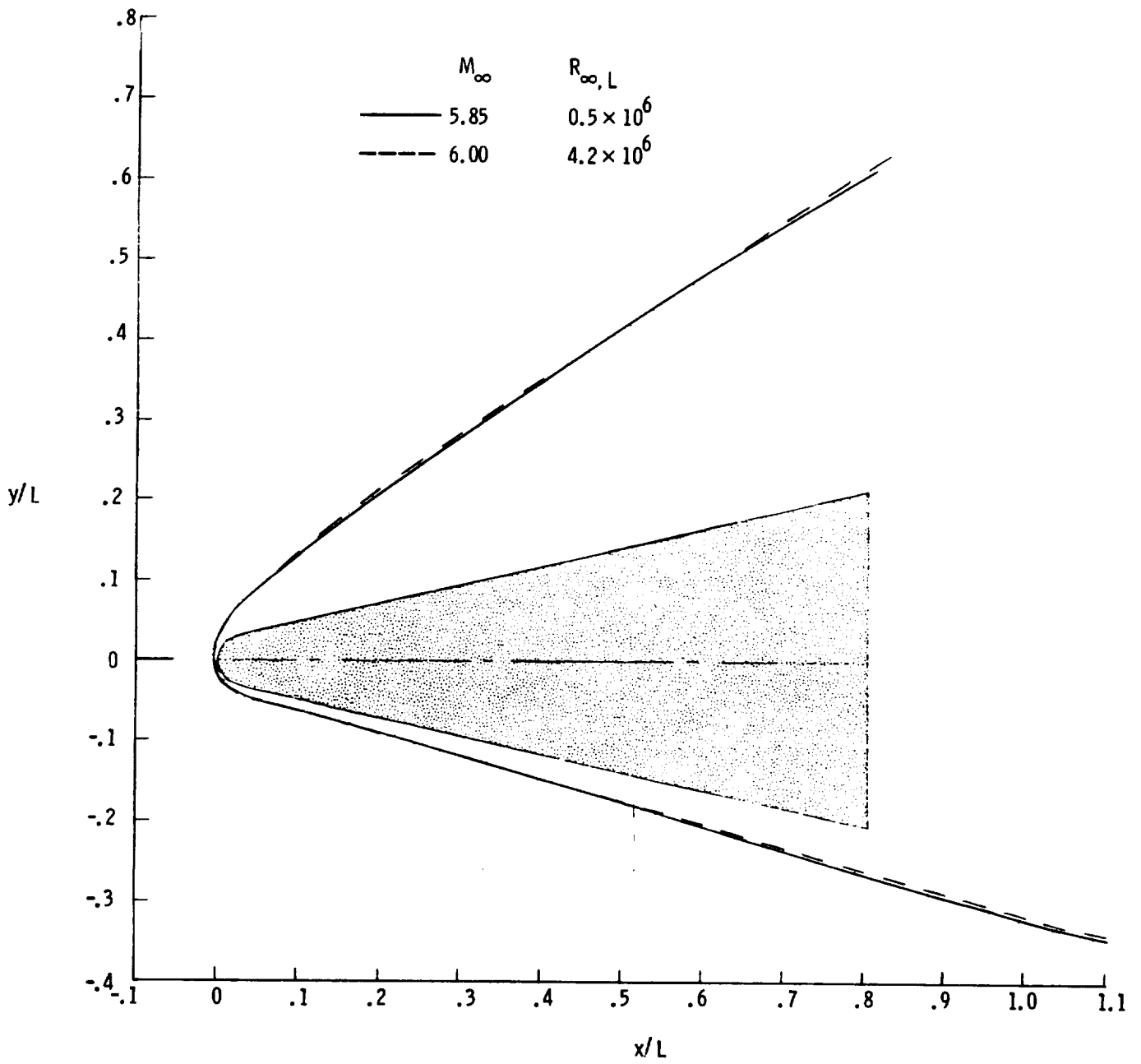
(c)  $\alpha = 20°$.

Figure 8.- Continued.
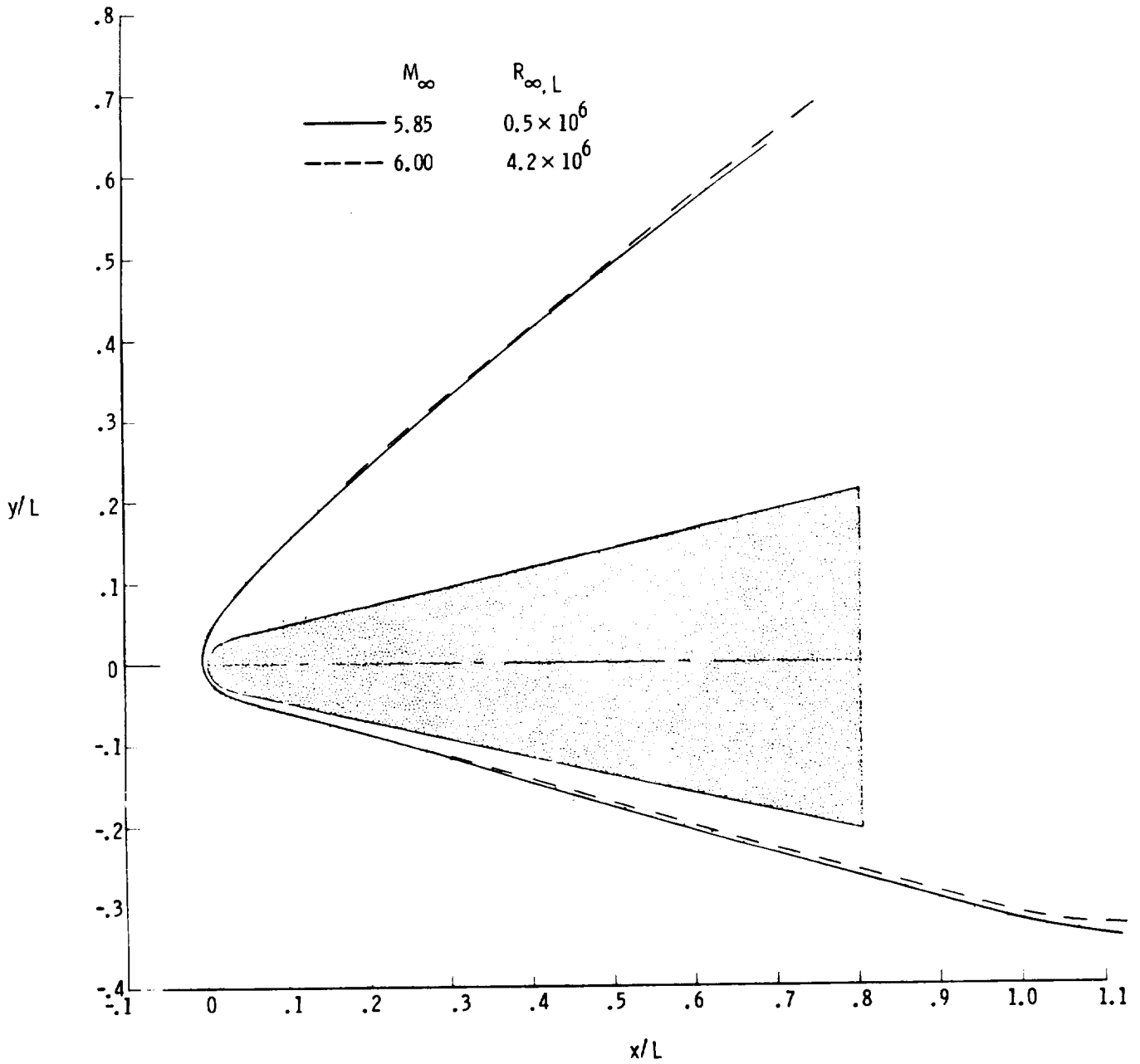
(d)  $\alpha = 25°$.

Figure 8.- Concluded.
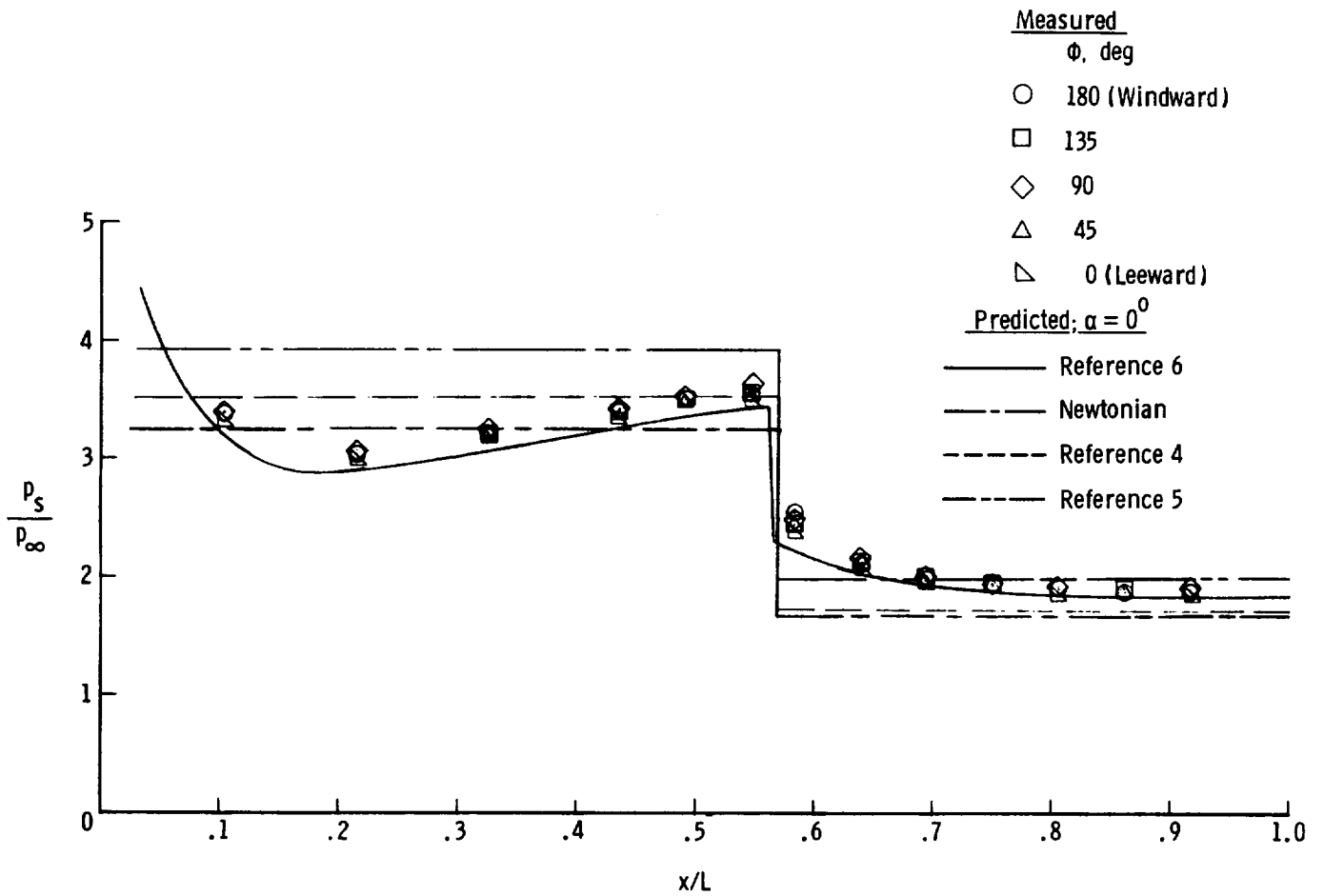
(a) $\alpha_m = 0°$.

Figure 9.- Pressure distributions for on-axis biconic at various nominal angles of attack. $M_\infty = 6.0$; $R_{\infty,L} = 5.3 \times 10^6$.
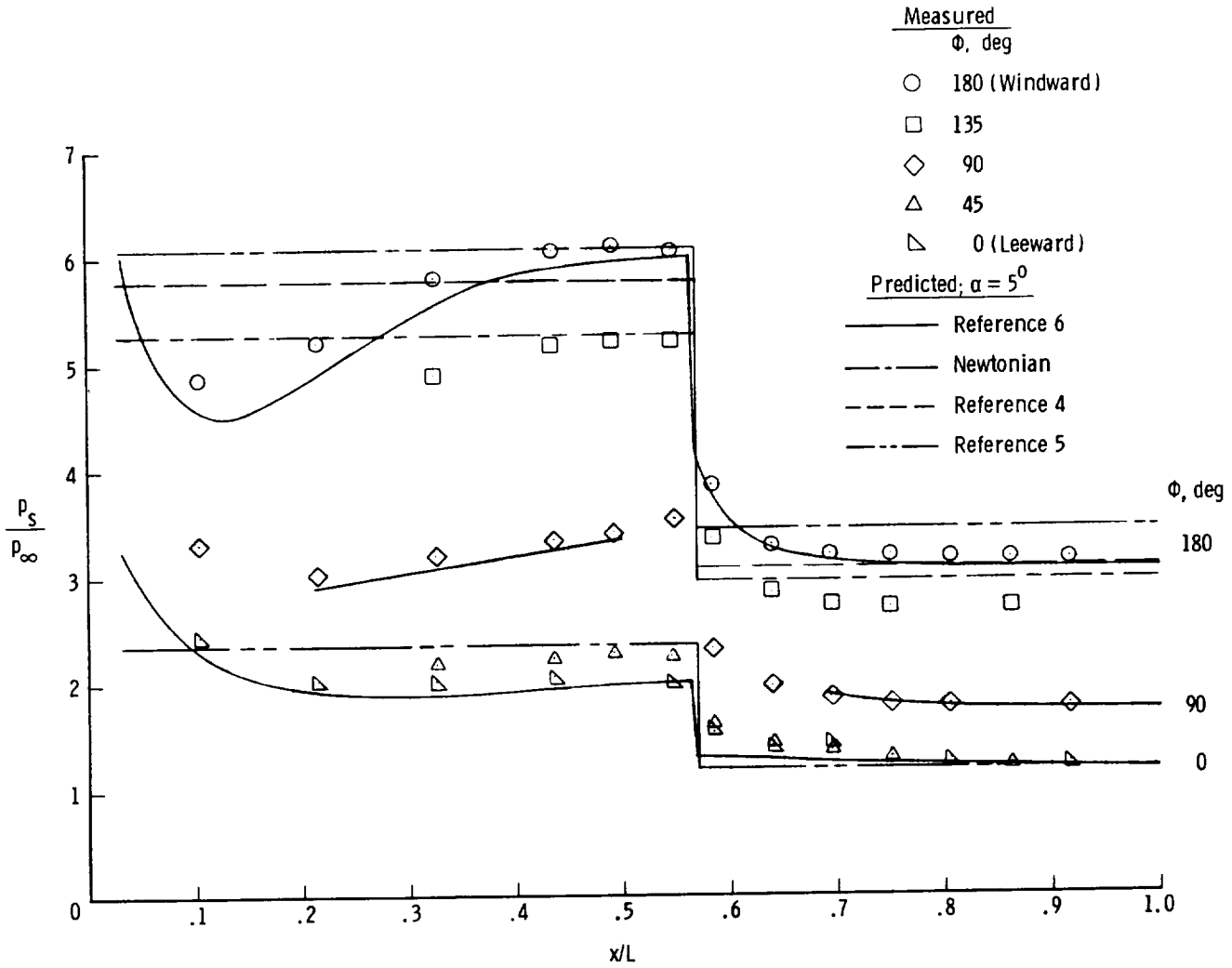
(b)   $\alpha_m = 5°$.

Figure 9.- Continued.
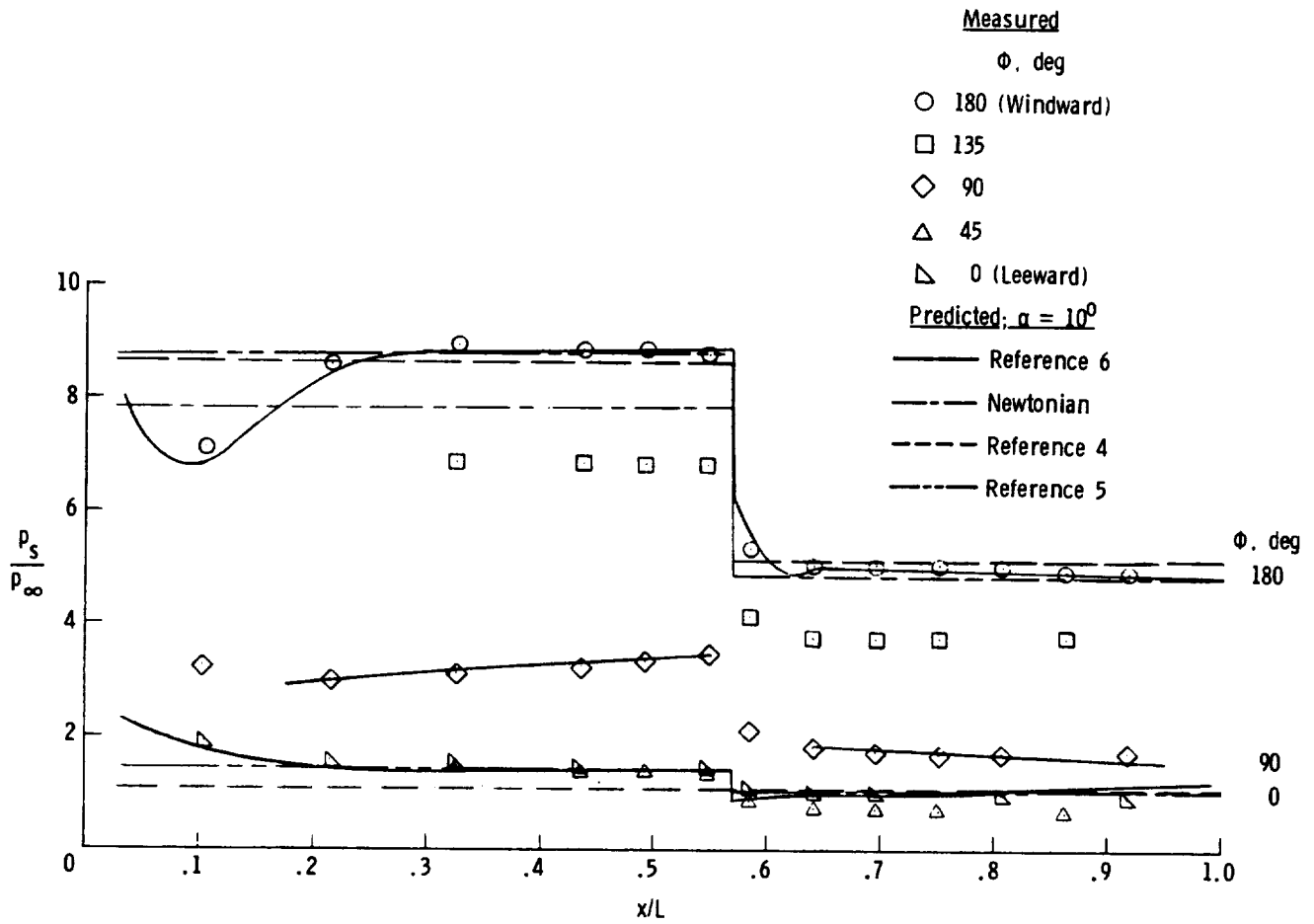
(c) $\alpha_m = 10.25°$.

Figure 9.- Continued.
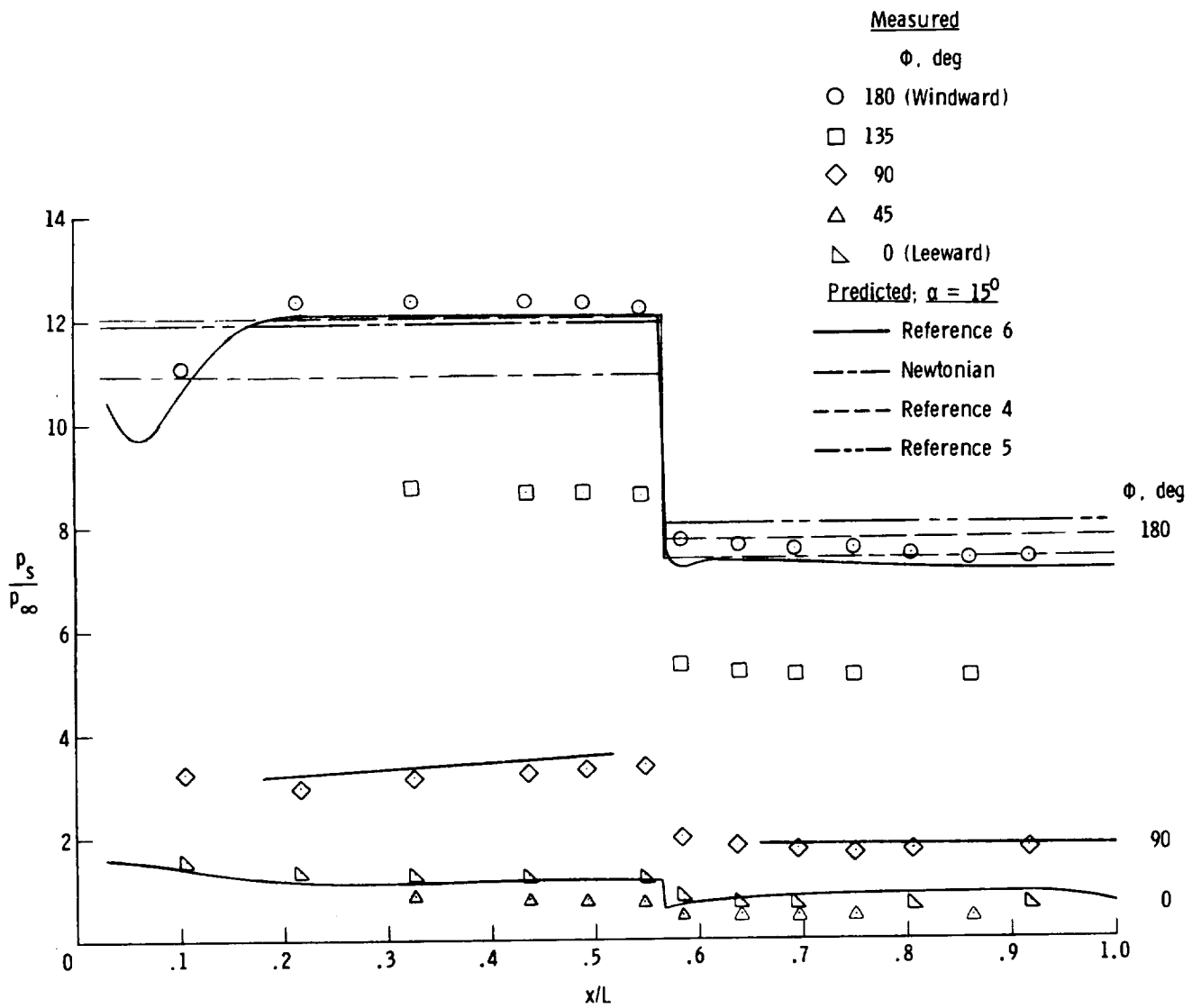
(d)  $\alpha_m = 15.5°$.

Figure 9.- Continued.
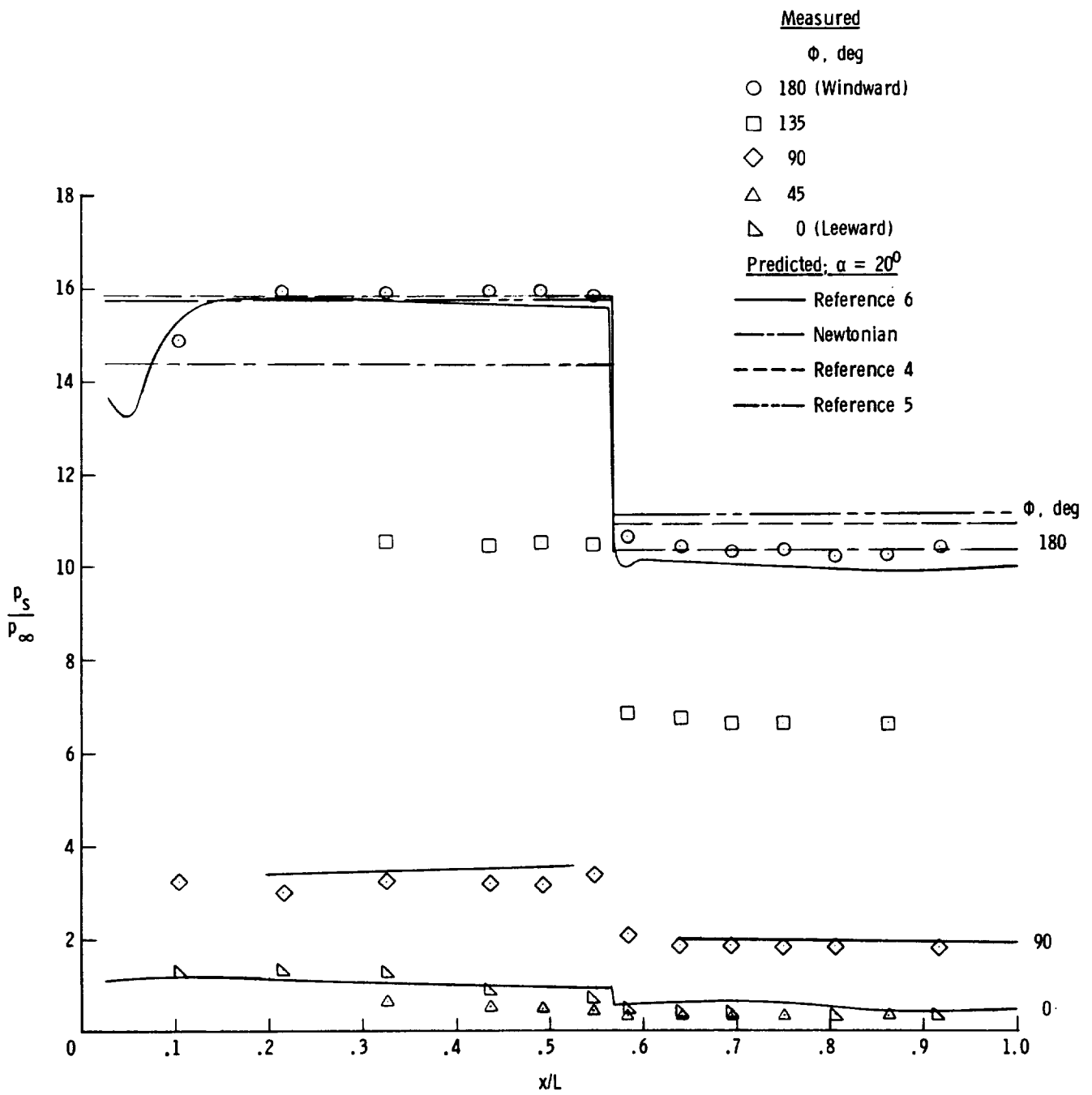
(e)  $\alpha_m = 20.7°$.

Figure 9.- Continued.
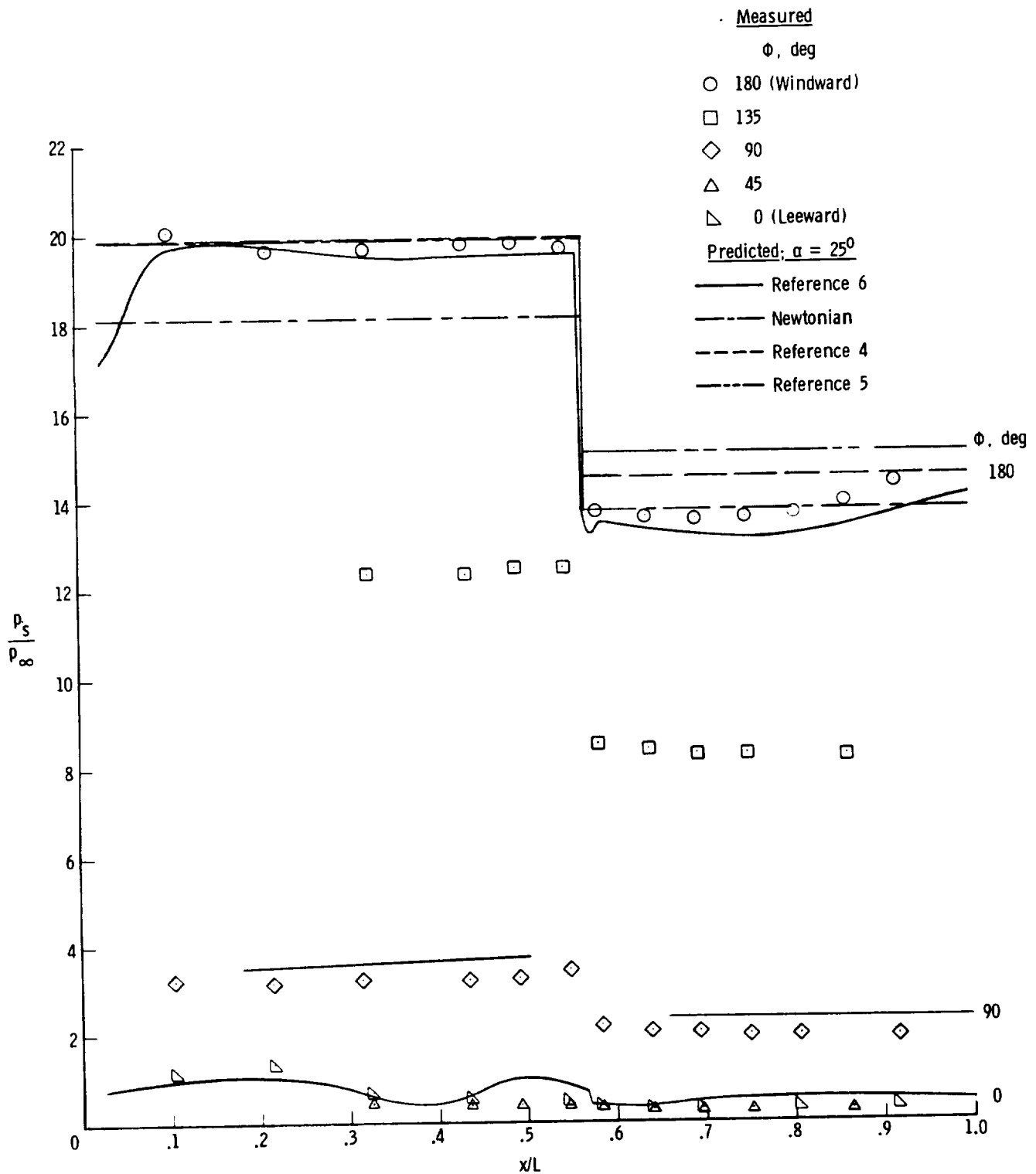
(f) $\alpha_m = 25.85°$.

Figure 9.- Concluded.
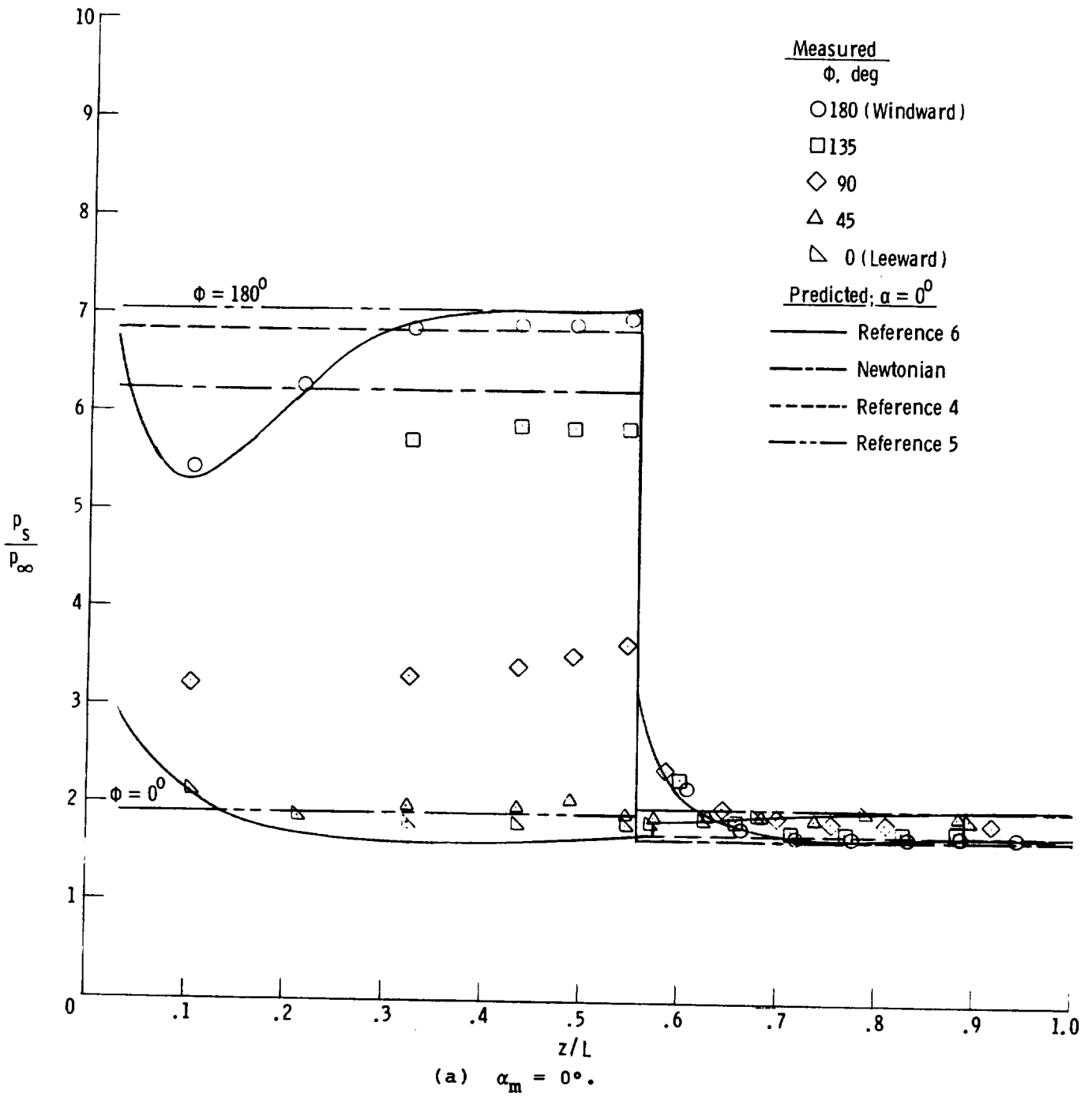
Figure 10.- Pressure distributions for bent-nose biconic at various nominal angles of attack. $M_\infty = 6.0$; $R_{\infty,L} = 5.3 \times 10^6$.
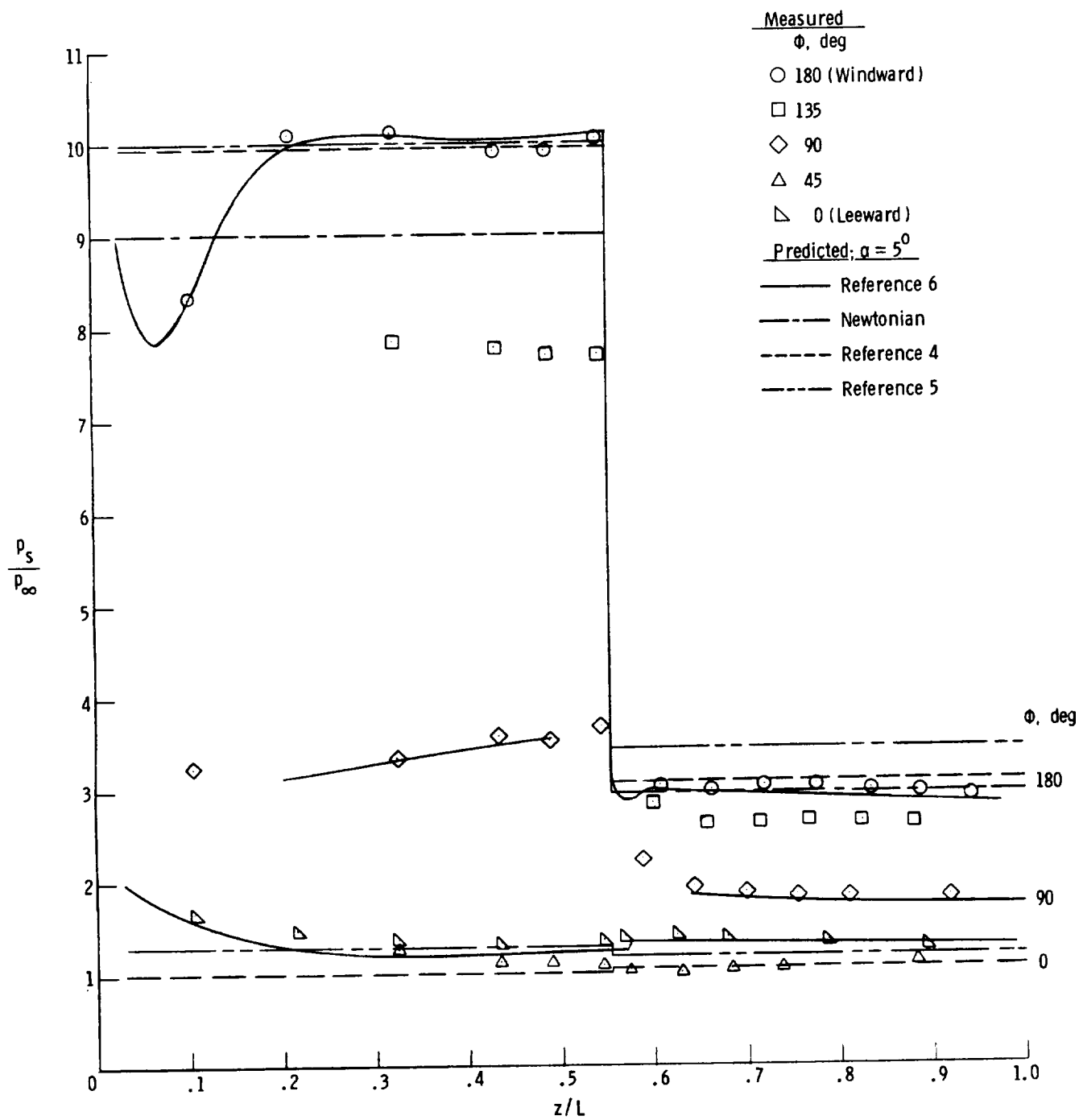
(b) $\alpha_m = 5°$.

Figure 10.- Continued.
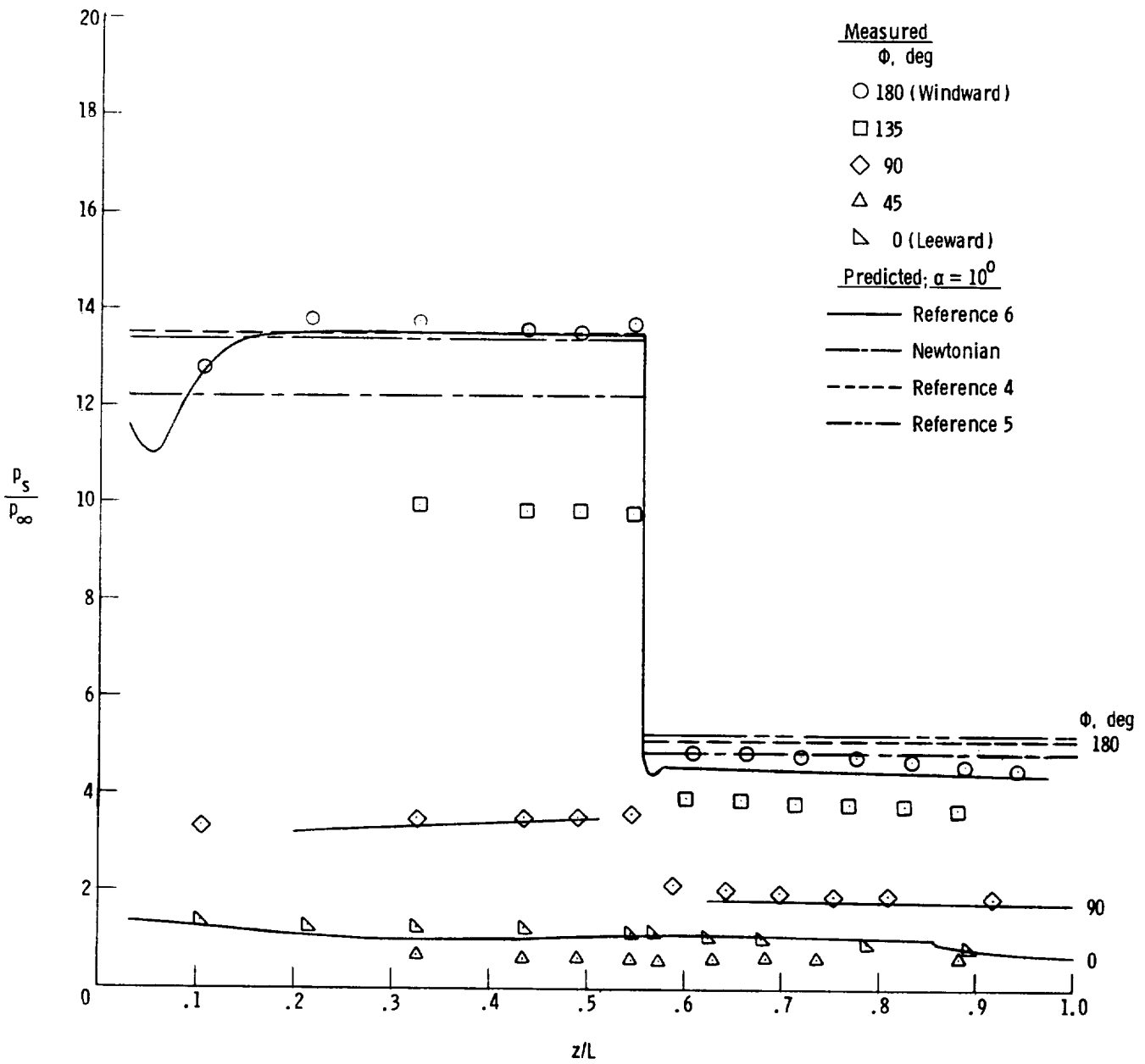
(c)  $\alpha_m = 10.6°$.

Figure 10.- Continued.
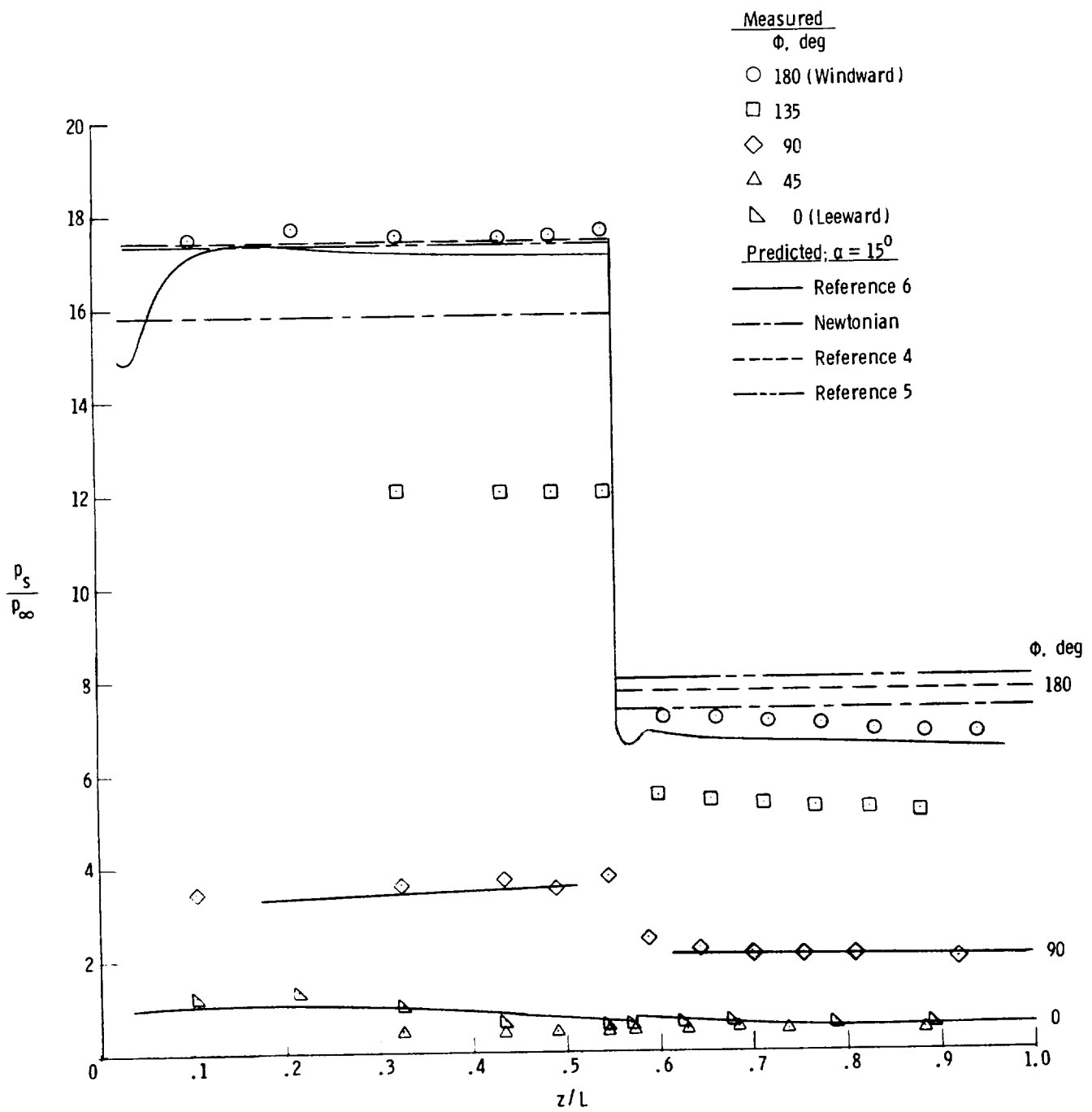
(d) $\alpha_m = 15.8°$.

Figure 10.- Continued.
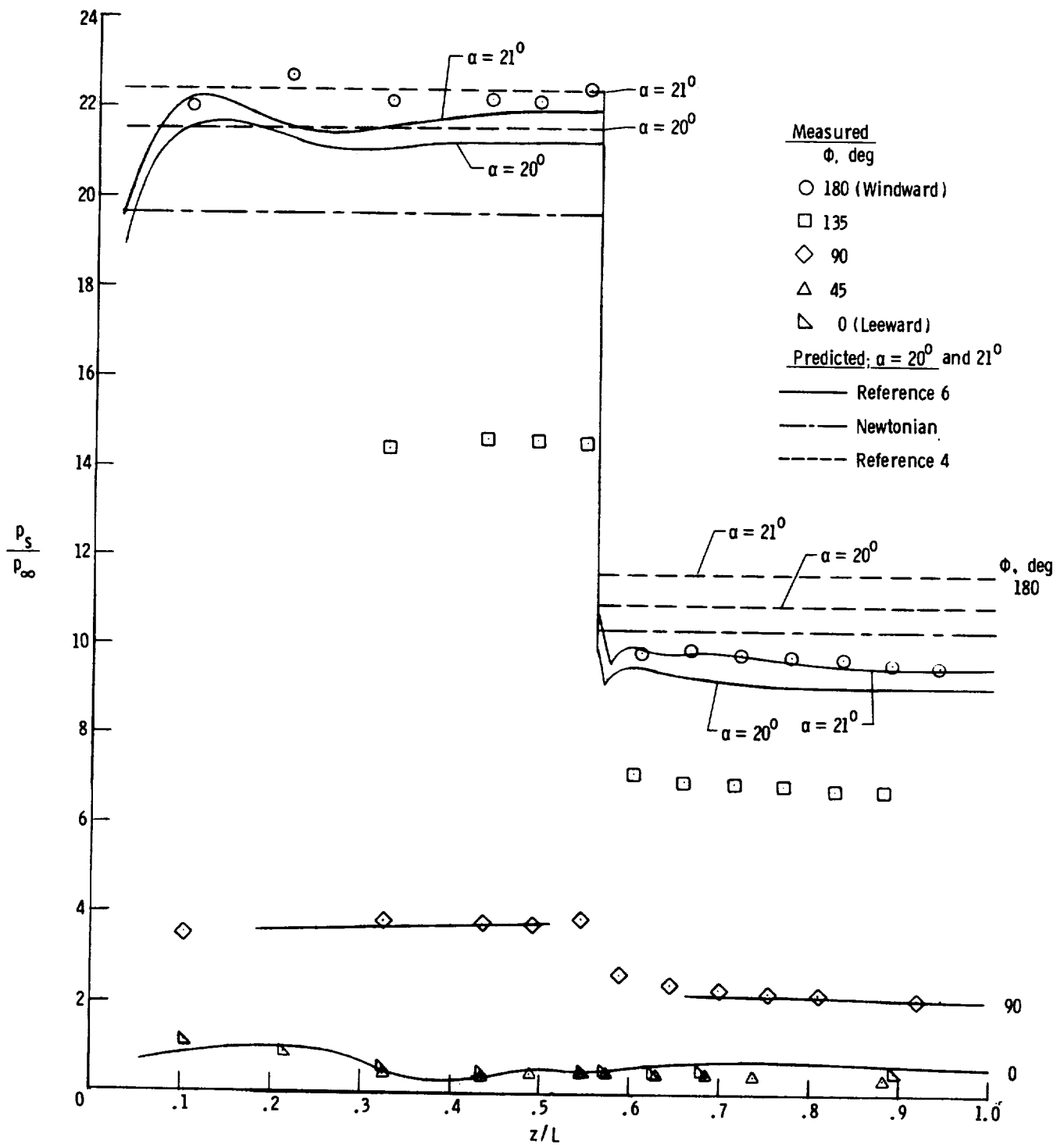
(e)  $\alpha_m = 21°$.

Figure 10.- Continued.
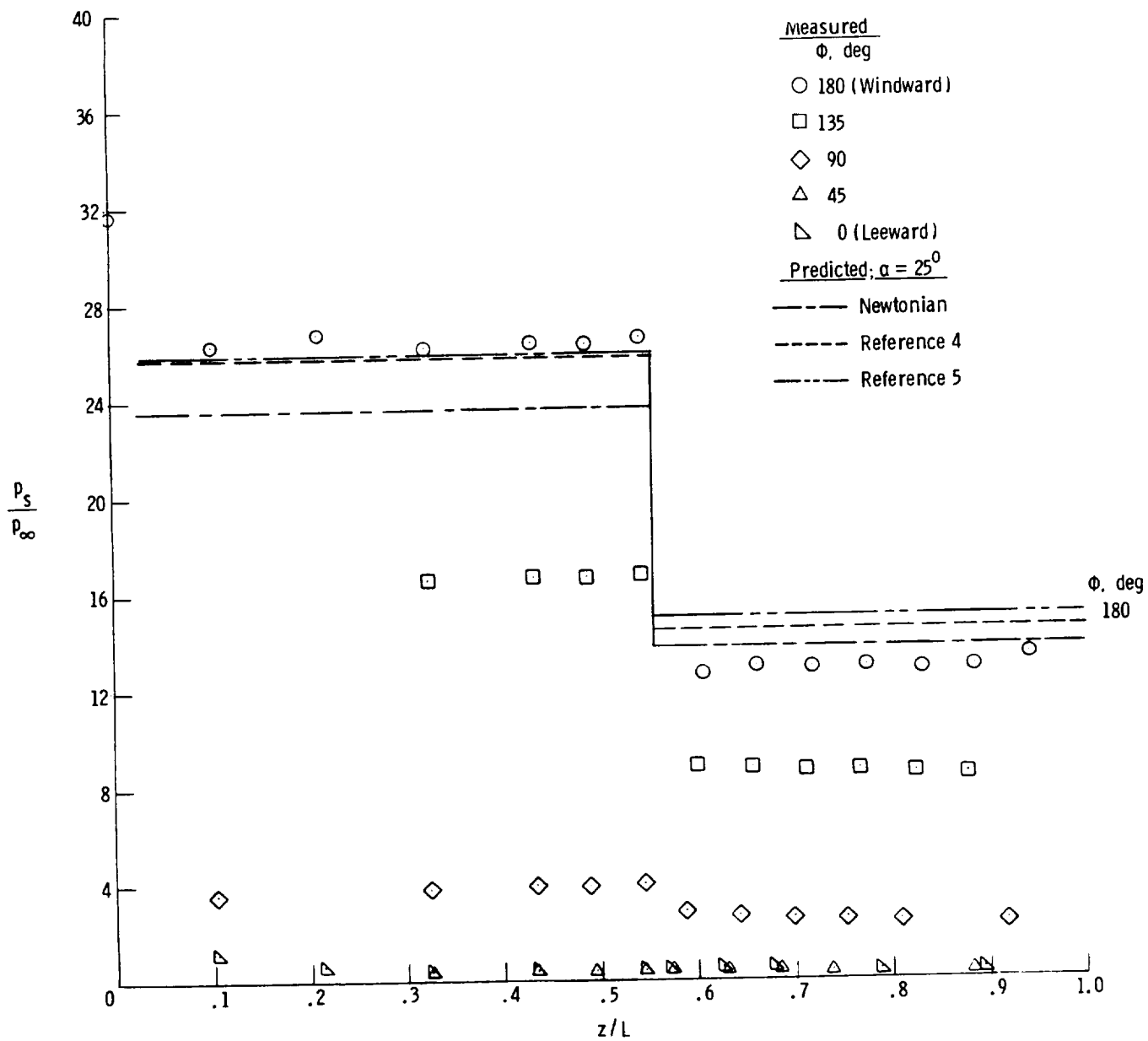
(f)  $\alpha_m = 26.25°$.

Figure 10.- Concluded.

Measured

$\Phi$, deg

○ 180 (Windward)

□ 135

◇ 90

△ 45

◁ 0 (Leeward)

Predicted; $\alpha = 0^0$

——————— Reference 6

— — — — Reference 4

—··—··— Reference 5

(a)  $\alpha_m = 0°$.
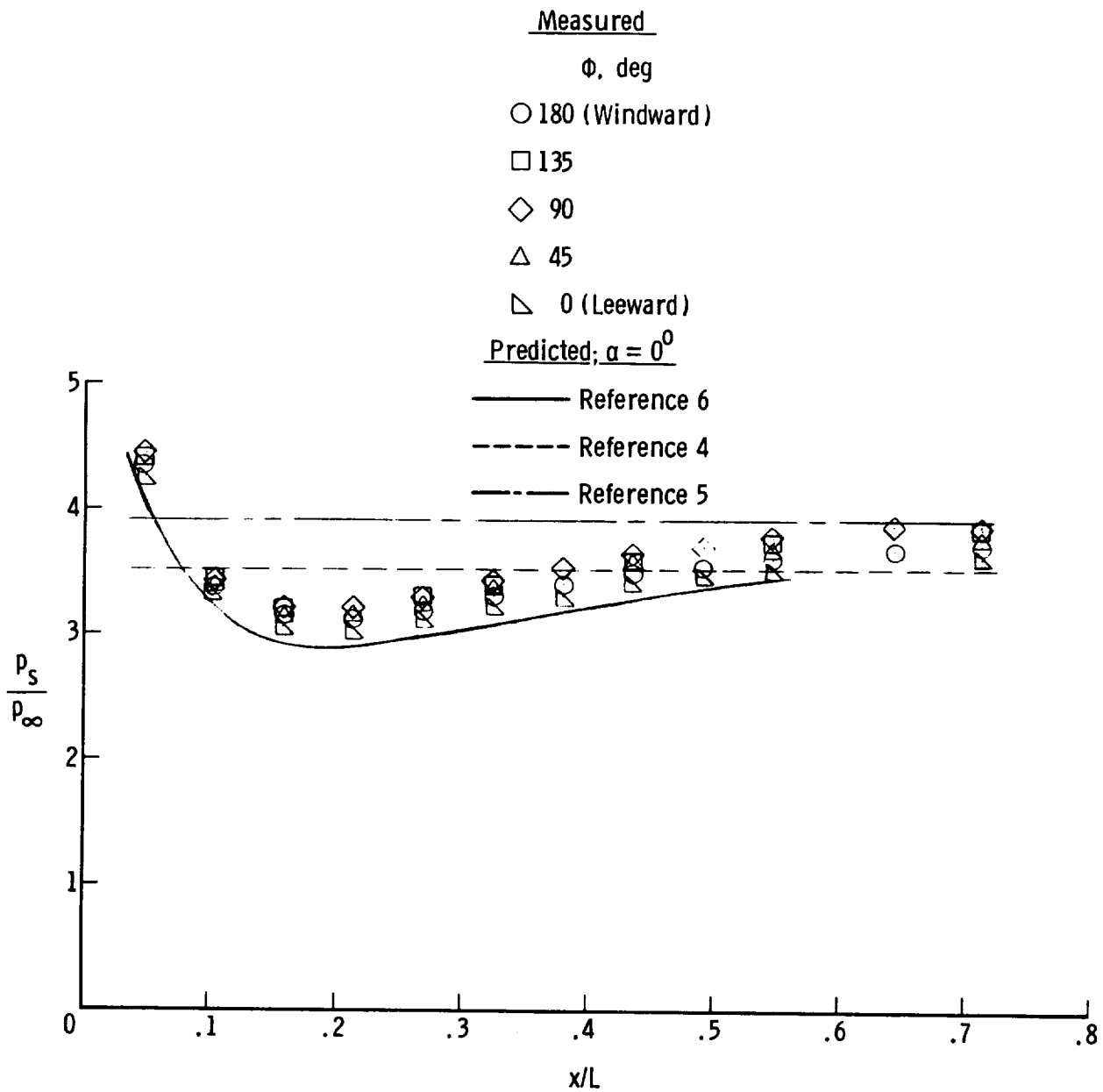
Figure 11.- Pressure distributions for sphere-cone at various nominal angles of attack.  $M_\infty = 6.0$;  $R_{\infty,L} = 4.2 \times 10^6$.  (L  used to nondimensionalize  x  is value for on-axis biconic.)
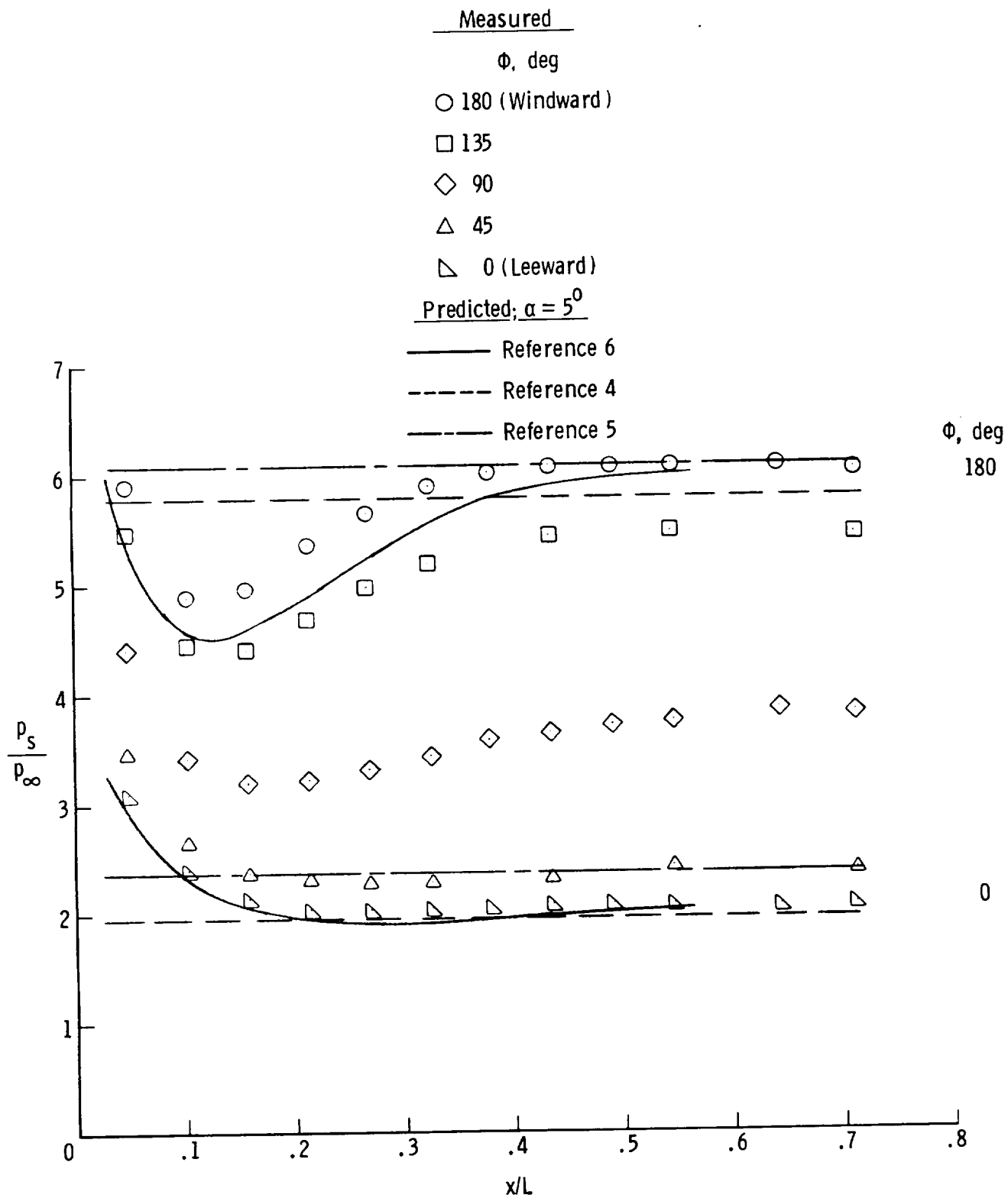
(b)  $\alpha_m = 5°$.

Figure 11.- Continued.
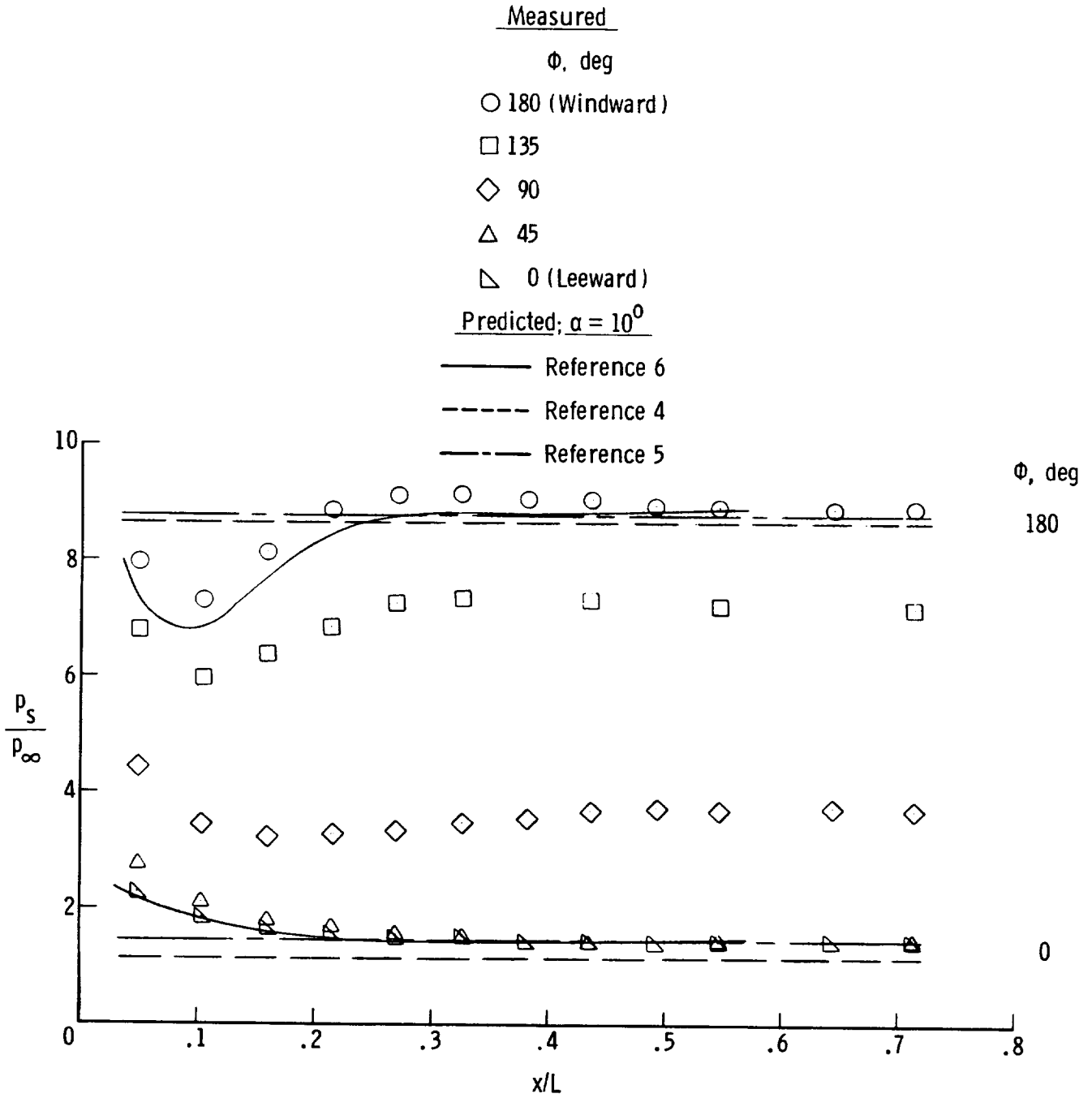
(c)  $\alpha_m = 10.55°$.

Figure 11.- Continued.

(d) $\alpha_m = 15.8°$.

Figure 11.- Continued.

Measured

Φ, deg

○ 180 (Windward)

□ 135

◇ 90

△ 45

◁ 0 (Leeward)

Predicted; $\alpha = 20^0$

——— Reference 6

— — — Reference 4

—·—·— Reference 5
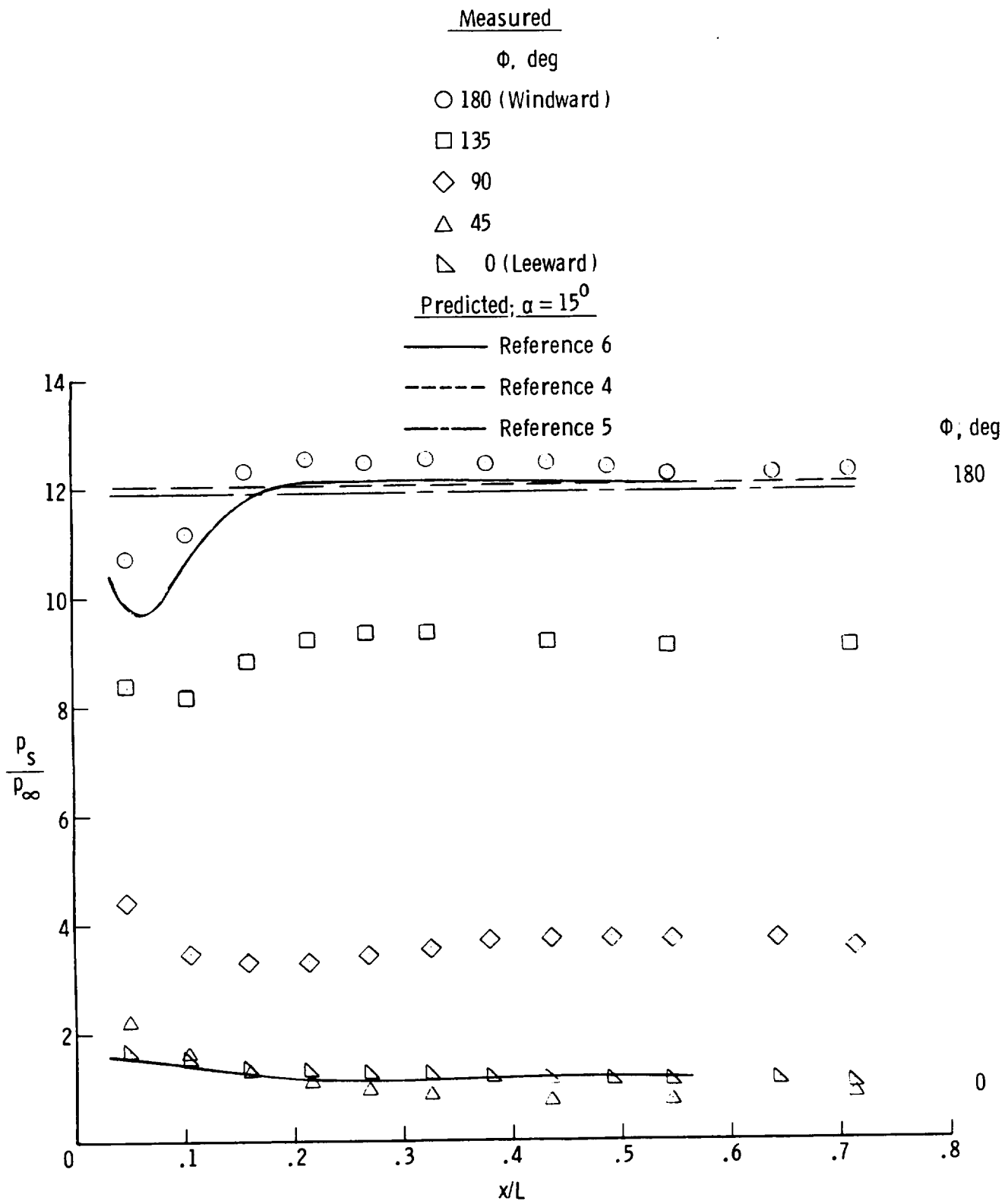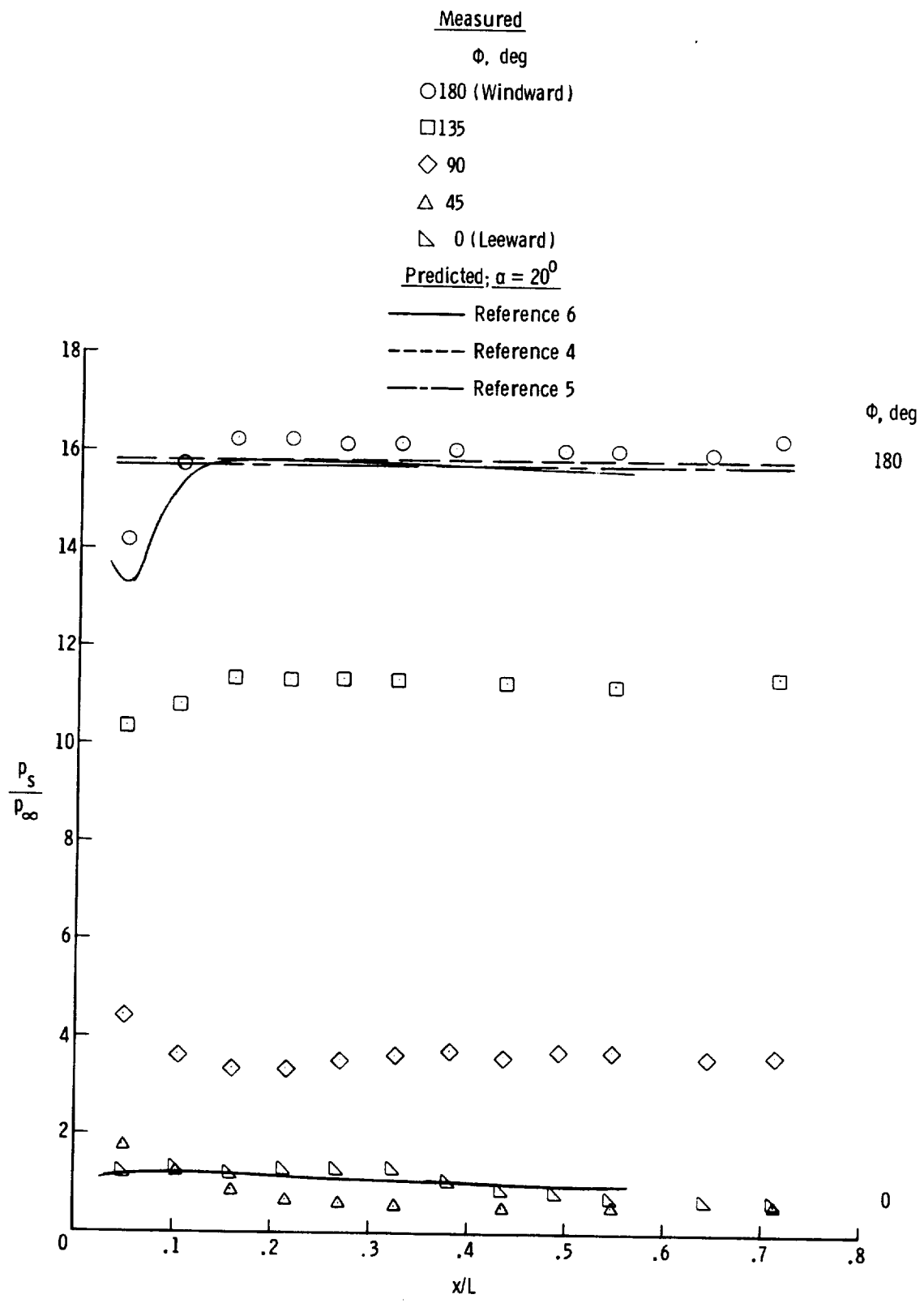
(e)  $\alpha_m = 21°$.

Figure 11.- Continued.
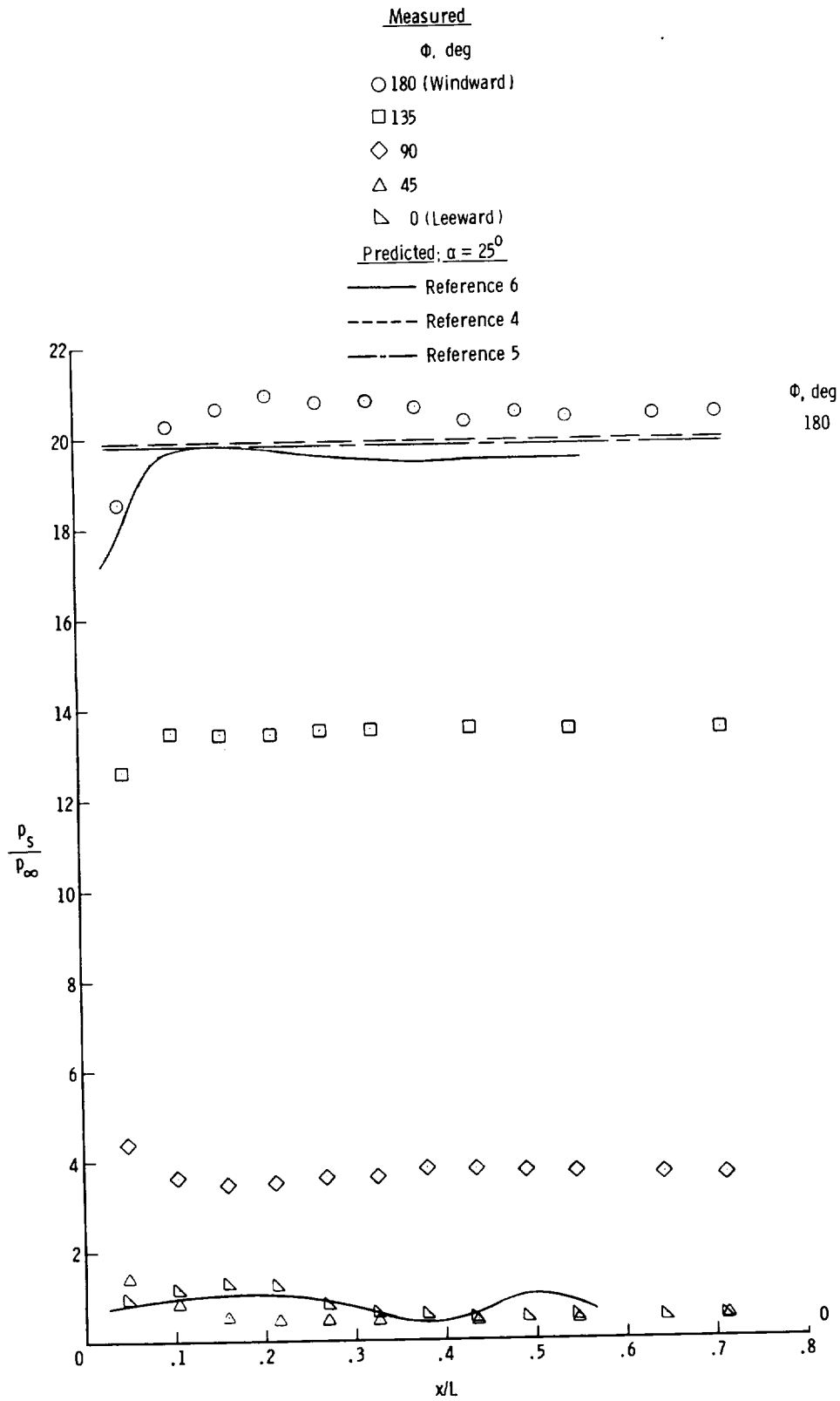
(f)  $\alpha_m = 26°$.

Figure 11.- Continued.

Φ, deg

180

$\dfrac{p_s}{p_\infty}$

x/L
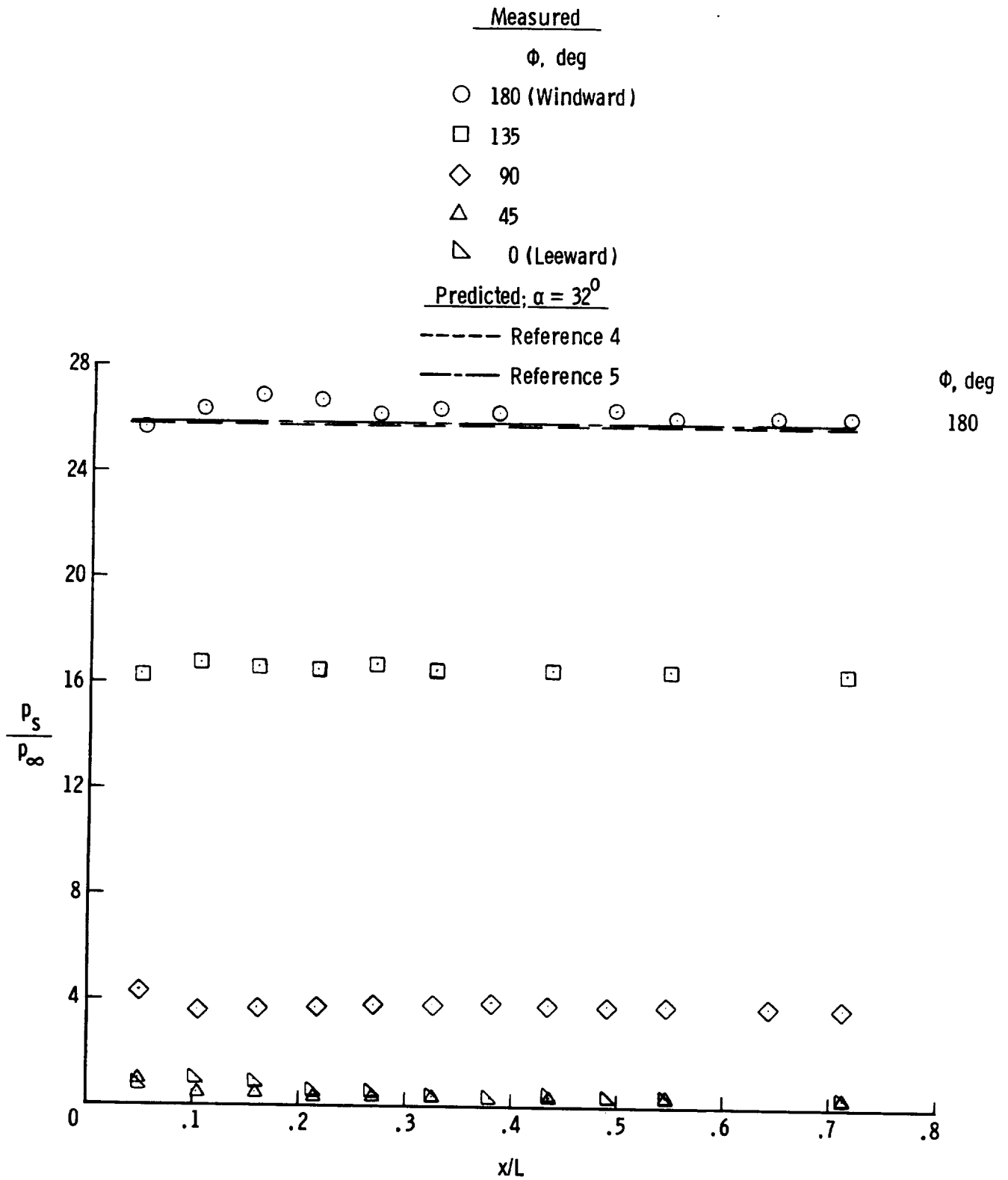
(g)  $\alpha_m$ = 33°.

Figure 11.- Concluded.
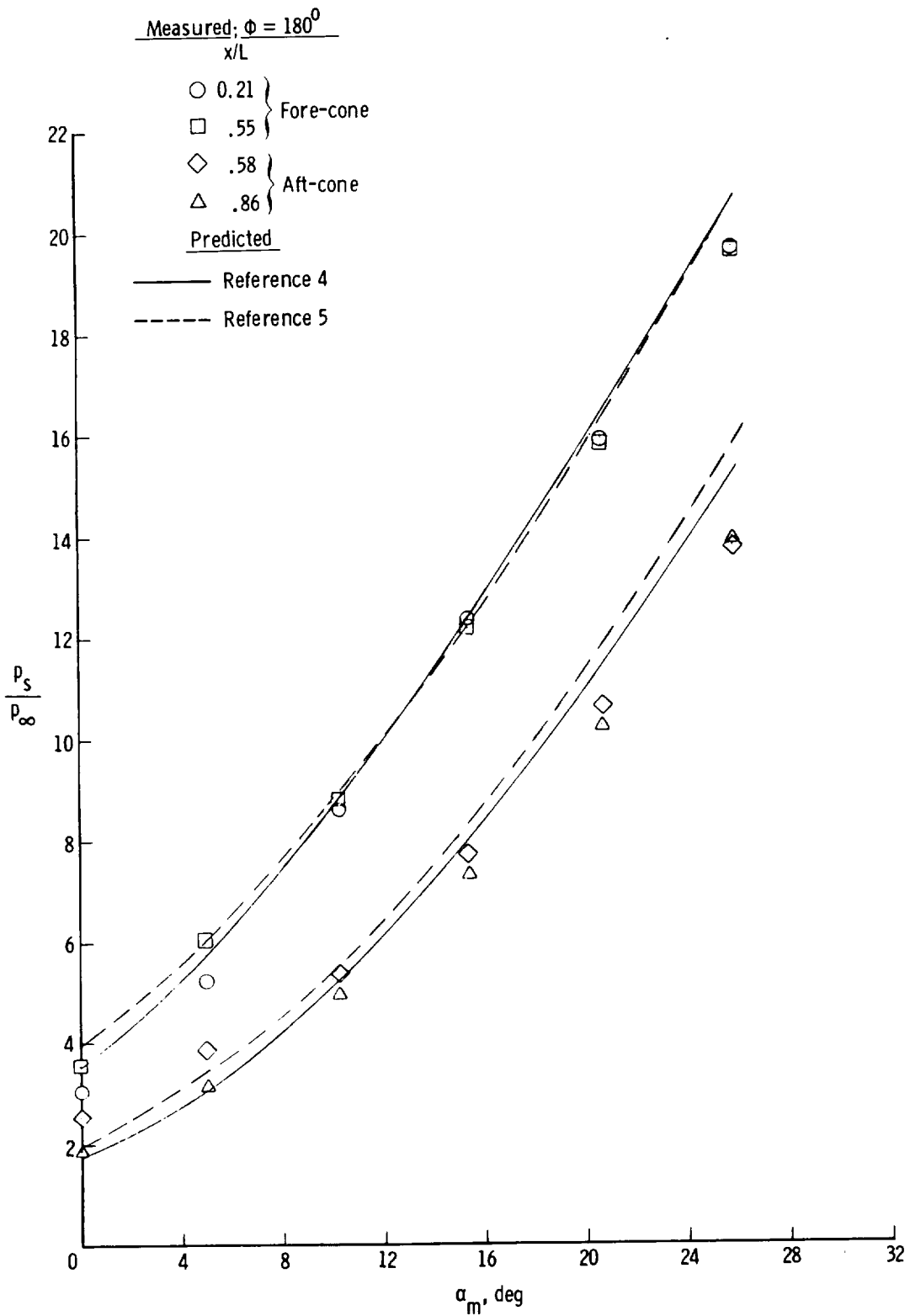
(a) On-axis biconic.

Figure 12.- Windward-ray pressure variation with angle of attack for on-axis and bent-nose biconic models. $M_\infty = 6.0$; $R_{\infty,L} = 5.3 \times 10^6$.
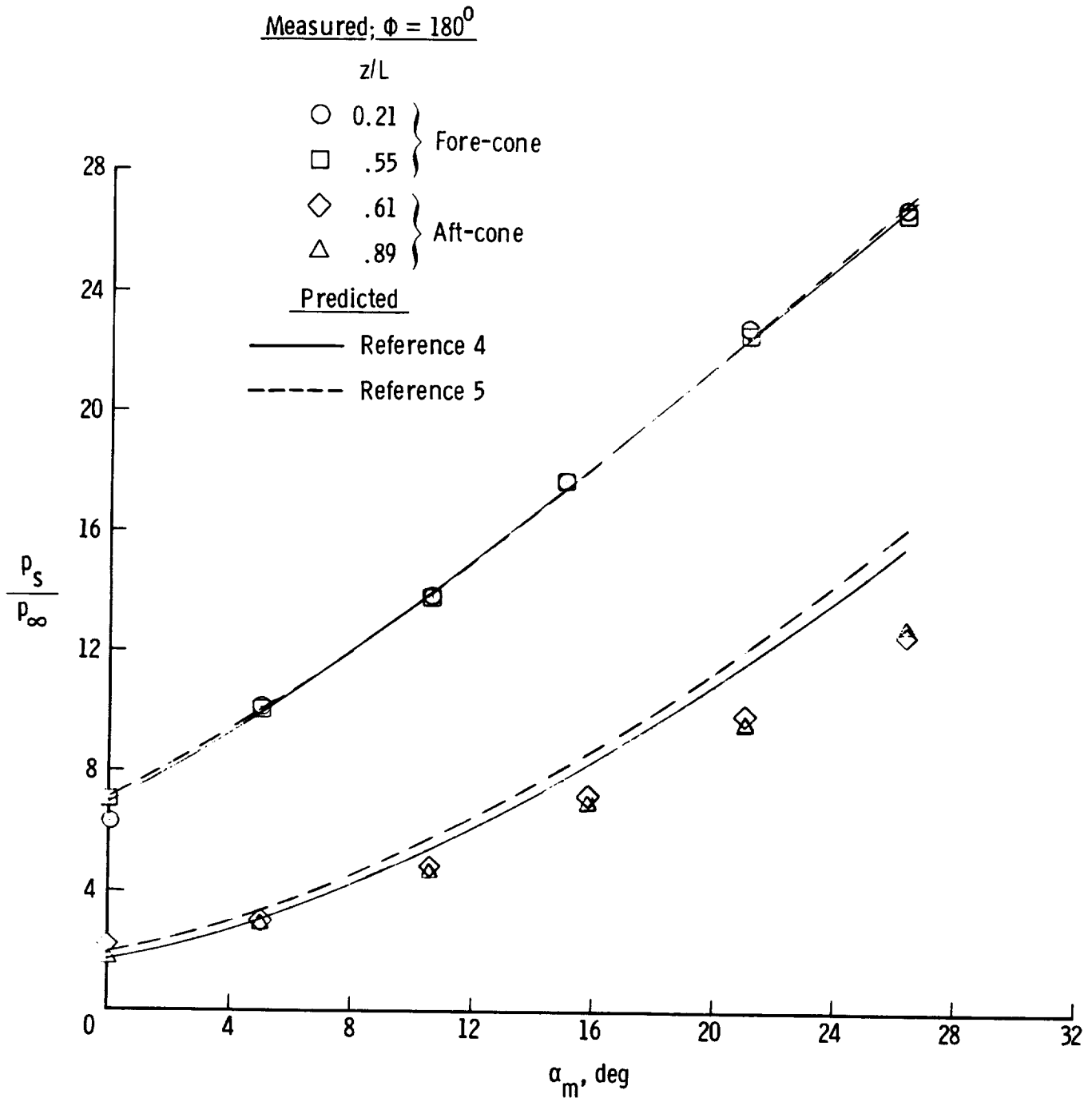
(b) Bent-nose biconic.

Figure 12.- Concluded.

Measured

$\Phi$, deg

○  180 (Windward)

□  135

◇  90

△  45

◁  0 (Leeward)

Open symbols - $R_{\infty, L} = 0.7 \times 10^6$; $M_\infty = 5.85$

Closed symbols - $R_{\infty, L} = 5.3 \times 10^6$; $M_\infty = 6.00$

Predicted (Reference 4); $\Phi = 180^0$

$M_\infty$

———  6.00

— — —  5.85
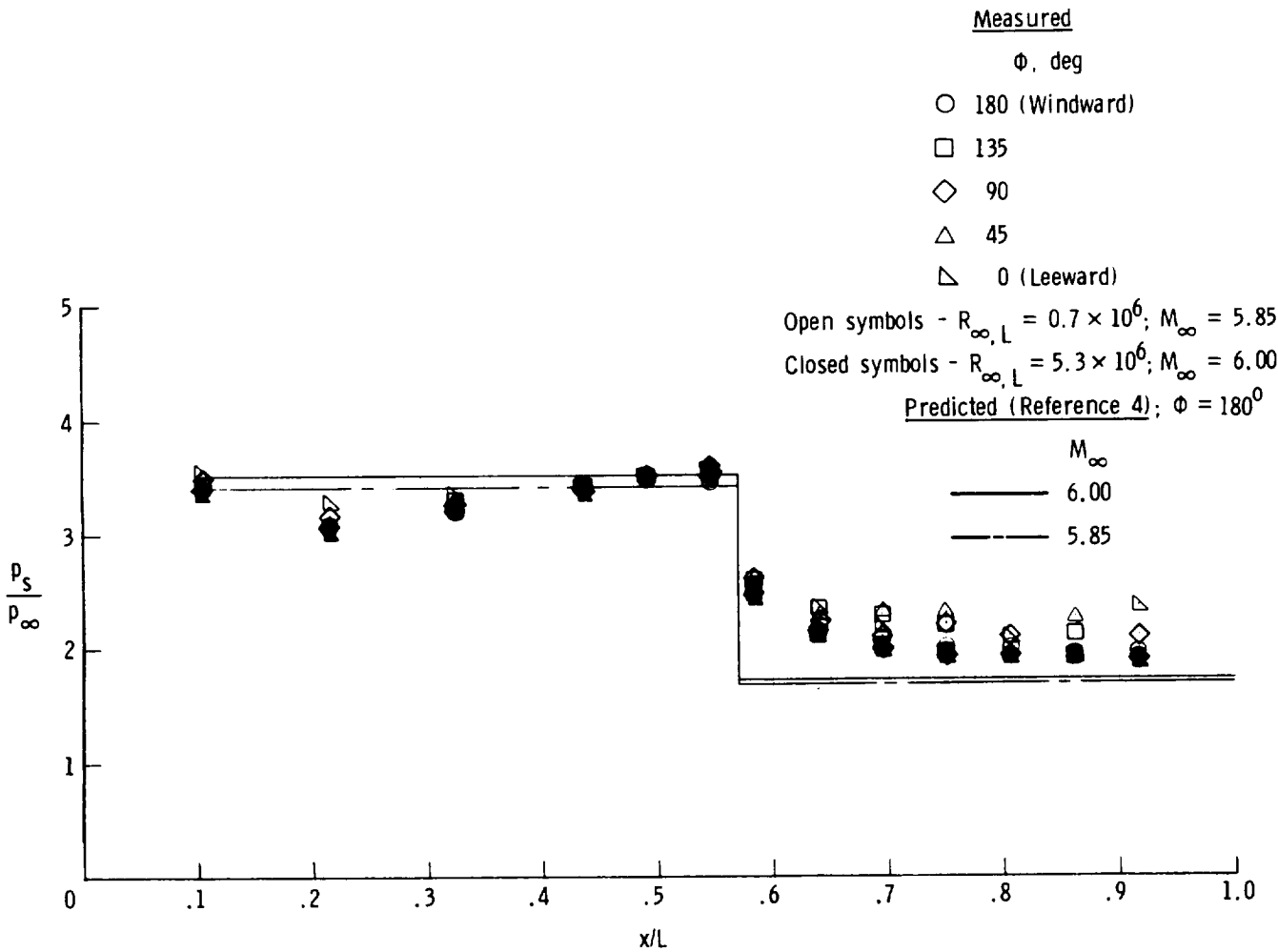
(a)  $\alpha = 0^\circ$.

Figure 13.- Effect of Reynolds number on pressure distributions for on-axis biconic at various nominal angles of attack.

(b)  $\alpha = 5°$.
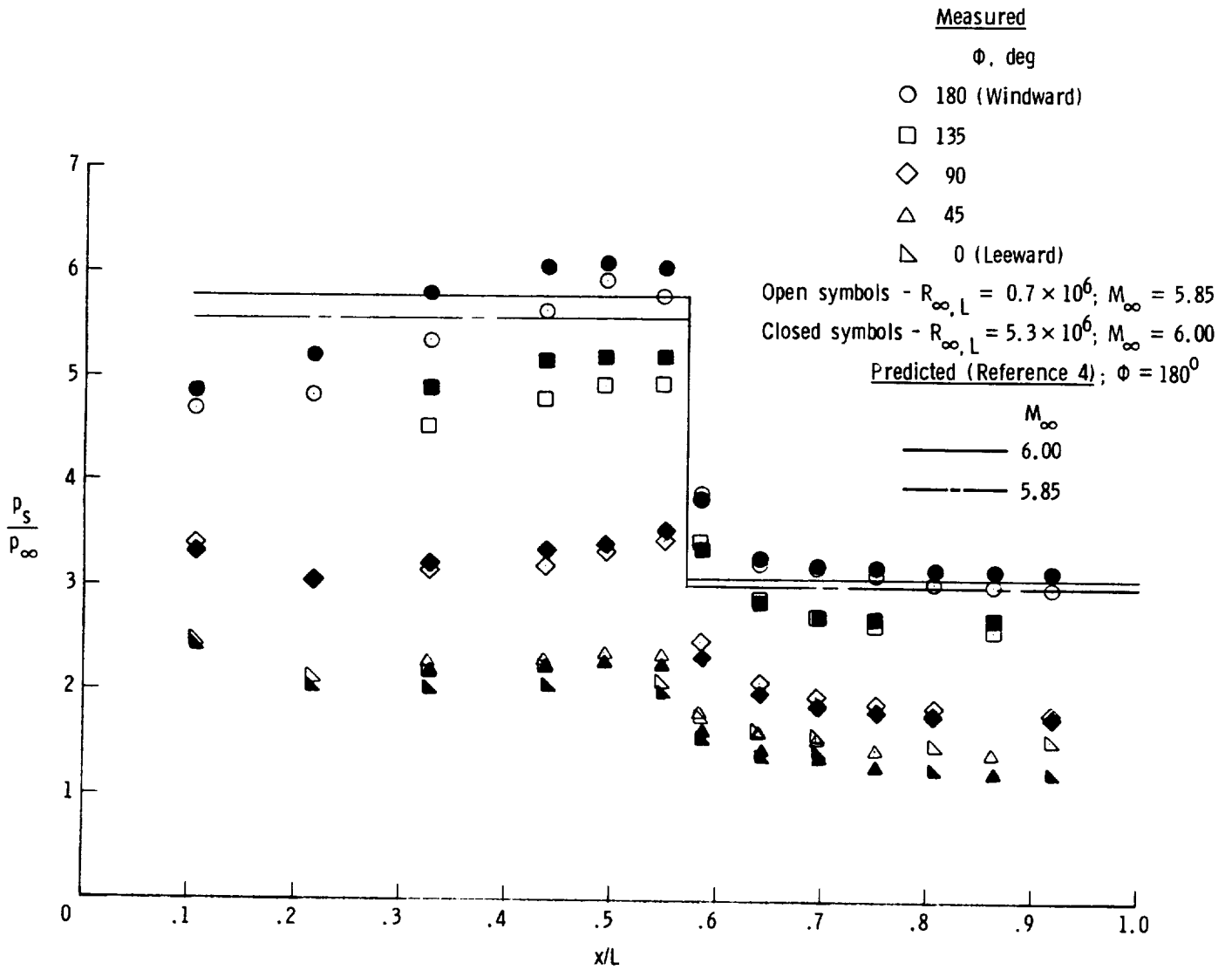
Figure 13.- Continued.
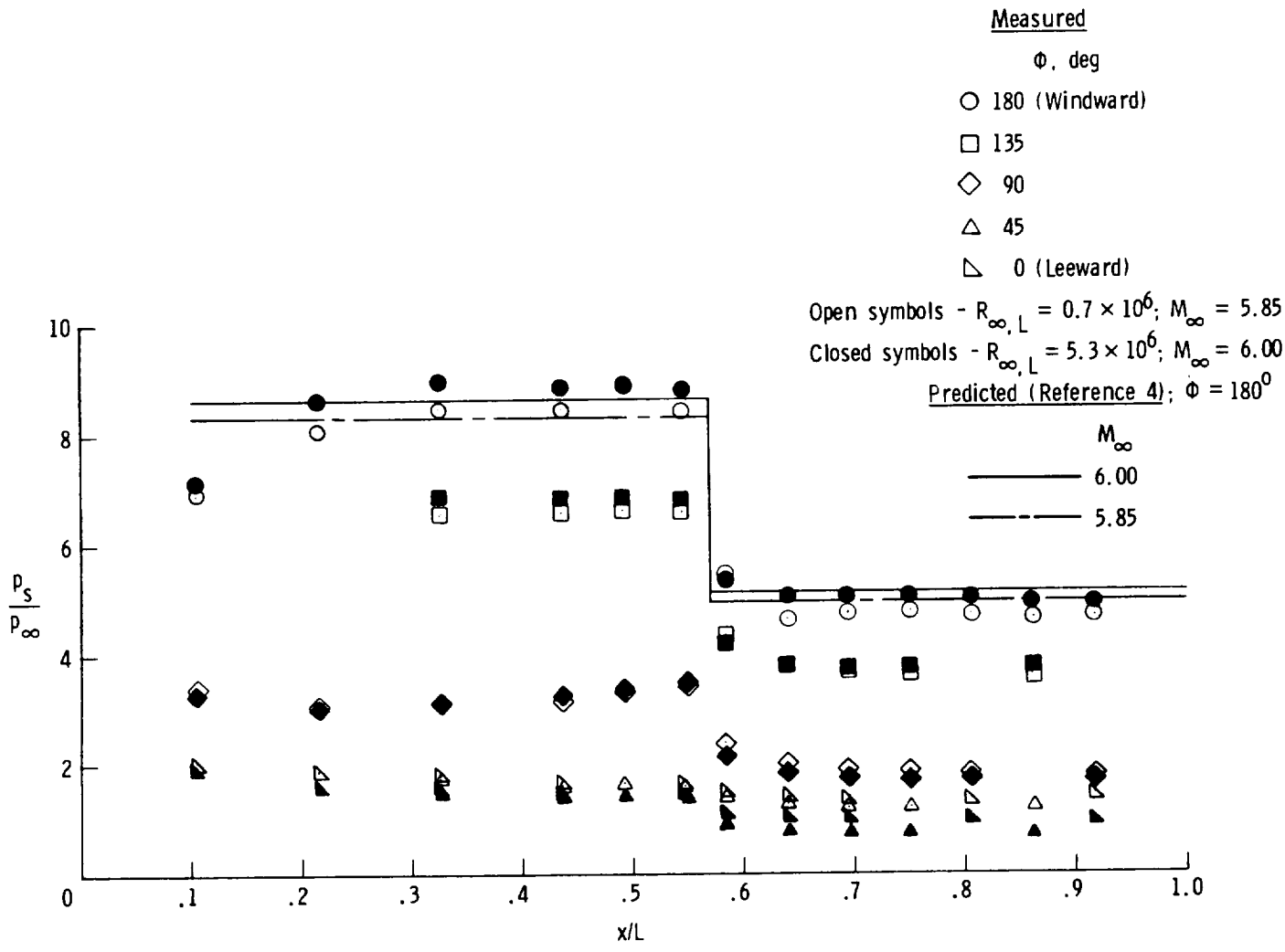
(c)  α = 10°.

Figure 13.- Continued.
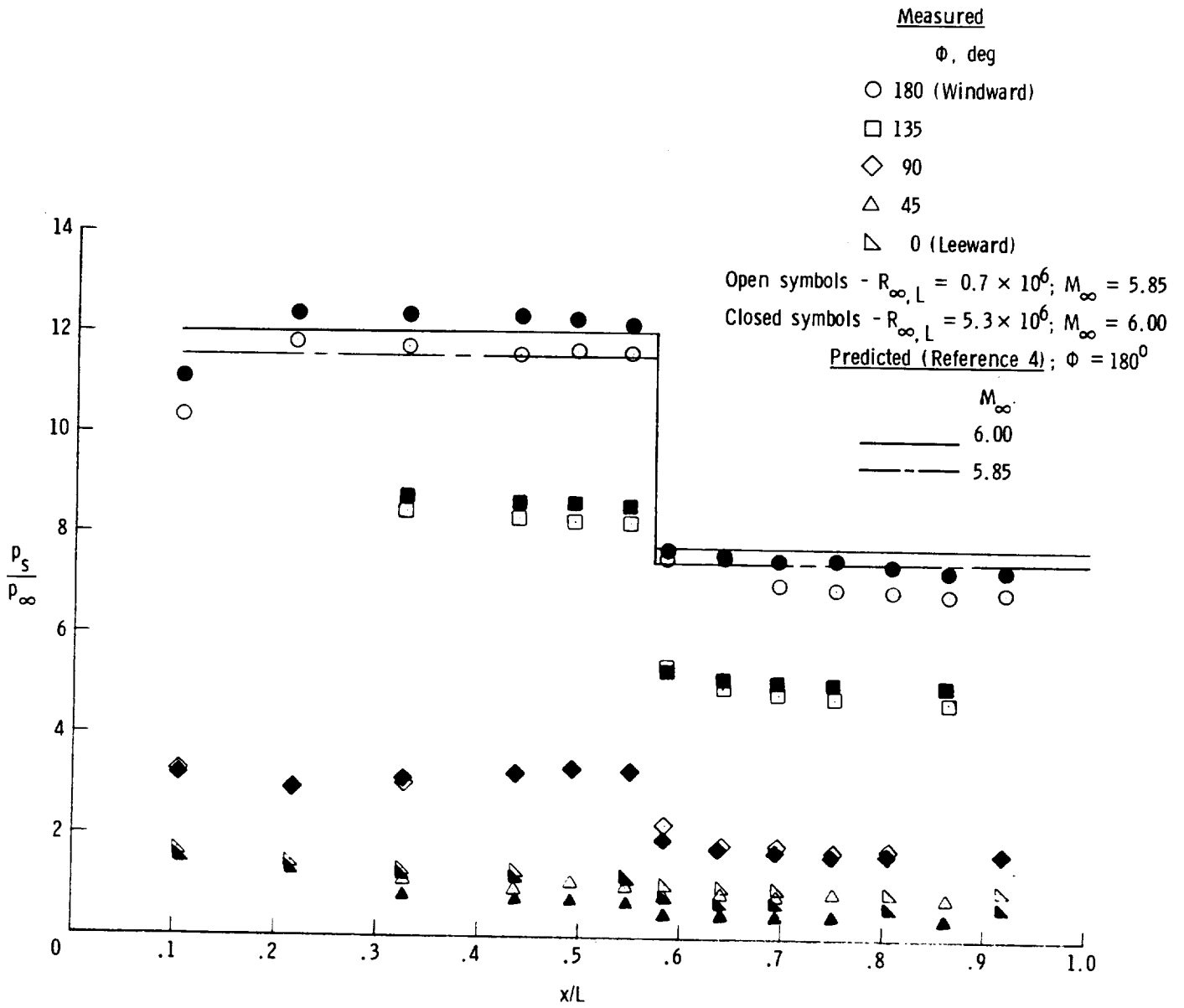
(d)  α = 15°.

Figure 13.- Continued.

(e)   $\alpha = 20°$.
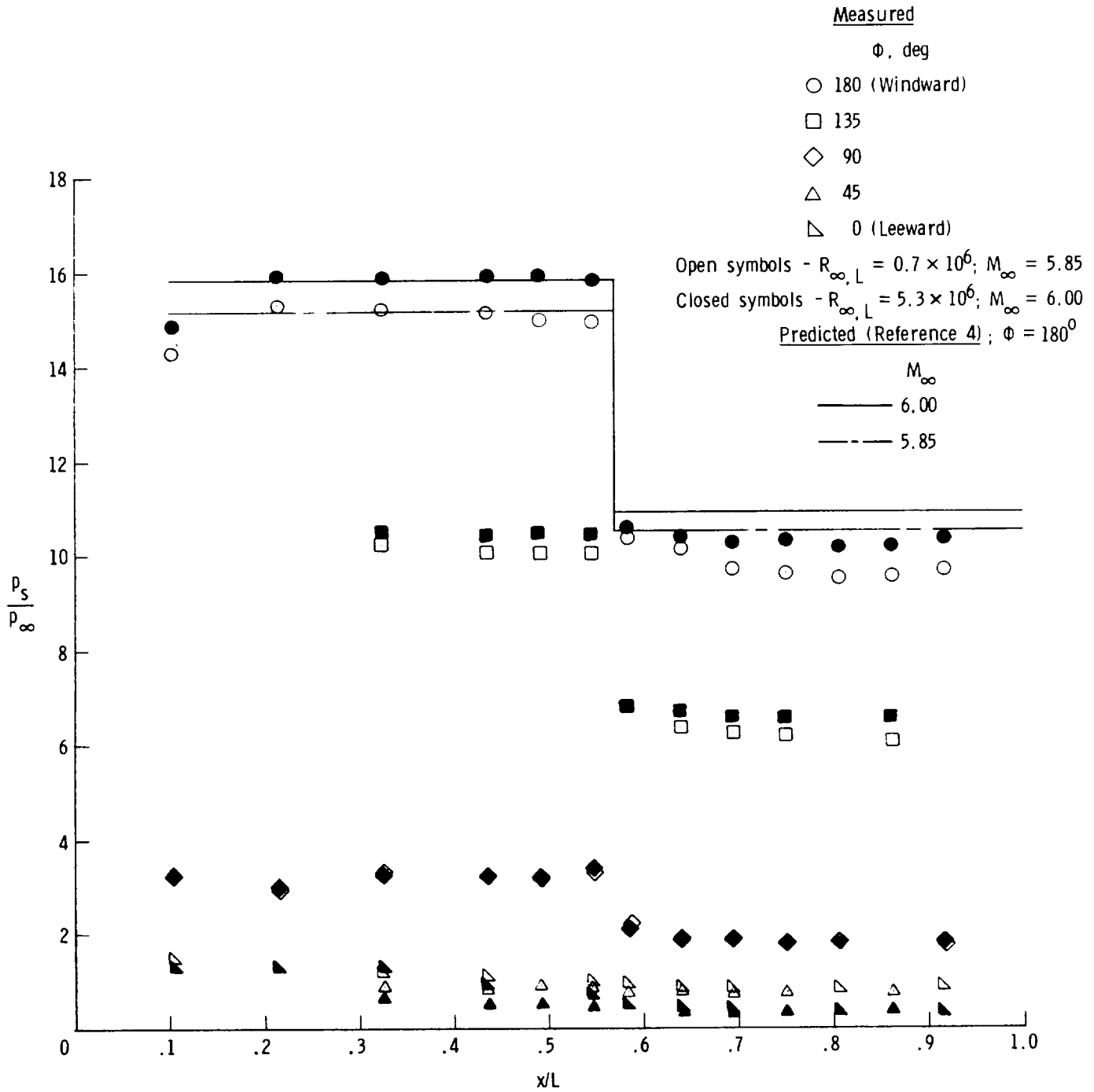
Figure 13.- Continued.
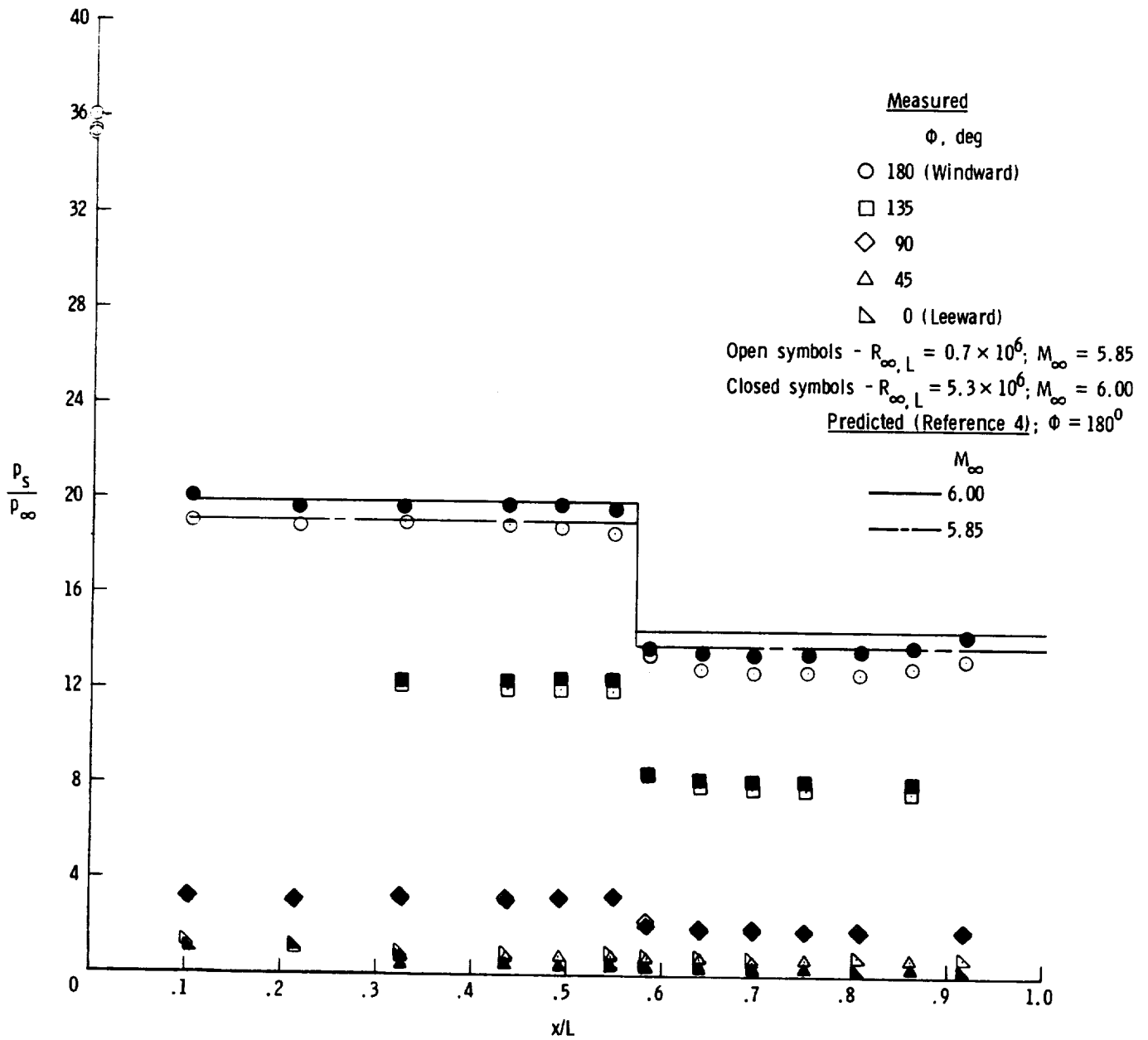
(f)   $\alpha = 25°$.

Figure 13.- Concluded.
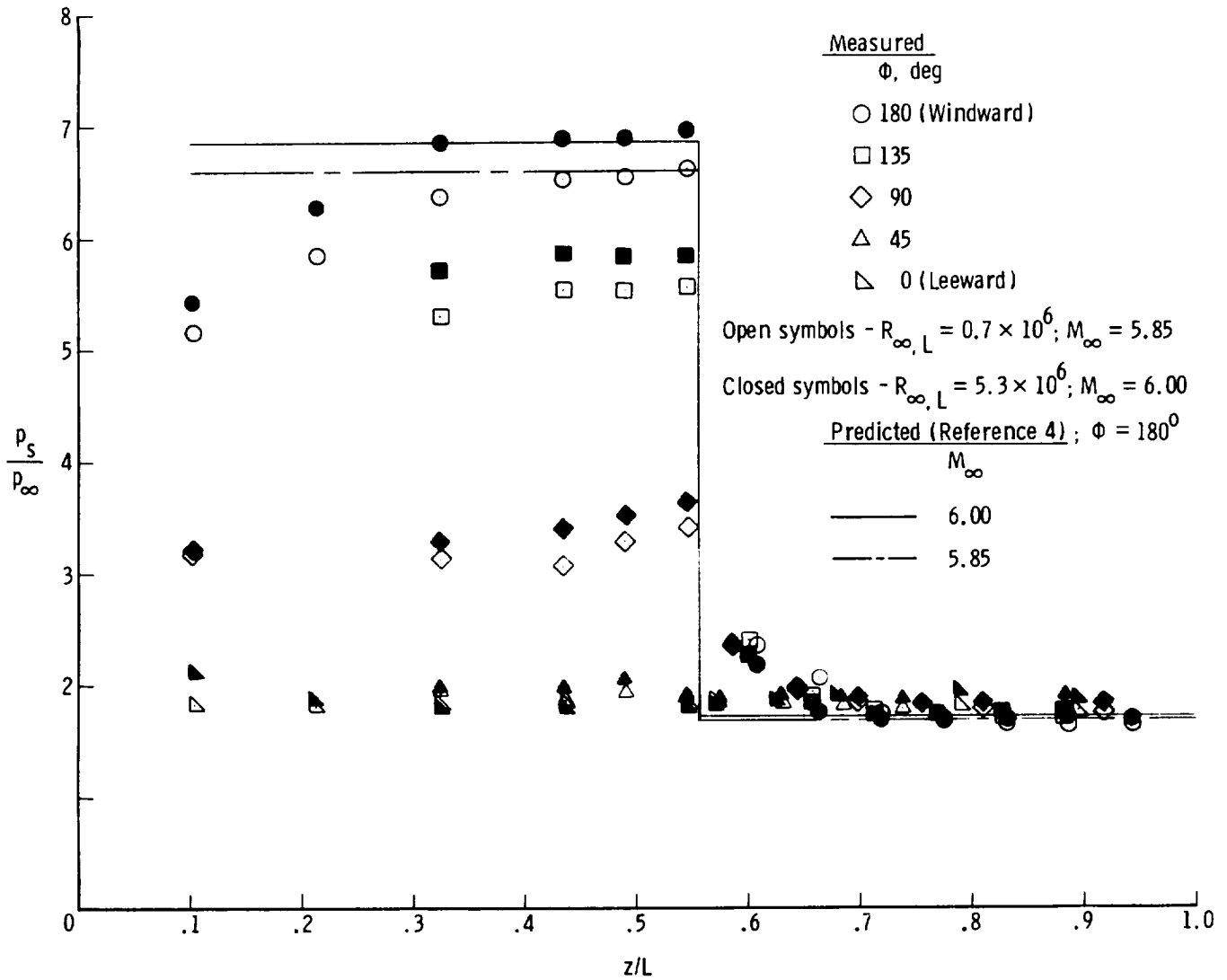
Figure 14.- Effect of Reynolds number on pressure distributions for bent-nose biconic at various nominal angles of attack.

(b)  α = 5°.
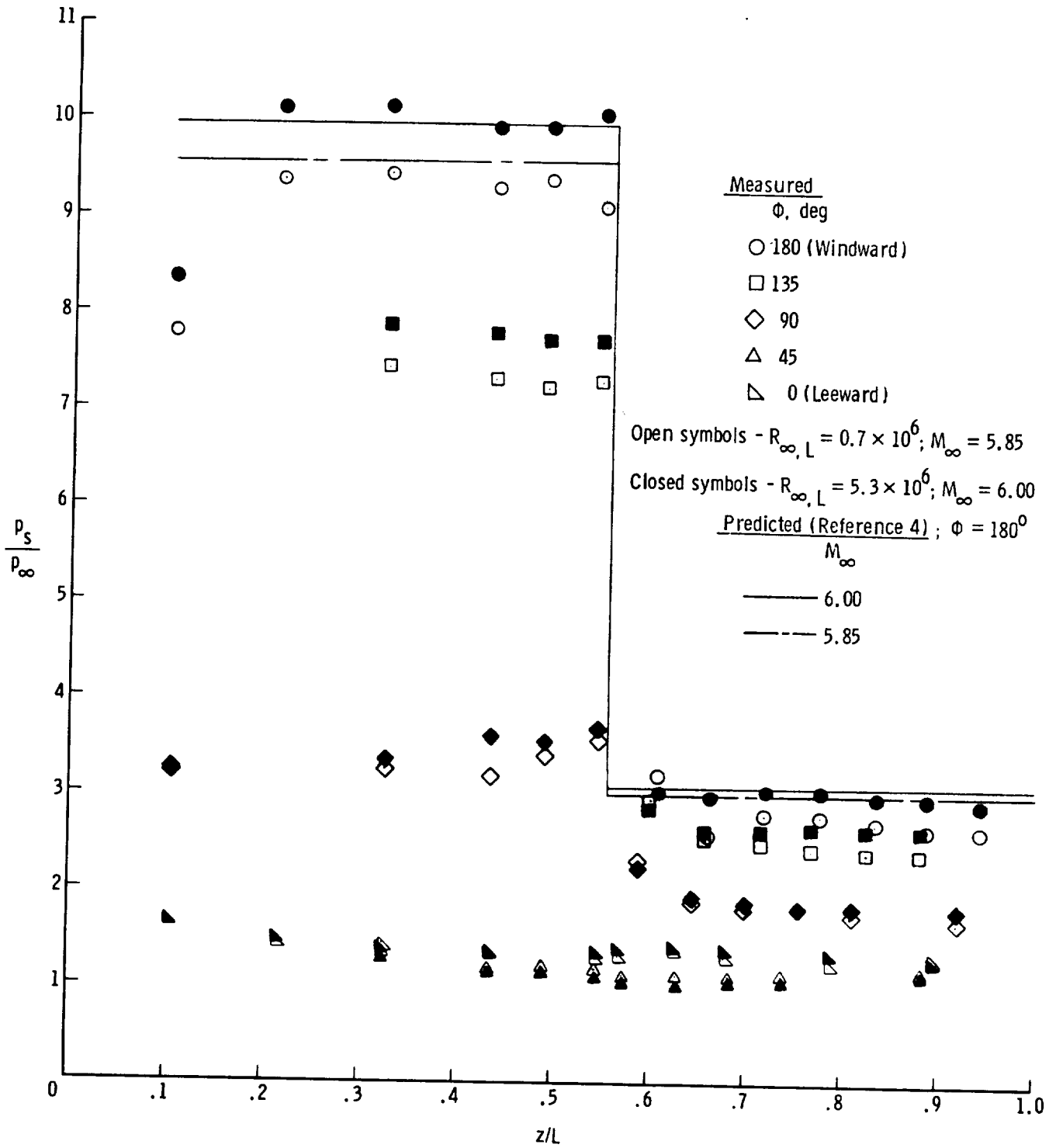
Figure 14.- Continued.
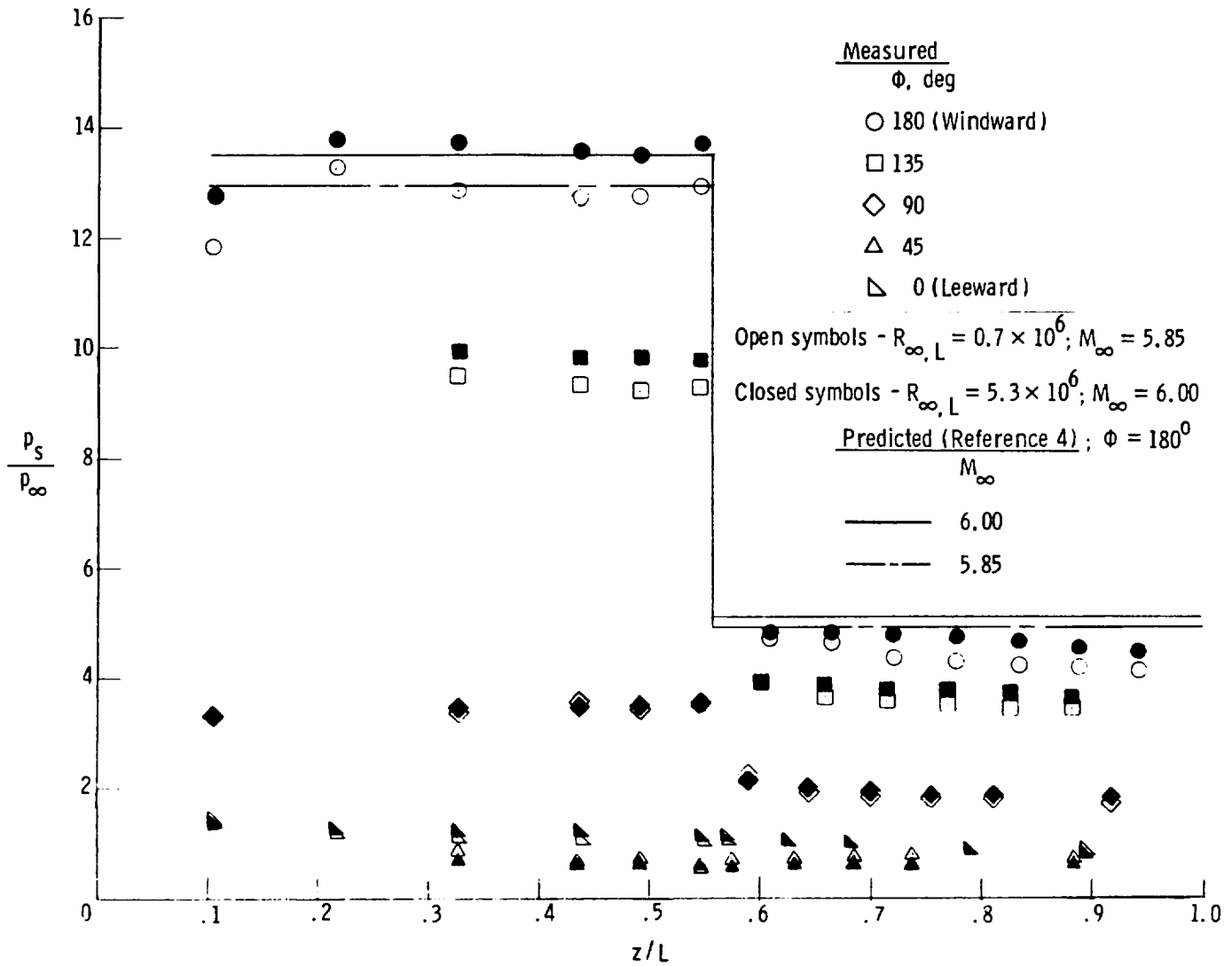
(c)  $\alpha = 10°$.

Figure 14.- Continued.
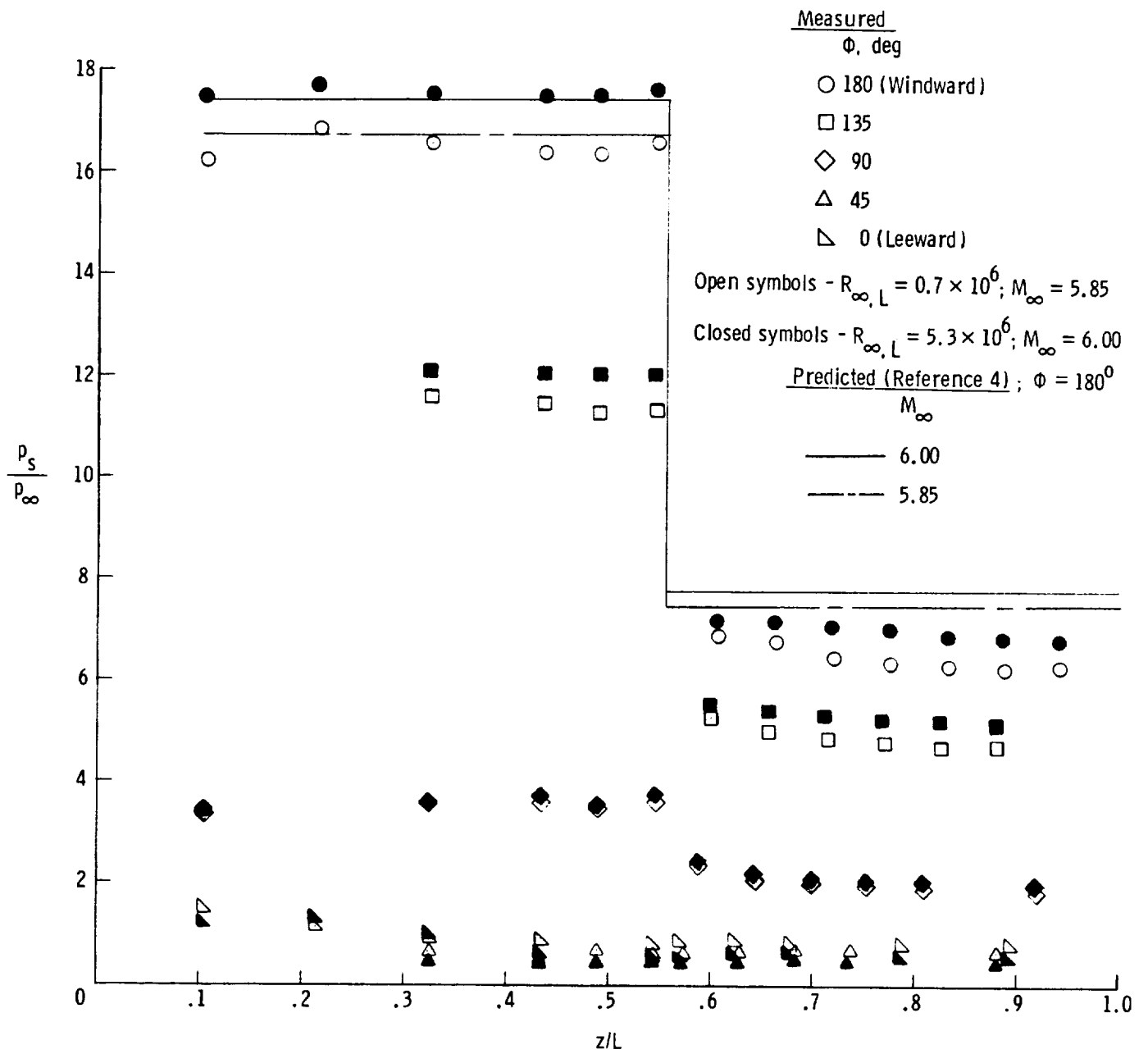
(d)  $\alpha = 15°$.

Figure 14.- Continued.
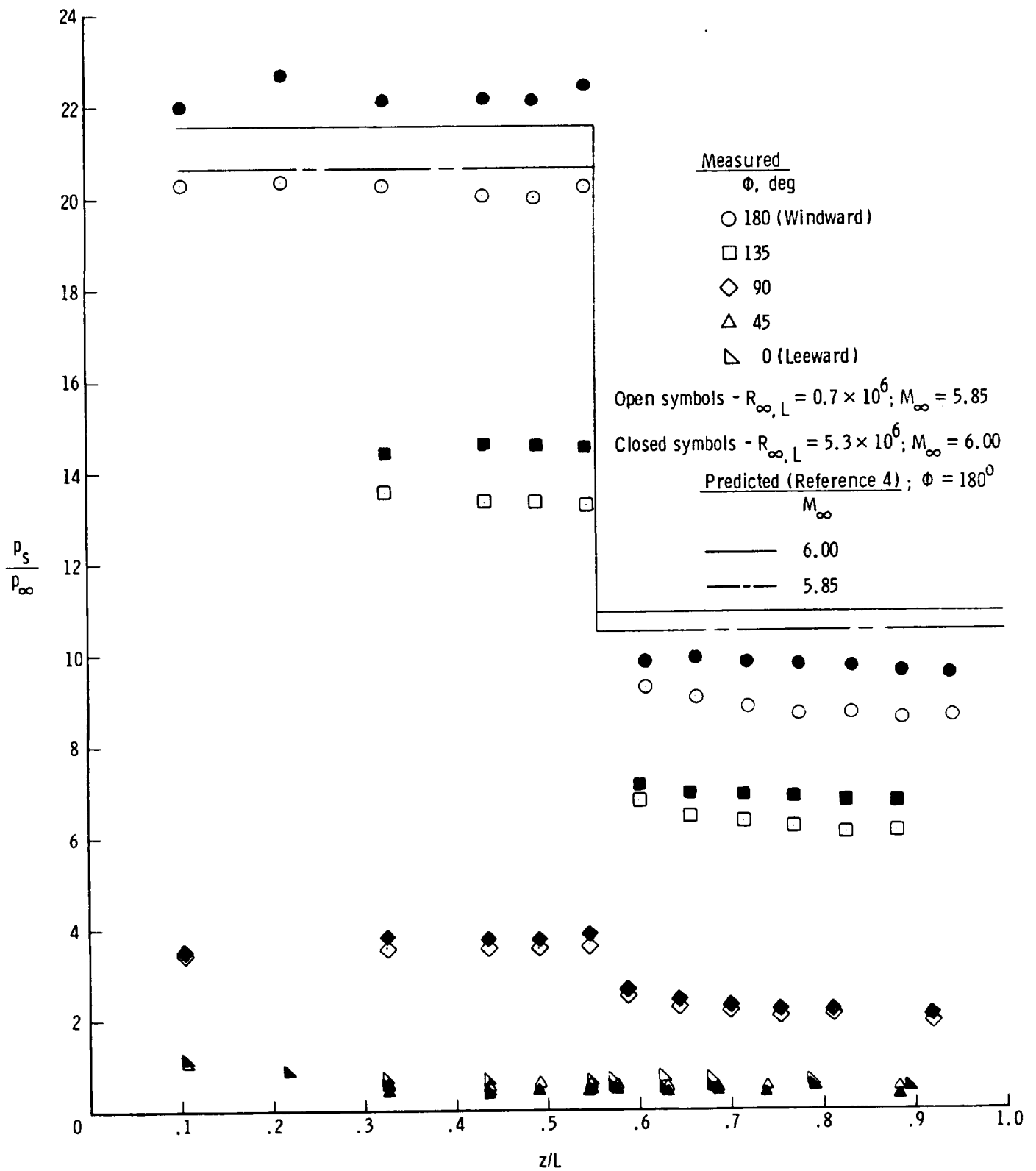
(e) $\alpha = 20°$.

Figure 14.- Continued.

(f)  $\alpha = 25°$.
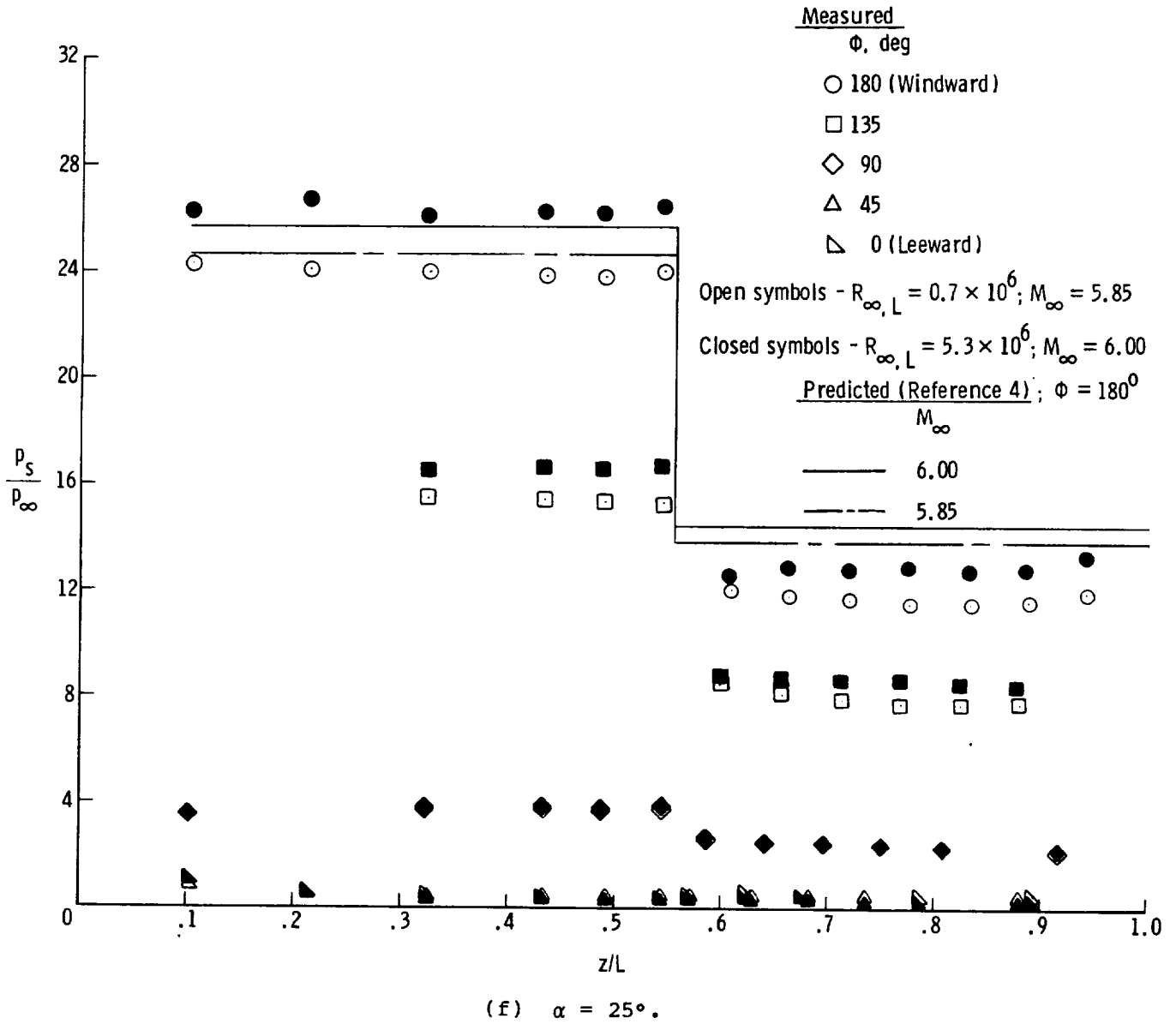
Figure 14.- Concluded.
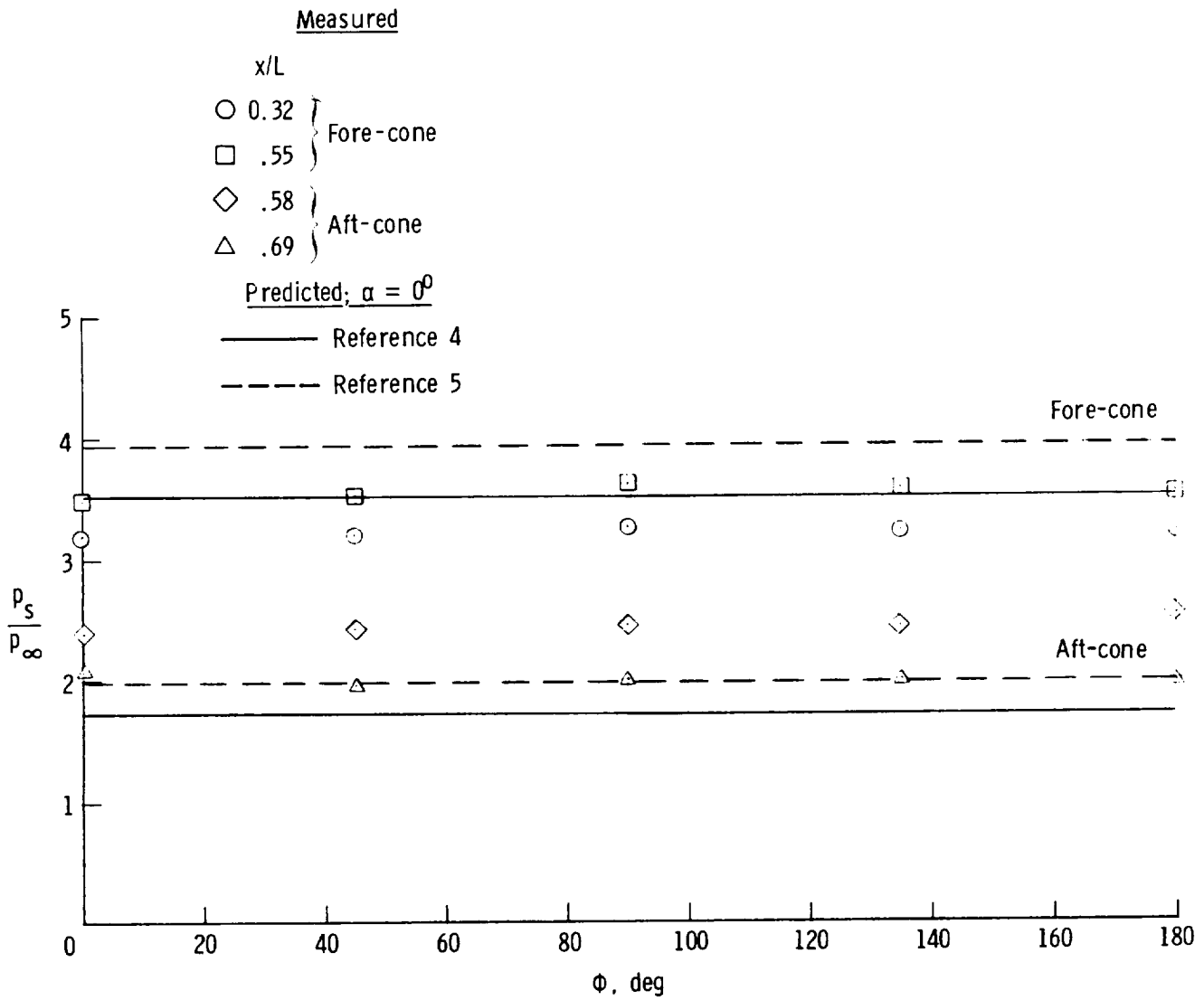
Figure 15.- Circumferential pressure distributions for on-axis biconic at various nominal angles of attack. $M_\infty = 6.0$; $R_{\infty,L} = 5.3 \times 10^6$.

(a) $\alpha_m = 0°$.
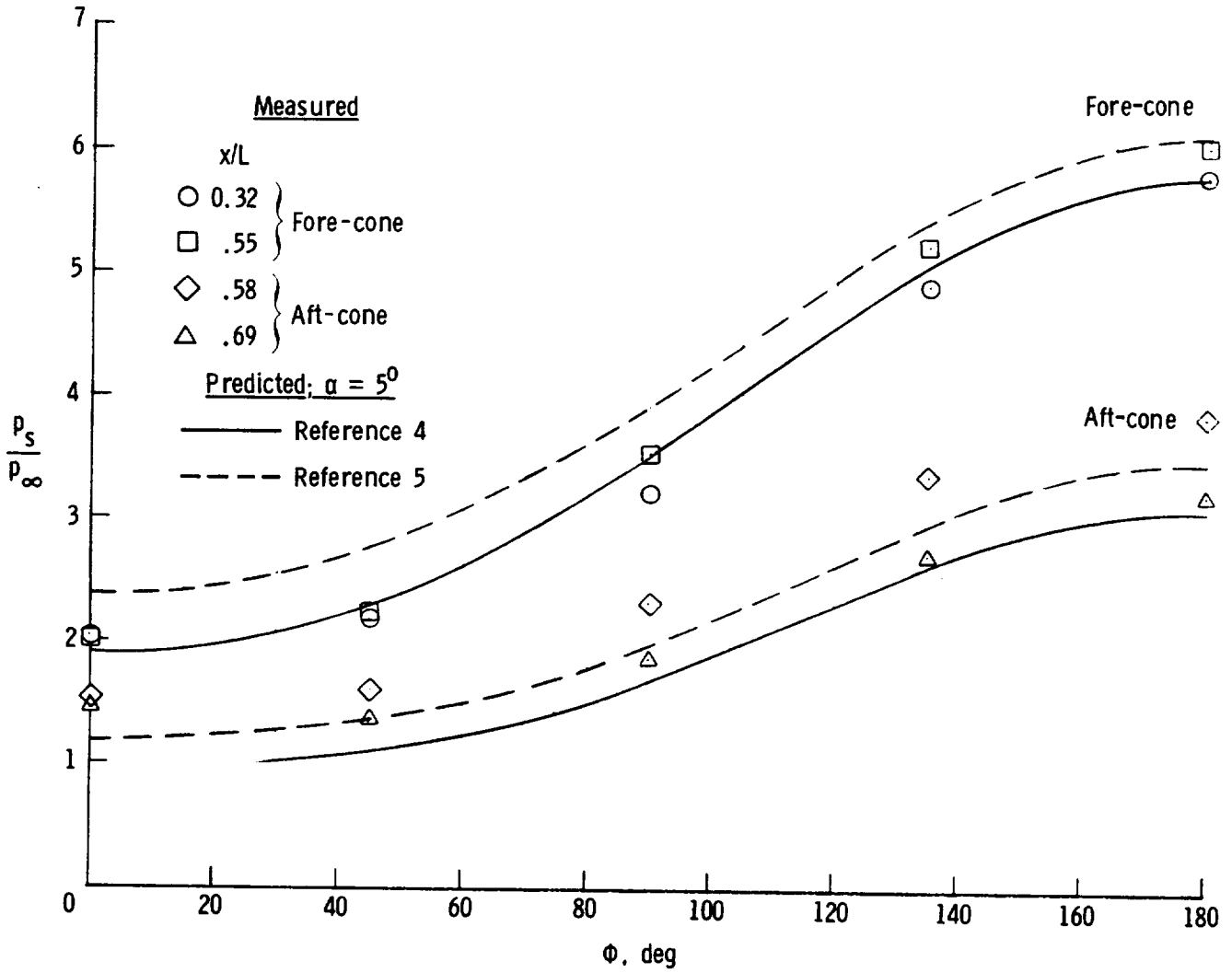
(b) $\alpha_m = 5°$.

Figure 15.- Continued.
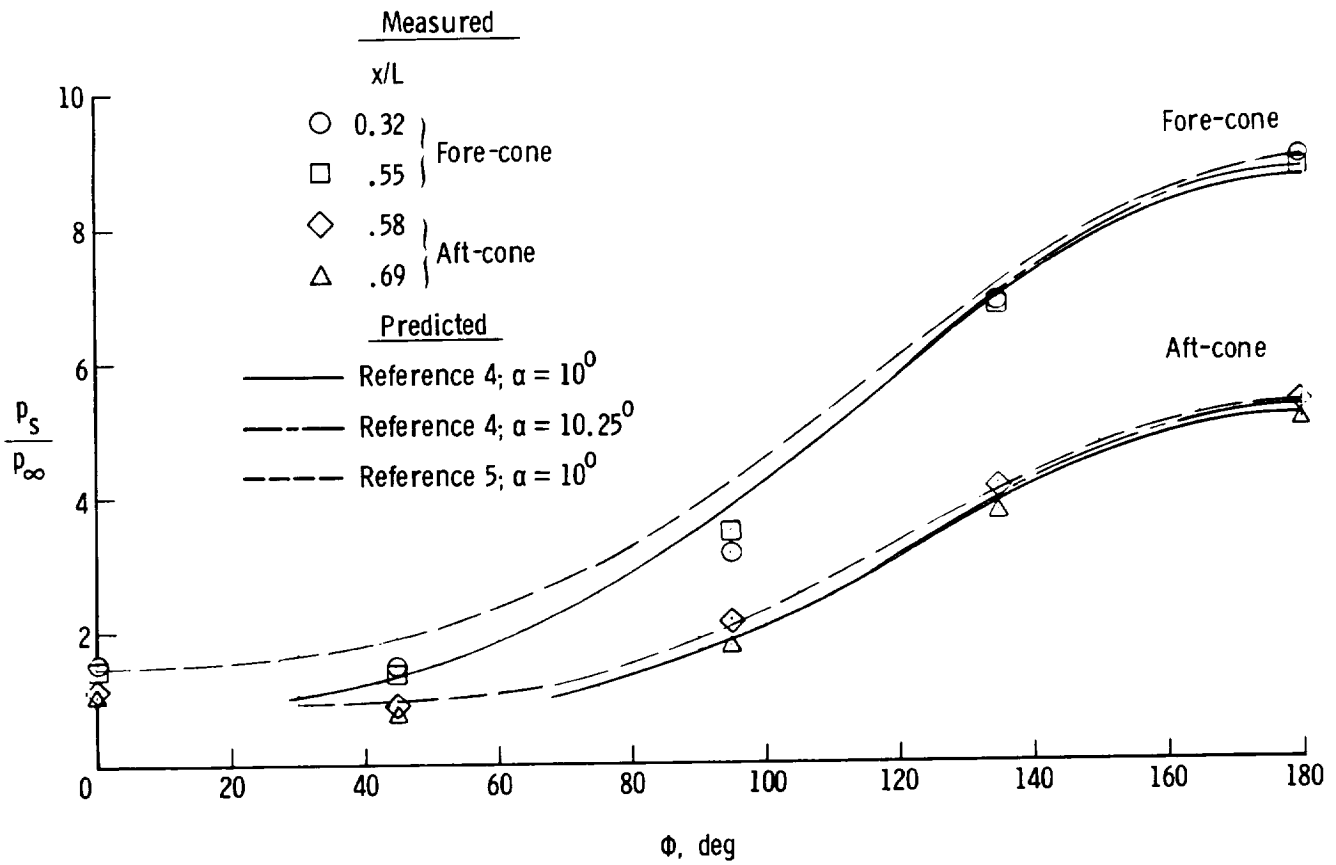
(c) $\alpha_m = 10.25°$.

Figure 15.- Continued.
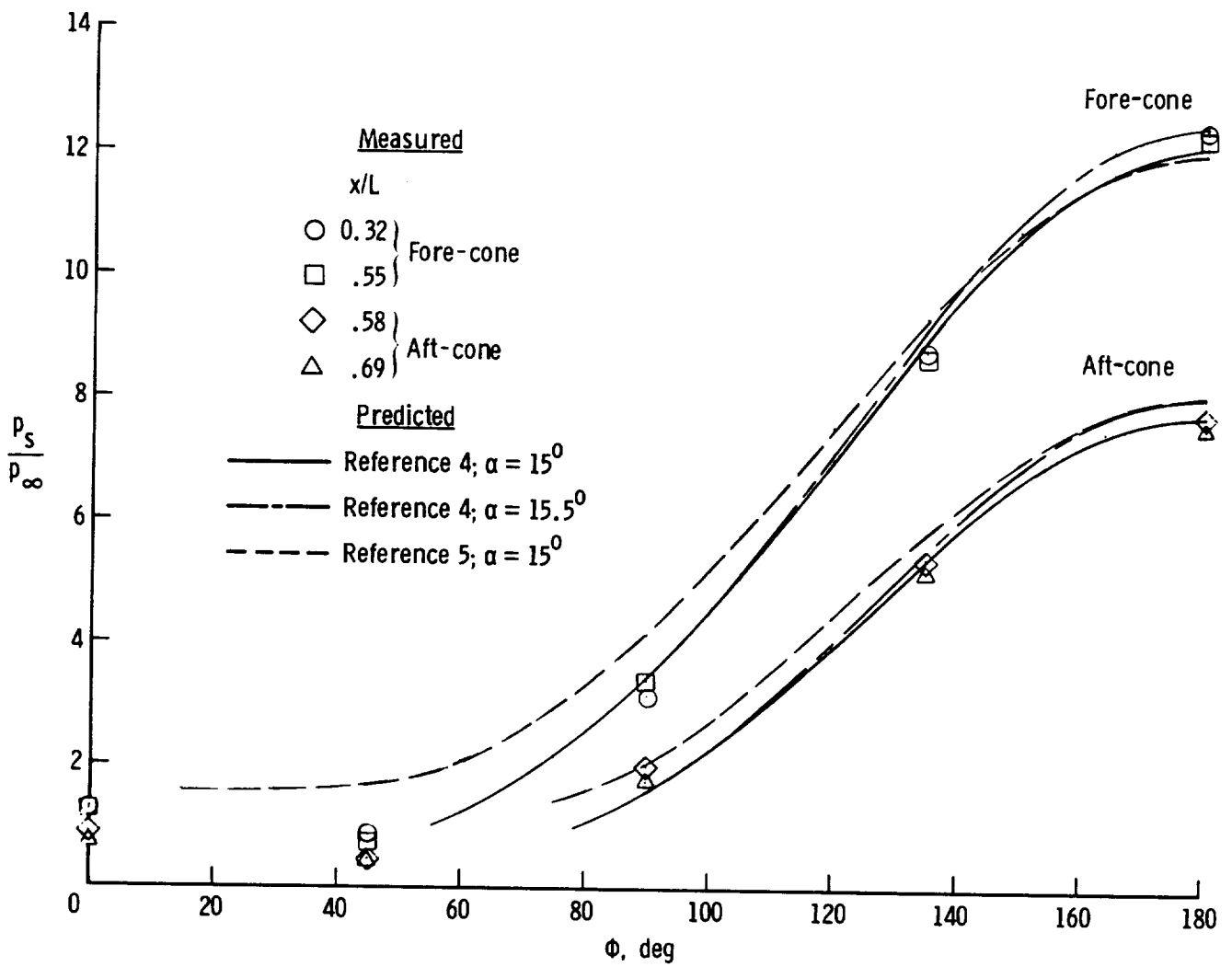
(d) $\alpha_m = 15.5°$.

Figure 15.- Continued.
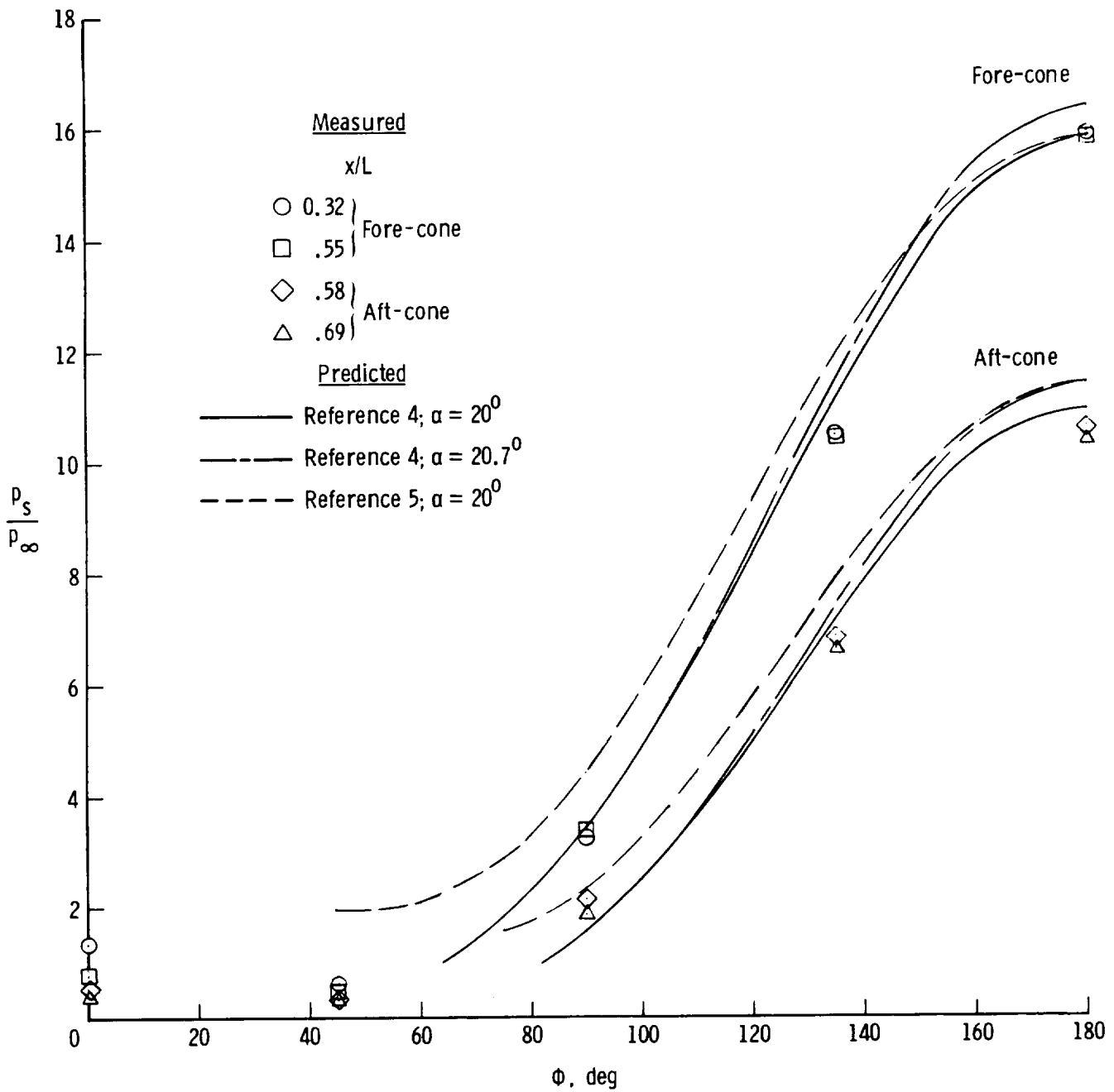
(e) $\alpha_m = 20.7°$.

Figure 15.- Continued.
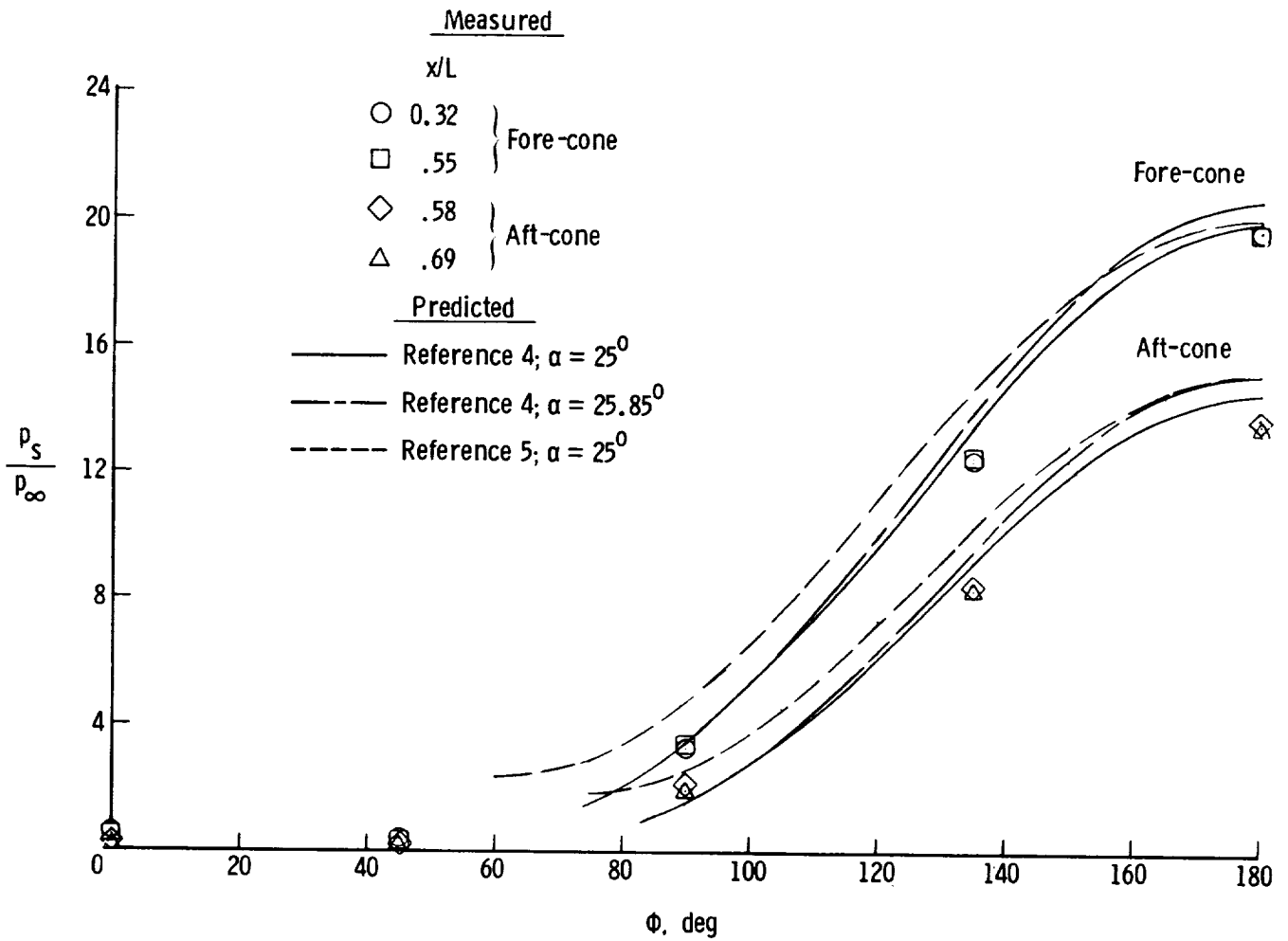
(f)  $\alpha_m = 25.85°$.

Figure 15.- Concluded.
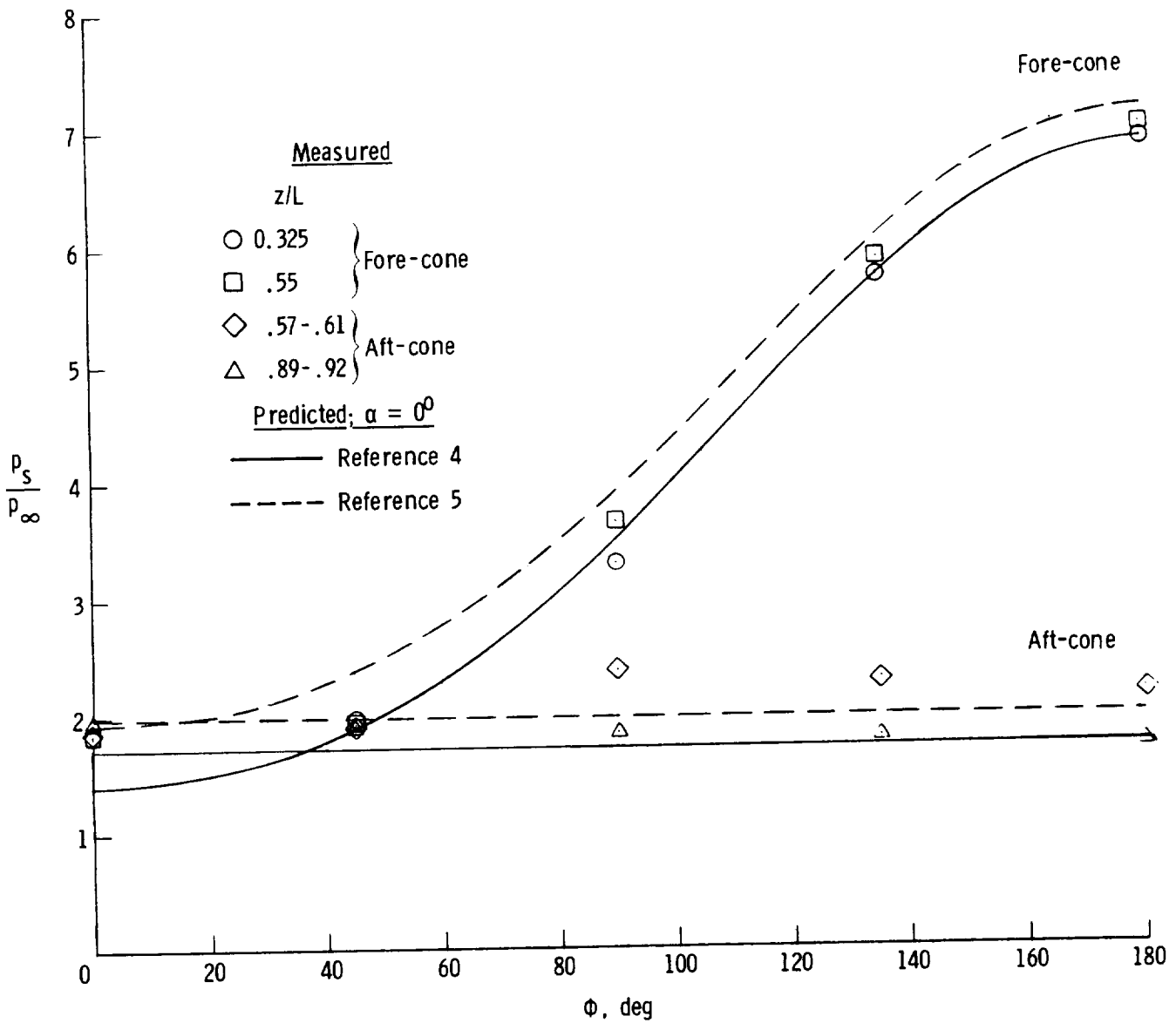
(a) $\alpha_m = 0°$.

Figure 16.- Circumferential pressure distributions for bent-nose biconic at various nominal angles of attack. $M_\infty = 6.0$; $R_{\infty,L} = 5.3 \times 10^6$.
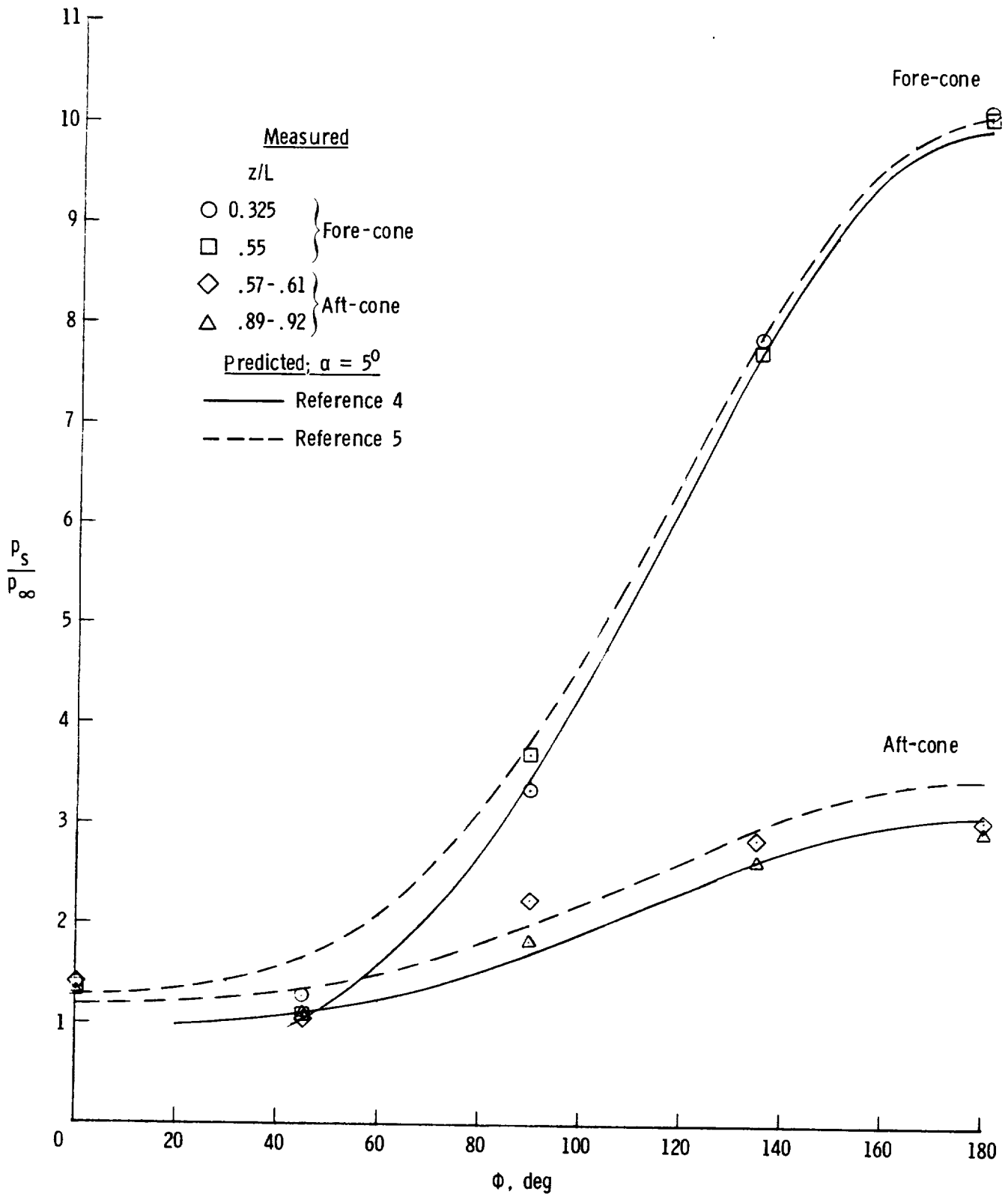
(b)  $\alpha_m = 5°$.

Figure 16.- Continued.

(c)  $\alpha_m = 10.6°$.

Figure 16.- Continued.

Measured

z/L

○ 0.325  }
□ .55     } Fore-cone

◇ .57 - .61 }
△ .89 - .92 } Aft-cone

Predicted

——— Reference 4; $\alpha = 15^0$

—·—· Reference 4; $\alpha = 15.8^0$

— — — Reference 5; $\alpha = 15^0$
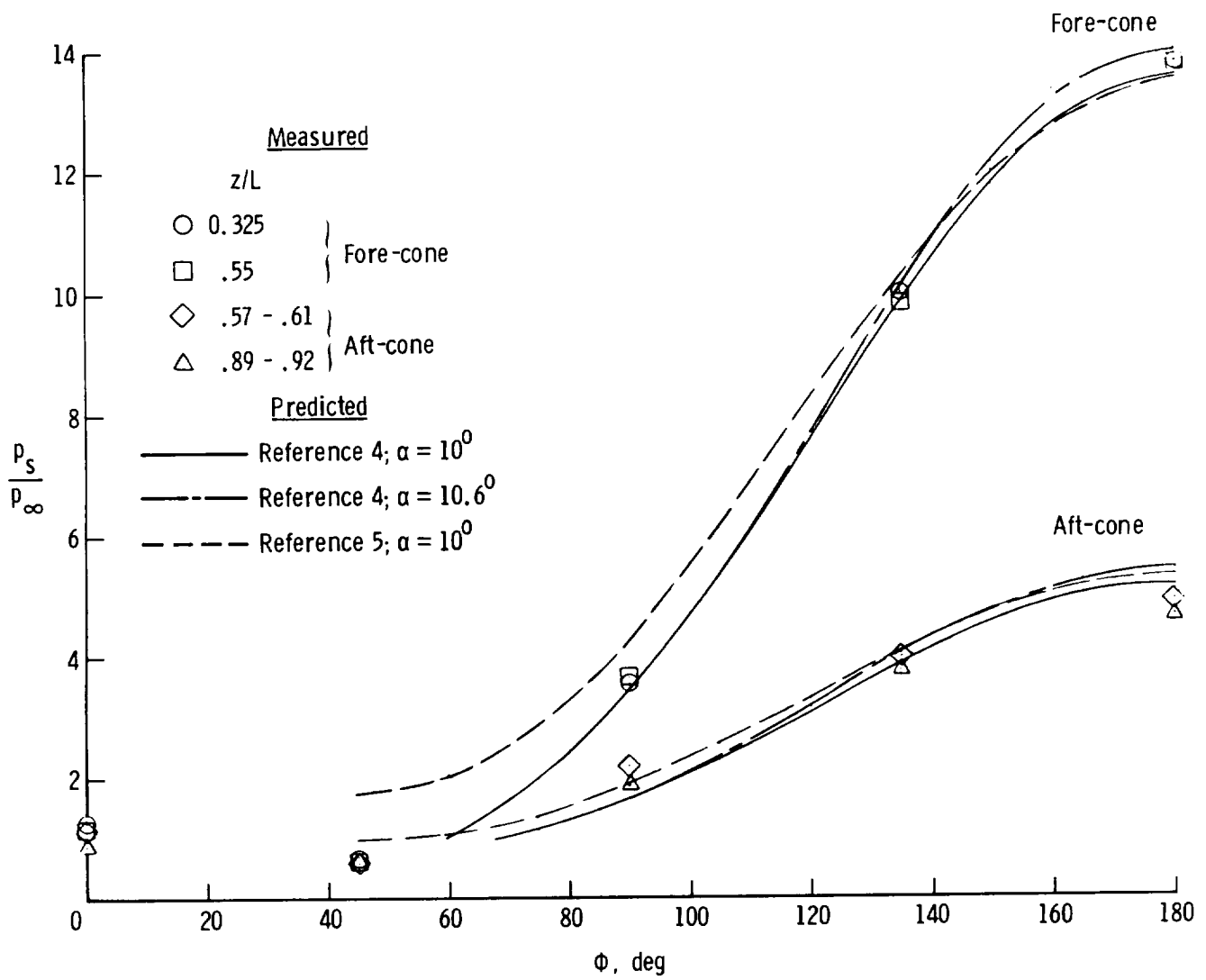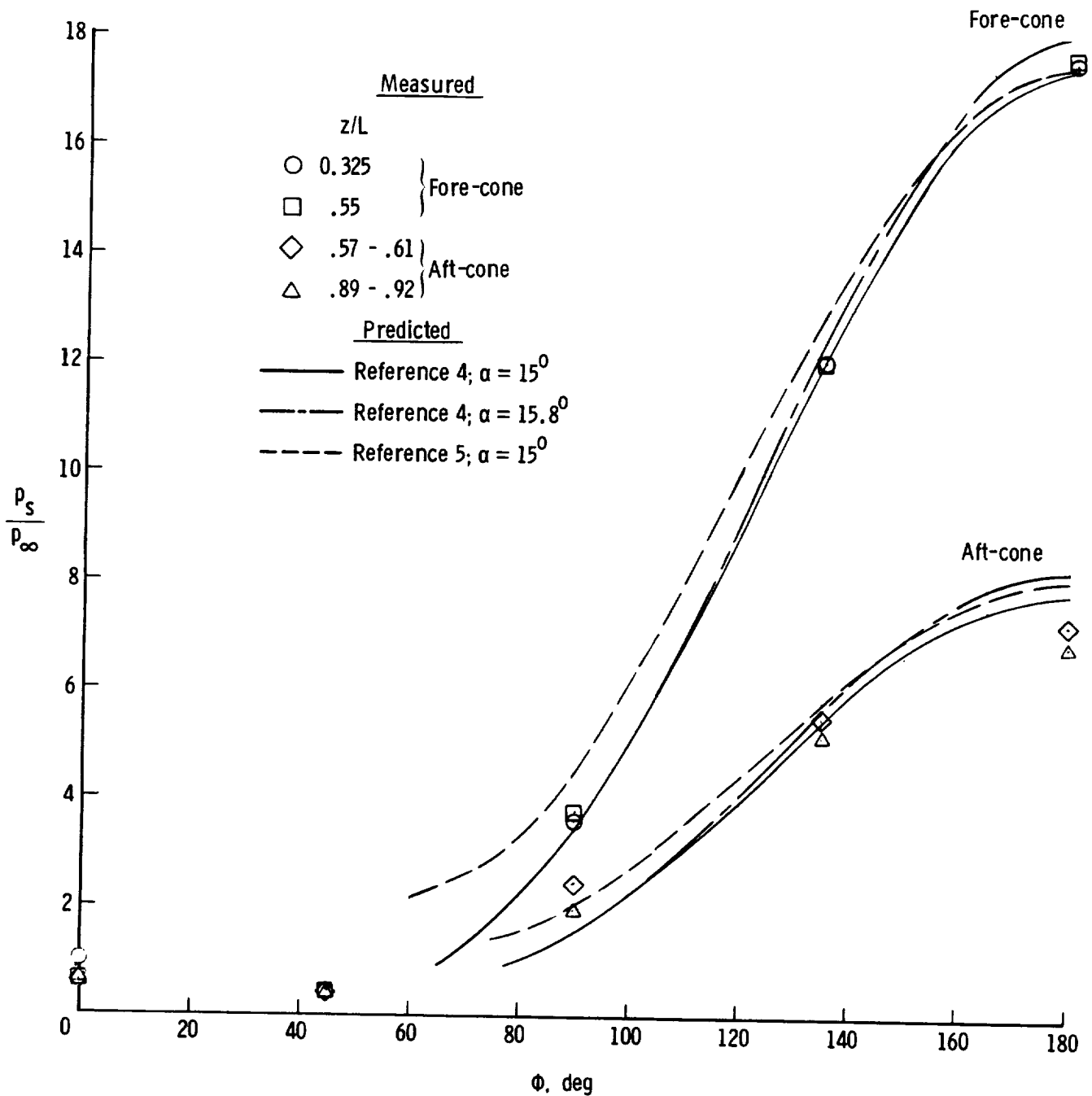
(d)  $\alpha_m = 15.8°$.

Figure 16.- Continued.
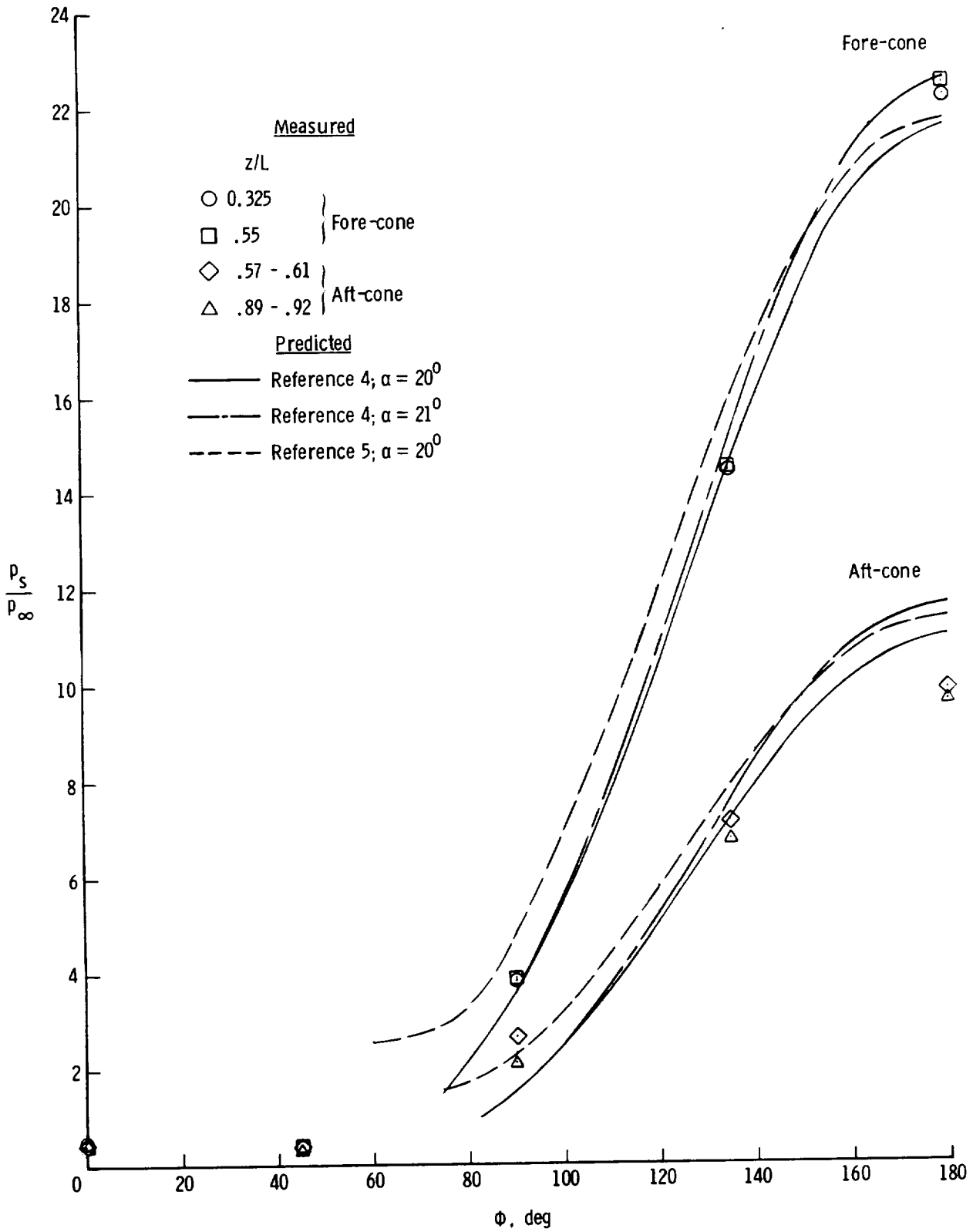
(e) $\alpha_m = 21°$.

Figure 16.- Continued.
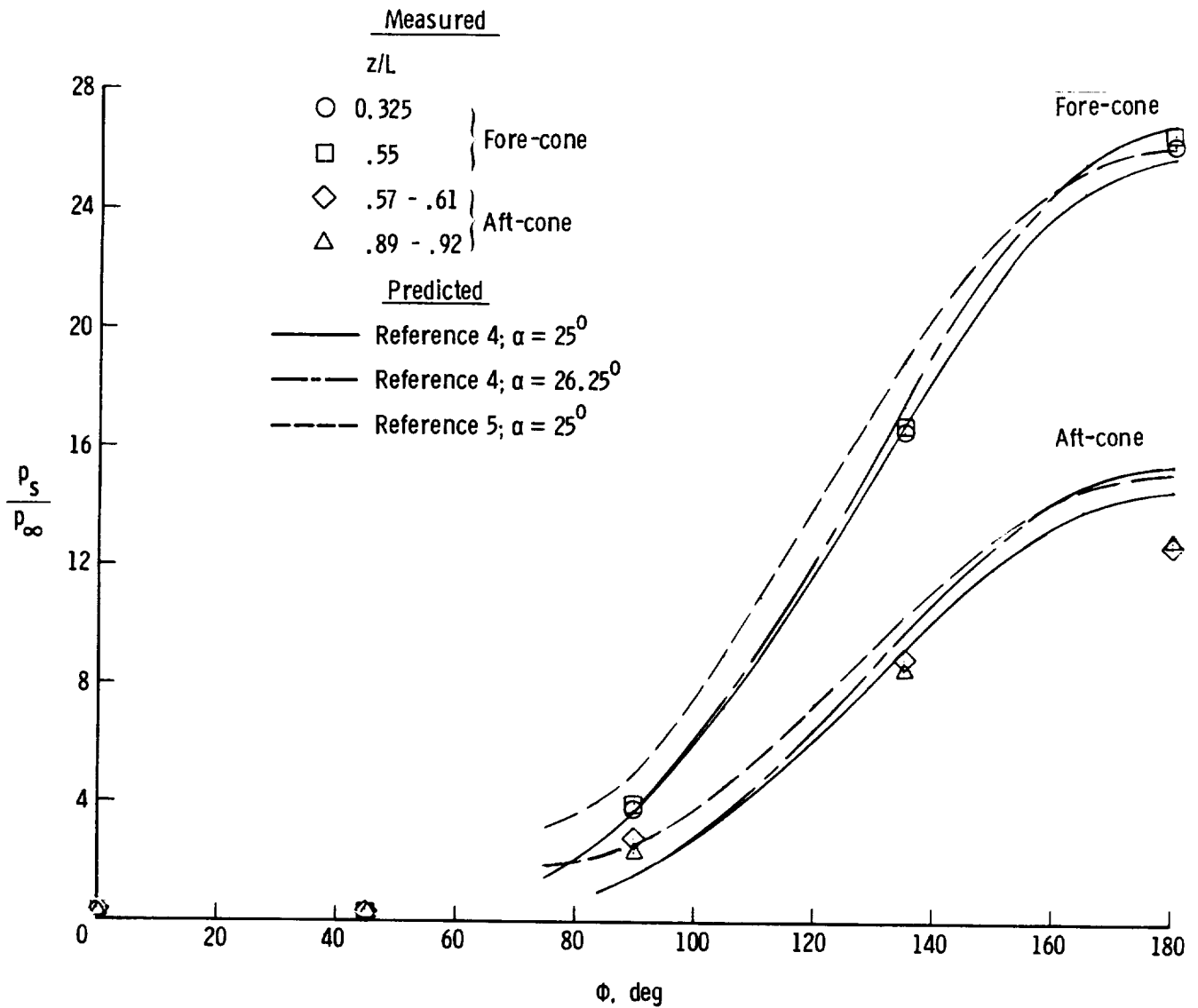
(f) $\alpha_m = 26.25°$.

Figure 16.- Concluded.
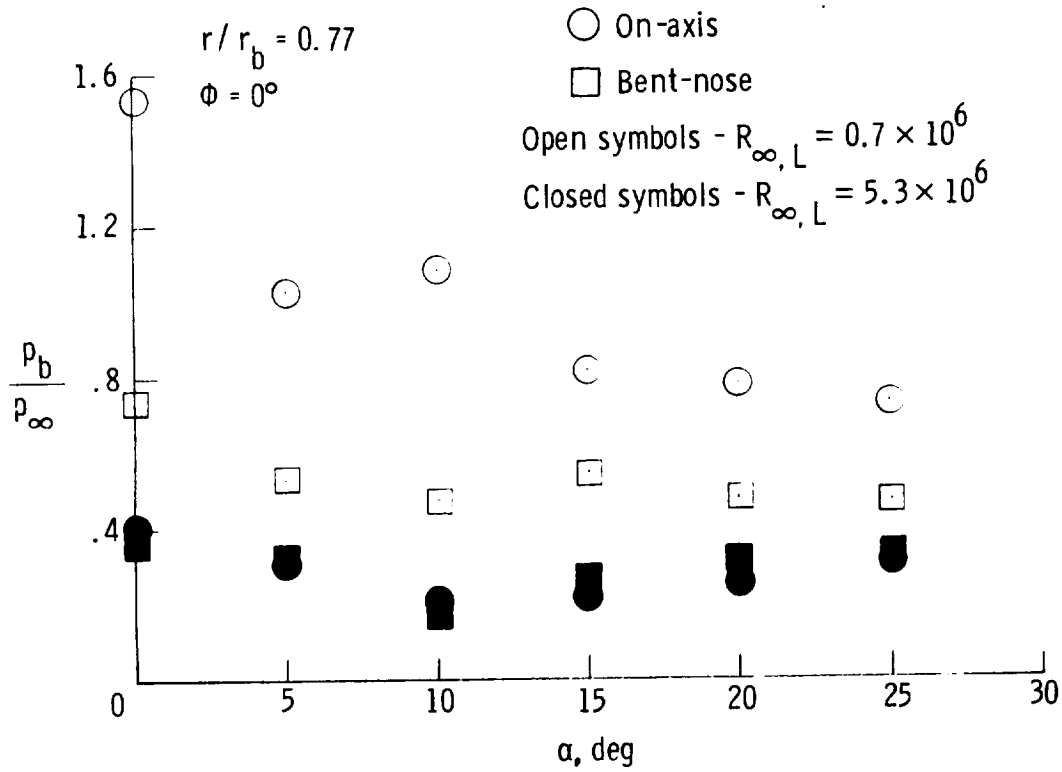
(a) Nondimensionalized by free-stream static pressure.
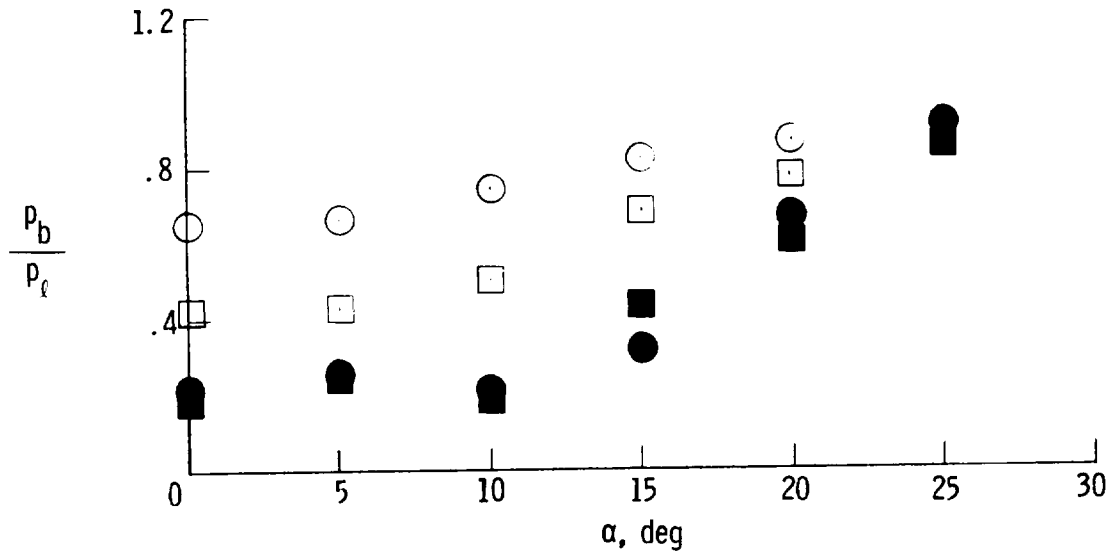


(b) Nondimensionalized by leeward surface pressure just upstream of base.

Figure 17.- Base pressure as a function of angle of attack for on-axis biconic and bent-nose biconic.
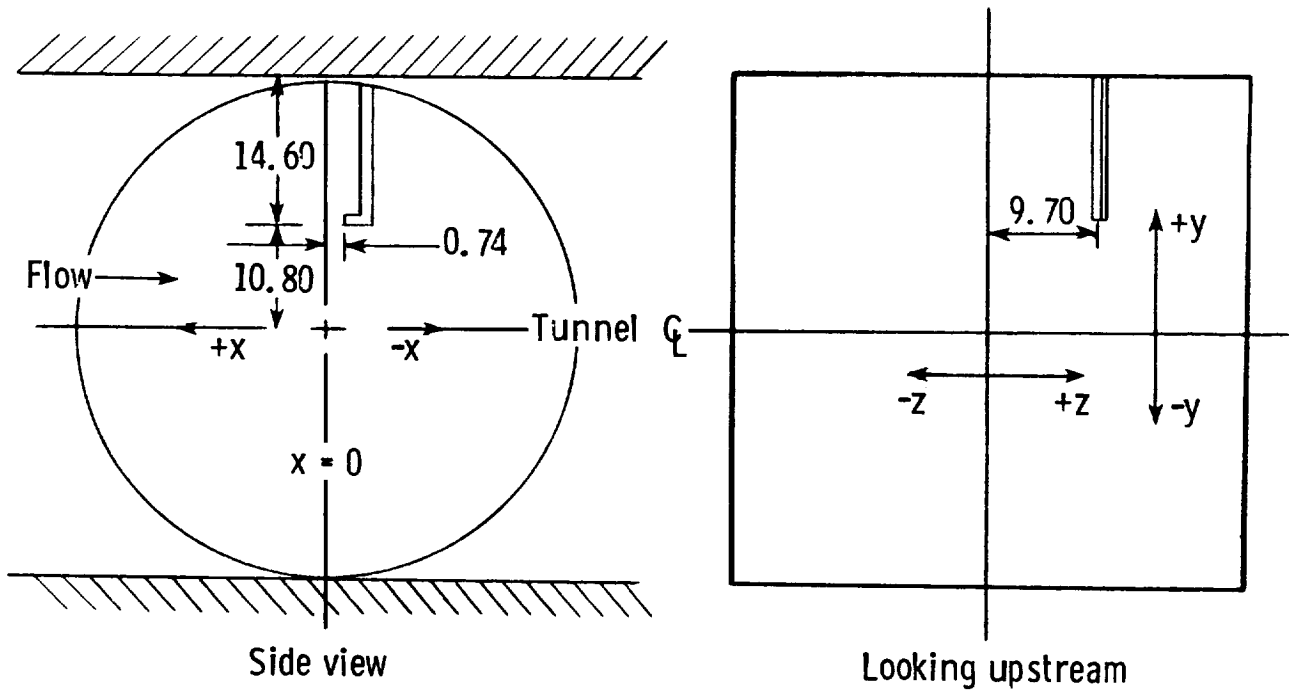
Figure 18.- Location of single pitot-pressure probe relative to centerline of schlieren window. All dimensions in cm.
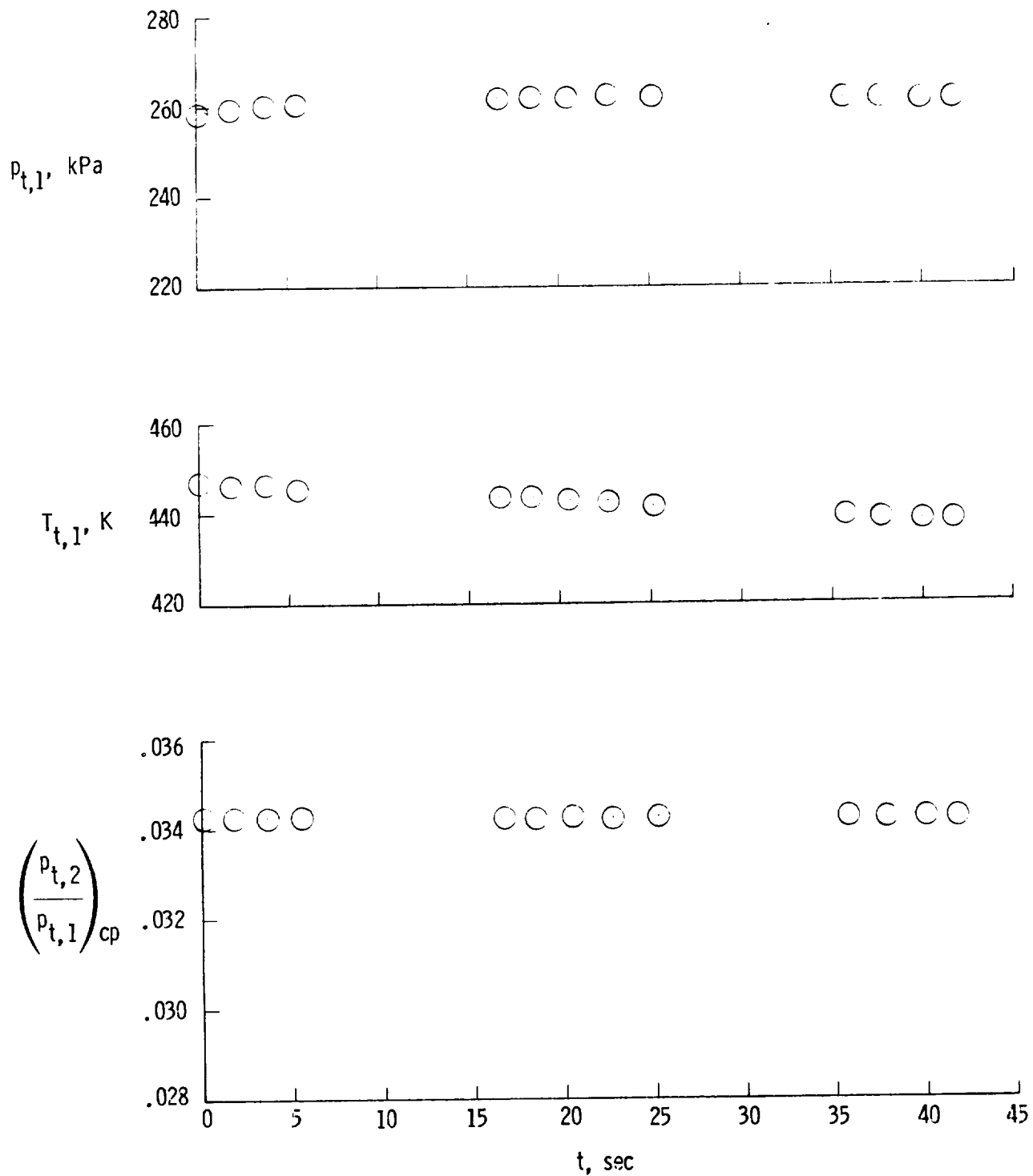
(a) $p_{t,1} \approx 0.26$ MPa.

Figure 19.- Time histories of reservoir pressure, reservoir temperature, and center-probe pitot-pressure ratio for two values of reservoir pressure and x = -2.4 cm.
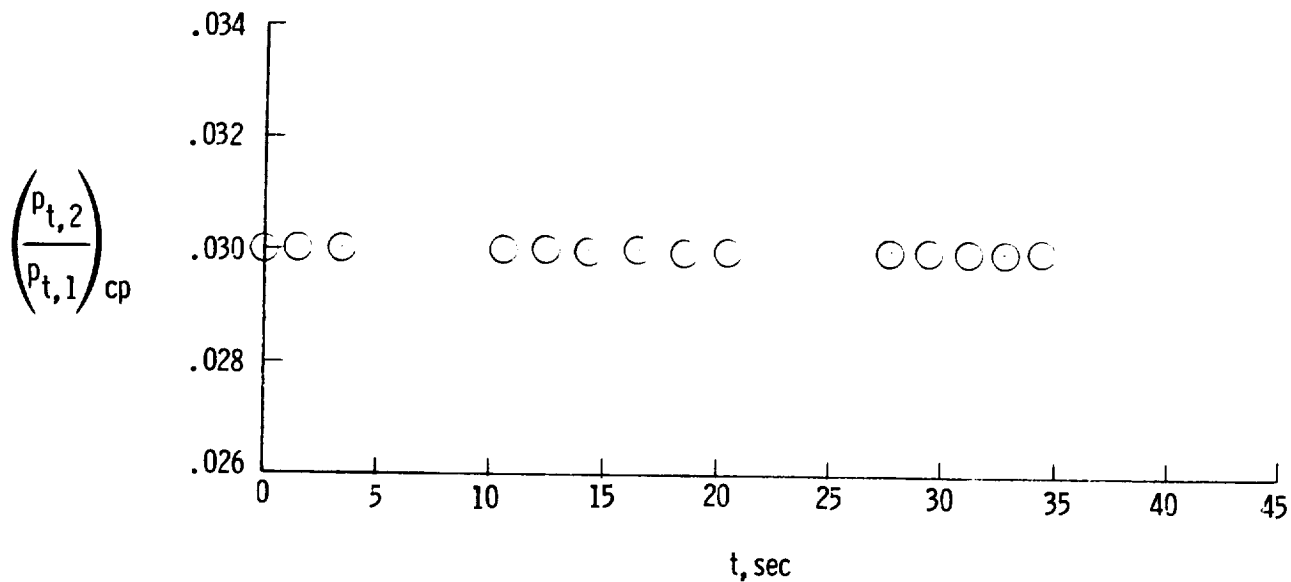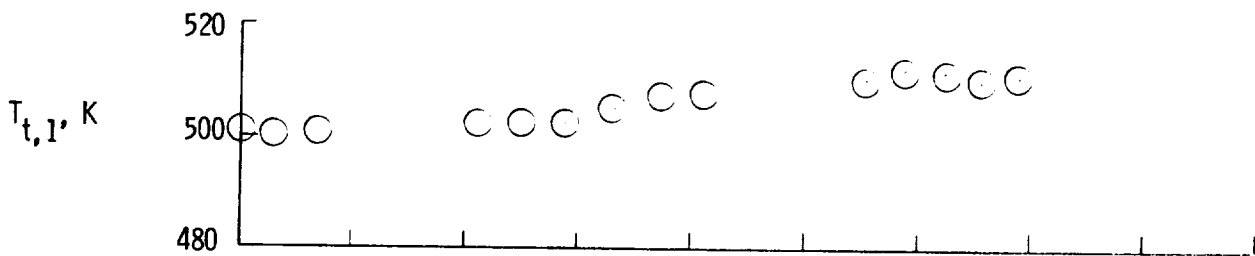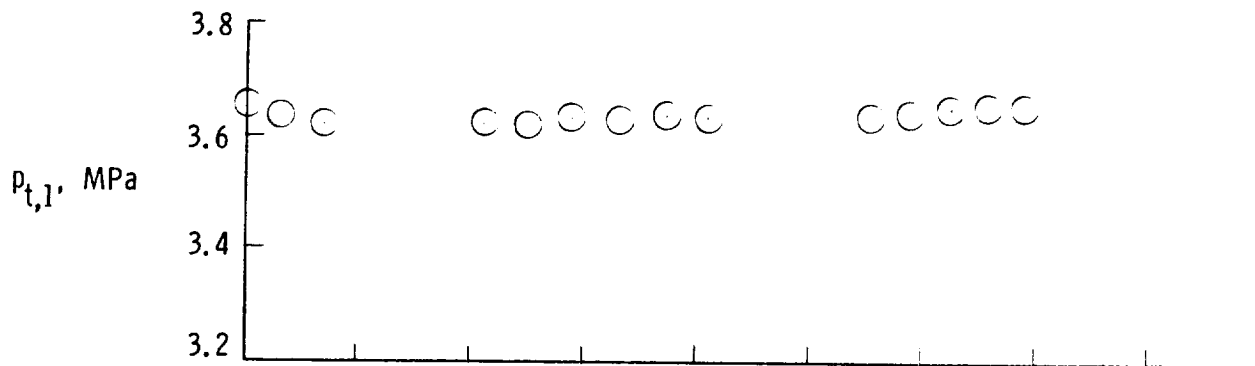
(b) $p_{t,1} \approx 3.6$ MPa.

Figure 19.- Concluded.
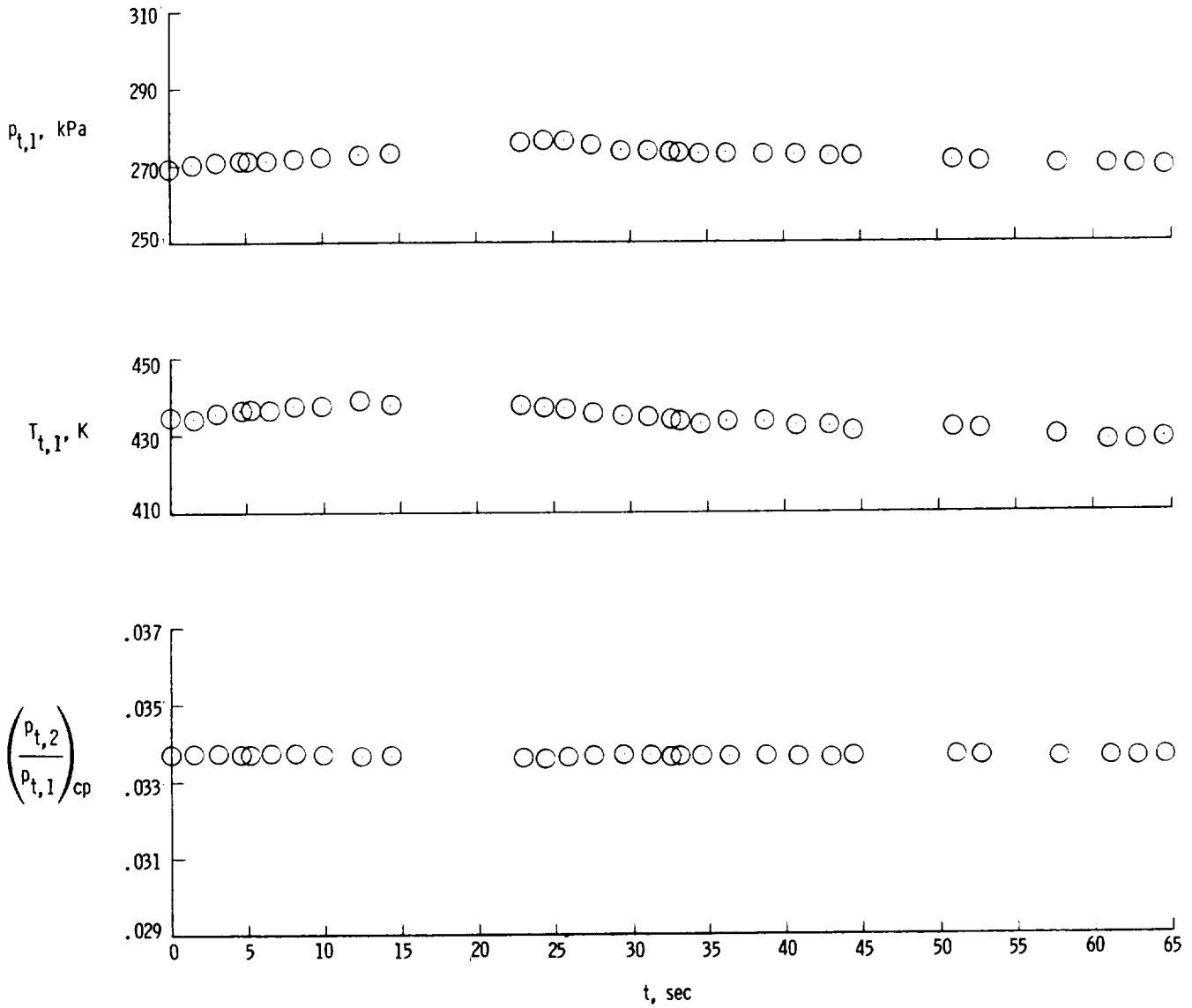
(a) $p_{t,1} \approx 0.27$ MPa.

Figure 20.- Time histories of reservoir pressure, reservoir temperature, and center-probe pitot-pressure ratio for two values of reservoir pressure and x = -24.2 cm.
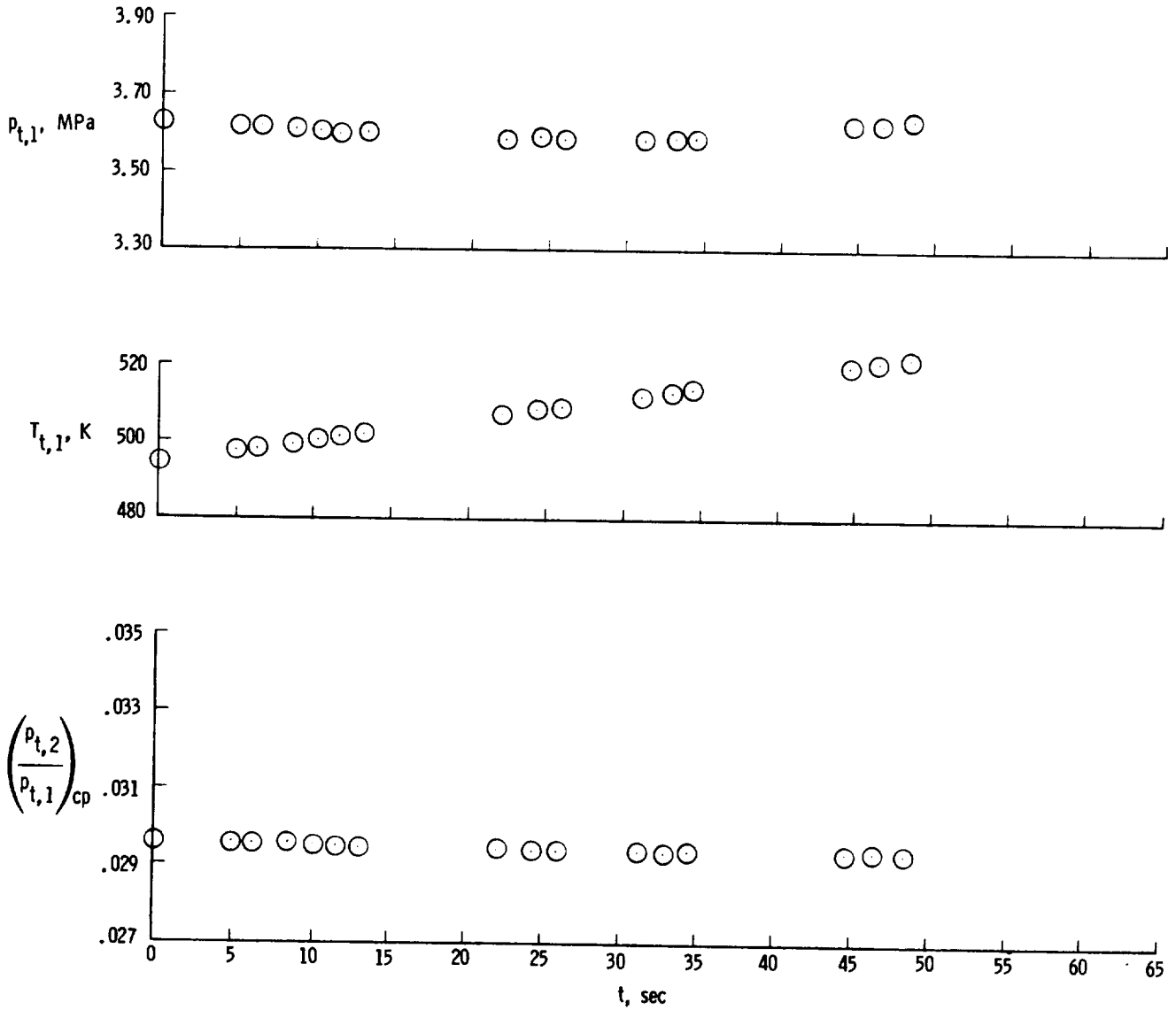
(b)  $P_{t,1} \approx 3.6$  MPa.

Figure 20.- Concluded.
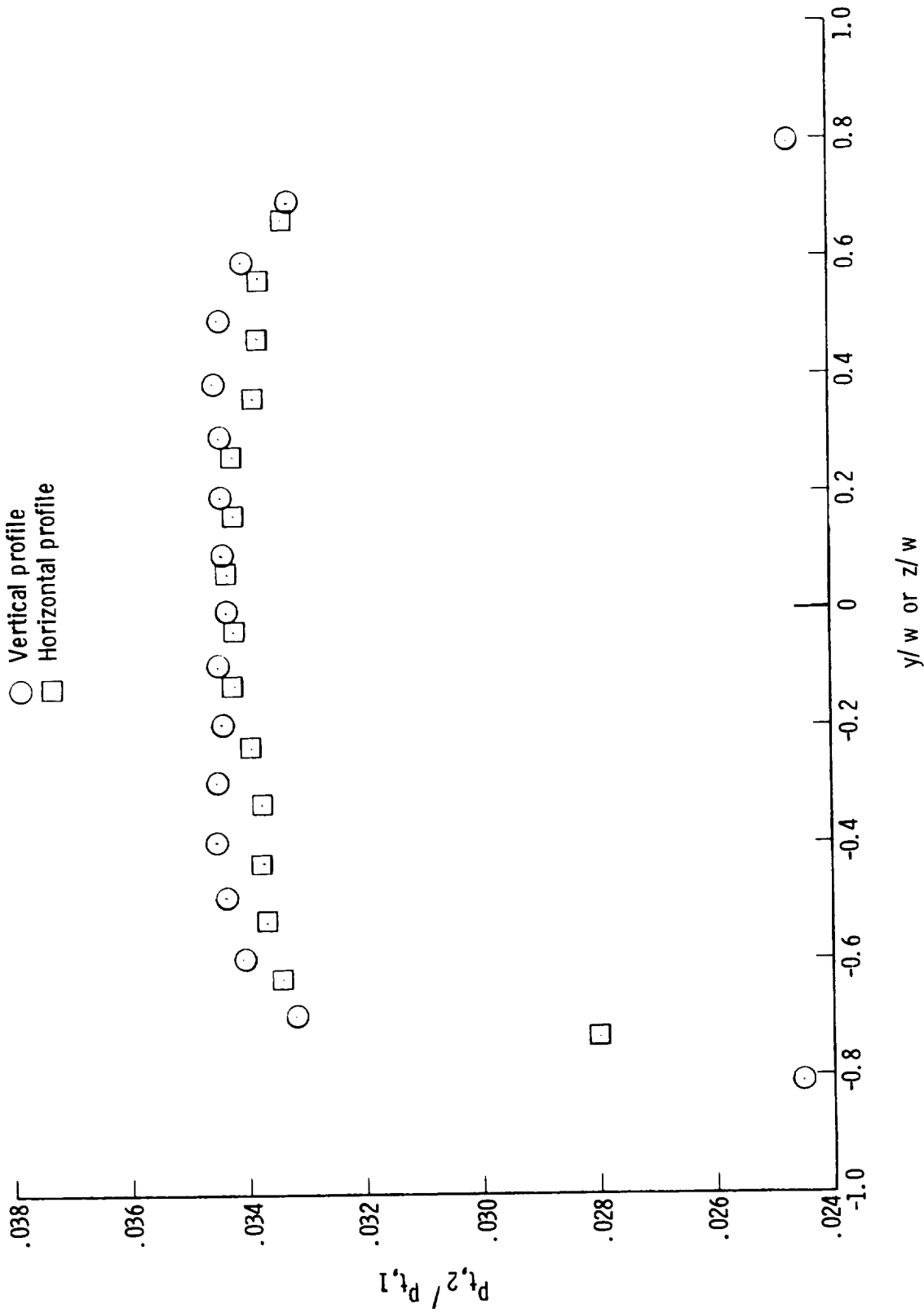
(a) $p_{t,1} \approx 0.26$ MPa; $T_{t,1} \approx 444$ K.

Figure 21.- Vertical and horizontal pitot-pressure profiles for a range of reservoir pressure and $x = -2.4$ cm. $w = 25.4$ cm.
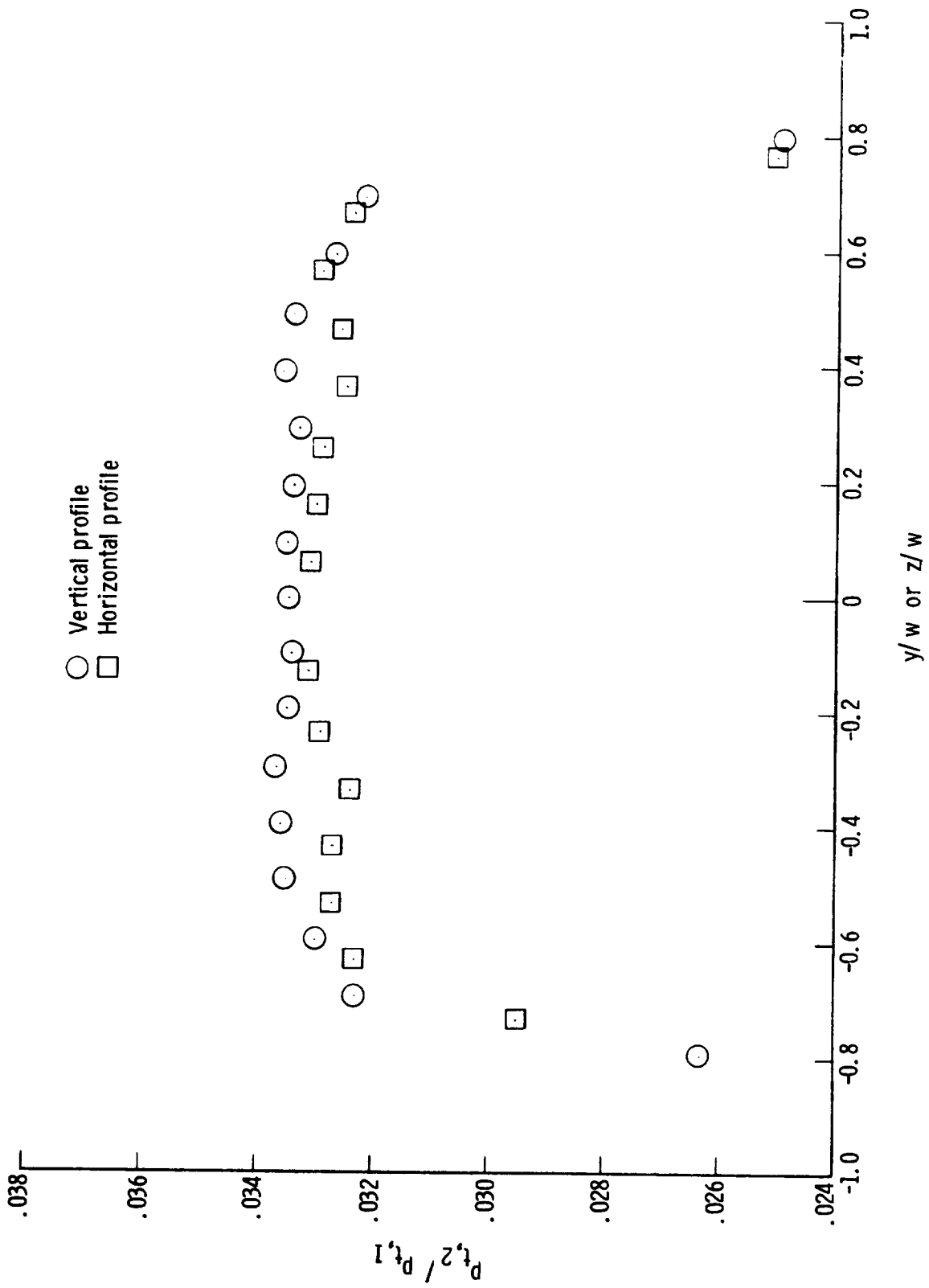
(b) $p_{t,1} \approx 0.40$ MPa; $T_{t,1} \approx 433$ K.

Figure 21.- Continued.
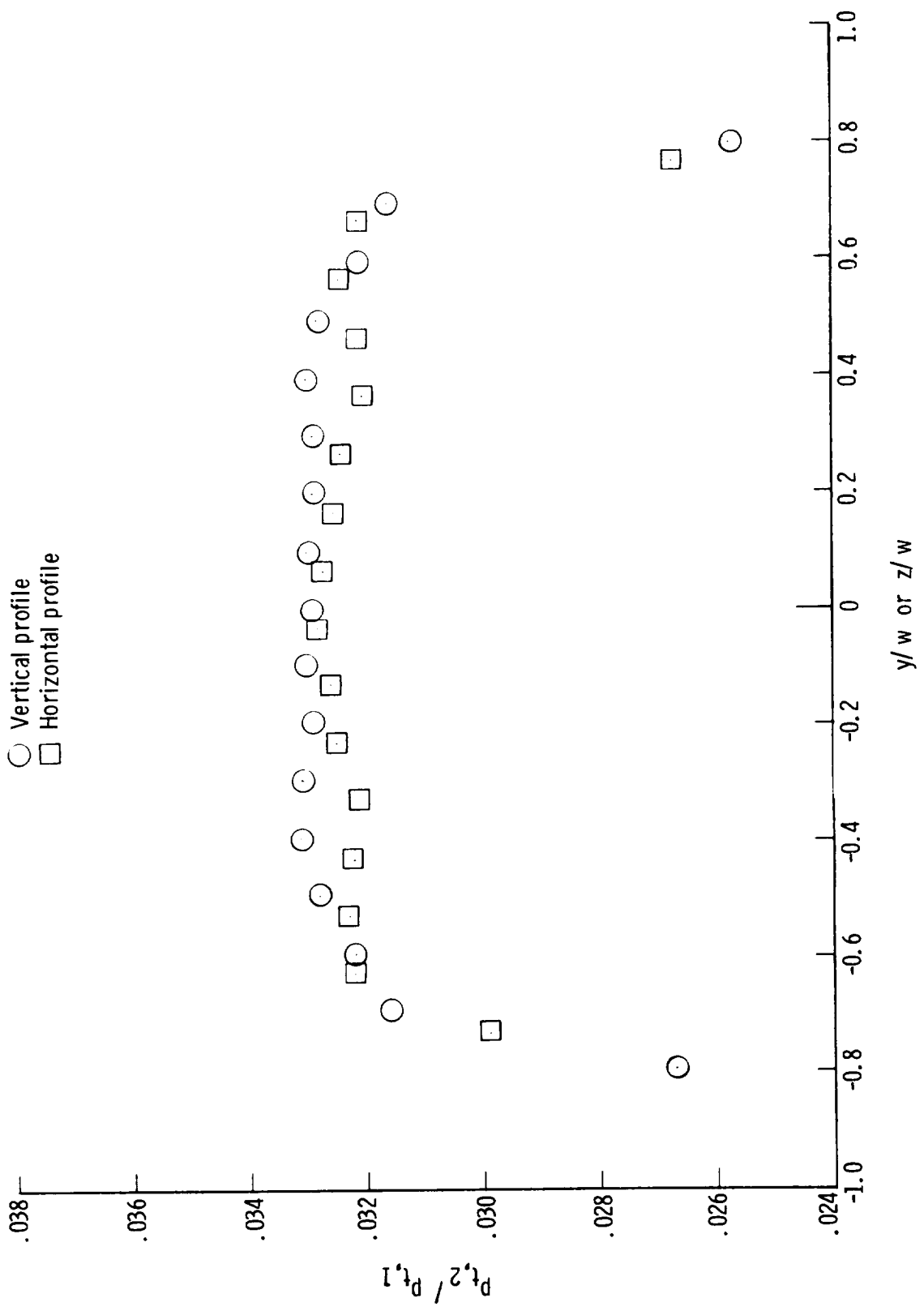
(c) $p_{t,1} \approx 0.50$ MPa; $T_{t,1} \approx 479$ K.

Figure 21.- Continued.
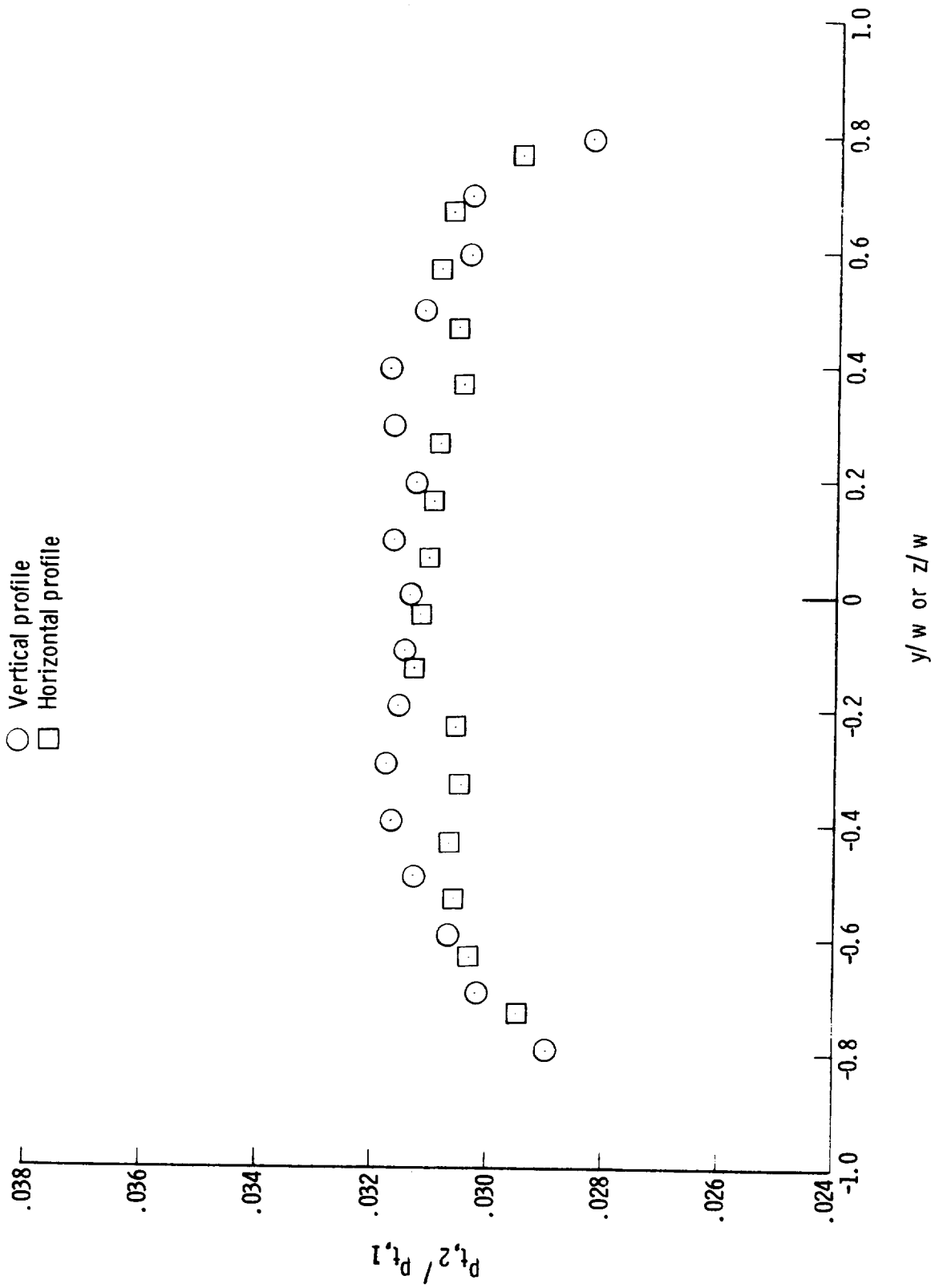
(d) $p_{t,1} \approx 1.13$ MPa; $T_{t,1} \approx 475$ K.

Figure 21.- Continued.
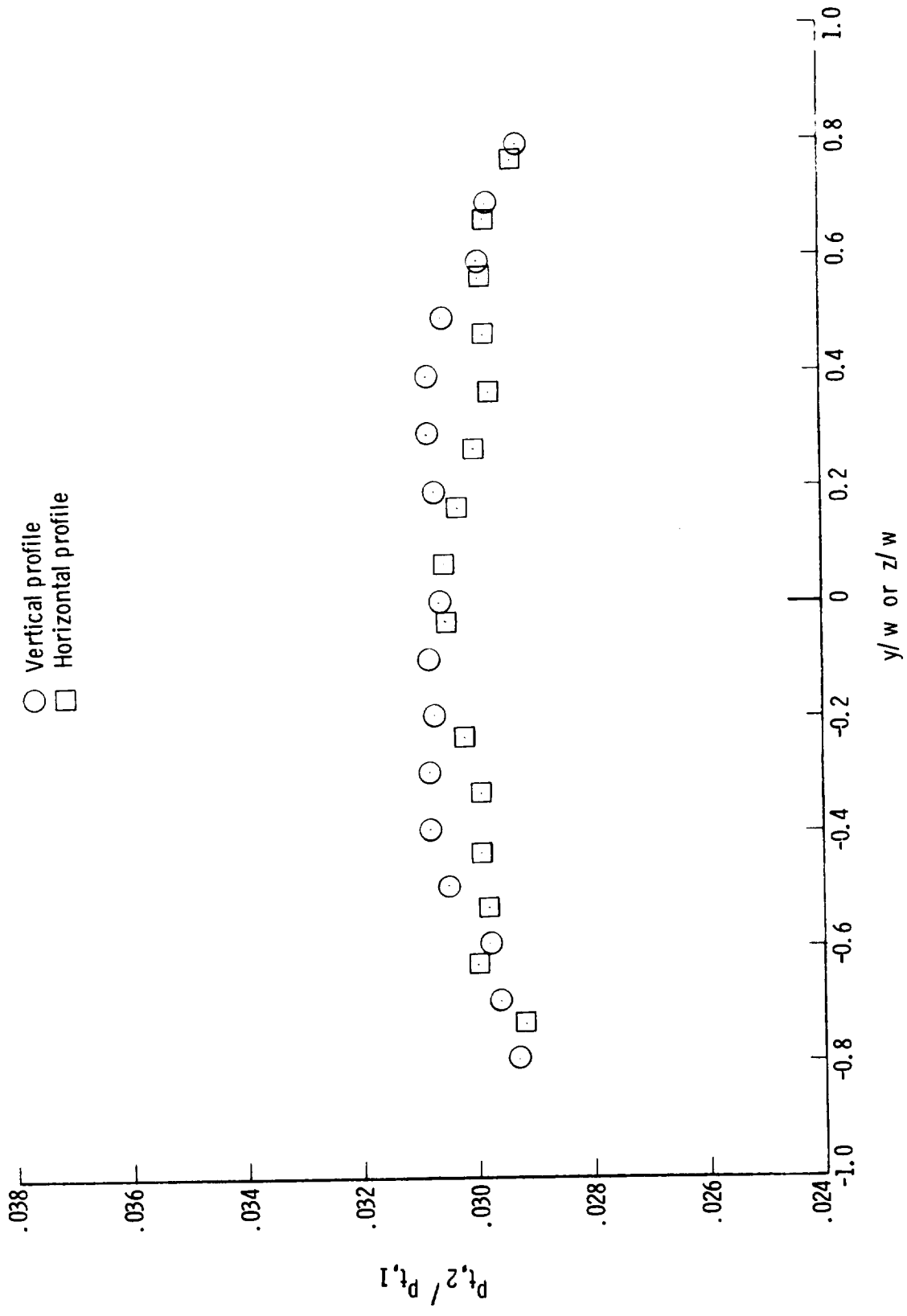
(e) $p_{t,1} \approx 2.18$ MPa; $T_{t,1} \approx 486$ K.

Figure 21.- Continued.
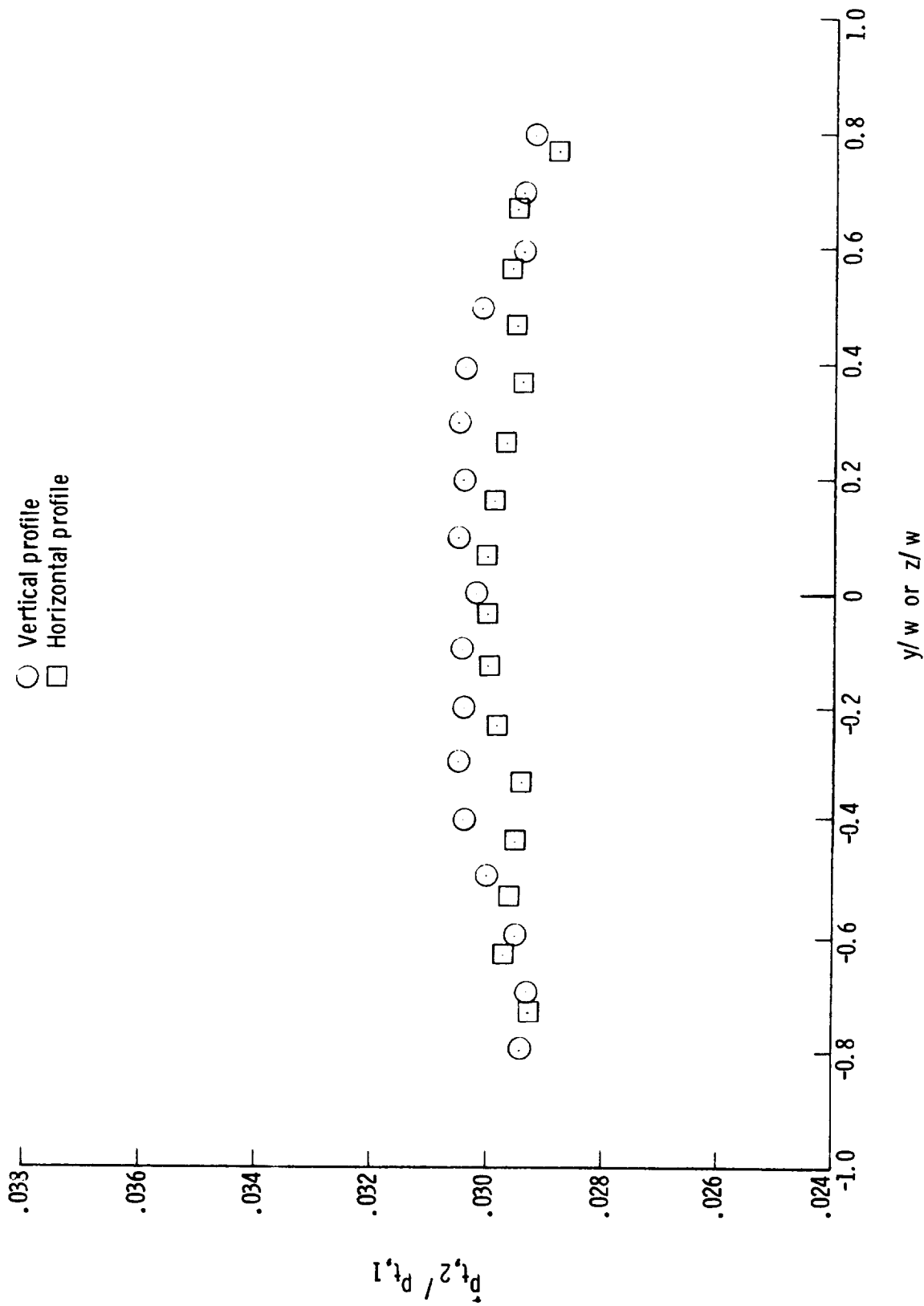
(f) $P_{t,1} \approx 3.06$ MPa; $T_{t,1} \approx 496$ K.

Figure 21.- Continued.
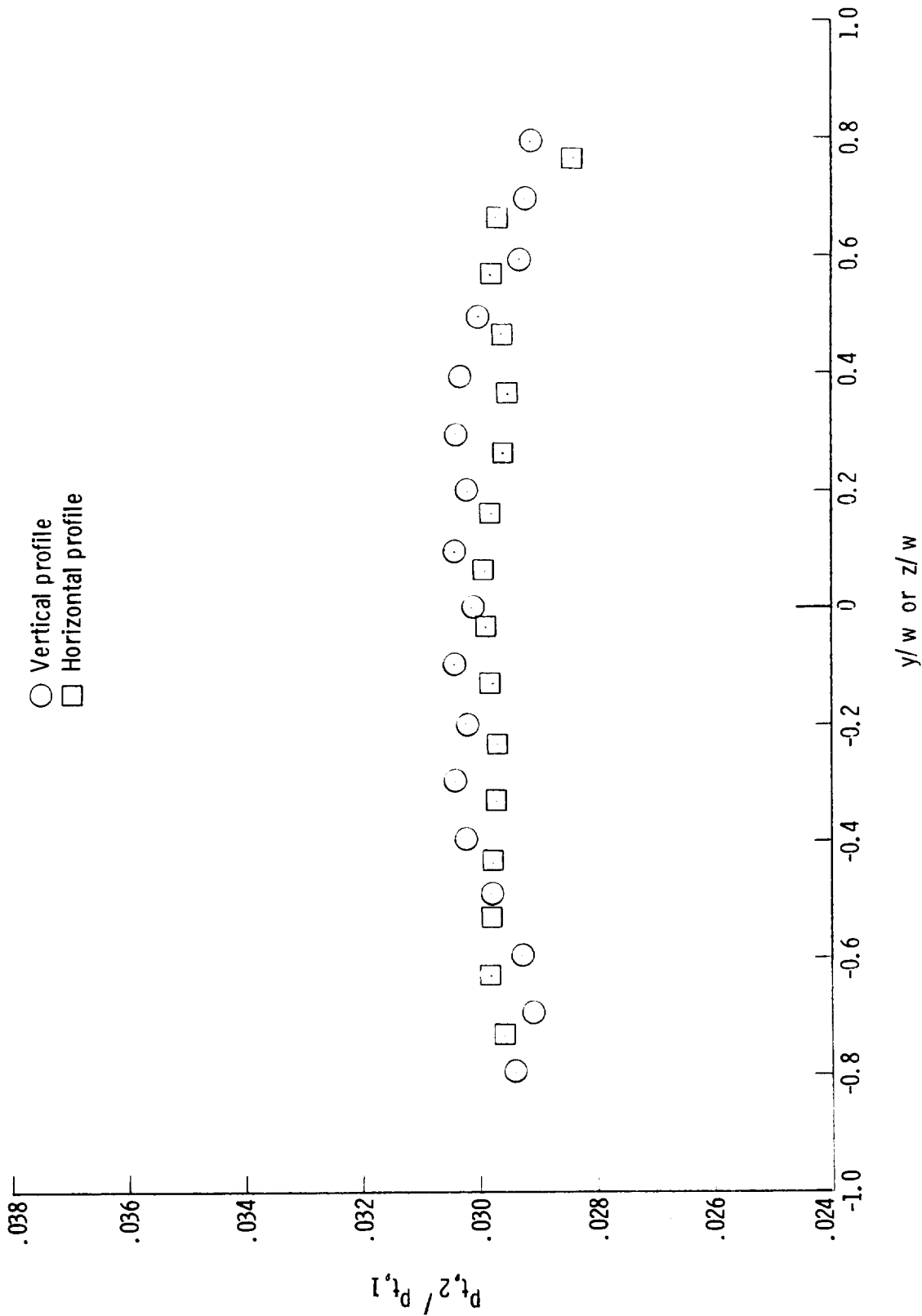
(g) $P_{t,1} \approx 3.63$ MPa; $T_{t,1} \approx 504$ K.

Figure 21.- Concluded.
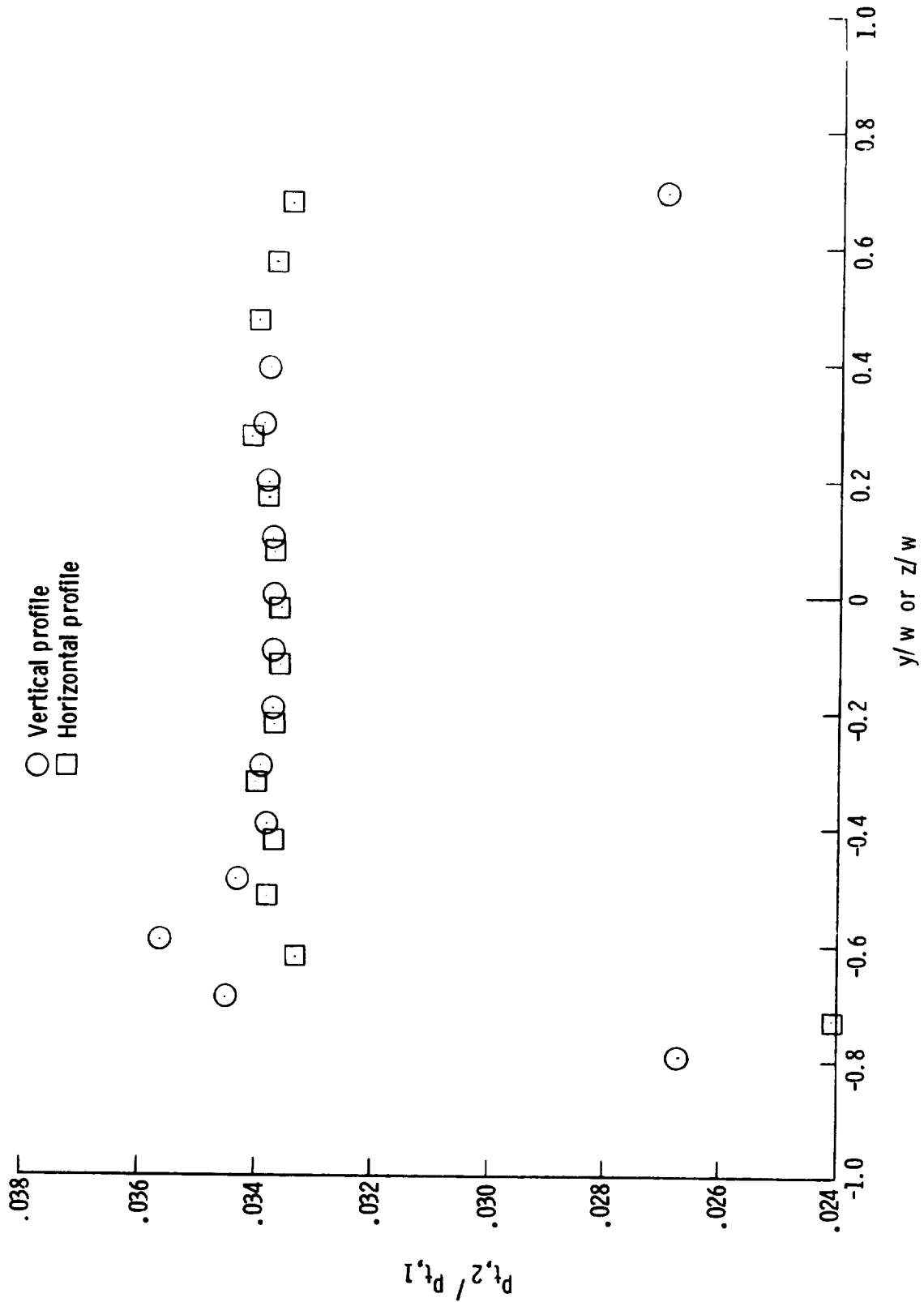
(a) $P_{t,1} \approx 0.27$ MPa; $T_{t,1} \approx 434$ K.

Figure 22.- Vertical and horizontal pitot-pressure profiles for a range of reservoir pressure and $x = -24.2$ cm. $w = 25.4$ cm.
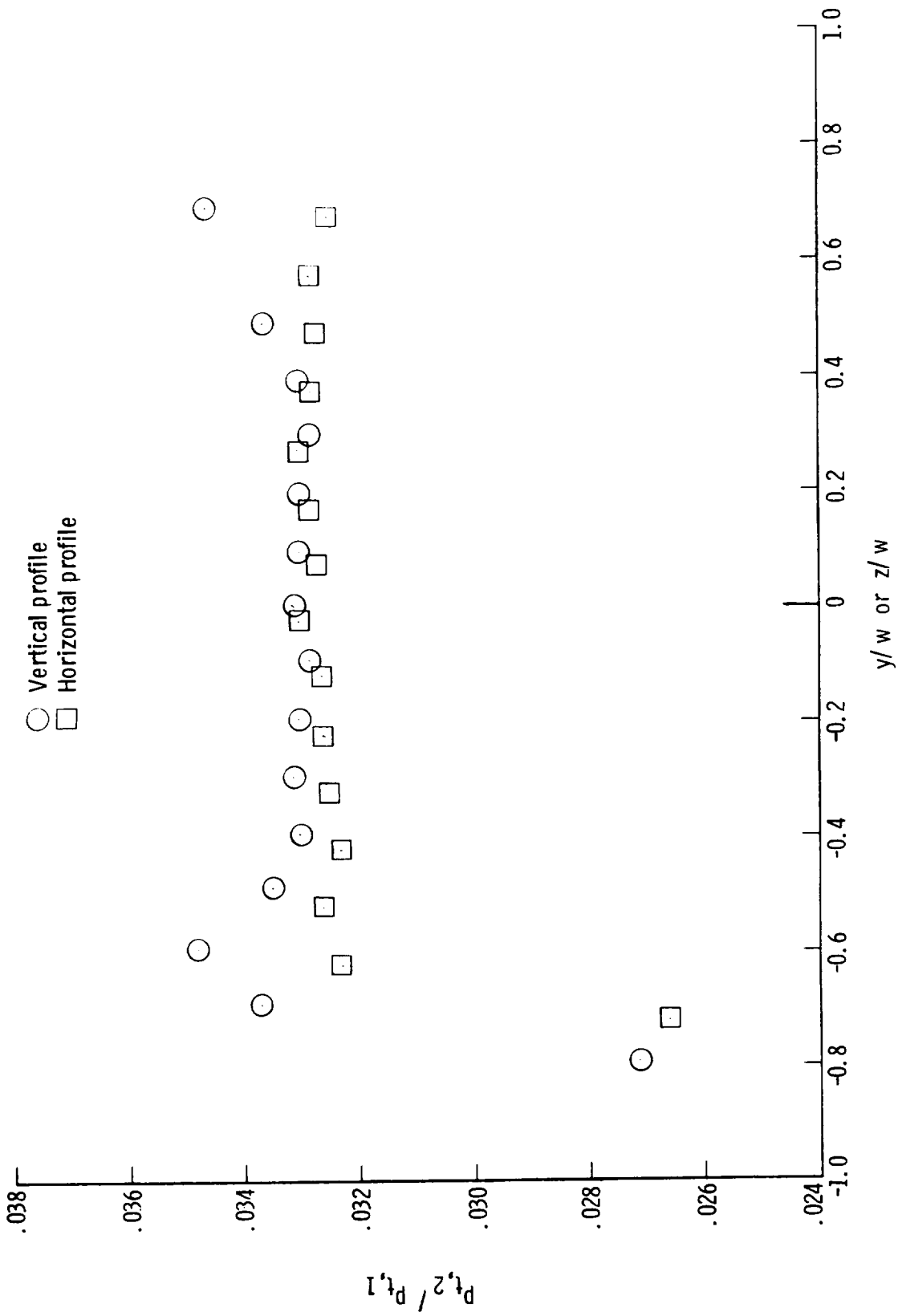
(b)  $p_{t,1} \approx 0.40$  MPa;  $T_{t,1} \approx 440$  K.

Figure 22.- Continued.
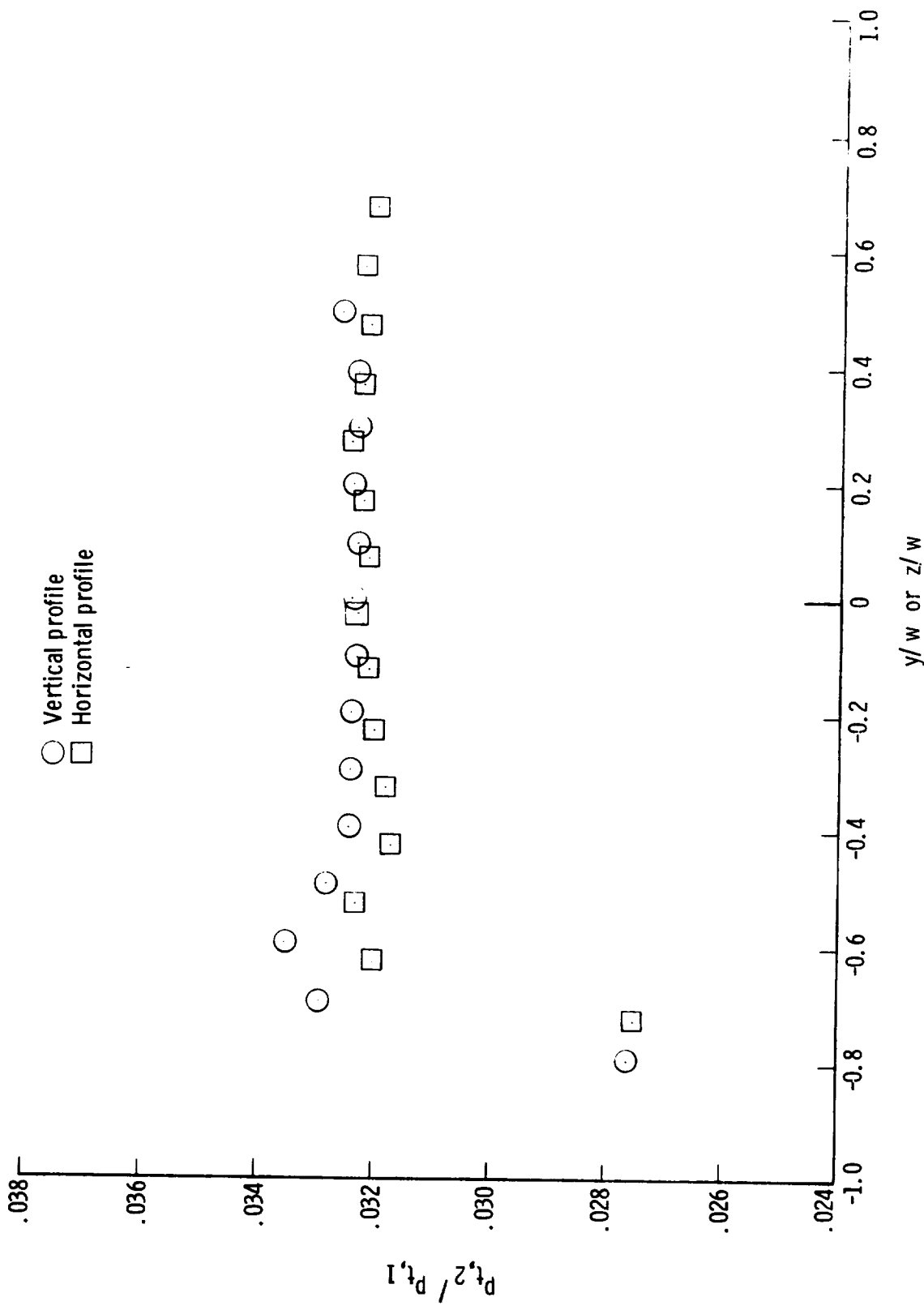
(c) $P_{t,1} \approx 0.51$ MPa; $T_{t,1} \approx 471$ K.

Figure 22.- Continued.
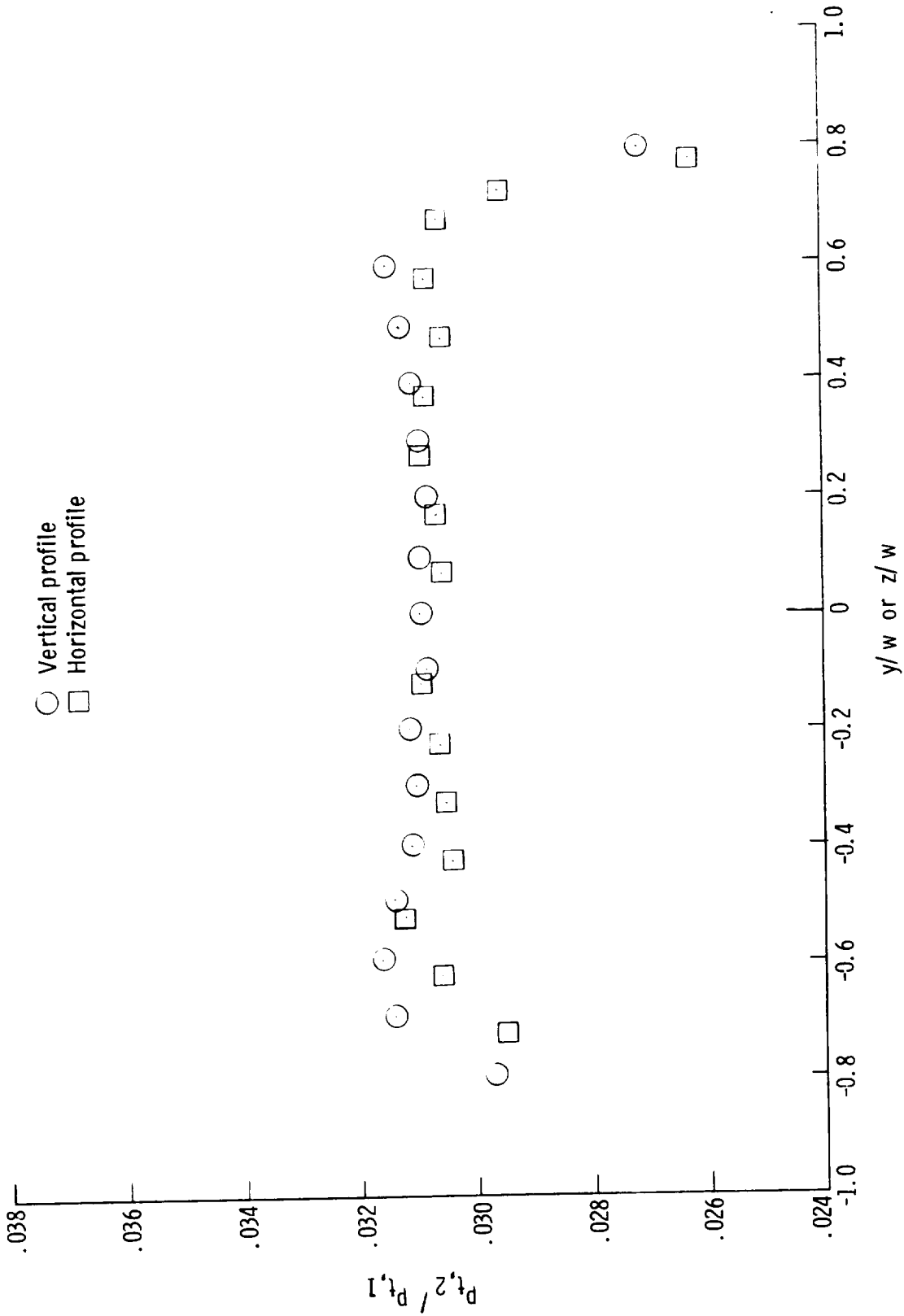
(d) $p_{t,1} \approx 1.14$ MPa; $T_{t,1} \approx 479$ K.

Figure 22.- Continued.
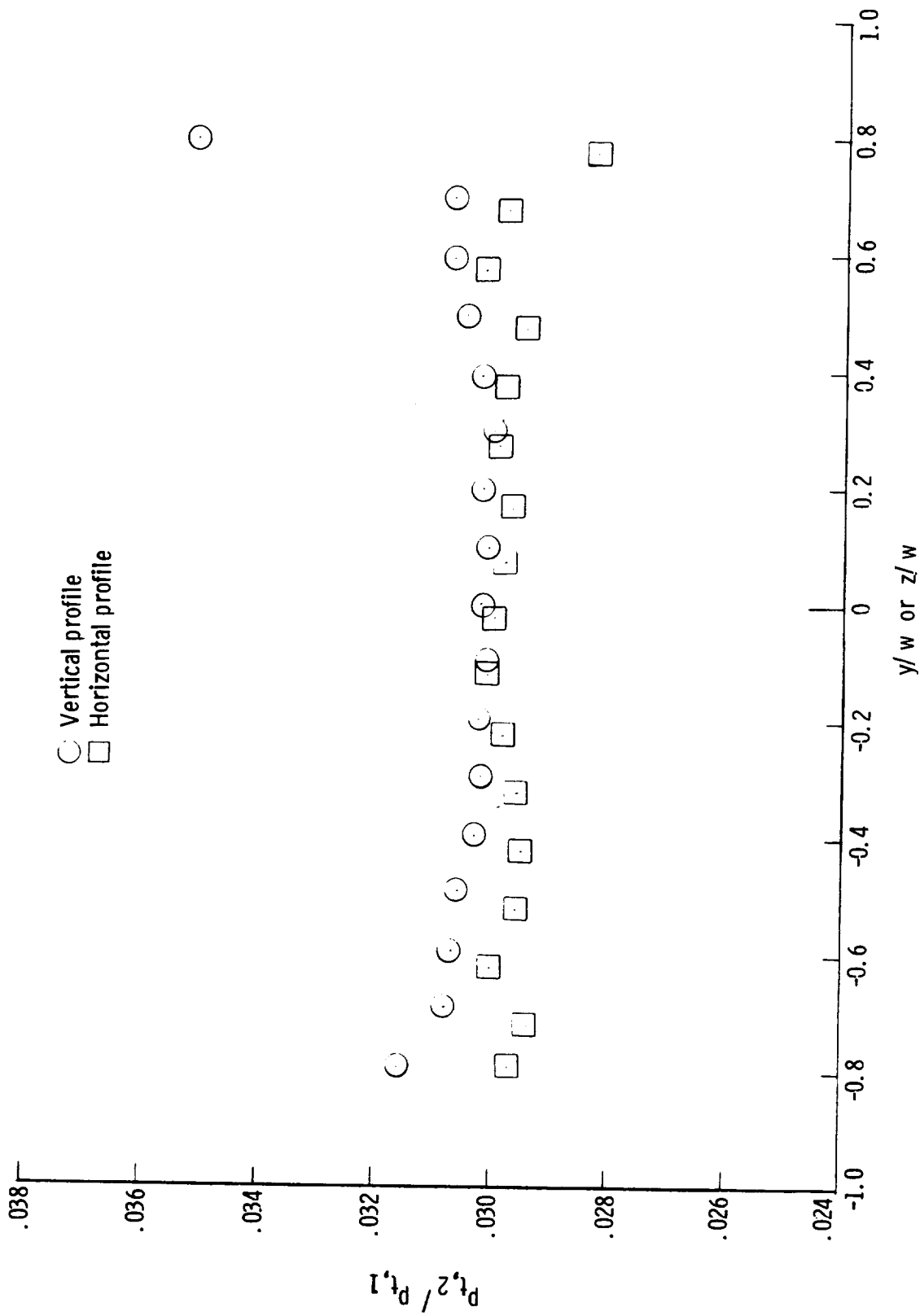
(e) $p_{t,1} \approx 2.18$ MPa; $T_{t,1} \approx 492$ K.

Figure 22.- Continued.
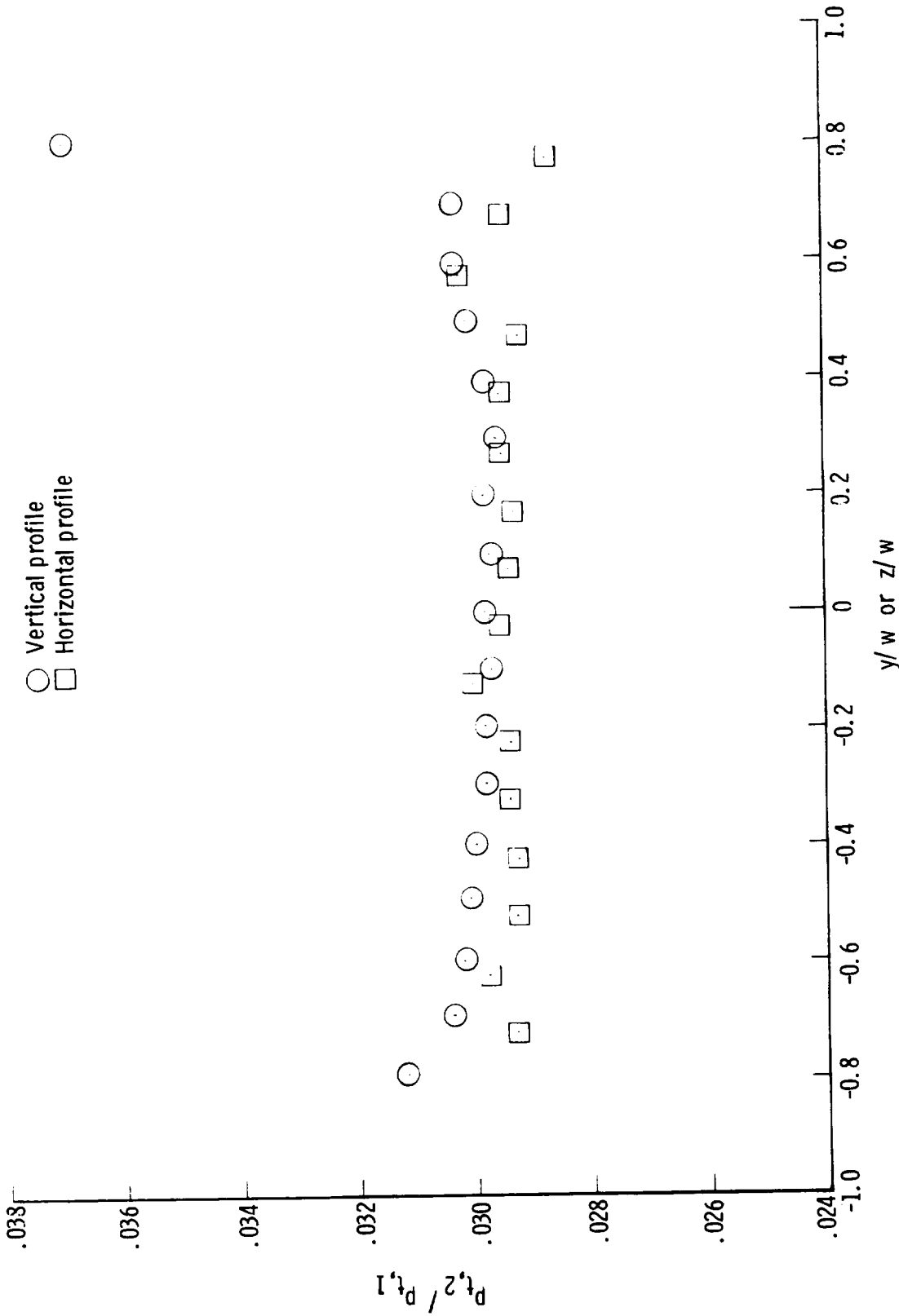
(f) $P_{t,1} \approx 3.06$ MPa; $T_{t,1} \approx 502$ K.

Figure 22.- Continued.
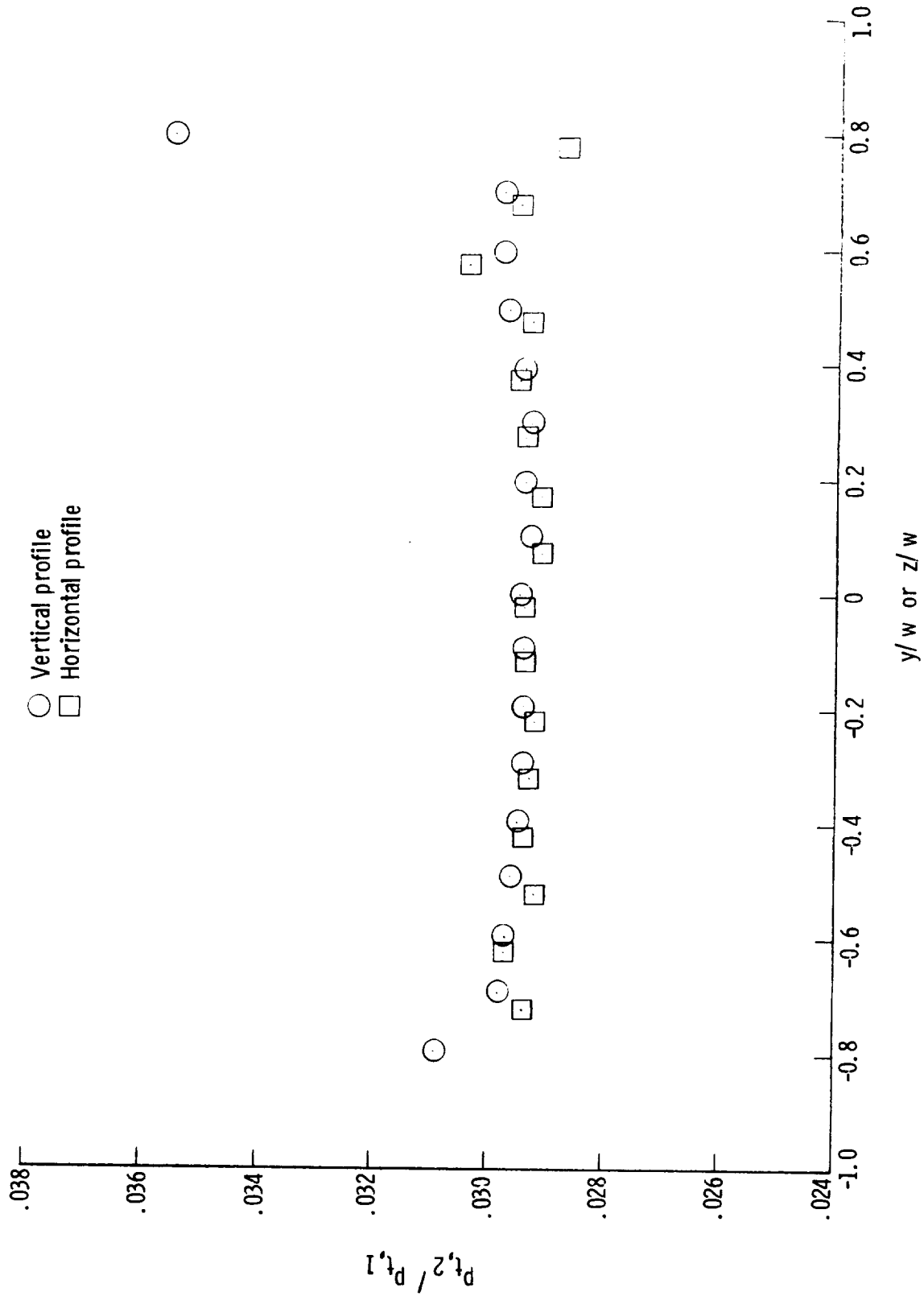
(g) $P_{t,1} \approx 3.60$ MPa; $T_{t,1} \approx 508$ K.

Figure 22.- Concluded.
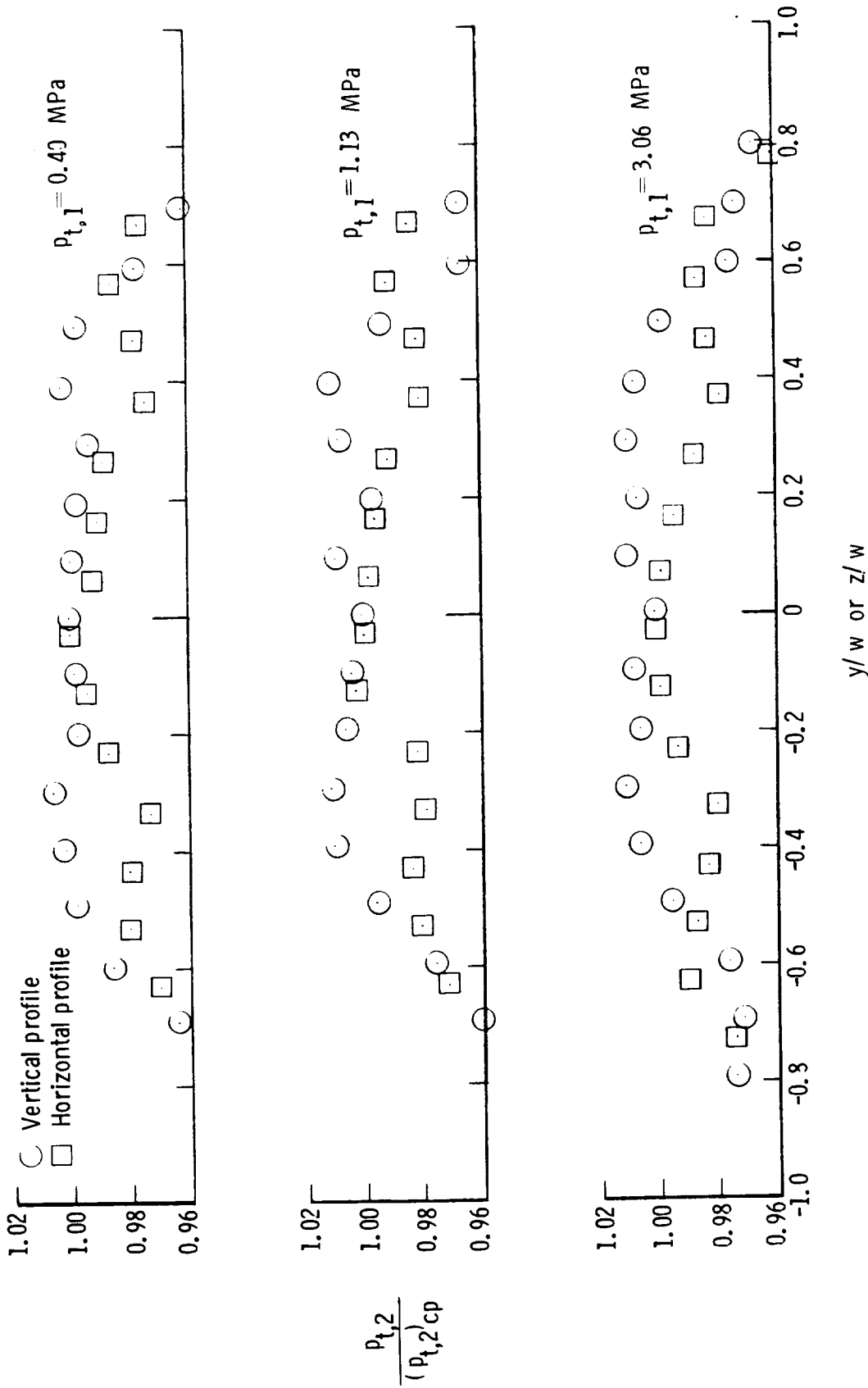
Figure 23.- Vertical and horizontal pitot pressure nondimensionalized by center-probe pitot pressure for several reservoir pressures. $x = -2.4$ cm.
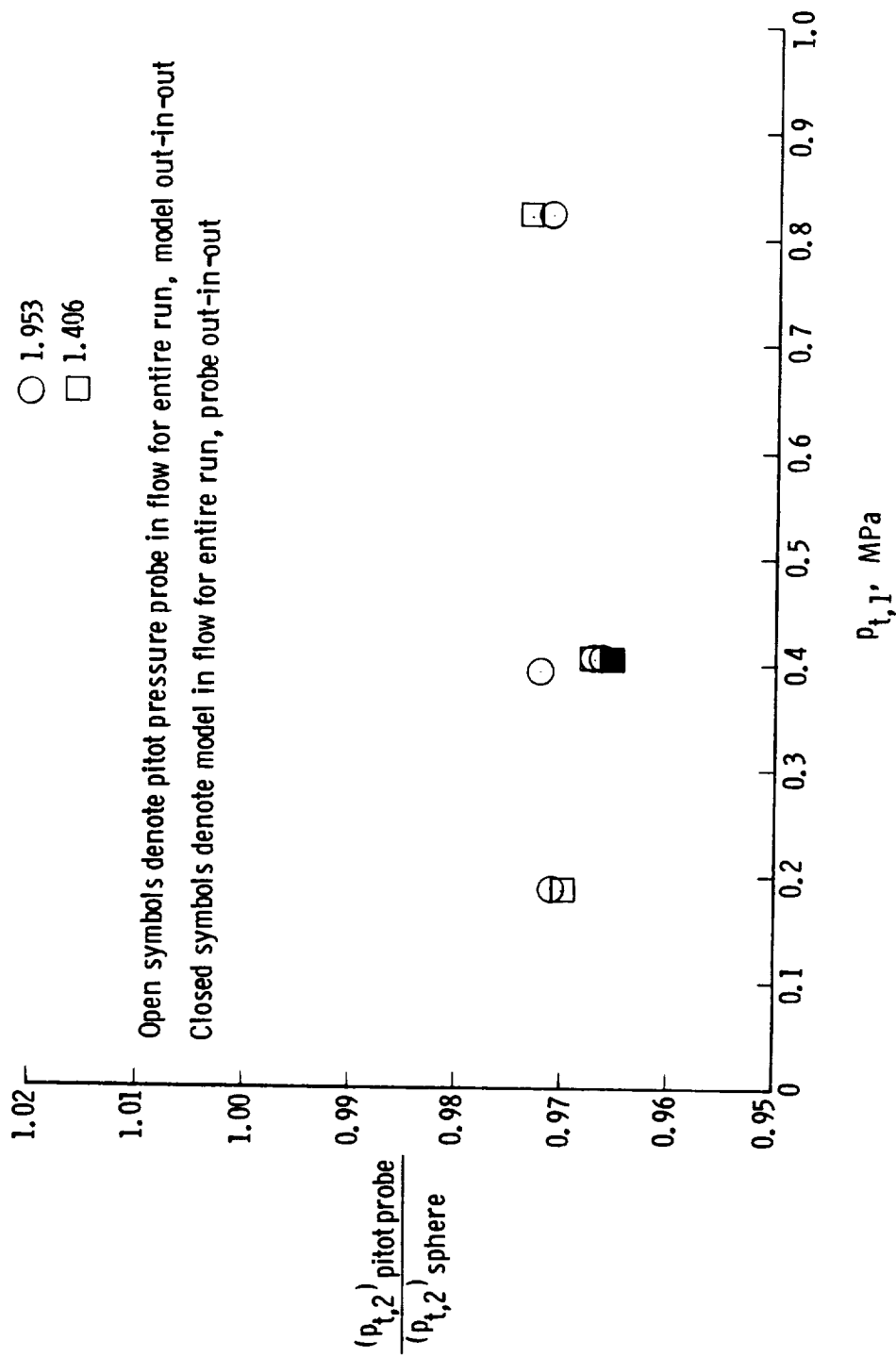
Figure 24.- Ratio of single pitot-probe pressure to sphere stagnation-point pressure as a function of reservoir pressure.